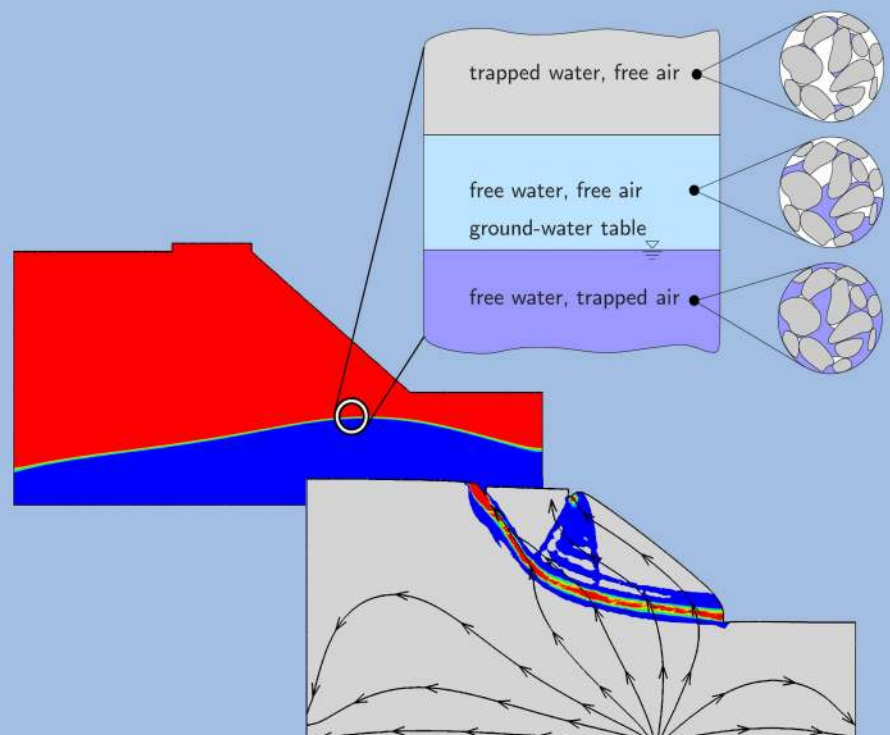


**Universität Stuttgart**  
Germany

**Institut für Mechanik (Bauwesen)**  
Lehrstuhl II, Prof. Dr.-Ing. W. Ehlers

# Coupled Deformation and Flow Processes of Partially Saturated Soil: Experiments, Model Validation and Numerical Investigations

Okan Avci



Report No.: II-26 (2013)



# **Coupled Deformation and Flow Processes of Partially Saturated Soil: Experiments, Model Validation and Numerical Investigations**

Der Fakultät Bau- und Umweltingenieurwissenschaften  
der Universität Stuttgart zur Erlangung der Würde  
eines Doktor-Ingenieurs (Dr.-Ing.)  
genehmigte Abhandlung

von

Dipl.-Ing. Okan Avci

aus

Waldshut-Tiengen

Hauptberichter: Prof. Dr.-Ing. Wolfgang Ehlers

Mitberichter: Prof. Dr.-Ing. Martin Schanz

Tag der mündlichen Prüfung: 11. Oktober 2013

Institut für Mechanik (Bauwesen) der Universität Stuttgart

Lehrstuhl für Kontinuumsmechanik

Prof. Dr.-Ing. W. Ehlers

2013

Report No. II-26  
Institut für Mechanik (Bauwesen)  
Lehrstuhl für Kontinuumsmechanik  
Universität Stuttgart, Germany, 2013

**Editor:**

Prof. Dr.-Ing. W. Ehlers

© Okan Avcı  
Institut für Mechanik (Bauwesen)  
Lehrstuhl für Kontinuumsmechanik  
Universität Stuttgart  
Pfaffenwaldring 7  
70569 Stuttgart, Germany

All rights reserved. No part of this publication may be reproduced, stored in a retrieval system, or transmitted, in any form or by any means, electronic, mechanical, photocopying, recording, scanning or otherwise, without the permission in writing of the author.

ISBN 3–937399–26–7  
(D 93 – Dissertation, Universität Stuttgart)

## Acknowledgements

The content of the presented work was carried out during my employment as a teaching assistant and research associate from 2005 until 2011 at the Institute of Applied Mechanics (Civil Engineering), at the University of Stuttgart. This would be not possible without the spadework of my supervisor Professor Wolfgang Ehlers at the field of the Theory of Porous Media as well as his broad knowledge in the field of continuum mechanics. I would like to thank Professor Wolfgang Ehlers for given me the opportunity to realise this work at his institute and, in particular, for his professional support at any time.

I am very grateful to the co-supervisor of my thesis Professor Martin Schanz for his auxiliary discussions and advices regarding my scientific research always when I met him at conferences and workshops.

The realisation of such a work is also not possible without the support of competent colleagues in a productive and pleasant atmosphere. For my happiness, I had great colleagues at the institute in an outstanding partnership, and to all of those I would like to say thank you. In particular, I would like to thank my former colleague and roommate Tobias Graf, who introduced me into the topic of theoretical and numerical investigations of partially saturated soils and for his proofreading of my thesis and as well Bernd Scholz, who supported me by reading up on the field of optimisation methods. I would also like to thank Arndt Wagner, Nils Karajan, Ayhan Acartürk and Hans-Uwe Rempfer for interesting and fruitful talks on different subjects related to this work. For the realisation of various experiments included in this thesis, I want to particularly thank the master craftsman Ralf Plonus for the construction of diverse experimental equipments and for carrying out many of the experiments.

Furthermore, I would like to thank Professor Bernd Markert for giving me constructive comments on my work. As a project scientist I worked in very close cooperation with him in the DFG Research Unit 'Coupling of Flow and Deformation Processes for Modelling the Movement of Natural Slopes'. He was besides Professor Wolfgang Ehlers the co-project leader of the research unit. I also want to thank the project partners of the research unit for the outstanding and successful cooperative work during the project phase.

And last but not at least, a great thank you to my family. They have been supporting me at any time during my educational development and, thus, give me the possibility to make up this thesis successfully. Especially, I would like to thank my brother Bircan Avcı for supporting me during our common study of civil engineering as well as for the very helpful discussions about my thesis and my sister Arzu Avcı for the very time-consuming proofreading of the work and for her constructive critical comments.

Stuttgart, October 2013

Okan Avcı

*Nie wird ein Mensch etwas entdecken,  
der sich vor einen Apparat setzt, beobachtet und ein Gesetz sucht,  
so wenig wie der, der nur nachdenkt, wie es sein könnte,  
ohne je die Natur zu befragen.*

Otto Teopltiz (1881-1940)



# Contents

<b>Deutsche Zusammenfassung</b>	<b>XIII</b>
Motivation . . . . .	XIII
Stand der Forschung . . . . .	XIV
Zielsetzung und Vorgehensweise . . . . .	XX
Gliederung der Arbeit . . . . .	XXIII
<b>Nomenclature</b>	<b>XXV</b>
Conventions . . . . .	XXV
Symbols . . . . .	XXVI
<b>1 Introduction and Overview</b>	<b>1</b>
1.1 Motivation . . . . .	1
1.2 State of the Art . . . . .	3
1.3 Aims and Scopes . . . . .	8
1.4 Outline of the Thesis . . . . .	11
<b>2 Continuum-Mechanical Fundamentals of the Theory of Porous Media</b>	<b>13</b>
2.1 Theoretical Basis . . . . .	13
2.2 Kinematical relations . . . . .	15
2.2.1 Motion function . . . . .	15
2.2.2 Deformation and strain measures . . . . .	17
2.2.3 Stress measures . . . . .	18
2.3 Balance relations . . . . .	19
2.3.1 General structure of the balance relations . . . . .	20
<b>3 Triaxial Experimental Investigations of Granular Materials</b>	<b>27</b>
3.1 Triaxial experimental . . . . .	27
3.1.1 Triaxial cell . . . . .	28
3.1.2 Volume-change monitoring . . . . .	29
3.1.3 Homogeneous standard triaxial tests . . . . .	31
3.2 Experimental observations of yielding and failure behaviour of sand . . . . .	34
3.2.1 Test-sand properties . . . . .	36
3.2.2 Characteristics of homogeneous test conditions . . . . .	36

<b>4</b>	<b>Constitutive Modelling</b>	<b>43</b>
4.1	Triphasic model for partially saturated sand . . . . .	43
4.2	Constitutive setting of the solid skeleton . . . . .	51
4.2.1	Elastic behaviour . . . . .	51
4.2.2	Plastic behaviour . . . . .	53
4.3	Constitutive setting of the mobile pore fluids . . . . .	60
<b>5</b>	<b>Numerical Treatment</b>	<b>65</b>
5.1	Finite-element method . . . . .	65
5.1.1	Weak formulation . . . . .	66
5.1.2	Spatial-domain discretisation . . . . .	69
5.1.3	Time-domain discretisation . . . . .	72
5.1.4	Solution of the non-linear system . . . . .	73
5.2	Parameter identification . . . . .	77
5.2.1	Gradient-based optimisation procedure . . . . .	79
5.2.2	<i>Lagrangean</i> dual problem (SQP method) . . . . .	80
5.2.3	Numerical sensitivity analysis . . . . .	82
<b>6</b>	<b>Calibration of the Partially Saturated Soil Model</b>	<b>87</b>
6.1	Mechanical behaviour of dry sand . . . . .	87
6.1.1	Calibration of the elasto-viscoplastic model . . . . .	88
6.1.2	Loading-path-dependent stress-strain behaviour . . . . .	93
6.1.3	Numerical model validation via simulation of sand box experiments . . . . .	98
6.2	Model calibration of the mobile pore fluids . . . . .	102
6.3	Numerical study of slope instabilities . . . . .	103
6.3.1	The slope conditions . . . . .	103
6.3.2	Numerical results and discussion . . . . .	104
<b>7</b>	<b>Numerical Investigation of a Slow-Moving Landslide</b>	<b>109</b>
7.1	Characteristics of the hillslope . . . . .	109
7.2	Idealisation of the hillslope to a 2-d cross section . . . . .	111
7.3	Numerical results and discussion . . . . .	113
<b>8</b>	<b>Modelling Internal Soil Erosion</b>	<b>117</b>
8.1	Restrictions of the erosion-soil model . . . . .	117
8.2	Partially saturated soil-erosion model . . . . .	118
8.3	Saturated soil erosion model . . . . .	122
8.4	Constitutive settings . . . . .	122
8.5	Numerical Examples . . . . .	125



---

8.5.1	1-d piping of a fully saturated column . . . . .	126
8.5.2	Cold production in oil saturated sand . . . . .	128
8.5.3	Numerical investigation of embankment problems . . . . .	130
<b>9</b>	<b>Conclusion</b>	<b>137</b>
9.1	Summary . . . . .	137
9.2	Outlook . . . . .	138
<b>A</b>	<b>Elementary Triaxial tests</b>	<b>141</b>
A.1	Deformation behaviour . . . . .	141
A.2	Boundary conditions . . . . .	141
<b>B</b>	<b>Important Relations</b>	<b>143</b>
B.1	Derivations of the total and effective quantities . . . . .	143
<b>C</b>	<b>Identified Triphasic Model of the GEBA Sand</b>	<b>145</b>
C.1	Parameters of the solid skeleton . . . . .	145
C.2	Parameters of the partially saturated zone . . . . .	146
	<b>Bibliography</b>	<b>147</b>
	<b>Curriculum Vitae</b>	<b>161</b>



# List of Figures

0.1	Veranschaulichung der gegenseitigen Abhängigkeiten der einzelnen Aufgabenfelder des Materialmodellierungsprozesses. . . . .	XXI
1.1	(left) Landslide (2009) in Nachterstedt, Germany, ( <a href="http://i418.photobucket.com/albums/pp263/glenlatterach/">http://i418.photobucket.com/albums/pp263/glenlatterach/</a> ) and (right) creeping Heumös hillslope in Ebnet, Austria ( <a href="http://www.grosshang.de">http://www.grosshang.de</a> ). . . . .	2
1.2	(left) The Teton Dam (1976) near Rexburg, Idaho, USA ( <a href="http://web.mst.edu/rogersda/teton_dam/">http://web.mst.edu/rogersda/teton_dam/</a> ) and (right) the Taum Sauk reservoir (2005) in Lesterville, Missouri, USA (Figure is taken from the United States Geological Survey published in Wikipedia). . . . .	2
1.3	Illustration of the individual task-field dependencies of the material modelling procedure. . . . .	9
2.1	REV of the qualitative micro-structure of a fluid saturated porous material (left), multi-component TPM macro model obtained by a volumetric homogenisation process, (right). . . . .	14
2.2	Motion of a superimposed multiphasic porous material with $\varphi^S$ as the solid skeleton and $\varphi^\beta$ as the fluid components where the solid and the fluids follows their own individual motion function. . . . .	16
3.1	(left) Assembled aluminium cell with a load piston of $\varnothing 2.5$ cm, (middle) dissembled parts, which are assembled in alphabetical order (A)-(E) where (F) is the socket of the specimen laying on (A) and (right) the top cell cover with the load piston of $\varnothing 10$ cm for extension tests. . . . .	29
3.2	P-v controller: (left) plunger cylinder on which a water tank capacity of $50 \text{ cm}^3$ is attached and (right) the p-v controller device. . . . .	30
3.3	(left) The controller test by which the load piston is driven down and up at constant cell pressure of 100 kPa and (right) the results of in-/outflow of cell water during the piston motion – comparison of measured data received by the p-v controller (the red curve with square dots) and the real motion of the plunger cylinder recorded by the dial gauge (the black curve with circle dots). . . . .	30
3.4	Systematic volume calibration error of the complete triaxial system. . . . .	31
3.5	Illustration of the stress path of a standard compression test with the confining pressure $\sigma^H = -p = \text{const.}$ in the principle stress space. . . . .	32
3.6	Illustration of the stress path of a standard compression test with $I_\sigma = \text{const.}$ in the principle stress space. . . . .	33
3.7	Standard cylindrical triaxial compression and extension loading paths presented in the hydrostatic (left) and deviatoric (right) stress planes. . . . .	34

3.8	Grain size distribution (GSD) of the GEBA fine sand (Germer and Braun [77]). . . . .	36
3.9	Triaxial compression test with a constant confining pressure of $\sigma_3 = 0.2$ MPa. 37	
3.10	Generic sketch of one of the triaxial stress path test for the determination of the contour of yield surfaces and the hardening behaviour presented (Tatsuoka and Ishihara [155]). . . . .	38
3.11	Sketch of the observed stress-strain behaviour of stress-path test 1 (a) and 2 (b). . . . .	40
3.12	Different types of stress-path experiments and evolution of the failure surfaces f-s (n-c) of the new concept and f-s (o-c) of the old concept, respectively. . . . .	40
3.13	Stress-path test 3: (left) the observed stress-strain behaviour and (right) the yielding behaviour. . . . .	41
4.1	Limit state described by the fully convex single-surface yield envelope $F(\boldsymbol{\sigma}_{Em}^S)$ . . . . .	53
4.2	Illustration of the yield surface characteristics of granular materials and its yielding behaviour: (left) the hydrostatic stress plane and (right) the deviatoric stress plane. . . . .	54
4.3	Sketch of the yield surface (y-s) evolution driven by plastic strains and the development of the stress-dependent failure surface (f-s) controlled by $I_\sigma$ . . . . .	60
4.4	Illustration of different zones of a partially saturated soil. . . . .	61
5.1	Comparison of the simulated and experimental data set, where $I_n$ is the error between the output quantities $ \Phi_n - \tilde{\Phi}_n $ determined at each discrete point of $n$ for given $U_n$ . . . . .	78
6.1	Unloading/reloading cycles of (a) a triaxial compression test and (b) a hydrostatic test of GEBA sand. . . . .	88
6.2	Triaxial compression tests and numerical simulations: (a) stress and volumetric strain vs. longitudinal strain and (b) stress progression in the hydrostatic plane. . . . .	90
6.3	Fixed failure surface with the old failure concept and stress-dependent failure surfaces of the new failure concept. . . . .	91
6.4	(a) Triaxial compression test and (b) evolution of the yield surfaces. . . . .	92
6.5	Triaxial compression/extension tests with constant stress invariants $I_\sigma^{c/e}$ : (a) shear stresses vs. strain and (b) shear stresses in the hydrostatic plane. . . . .	93
6.6	Experiment and simulation of the stress-path test 1 with growing and fixed failure surfaces. . . . .	94
6.7	Experiment and simulation of the stress-path test 2. . . . .	95

6.8	Computational results of evolving yield surfaces during the stress-path test 2: (a) first shear loading at $\sigma_3^{H1}$ , (b) unloading and second shear loading at $\sigma_3^{H2}$ , (c) unloading and reduction of $\sigma_3^{H2}$ to $\sigma_3^{H1}$ , (d) third shear loading and softening at $\sigma_3^{H1}$ . . . . .	96
6.9	Preconsolidated triaxial compression tests with confining pressures of $\sigma_3^{H1} = 0.05$ MPa and $\sigma_3^{H2} = 0.1$ MPa: (a) shear stress vs. longitudinal strain, (b) hydrostatic stress vs. volumetric strain. . . . .	97
6.10	Evolution of the yield surface: (a) preconsolidation phase up to $I_\sigma^{H2} = -2.85$ MPa, (b) shearing phase at constant $\sigma_3^{H1} = 0.05$ MPa and (c) at constant $\sigma_3^{H2} = 0.1$ MPa. . . . .	98
6.11	(a) Experimental box and (b) mechanical device for adjusting the slope angle. . . . .	99
6.12	Geometry and dimensions of the experimental box tests [cm]. . . . .	100
6.13	Failure sand-box experiments and numerical simulations of shear bands illustrated by $\ \epsilon_{Sp}\ $ : (a) and (b) foundation-failure problem, (c) and (d) slope-failure problem with a slope angle of $20^\circ$ . . . . .	100
6.14	Stress-displacement curves for the foundation-failure experiment (found.) and both slope-failure experiments with slope angles of $20^\circ$ (slope <sup>20</sup> ) and $30^\circ$ (slope <sup>30</sup> ) computed by (a) the new failure concept and (b) the old failure concept. . . . .	101
6.15	Evolution of the yield surface in point A during the foundation-failure simulation at different calculation times using (a) the new failure concept and (b) the old failure concept. . . . .	101
6.16	(left) Capillary pressure-saturation-relation and (right) relative permeability functions. . . . .	102
6.17	(left) Geometry and dimension of the slope in centimetres and (right) computed water saturation for a water table on the left side of the slope ( $h_{wl}$ ) = the water head on the right side of the slope ( $h_{wr}$ ) = 10 cm; $q$ is the mechanical load and $s^W$ is the water saturation. . . . .	103
6.18	FE mesh with 11347 triangle elements. . . . .	104
6.19	Case A at time 1389 s: (left) water table (w-t) at slope failure and (right) streamlines of water seepage flow and shear band. . . . .	105
6.20	Case B at time 1290 s: (left) water table (w-t) at slope failure and (right) streamlines of water seepage flow and shear band. . . . .	105
6.21	Case C: (left) water table (w-t) at failure (higher dividing line: $\dot{h}_{wm} = 11$ cm/s; lower line: $\dot{h}_{wm} = (11/600)$ cm/s) and (right) streamlines of water seepage flow and shear band at 30.8 s after increase of the load (the fast case). . . .	106
6.22	Case D: (left) water table (w-t) at failure (higher dividing line: $\dot{h}_{wm} = 11$ cm/s; lower line: $\dot{h}_{wm} = (11/600)$ cm/s) and (right) streamlines of water seepage flow and shear band at 20.7 s after increase of the load (the fast case). . . .	106

6.23	The accumulated plastic strains $\ \epsilon_{Sp}\ $ of Case C (the 5-s case): (left) the intermediate state at 20.7 s and (middle) 27.3 s after applying the load, and (right) the state at failure at 29.4 s. . . . .	107
6.24	Load-displacement curves of the load platen; $q$ is the mechanical load and $u$ is the vertical displacement. . . . .	107
6.25	Displacement and water pressure in point A (see Figure 6.17) versus time proceeding of (left) cases C and (right) case D. . . . .	108
7.1	The Heumös slope in Ebnet, Vorarlberg (Austria): (left) the view from north to south and (right) from east to west. . . . .	110
7.2	Topview of the Heumös slope: annual average mass movement of the slope measured at the slope surface (Depenthal and Schmitt [37]); the red line from west to east represents the investigated cross-section and the dotted red line illustrated the north-south cross-section (Ehlers et al. [57]); HH4, HH5 and HH6 are boreholes. . . . .	110
7.3	The substructure of the investigated cross-section is subdivided into three strata determined by refraction seismic (Rumpf et al. [131]). . . . .	111
7.4	Representative cross-section through the Heumös slope from west to east; $\dot{h}_{pw}$ is the pore water infiltration rate per week. . . . .	112
7.5	Evolution of the water saturation $s^W$ . . . . .	113
7.6	Evolution of shear bands determined by the accumulated plastic strains $\ \epsilon_{Sp}\ $ . . . . .	114
7.7	(top) Developed shear bands and (bottom) the corresponding water saturation. . . . .	115
8.1	Triaxial compression test with a confining pressure of $\sigma_2 = \sigma_3 = 0.2$ MPa = const. and the corresponding simulation applying the general (sim-gen) and the simplified hardening model (sim-simpl). . . . .	124
8.2	Sketch of the 1-d column piping problem. . . . .	126
8.3	1-d piping simulation results: (a) solid fraction $n^S$ ; (b) solid production $\hat{n}^S$ . . . . .	127
8.4	1-d piping simulation results: (a) shear modulus $\mu^S$ ; (b) loading-displacement curves related to the loading boundary. . . . .	127
8.5	Sand sample with the hydraulic loading condition. . . . .	128
8.6	Porosity propagation along the axis of the wormhole: (a) at the initial state; (b) after developing (Tremblay et al. [158]). . . . .	129
8.7	Degradation of $n^S$ starting with a homogeneous solidity distribution. . . . .	129
8.8	(a) Initial solidity $n_{0S}^S$ (inhomogeneous distribution), (b) degeneration of $n^S$ . . . . .	130
8.9	Geometry and dimensions of the embankment in [m]. . . . .	131
8.10	Loading phases $LP_i$ corresponding to the time ( $t$ ) and the w-t ( $h$ ) with respect to the slope toe: $t_1 = 24$ h, $t_2 = 192$ h, $t_3 = 216$ h and $t_{fail} \approx 226.5$ h; $h_1 = 3$ m and $h_2 = 2$ m. . . . .	132

8.11	Progression of $n^E$ and $\hat{n}^S$ (left) and $u_h$ and $\mathbf{w}_L$ over time $t$ of the right slope toe. . . . .	132
8.12	Simulation results at the end of LP <sub>2</sub> and at the failure state in LP <sub>4</sub> : (top) liquid saturation $s^L$ ; (bottom) solidity $n^S$ . . . . .	133
8.13	Evolution of shear bands: (left) at the end of LP <sub>2</sub> ; (middle) intermediate state in LP <sub>4</sub> at $t = 225$ s; (right) at failure state in LP <sub>4</sub> at time $t_{fail}$ . . . . .	133
8.14	Deformed mesh at the final state (left) 10-times and (right) 100-times magnification of the deformations. . . . .	134
8.15	Evolving of the material parameters (left) $\mu^S$ , (middle) $\epsilon$ and (right) $\delta$ . . .	134
8.16	Initiation of embankment failure caused by backward erosion: illustrating the development of a pipe within the core through backward erosion triggered by hydraulic gradient (Figure is abstracted from Foster et al. [71]).	134
8.17	Geometry and dimensions of the embankment with central core in [m]. . .	135
8.18	(top) Simulation results after the second loading phase and (bottom) during the third loading phase (failure state): (left) liquid saturation $s^L$ and (right) solidity $n^S$ . . . . .	136
8.19	(left) Deformed FE mesh at the final state with 10-times magnification and (right) the evolved shear band. . . . .	136
A.1	(left) Undeformed (initial) state and (right) homogeneous deformed state of a cylindrical sand specimen. . . . .	141
A.2	Idealisation of the cylindrical specimen for numerical computations. . . . .	142





# List of Tables

5.1	The global iteration algorithm for the determination of the primary variables $\mathbf{U}_n$ at the <i>Gauss</i> point at time $t_n$ . . . . .	74
5.2	The local iteration algorithm to determine the internal variables $\mathcal{I}_n$ at each single <i>Gauss</i> point within the $i$ -th global <i>Newton</i> iteration step at time $t_n$ . For reason of clarity, the index $i$ is omitted. . . . .	75
5.3	The local system of equations $\mathbf{R}_n^{loc}$ at the current time iteration step $n$ and $i$ denotes the index number $j = [1 - 4]$ of the hardening parameters $p_j = \{\beta, \delta, \epsilon, \gamma\}$ . . . . .	76
5.4	Overview of the best-knowing approximation matrices of $\mathbf{H}_i$ . . . . .	80
6.1	Boundary values and loading data of the investigated slope scenarios. . . .	104
8.1	Material parameters of the <i>Hookean</i> law, the <i>Mises</i> plasticity law without hardening and the erosion law. . . . .	127
8.2	Material parameters of the <i>Hookean</i> law and the erosion law. . . . .	130
C.1	Elasto-viscoplastic material parameters, cf. Ehlers and Avcı [56]. . . . .	145
C.2	<i>Van Genuchten</i> material parameters of the GEBA sand. . . . .	146



# Deutsche Zusammenfassung

Der Boden unter einem Bauwerk trägt dessen gesamte Last, einschließlich der auf ihn wirkenden Windlasten. Die Summe dieser Lasten wird über die Fundamente in den Boden übertragen. Entsprechend ist der Boden eins der Hauptglieder in der Stabilitätskette der gesamten Konstruktion. Der Boden muss die Aufnahme der Lasten mit möglichst geringen Deformationen erfolgen, denn andernfalls besteht die Gefahr eines Böschungs- oder Grundbruchversagens, was mit einer Instabilität bzw. mit einer Einsturzgefährdung des Bauwerks einhergeht. Des Weiteren kann ein Bodenversagen aus starken Niederschlagsereignissen oder Erdbeben hervorgehen und zu Hangrutschungen führen oder Dämme zum Versagen bringen und damit katastrophale Schäden für Mensch und Natur anrichten. Bevor das destruktive Versagen eintritt, kommt es zum abrupten Verlust der Tragfähigkeit des Bodens durch die im Boden stattfindenden verschiedenen physikalischen Vorgänge, wie die Lokalisierung von plastischen Deformationen. Da der Boden hauptsächlich aus einem Korngerüst besteht, bei dem die Lasten über Normal- und Reibungskräfte zwischen den Körnern getragen werden, ist jede Erhöhung der Bodenbelastung stets mit plastischen Deformationen verbunden. Des Weiteren wird das Deformationsverhalten des Bodens zusätzlich durch die strömenden Porenfluide, Wasser und Luft, stark beeinflusst. Es besteht also eine starke Kopplung zwischen den Deformations- und Strömungsprozessen. Insofern sind die experimentelle Untersuchung und die theoretische Modellierung des Bodenverhaltens eine große Herausforderung für den Ingenieur und Forscher. Nur auf der Basis einer detaillierten Erforschung des Bodenverhaltens ist es möglich, realistische Versagensprognosen von Naturhängen oder Dämmen durch Vorausberechnungen zu geben. Für die Realisierung dieser Ziele werden hoch entwickelte Materialmodelle für Böden sowie effiziente und robuste numerische Berechnungsmethoden benötigt. Der Einsatz von Computersimulationen wird in solchen geomechanischen Fragestellungen immer wichtiger werden, weil anhand der Simulation das Verständnis über die ablaufenden komplexen, physikalischen Prozesse deutlich verbessert werden kann.

## Motivation

In den letzten Jahren ist die Anzahl von Hangrutschungen, die durch lang anhaltende starke Niederschlagsereignisse ausgelöst werden, weltweit angestiegen. Als Beispiel hierzu ist der Erdrutsch im Jahr 2009 in Nachterstedt (Deutschland) zu nennen, bei dem sich etwa 1 Million Kubikmeter Erde löste und in den Concordia-See rutschte. Dieser See wurde durch kontrolliertes Fluten einer stillgelegten Mine künstlich angelegt, wofür der Grundwasserspiegel stufenweise erhöht wurde. Dies war aber letztendlich der Grund für das Versagen der Böschung. Im Gegensatz zu diesem schlagartig eintretenden Erdrutsch sind Hangbewegungen wie die des *Heumöser* Hangs langsam und unstetig. Dieser Hang, der in Ebnit in der Nähe von Dornbirn (Österreich) liegt, kriecht etwa im Durchschnitt 10 cm im Jahr, und dies – bis jetzt – ohne Anzeichen auf ein abruptes Abrutschen des Hangs. Daher ist es von besonderem Interesse, das Gefahrenpotential von solchen kri-

tischen Hängen zu analysieren, bevor es tatsächlich zum Versagen kommt. Dazu können Computeranalysen einen großen Beitrag leisten, indem sie mögliche Hangbewegungen und -rutschungen prognostizieren.

Im Angesicht der immer häufiger auftretenden Hochwasserereignisse sind viele dicht besiedelte Gebiete in der Nähe von Seen und Flüssen permanent gefährdet. Der Schutz von solchen Hochwassergebieten durch Dämme und Deiche erlangt immer mehr eine gewichtige Bedeutung. Ein weiterer nennenswerter Aspekt ist hier die globale Klimaerwärmung und das damit verbundene Abschmelzen der polaren Eiskappen mit verheerenden Folgen eines steigenden Meeresspiegels. Des Weiteren werden Dämme nicht nur zum Schutz vor Hochwasser gebaut, sondern auch immer mehr zur Gewinnung von regenerierbaren Energien eingesetzt. So werden durch das Aufstauen von Flüssen hohe Wasserkräfte generiert, um dann entsprechend Turbinen anzutreiben. Die riesige, aufgestaute Wassermenge besitzt allerdings eine enorme zerstörerische Kraft, die bei einem Dammbruch, wie z. B. beim Versagen des Teton Damms (1976) oder des Taum Sauk Damms (2005), für Mensch und Natur eine große Gefahr bedeutet. Der Einsturz dieser Dämme wurde durch eine innere Erosion des Bodens induziert. Bei der inneren Erosion werden die Körner von der Kornstruktur des Bodens durch die Strömungskraft des Porenwassers gelöst, so dass die Porosität des Bodens zunimmt, und der Boden hierdurch fortlaufend seine Tragfähigkeit verliert, bis schließlich der Damm zusammenbricht. Aus diesem Grund ist es wichtig, kritische Schwachstellen in der Dammkonstruktion so früh wie möglich zu erkennen, um rechtzeitig notwendige Gegenmaßnahmen einzuleiten. Hierzu können Computersimulationen von Dämmen helfen, kritische Schwachstellen einer Konstruktion zu finden.

## Stand der Forschung

Genaue numerische Berechnungen von komplexen geotechnischen Problemstellungen gewinnen immer mehr an Bedeutung. Diese Anforderungen beziehen sich insbesondere auf fundierte Vorhersagen des Spannungs-Dehnungsverhaltens von granularen Materialien unter sich ständig ändernden mechanischen und hydraulischen Belastungsbedingungen. In der Hinsicht besteht der Bedarf an geeigneten mathematischen Materialmodellen, die jeweils die Fähigkeit besitzen, das Verhalten von teilgesättigten deformierbaren Böden realistisch abzubilden. Im Folgenden wird ein Überblick über die Forschungsthemen gegeben, die in dieser Arbeit behandelt werden.

### *Konstitutivmodellierung von teilgesättigten Böden*

Teilgesättigte Reibungsmaterialien werden im Allgemeinen durch ein Dreiphasenmodell beschrieben. Die individuellen Phasen sind das materiell inkompressible, elastisch-plastische oder elastisch-viskoplastische Festkörperskelett, das materiell inkompressible Porenwasser und die materiell kompressible Porenluft. Basierend auf einem kontinuumsmechanischen Ansatz haben Ehlers und Blome [58] oder Ehlers et al. [64] im Rahmen der Theorie Poröser Medien (TPM) das Dreiphasenmodell in einer thermodynamisch konsistenten Form hergeleitet. Die TPM ist ein erweitertes Modell der Mischungstheorie (MT) im Kontext des Konzepts der Volumenanteile. Im Gegensatz zur MT berücksichtigt die

TPM die mikro-strukturellen Informationen des porösen Materials in einer homogenisierten Weise. Die Mischungstheorie findet vorwiegend Anwendung in der chemischen Ingenieurwissenschaft, wo Mischungen mit chemisch reagierenden (mischbaren) Konstituierenden beschrieben werden. Bei dergleichen Mischungen ist die mikrostrukturelle Information im System prinzipiell irrelevant. Die vorwiegende Entwicklung der MT geht auf die Arbeiten von Truesdell und Toupin [163], Bowen [19] sowie Truesdell [161] zurück, wohingegen die grundlegenden Ansätze und Herleitungen der TPM in den Arbeiten von Bowen [20, 21], de Boer [13, 14], de Boer und Ehlers [15, 16] oder Ehlers [46, 47, 52, 53] sowie in den darin zitierten Arbeiten zu finden sind.

Eine anspruchsvolle Aufgabe im Bereich der Geomechanik ist die Bestimmung des komplexen Spannungs- und Dehnungsverhaltens von kohäsionslosen granularen Materialien wie Sand. Um das plastische Verhalten solch eines Materials numerisch zu beschreiben, wurden in den letzten sechs Jahrzehnten verschiedene Fließfunktionen entwickelt, vgl. z. B. die Arbeiten [12, 32, 38, 39, 96, 100, 121, 128]. Die Vor- und Nachteile von einigen dieser Fließfunktionen werden in [49] ausführlich diskutiert. In der vorliegenden Arbeit wird das Einflächenfließkriterium von Ehlers [48] verwendet, welches abwärtskompatibel zu anderen plastischen Modellen ist, wie z. B. zu dem bekannten *Drucker-Prager*-Kriterium oder dem *von-Mises*-Kriterium für nicht poröse Materialien. Charakteristisch ist, dass granulare Materialien bereits mit der ersten Belastung ein hochgradig nicht-lineares Materialverhalten aufzeigen, welches mit elastischen und plastischen Deformationen gekoppelt ist. Das entsprechende Verfestigungsverhalten wird durch die Entwicklung der Fließkontur beschrieben und dabei entweder durch die plastische Arbeit [66] oder durch die plastischen Dehnungen [67] gesteuert. Durch die Zerlegung der plastischen Verzerrung in einen volumetrischen und einen deviatorischen Anteil ist es möglich, das isotrope Verfestigungs- und Entfestigungsverhalten in einer einfachen und effizienten Art zu modellieren, vgl. Krenk [96], Desai [40] (Seite 181) und Scholz [137]. Die Verfestigung der Fließfläche wird hier durch eine konstante Bruch- bzw. Grenzfließfläche begrenzt, die die Fließfläche bei maximaler Deviatorspannung wiedergibt. Diese Annahme wurde experimentell von Ehlers und Avci [56] untersucht mit dem Ergebnis, dass die Bruchfläche zum einen variabel ist und zum anderen vom Spannungszustand abhängt. Das bedeutet, dass das granulare Material bestrebt ist, im Bruchzustand eine möglichst kleine Grenzfließfläche zu generieren. Als Konsequenz auf das spannungsabhängige Bruchverhalten haben Ehlers und Avci [56] eine variable Funktion für die sich entwickelnde Grenzfließfläche eingeführt. Diese wird vom hydrostatischen Spannungszustand reguliert. In dieser Arbeit wird diese besondere Eigenschaft von granularem Material hinsichtlich der experimentellen Untersuchungen und der konstitutiven Modellierung im Detail diskutiert. Die daraus gewonnene Erkenntnis zeigt, dass dieses Bruchverhalten für die genaue Modellierung von Anfangsrandwertproblemen (ARWP) wesentlich ist.

Um den charakteristischen Eigenschaften teilgesättigter Böden Rechnung zu tragen, postulierten Alonso et al. [1], Bolzon et al. [18] und Laloui und Nuth [102], dass die Fließfläche im Rahmen der elastisch-plastischen Theorie eine Funktion des Spannungszustands sowie der Porenwassersättigung ist. Im Gegensatz hierzu wird beim effektiven Spannungskonzept (vgl. z. B. bei Skempton [146], Ehlers und Blome [58] oder Ehlers et al. [57, 64]) der Einfluß der Kapillareigenschaft des Bodens auf das elastisch-plastische Verhalten durch

den resultierenden Porendruck berücksichtigt. In der ungesättigten Zone reduziert der negative Porenfluiddruck, der dem Kapillardruck entspricht, die effektive Festkörperspannung. Folglich können das plastische Verhalten und die Sättigungseigenschaft des Bodens hier entkoppelt betrachtet werden. Diese Entkopplung vereinfacht auch die experimentelle Ermittlung des mechanischen und hydraulischen Verhaltens des Bodens sowie die Parameteridentifikation. Basierend auf dem effektiven Spannungskonzept haben Ehlers et al. [57] den Versteifungseffekt einer Böschung infolge der Kapillarwirkung im Boden numerisch untersucht.

### *Experimentelle Untersuchung*

Ausgehend von nicht-mischbaren Materialien in Verbindung mit dem *Prinzip der Phasentrennung* können das Deformationsverhalten sowie die hydraulischen Eigenschaften des teilgesättigten Bodens entkoppelt untersucht werden, indem nur einer dieser beiden Prozesse für die jeweilige Untersuchung aktiviert wird. Die mechanisch-hydraulischen Kopplungsmechanismen werden dann anschließend durch Konstitutivansätze berücksichtigt. Dadurch werden die experimentelle Untersuchung und die theoretische Modellierung des Bodens deutlich vereinfacht. Demzufolge können die Spannungs-Dehnungscharakteristika des Festkörperskeletts des zu untersuchenden teilgesättigten Bodens anhand von fluidgesättigten (Porenluft oder -wasser) Proben unter homogenen Randbedingungen durch Triaxialversuche bestimmt werden. Dahingegen können die hydraulischen Eigenschaften des Bodens wie die Permeabilität, die Bewegung der Porenfluide in der ungesättigten Zone, etc., durch deformationsfreie Experimente erfasst werden, d. h., ohne externe Belastung der Bodenprobe, cf. Ehlers et al. [57].

Kohäsionslose granulare Reibungsmaterialien wie Sand sind statisch nur dann stabil, wenn sie unter hydrostatischem Druck stehen. Daher wird das Materialverhalten eines Sands durch Triaxialversuche bestimmt. Hier wird die Sandprobe in der Triaxialzelle in eine Latexmembran eingepackt und durch entgastes Zellwasser unter Vorspannung gesetzt. Der Wasserdruck, der auf die Probe wirkt, wird dabei mit einem Volumen-Druck-Messgerät reguliert. Die zentrale Herausforderung bei der Durchführung von Triaxialversuchen besteht darin, die Volumendeformation der Probe exakt zu messen. Hierzu werden in der einschlägigen Literatur verschiedene Methoden mit unterschiedlichen Anforderungen an die Volumenmessgenauigkeit vorgeschlagen. Die meisten dieser Methoden wurden von Alva-Hurtado und Selig [2] oder von Geiser et al. [74] dokumentiert, wobei Alva-Hurtado und Selig [2] die Messmethoden in drei Kategorien unterteilen. Die erste und zweite Kategorie stehen jeweils für eine Methode, bei der das ein- und ausströmende Zellwasser infolge Probendeformation gemessen bzw. bei der die Porenvolumenänderung durch die Messung des Zu- und Abflusses des Porenwassers ermittelt wird. Die letztgenannte Methode ist jedoch nur mit gesättigten Proben und drainierten Randbedingungen durchführbar. Im Gegensatz zu den Methoden der ersten beiden Kategorien wird beim Ansatz der dritten Kategorie die Volumendehnung durch Wegmesser direkt an der Probe gemessen.

Im Rahmen dieser Arbeit werden Triaxialversuche mit homogenen und drainierten Bedingungen durchgeführt. Folglich kommen hier alle drei Kategorien in Frage. Den einfachsten und unkompliziertesten Ansatz, um Volumenänderungen einer Probe zu messen, liefert die Methode der ersten Kategorie. Bei ihr spielen die Steifigkeit und das Fassungsver-

mögen der Zelle hinsichtlich der Fehlerkalibrierung eine zentrale Rolle. Leong et al. [105] haben von verschiedenen Triaxialzellen, wie z. B. von Triaxialzellen aus Acrylglas, aus Stahl oder von Konstruktionen aus doppelwandigen Zellen, den diesbezüglichen Messfehler analysiert. Ihren Untersuchungen nach liefern die Zelldeformation und die benötigte Menge an Zellwasser den Hauptanteil des Messfehlers. In Anbetracht dieser beiden Fehlerquellen wird in der vorliegenden Arbeit eine neue steife Triaxialzelle aus Aluminium vorgestellt, deren Kapazität genau auf die Volumendehnung der Probe optimiert ist. Damit konnte der absolute Kalibrierungsfehler der Triaxialversuchsanlage deutlich minimiert werden, vgl. Ehlers et al. [57].

Zur Kalibrierung der Konstitutivgleichungen des Spannungs-Dehnungsverhaltens des zu untersuchenden Sands sind in dieser Arbeit etliche Triaxialexperimente an zylinderförmigen, trockenen und dicht gepackten Sandproben unter homogenen und drainierten Randbedingungen durchgeführt worden. Dieser Satz an Experimenten besteht zum einem aus hydrostatischen Kompressionsversuchen und zum anderen aus Kompressions- und Extensionsscherversuchen mit unterschiedlichen Vorspannungen, um die Abhängigkeit des Materialverhaltens vom isotropen Spannungszustand zu untersuchen. In diesem Zusammenhang konnte durch spannungspfadabhängige Triaxialversuche eine wesentliche Eigenschaft des Sands in Bezug auf das Fließ- und Bruchverhalten ermittelt werden.

### *Parameteridentifikation*

Durch stetig verbesserte experimentelle Verfahren nimmt das Wissen über das physikalische Verhalten von Böden stetig zu. Dieses Wissen erlaubt in der Tat, immer anspruchsvollere Materialmodelle zu entwickeln. Die Weiterentwicklung der Modelle hat allerdings zumeist zur Folge, dass die Anzahl der Materialparameter zunimmt. Insofern wird die Bestimmung der Materialparameter immer schwieriger, so dass der Einsatz von Optimierungsverfahren für deren Identifizierung unumgänglich wird. Die Parameteridentifizierung erfolgt durch die inverse Berechnung der Experimente, wobei die Rechnung stets mit verbesserten Parametern wiederholt wird. Der verbesserte Parametersatz wird durch den Einsatz von gradienten-basierten Optimierungsverfahren ermittelt. Die zugrunde liegende Iteration ist hier dann beendet, wenn der optimale Parametersatz gefunden ist, der die experimentellen Ergebnisse bestmöglich approximiert. Die Optimierungsaufgabe der Parameteridentifikation wird durch eine vorgegebene Zielfunktion ausgedrückt. Diese ist durch die Summe der Quadrate der Approximationsfehler definiert, die es zu minimieren gilt. Dieses Vorgehen wird auch als die *Methode der kleinsten Fehler-Quadrate* bezeichnet.

Die Strategien verschiedener Optimierungsmethoden, die zur Lösung der Zielfunktion eingesetzt werden, werden in deterministische (reproduzierbare) Verfahren (Luenberger und Ye [109], Bertsekas [8] und Spellucci [147]) und in stochastische (nicht reproduzierbare) Verfahren (Bäck und Schwefel [4] und Schwefel [142]) differenziert. Des Weiteren werden die Verfahren der ersten Gruppe in die Kategorien gradienten-basierte und gradienten-freie Methoden unterteilt. Zu der ersten Kategorie, also zu den gradienten-basierten Methoden, gehören die *Newton*-Verfahren und die *Quasi-Newton*-Verfahren. Im Gegensatz zu den erstgenannten Verfahren approximieren die zweitgenannten – hierzu zählen z. B. das *Gauss-Newton*-Verfahren, das *Levenberg-Marquardt*-Verfahren oder das *BFGS* (*Broyden-Fletcher-Goldfarb-Shannon*)-Verfahren – die rechenaufwendige *Hesse*-Matrix (diese Ma-

trix stellt die zweite Ableitung der Zielfunktion dar) – auf der Basis der ersten Ableitung der Zielfunktion. Die Kategorie der gradienten-freien Verfahren umfasst ebenso zwei große Gruppen. Diese sind auf der einen Seite die deterministisch-basierten *Simplex* Methoden, vgl. Nelder und Mead [119], und auf der anderen Seite die stochastischen Methoden. Ein Überblick über die wichtigsten Optimierungsverfahren ist z. B. in Rao [129] zu finden.

Die Lösung eines Optimierungsproblems ist aufgrund der großen Anzahl der Parameter meist nicht eindeutig. So liegt das hier angestrebte Ziel darin, die optimale Kombination der Parameter zu finden, die unter den vielen vorhandenen lokalen Minima das globale Minimum des Optimierungsproblems repräsentiert. Allerdings führen nicht alle Optimierungsmethoden zum optimalen Parametersatz, anhand dessen die beste Übereinstimmung zwischen den experimentellen und numerischen Ergebnissen erreicht wird. Welche Methode nun zur Lösung des betrachteten Problems am besten geeignet ist, hängt von den Anforderungen des formulierten Optimierungsproblems ab. Zum Beispiel ist die Qualität der Lösung von gradienten-basierten Optimierungsverfahren stark von den Anfangswerten der Parameter abhängig, weil jeder neu verbesserte Parametersatz in Richtung des steilsten Abstiegs der Zielfunktion ermittelt wird. Folglich endet der Optimierungsprozess meist in einem der lokalen Minima. Demgegenüber decken stochastische Verfahren, wie die Evolutionsstrategien, ein breites Optimierungsgebiet ab. Die Wahrscheinlichkeit das globale Minimum zu finden, ist in dem Fall deutlich größer. Jedoch benötigen diese Verfahren eine hohe Anzahl an Auswertungen der Zielfunktion, insbesondere bei Optimierungsproblemen mit vielen Parametern (Mahnken [111]).

#### *Numerische Untersuchungen von Hangrutschungen*

Numerische Untersuchungen von Naturhängen mit der Finite-Elemente-Methode (FEM) werden immer wichtiger. Denn zum einen kann man durch numerische Stabilitätsuntersuchungen von bestehenden aber gefährdeten Hängen mögliche Versagensprognosen geben und zum anderen kann man durch Simulationen von bereits ereigneten Hangrutschungen eine Modellverifizierung vornehmen. Zum Beispiel haben Ferrari et al. [72] in diesem Zusammenhang die Hangrutschung der Steinernase im Kanton Aargau (Schweiz) nachsimuliert. Diese Berechnungen basieren auf einer schwach gekoppelten mechanischen und hydraulischen Simulationsmethode, bei der fortlaufend die entsprechenden Randbedingungen aktualisiert werden. Die entsprechenden Modellparameter wurden in dieser Arbeit auf der Basis der Daten eines am Hang durchgeführten Langzeitmonitorings identifiziert. Einen anderen vollgekoppelten Ansatz, verfolgen hingegen Ehlers et al. [57] in ihrer Arbeit, worin basierend auf einem vollgekoppelten Modell der Heumöser Hang in Ebnet (Österreich) entlang idealisierte Querschnitte (Lindenmaier [107]) numerisch untersucht wurde. Wenn jedoch Hangrutschungen anhand von anspruchsvolleren Materialmodellen untersucht werden sollen, z. B. bei besonderem Interesse des Einflusses der interagierenden hydraulischen und mechanischen Prozesse, ist es ein gängiges Vorgehen, auf idealisierte und wohldefinierte Hanggeometrien zurückzugreifen (Darve und Laouafa [35], Tsaparas et al. [164], Ehlers et al. [57, 64], Klubertanz et al. [94]). Allerdings erfordern zuverlässige Vorhersagen über das Stabilitätsverhalten von Hängen auf der Basis von FEM Analysen eine hohe räumliche Auflösung der Lokalisierungszone von plastischen Deformationen. In dieser Hinsicht haben Ehlers et al. [64] zur hinreichend genauen Bestimmung der Scher-



bänder in teilgesättigten Böden ortsadaptive Methoden angewendet. Große dreidimensionale Baugrubenprobleme wurden von Ammann [3], Wieners et al. [177] und Graf [78] auf einem Multiprozessorsystem parallel berechnet (ohne Ortsadaptivität). Das plastische Fließverhalten des Bodens wurde in diesen Arbeiten jedoch ohne die Ver- und Entfestigungseigenschaft des Materials simuliert.

#### *Simulation der inneren Erosion*

Das Ablösen der Körner von der Kornstruktur des Bodens durch die Sickergeschwindigkeit des Porenwassers und der anschließende Transport dieser Körner durch das Netzwerk von Porengängen werden als die innere Erosion des Bodens bezeichnet. Ziems [183] ist hier genauer und differenziert zwischen der inneren Erosion und der inneren Suffusion. Diese unterscheiden sich darin, dass die Suffusion sich nur auf den Transport des Klein- oder Feinkornanteils des Bodens beschränkt – so bleibt die Haupttragstruktur des Bodens, die vom Grobkornanteil gebildet wird, hier unberührt – und dass die Erosion alle Körner der Struktur umfasst. Im Erosionsfall kann die Hauptkornstruktur dementsprechend durch hohe Sickergeschwindigkeiten lokal aufgebrochen werden, so dass sich langsam fortschreitend ein Erosionskanal entwickeln kann, vgl. Bendahmane et al. [6], Wan und Fell [170] und Indraratna et al. [90]. In diesem Sinne ist die Suffusion ein Sonderfall der Erosion, welche nur bei niedrigen Sickergeschwindigkeiten vorzufinden ist. In dieser Arbeit wird nur die innere Suffusion betrachtet und im Folgenden allgemein als innere Erosion bezeichnet. Ein innerer Erosionsprozess ist insbesondere bei Dämmen vorzufinden. Dieser kann die Tragfähigkeit des Bodens sowie dessen Dichtheit gegen die Infiltration des aufgestauten Wassers lokal entscheidend herabsetzen und im schlimmsten Fall ein Dammversagen auslösen.

Eine kontinuumsmechanische Beschreibung von erodierbaren gesättigten Böden wurde von Vardoulakis et al. [168] und Wang und Wan [173] vorgestellt. Sie verwenden ein allgemein bekanntes Zweiphasenmodell, das aus einer Festkörperphase und einer Porenfluidphase besteht und erweitern diese um eine Erosionsphase. Die Erosionsphase repräsentiert die gelösten und die im Fluid freibeweglichen Körner. Auf diesem Modellansatz basierend haben Steeb und Diebels [151] im Rahmen der TPM ein Dreiphasenmodell für erodierbare gesättigte Böden in einer thermodynamisch konsistenten Darstellung hergeleitet. Der Fluidisierungsprozess der Kornstruktur wird in dem Fall durch den Massenaustausch bzw. die Massenproduktion zwischen der Festkörper- und der Fluidphase beschrieben. Die antreibende Kraft ist hier die Sickergeschwindigkeit des Porenfluids, vgl. Vardoulakis et al. [168] und Steeb et al. [153], oder des Porengases, vgl. Steeb [150]. Angesichts dessen, dass die Suffusion nur auf den Anteil der Feinkorngrößen beschränkt ist, haben Steeb et al. [153] die gesamte Kornstruktur in einen stabilen Anteil, der den nicht erodierbaren Anteil der Struktur darstellt, und in einen instabilen erodierbaren Feinkornanteil unterteilt. Jedoch führt dieses Vorgehen zu einer größeren Anzahl an Bilanzgleichungen für das kontinuumsmechanische Problem.

Das mechanische Verhalten eines Bodens wird nur vom Suffusionsprozess beeinflusst, wenn der Grobkornanteil weniger als 70 % beträgt. Diese Eigenschaft wurde für Böden wurde von Vallejo [165] durch Triaxialversuche an Proben beobachtet, die mit verschiedenen Mengenverhältnissen von zwei unterschiedlich großen Glaskugeln homogen aufgebaut

wurden. Er hat dabei festgestellt, dass die maximale Festigkeit einer Probe bei minimaler Porosität erreicht wird. Diese ergibt sich dann, wenn zwischen dem Klein- und Großkugelanteil ein optimales Verhältnis besteht. Das Haupttraggerüst des Bodens wird in dem Fall hauptsächlich vom Großkornanteil gebildet. Die Festigkeit wird aber dennoch anteilig vom Klein- und Großkorn bestimmt. So werden die mechanischen Eigenschaften des Bodens ausgehend vom besagten optimalen Verhältnis durch Variation des Kleinkornanteils entsprechend reduziert. Ein ähnliches Verhalten wurde auch bei Sand-Ton-Mischungen beobachtet (Vallejo et al. [166] und Sterpi [154]). Bezieht man diese Ergebnisse nun auf die innere Suffusion, so ergibt sich als Konsequenz, dass der Verlust des Feinkornanteils im Boden und die damit verbundene Zunahme der Porosität sowohl die Steifigkeit als auch die Festigkeit des Bodens reduziert. Das hat natürlich zur Folge, dass der Reibwiderstand des Bodens gegen Scherkräfte abnimmt und die Deformation unter der gegenwärtigen Last hingegen zunimmt.

Aufgrund der inneren Erosion werden die Steifigkeit und die Festigkeit des Bodens durch die Zunahme der Porosität degradiert. Entsprechend dazu haben Papamichos und Vardoulakis [124] oder Wood et al. [179] die Fließfläche in Abhängigkeit der zunehmenden Porosität im Sinne der Materialentfestigung reduziert. Steeb et al. [153] haben indessen durch Einführung einer Schädigungsvariable, wie sie im Kontext der Modellierung des Schädigungsverhaltens von spröden Materialien benutzt wird, einen Ansatz zur Abminderung der elastischen Parameter vorgestellt, vgl. Kachanov [91] oder Rempfer [130] bei Schädigung von Mehrphasenmaterialien. In diesem Zusammenhang ist das grundlegende Ziel dieser Arbeit, die Umsetzung der inneren Erosion in ein gekoppeltes, geschlossenes Bodenmodell, mit der Intention physikalisch anspruchsvolle geotechnische Problemstellungen numerisch zu untersuchen. Dafür müssen aber aufgrund der Prozesskomplexität der inneren Erosion dennoch einige Vereinfachungen getroffen werden, z. B. bezüglich der Modellidealisierung und der konstitutiven Beschreibung des Bodens.

## Zielsetzung und Vorgehensweise

Um ein reales ARWP numerisch zu untersuchen, muss zunächst dessen Materialverhalten entsprechend der Belastungsart des realen Problems analysiert werden. Denn die Belastungsbedingung – diese kann statisch, dynamisch oder zyklisch sein – gibt für das beim ARWP zugrundeliegende Material vor, auf welche Weise es im Hinblick auf die Bestimmung seiner Materialeigenschaften wie beispielsweise elastisches, elastisch-(visko)plastisches oder viskoelastisches Verhalten zu untersuchen ist. Daher müssen hier entsprechend geeignete experimentelle Verfahren ausgewählt werden. Anhand der Ergebnisse von Kalibrierungsexperimenten\* wird entweder ein konstitutives Materialmodell entwickelt oder ein geeignetes aus den bereits vorhandenen ausgewählt. Betreffend der Zielformulierung der vorliegenden Arbeit kann an dieser Stelle festgehalten werden, dass das Material

---

\*Kalibrierungsexperimente sind Elementversuche, die sich besonders durch ihre einfache Belastungs- und Randbedingungen kennzeichnen. Durch die einfache Wahl der Systembedingungen soll eine homogene Spannungs-Deformationsverteilung innerhalb der Probe sowie die Reproduzierbarkeit der Experimente gewährleistet werden. Diese Versuche bilden das wahre Materialverhalten überwiegend ab und werden zur Kalibrierung der Konstitutivgleichungen bzw. zur Identifikation der Materialparameter verwendet.

des realen Problems aus teilgesättigtem Sand besteht. Solcher Sand kommt nahezu in allen geomechanischen Problemstellungen vor. Das Ziel ist hier eine möglichst genaue Simulation des Deformations- und Strömungsprozesses des teilgesättigten Sands durchzuführen, um damit die Basis für eine realistische Simulation des ARWP zu schaffen. Dafür werden die verwendeten Materialgesetze auf der Grundlage des Dreiphasenbodenmodells geprüft und verbessert, vgl. [57], insbesondere die Modellierung des Spannungs-Dehnungsverhaltens. So wurden für dieses Vorhaben diverse Experimente durchgeführt, um die verwendeten Konstitutivmodelle letztendlich zu verifizieren und zu validieren, vgl. [56, 57].

Die Prozedur zur Untersuchung des Bodenmodells kann grob in die folgenden drei Aufgabenfelder unterteilt werden: *Experimentelle Untersuchung*, *Konstitutive Modellierung* und *Parameteridentifikation*. Diese Aufgabenfelder sind in Abb. 0.1 als Kreislaufschema abgebildet, worin die gegenseitigen Abhängigkeiten der Felder zu erkennen sind. Das kalibrierte Materialmodell wird hier auf der Basis von Vorsimulationen zusätzlicher Experimente oder durch numerische Untersuchungen von ARWP validiert. Damit werden die anderen Aufgabenfelder direkt oder indirekt mit überprüft. Dementsprechend ist die *Modellvalidierung* im Zentrum des Kreislaufschemas platziert. Die Inhalte können im Kontext der Bodenmodellierung grob zusammengefasst wie folgt wiedergegeben werden:

**Experimentelle Untersuchung.** In Abhängigkeit von der Art der Belastung des realen Problems wird die experimentelle Untersuchung des Bodenmaterials entweder unter quasi-statischen oder dynamischen Belastungsbedingungen durchgeführt. Zum Beispiel neigen granulare Materialien unter dynamischer Belastung zur Bodenverflüssigung. Kennzeichnend für dieses Verhalten ist ein plötzlicher Verlust der Bodensteifigkeit [26, 28, 86, 132]. In dieser Arbeit werden die Materialeigenschaften des Sands ausschließlich unter quasi-statischer Belastung untersucht. Böden weisen im Allgemeinen eine isotrope (Aufwei-

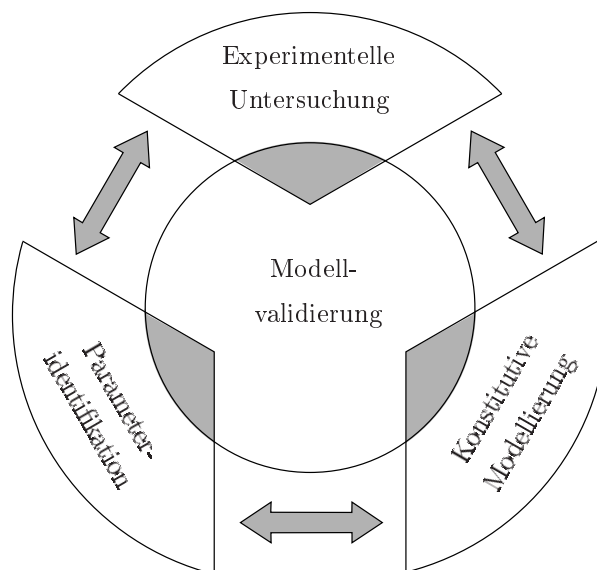


**Abbildung 0.1:** Veranschaulichung der gegenseitigen Abhängigkeiten der einzelnen Aufgabenfelder des Materialmodellierungsprozesses.

tung der Fließfläche) sowie eine kinematische (translatorische Verschiebung des Zentrums der Fließfläche) Verfestigungseigenschaft auf. Die kinematische Verfestigung tritt bei zyklischen Kompressions-Extensions-Wechselbelastungen auf (*Bauschinger-Effekt*). Da hier keine zyklischen Belastungen für das reale Problem vorgesehen sind, kann die kinematische Verfestigung dementsprechend sowohl von der experimentellen Untersuchung als auch von der Konstitutivmodellierung ausgeschlossen werden. Gleichwohl müssen aber möglichst alle Eigenschaften des Materials, die für das reale Problem relevant sein können, durch die jeweiligen Experimente erfasst und durch die konstitutiven Modelle abgebildet werden.

**Konstitutive Modellierung.** Zur numerischen Modellierung des Materialverhaltens werden mathematische Modelle auf der Grundlage von experimentellen Ergebnissen entwickelt. Hierzu stehen verschiedene mathematische Ansätze zur Verfügung. Diese sind z. B. empirische, rheologische oder konstitutive Modellierungsansätze. Nach Mahnken [111] erfüllen empirische und rheologische Modelle – im Gegensatz zu Konstitutivmodelle – nicht notwendigerweise den zweiten Hauptsatz der Thermodynamik. Denn beispielsweise sind die empirischen Modelle im Grunde nur bestrebt, die experimentellen Daten, vorzugsweise, mit möglichst wenigen Parametern zu approximieren, ohne dabei zwingende physikalische Restriktionen zu erfüllen. Indessen beschreiben die rheologischen Modelle komplexes Materialverhalten durch Verknüpfungen von rheologischen Basiselementen wie Wegfeder, viskoser Dämpfer und Reibelement, mit dem Nachteil, dass mit fortschreitender Modellkomplexität die Anzahl der Materialparameter zunimmt. Im Vergleich zu diesen beiden Modellansätzen basieren die thermodynamisch konsistenten Konstitutivmodelle, die im Rahmen einer Kontinuumsmechanik entwickelt werden, auf phänomenologischen Beobachtungen von physikalischen Prozessen, die experimentell bestimmbar und messbar sind. In dieser Arbeit wird der zuletzt genannte Modellierungsansatz weiterverfolgt, also die phänomenologische Vorgehensweise der konstitutiven Materialbeschreibung.

**Parameteridentifikation.** Zur effizienten und schnellen Lösung von restringierten Optimierungsproblemen, die aus einem Hauptproblem und aus sekundären Restriktionen mit Gleichheits- und Ungleichheitsbedingungen bestehen, ist die *Sequentielle Quadratische Programmierung* (SQP) ([17, 87, 135, 136, 149]) eine bevorzugte Wahl. Die SQP-Methode gehört zu der Gruppe der gradienten-basierten Verfahren und löst das Optimierungsproblem in einer *Lagrange*-Formulierung. Trotz der Tatsache, dass gradienten-basierte deterministische Verfahren nur die lokale Lösung des Optimierungsproblems in der Regel finden, hat sich die SQP-Methode für den Einsatz im Rahmen der Parameteridentifikation sehr gut etabliert. Da die Wahl der Startwerte der Parameter bei dieser Methode einen großen Einfluss auf die Lösung des Optimierungsproblems hat, muss der Anwender dieser Methode insofern gute Kenntnisse über das Materialverhalten und über die Konstitutivbeziehungen im verwendeten Materialmodell verfügen. Des Weiteren wird hier zur Berechnung des Gradienten der Zielfunktion eine umfangreiche Sensitivitätsanalyse der Optimierungsparameter hinsichtlich der zu kalibrierenden physikalischen Größen benötigt.

**Modellvalidierung.** Das kalibrierte Materialmodell wird durch numerische Berechnungen von zusätzlichen Experimenten validiert. Diese Experimente müssen unabhängig von jenen Experimenten sein, die für die Kalibrierung des Modells verwendet wurden, und sollten zudem inhomogene Deformationsverteilungen und Lokalisierungen von plastischen Scherzonen aufweisen. Hierdurch kann die Qualität der Modellierung des plastischen Ma-

terialverhaltens überprüft werden. Für den Fall, dass die Validierung des Materialmodells nicht erfolgreich ist, obwohl die Elementversuche vom Materialmodell richtig wiedergegeben wurden, muss die Ursache für dieses Problem in den drei Feldern des Materialidentifikationsprozesses (Abb. 0.1) gesucht werden. Ein eventueller Grund für den Fehler könnte sein, dass das Materialverhalten durch die vorhandenen Elementversuche nicht vollständig abgedeckt wird und bestimmte physikalische Eigenschaften des Materials erst durch die Validierungsexperimente aktiviert werden. Folglich müssen diese Eigenschaften durch zusätzliche Elementversuche erfasst und durch Konstitutivmodelle entsprechend abgebildet werden. Ansonsten kann der Fehler der Validierungsrechnung durch das angewendete numerische Verfahren resultieren, z. B. infolge der Netzabhängigkeit der Lösung. Dieser Fehler kann durch numerische Konvergenzstudien mit feineren Diskretisierungsstufen des Finite-Elemente Netzes untersucht werden. Letztendlich ist der Modellidentifikationsprozess dann beendet, wenn der Validierungsvorgang erfolgreich abgeschlossen ist.

**Simulation von ARWP.** Ausgehend von einem erfolgreich abgeschlossenen Prozess der Modellkalibrierung und -validierung können unter Verwendung dieses Materialmodells numerische Analysen von realistischen ARWP durchgeführt werden.

## Gliederung der Arbeit

Beginnend mit dem **Kapitel 2** wird das grundlegende Konzept der TPM, welches zur Beschreibung von porösen Mehrphasenmaterialien entwickelt wurde, eingeführt. Darin werden die kinematischen Relationen der einzelnen Konstituierenden und die mechanischen Bilanzgleichungen des Mehrphasenmaterials angegeben. Die komplexen Zusammenhänge von porösen Mehrphasenmaterialien, die aus einer Festkörpermatrix und einem oder mehreren Porenfluidkomponenten bestehen, werden in einem bekannten kontinuumsmechanischen Rahmen eines Einphasenmaterials erläutert.

Das poröse Material, das in dieser Arbeit untersucht wird, ist der GEBA<sup>†</sup>-Sand. Das mechanische Verhalten des GEBA-Sands wird durch Triaxialversuche bestimmt. Hierzu werden in **Kapitel 3** die experimentelle Versuchsausrüstung sowie die Eliminierung des Messfehlers der Versuchsaapparatur aufgezeigt. Des Weiteren werden in diesem Kapitel die grundlegenden Triaxialbelastungspfade im Hauptspannungsraum erläutert, ferner wird hier auch das komplexe Spannungs-Dehnungsverhalten des dichten Sands ausführlich diskutiert. In diesem Kapitel werden ebenfalls die noch neu beobachteten Phänomene zum Fließ- und Bruchverhalten des Sands präsentiert.

Basierend auf den experimentellen Ergebnissen aus den Triaxialversuchen und aus dem Einsatz der TPM werden in **Kapitel 4** die konstitutiven Beziehungen für den teilgesättigten Sand in einer thermodynamisch konsistenten Weise unter Berücksichtigung der Interaktionen zwischen den Konstituierenden hergeleitet. Hierzu wird für die materiell inkompressible Festkörpermatrix ein nichtlineares Elastizitätsgesetz und ein plastischer Verfestigungs- und Entfestigungsansatz für das Fließverhalten formuliert. Für die kompressible Porenluft (Porengas) wird eine bekannte Konstitutivbeziehung hergeleitet, wobei

---

<sup>†</sup>Sand aus der Gebenbacher Sandgrube (Handelsname GEBA, Dorfner, Hirschau, Deutschland)

das Porenwasser als materiell inkompressibel angenommen wird.

In **Kapitel 5** wird die numerische Umsetzung des Dreiphasenmodells – d. h., die Diskretisierung der Hauptbilanzgleichungen in Ort und Zeit – unter Berücksichtigung der Konstitutivgleichungen im Rahmen der FEM präsentiert. Außerdem wird in diesem Kapitel der Optimierungsprozess zur Lösung des nichtlinearen Optimierungsproblems der Parameteridentifikation diskutiert. Dabei liegt der Fokus auf der gradienten-basierten SQP Methode mit semi-analytischer Berechnung der Sensitivitäten.

Die Kalibrierungs- und Validierungsergebnisse des Dreiphasenmodells für den GEBA-Sand werden in **Kapitel 6** präsentiert. Die Kalibrierung des Festkörpermodells wird durch Triaxialexperimente vorgenommen. Die Modellvalidierung erfolgt indessen durch numerische Berechnungen von kleinskaligen Versagensexperimenten. Dahingegen werden die Konstitutivmodelle zur Beschreibung des Sättigungsverhaltens des Sands anhand von deformationsfreien hydraulischen Experimenten bestimmt. Anschließend wird das vollständig kalibrierte Dreiphasenmodell durch Simulation von Böschungsbruchversuchen im Technikmaßstab numerisch validiert. Dabei erfolgt die Belastung der Böschung sowohl durch mechanische als auch durch hydraulische Kräfte.

Ausgehend vom kalibrierten Bodenmodell werden in **Kapitel 7** die numerischen Untersuchungen des kriechenden realen Heumöser Hangs gezeigt. Der Heumöser Hang besitzt ein äußerst komplexes Deformations- und Strömungsverhalten. Diese Komplexität basiert nicht nur auf der starken Heterogenität des Hangmaterials, sondern ist auch mit der schwierigen Topologie und Untergrundstruktur des Hangs verbunden. Der Heumöser Hang wurde im Rahmen der von der Deutschen Forschungsgemeinschaft (DFG) geförderten Forschergruppe 581 ‚Großhang‘ eingehend wissenschaftlich untersucht. Die Forschergruppe hat zur Verwirklichung der hier gezeigten numerischen Simulationen des Heumöser Hangs entscheidend dazu beigetragen.

In **Kapitel 8** wird der Modellierungsansatz des inneren Erosionsprozesses von Böden im Rahmen der TPM beschrieben. Hierzu wird das Dreiphasenmodell um die Porositätsentwicklung des Bodens durch Ablösen des Feinkornanteils vom Festkörperskelett erweitert. Mit Hilfe dieses Bodenerosionsmodells werden in diesem Kapitel einige typische Erosionsprobleme untersucht.

In **Kapitel 9** werden alle behandelten Themenpunkte zusammengefasst und einige Anmerkungen für zukünftige Forschungsmöglichkeiten bezüglich dieser Themen gegeben. Des Weiteren sind im **Anhang** Informationen und Ausarbeitungen zu einigen ausgewählten Sachverhalten angegeben, um damit das Verständnis der Arbeit zu erleichtern.

# Nomenclature

In this monograph, the conventions of the nomenclature most closely correspond to the common modern tensor calculus, such as given in the textbook of de Boer [11] and of the lecture notes on vector and tensor calculus of Ehlers [55]. Therein, detailed explanations of applied notations and rules can be found. With regard to the nomenclature of the porous-media theories, the well-established conventions discussed in [14] and [47, 52] are adhered in this monograph.

## Conventions

### *Basic conventions*

---

$(\cdot)$	placeholder for arbitrary physical quantities
$s, \epsilon, \dots$	scalars (0-th order tensors)
$\mathbf{s}, \mathbf{t}, \dots$	vectors (1-st order tensors)
$\mathbf{S}, \boldsymbol{\sigma}, \dots$	2-nd order tensors
$\overset{n}{\mathbf{S}}, \overset{n}{\mathbf{T}}, \dots$	$n$ -th or higher-order tensors
$\mathbf{s}, \mathbf{t}, \dots$	general column vectors ( $n \times 1$ )
$\mathbf{S}, \mathbf{T}, \dots$	general matrices ( $n \times m$ )

### *Index and suffix conventions*

---

$i, j, k, l, \dots$	indices as super- or subscripts range from 1 to $N$ , whereas, for $N = 3$ , the three dimensional physical space is denoted
$(\cdot)_\alpha$	subscripts indicate kinematical quantities of a constituent within porous-media or mixture theories
$(\cdot)^\alpha$	superscripts indicate the belonging of non-kinematical quantities to a constituent within mixture theories
$(\cdot)'_\alpha$	material time derivative following the motion of a constituent $\alpha$ with the solid and fluid constituents $\alpha = \{S, F\}$
$(\cdot)_{0\alpha}^\alpha$	initial value of a non-kinematical quantity with respect to the referential configuration of $\alpha$
$(\cdot)_{Se}, (\cdot)_{Sp}$	subscripts ‘elastic’ and ‘plastic’ indicate elastic and plastic solid parts associated with plastic solid deformations
$(\cdot)_E^\alpha$	extra (effective) quantities
$(\cdot)_{Em}^\alpha$	purely mechanical extra (effective) quantities
$(\cdot)^D, (\cdot)^H, (\cdot)^V$	deviatoric, hydrostatic and volumetric part of a tensor
$(\cdot)^h$	superscript indicates quantities in the discrete space ( $\Omega \approx \Omega^h$ )

## Symbols

**Remark:** The set of calibrated material parameters of the elasto-viscoplastic triphasic partially saturated soil model is presented in Table C.1 and C.2. Hence, these parameters are not listed in the nomenclature.

## Greek letters

Symbol	Unit	Description
$\alpha$		constituent identifier, i. e., $\alpha = \{S, F\}$
$\alpha_i$	[ - ]	internal plastic variables defining the isotropic hardening
$\beta$		fluid component identifier, i. e., $\beta = \{W, A, E\}$
$\Gamma(\cdot)$		<i>Neumann</i> or <i>Dirichlet</i> boundaries
$\varepsilon, \varepsilon^\alpha$	[ J/kg ]	mass specific internal energy of $\varphi$ and $\varphi^\alpha$
$\hat{\varepsilon}^\alpha$	[ J/m <sup>3</sup> s ]	volume-specific direct energy production
$\varepsilon_{vp}$	[ - ]	equivalent plastic strain
$\varphi, \varphi^\alpha$		overall mixture and the constituent $\alpha$
$\zeta$	[ s/m ]	parameter governs the process speed of erosion
$\hat{\zeta}^\alpha$	[ J/K m <sup>3</sup> s ]	volume-specific direct entropy production of $\varphi^\alpha$
$\eta, \eta^\alpha$	[ J/K kg ]	mass-specific entropy of $\varphi$ and $\varphi^\alpha$
$\hat{\eta}, \hat{\eta}^\alpha$	[ J/K m <sup>3</sup> s ]	volume-specific total entropy production of $\varphi^\alpha$
$\theta, \theta^\alpha$	[ K ]	absolute <i>Kelvin's</i> temperature of $\varphi$ and $\varphi^\alpha$
$\Theta$	[ rad ]	<i>Lode</i> angle
$\lambda$	[ s ]	plastic consistency parameter (plastic multiplier)
$\rho$	[ kg/m <sup>3</sup> ]	density of the overall aggregate $\varphi$
$\rho^\alpha, \rho^{\alpha R}$	[ kg/m <sup>3</sup> ]	partial and effective density of $\varphi^\alpha$
$\hat{\rho}^\alpha$	[ kg/m <sup>3</sup> s ]	volume-specific mass production of $\varphi^\alpha$
$\Phi_n, \tilde{\Phi}_n$	[ - ]	simulation and experimental output quantities
$\Phi_0^k$	[ - ]	maximal value of the respective experimental data $k$
$\phi_{\mathbf{u}_S}^i, \phi_{pa}^i$	[ - ]	shape functions of the FE discretisation
$\phi_{pw}^i$		
$\sigma_{peak}^H$	[ MPa ]	peak shear stress reached at the constant confining triaxial cell pressure $\sigma_3^H = -p$
$\psi, \psi^\alpha$	[ J/kg ]	mass-specific <i>Helmholtz</i> free energy of $\varphi$
$\Psi^S$	[ J/m <sup>3</sup> ]	volume-specific solid <i>Helmholtz</i> free energy
$\Omega, \partial\Omega$		spatial domain and boundary of the aggregate body $\mathcal{B}$
$\Omega_e, \Omega^h$		one finite element and approximated spatial domain of $\Omega$
$\hat{\Omega}_e$		one and reference finite element in local coordinates



$\lambda_{\mathcal{W}}$	[-]	active <i>Lagrange</i> parameter set of inequality constrains
$\xi_i$	[-]	local coordinates of the reference finite element
$\chi_\alpha, \chi_\alpha^{-1}$	[m]	motion and inverse motion function of $\varphi^\alpha$
$\varepsilon_S$	[-]	geometrical linear solid strain tensor
$\sigma^S$	[MPa]	geometrical linear total solid stress tensor
$\sigma_{Em}^{S trial}$	[MPa]	elastic trial stress tensor of the elastic predictor step
$\tau^\alpha$	[MPa]	<i>Kirchhoff</i> stress tensor of $\varphi^\alpha$

## Latin letters

Symbol	Unit	Description
$a_{p_j}$	[MPa]	scalar-valued function governed by the stress invariants $I_\sigma$ , $\mathbb{I}_\sigma^D$ and $\mathbb{III}_\sigma^D$ to control the hardening parameters $p_j$
Cu	[-]	uniformity coefficient
$d, D$	[-]	damage variables (D=1-d)
$d(\cdot)$		differential operator
$dm^\alpha$	[kg]	local mass element of $\varphi^\alpha$
$dv^\alpha$	[m <sup>3</sup> ]	local volume element of $\varphi^\alpha$
$dv$	[m <sup>3</sup> ]	actual volume element of $\varphi$
$d\hat{v}$	[m <sup>3</sup> ]	reference volume element of $\Omega_e$
$dV_\alpha$	[m <sup>3</sup> ]	reference volume element of $\varphi^\alpha$
$D$	[-]	dimension in space $D \in \{1, 2, 3\}$
$e$	[-]	soil void ratio
$e_{max}, e_{min}$	[-]	maximal and minimal soil void ratio
$\hat{e}^\alpha$	[J/m <sup>3</sup> s]	volume-specific total energy production of $\varphi^\alpha$
$f(\mathbf{s})$	[-]	object function or <i>Least-Square</i> function
$F, G$	[MPa]	plastic yield and potential function
$I_n$	[-]	simulation error $\Phi_n - \tilde{\Phi}_n$ at discrete output values $u_n$
$I_D$	[-]	soil density index
$J_\alpha$	[-]	<i>Jacobian</i> determinant of $\varphi^\alpha$
$K$	[-]	measured experimental data sets
$n^\alpha$	[-]	volume fraction of $\varphi^\alpha$
$\hat{n}^\alpha$	[1/s]	volume production of $\varphi^\alpha$
$n_e, n_p$	[-]	degradation exponent of elastic and plastic parameters
$n_e^S, n_p^S$	[-]	elastic and plastic part of the solid volume fraction
$n_{lim}^E$	[-]	actual limit of the eroded grain volume fraction $n^E$
$n_{0lim}^E, n_{max}^E$	[-]	initial and maximal limit of $n^E$

$n_{iS}^S$	[-]	eroded initial solid volume fraction
$N_{eq}, N_{iq}$	[-]	number of equality and inequality constrains
$N_K$	[-]	number of discrete data points of $K$
$p^C$	[-]	capillary pressure of the partially saturated soil zone
$p^{FR}$	[MPa]	overall pore fluid pressure $p^{FR} := p$
$p^{\beta R}$	[MPa]	effective pore pressure of $\varphi^\beta$ (primary variables)
$P^\alpha$		material point of $\varphi^\alpha$
$\bar{q}^A$	[kg/m <sup>2</sup> s]	area-specific mass efflux of $\varphi^A$ over the boundary $\Gamma_q$
$r, r^\alpha$	[J/kg s]	mass-specific external heat supply of $\varphi$ and $\varphi^\alpha$
$R$	[MPa]	radius in the deviatoric principle stress space
$R_c, R_e, R_s$	[MPa]	compression, deviatoric and shear radius
$\bar{R}^A$	[J/kg K]	specific gas constant of the pore air ( $\bar{R}^A = 287.058$ J/kg K)
$s^\beta$	[-]	saturation of the fluid components $\varphi^\beta$ related to $n^F$
$t, \Delta t$	[s]	time and time increment
$t_i$	[MPa]	thermodynamical internal stress (hardening variables)
$u_n$	[-]	discrete value of physical input quantities
$\bar{v}^W$	[m/s]	area-specific volume efflux of $\varphi^W$ over the boundary $\Gamma_v$
$V, V^\alpha$	[m <sup>3</sup> ]	overall volume of $\mathcal{B}$ and $\mathcal{B}^\alpha$
$\mathbf{b}, \mathbf{b}^\alpha$	[m/s <sup>2</sup> ]	mass-specific body force vector action on $\mathcal{B}$ and $\mathcal{B}^\alpha$
$\mathbf{d}_\alpha$	[m/s]	diffusion velocity vector of $\varphi^\alpha$ concerning to $\dot{\mathbf{x}}$
$\mathbf{d}_{\alpha F}$	[m/s]	diffusion velocity vector of $\varphi^\beta$ concerning to $\dot{\mathbf{x}}_F$
$\mathrm{d}\mathbf{a}$	[m <sup>2</sup> ]	oriented actual area element of $\varphi$
$\mathrm{d}\mathbf{A}_S$	[m <sup>2</sup> ]	oriented reference area element of $\varphi^S$
$\mathrm{d}\mathbf{f}^\alpha$	[N]	actual force vector of $\varphi^\alpha$
$\mathrm{d}\mathbf{x}$	[m]	actual line element of $\varphi$
$\mathrm{d}\mathbf{X}_\alpha$	[m]	reference line element of $\varphi^\alpha$
$\mathbf{f}_{u,ext}, \mathbf{f}_{u,int}$	[N]	vector of all external and internal nodal forces of the FEM
$\mathbf{f}_{u,ext}^e, \mathbf{f}_{u,int}^e$	[N]	vector of external and internal nodal forces of an element
$\mathbf{f}_{ni}^s$	[N]	global sensitivity load term
$\mathbf{g}$	[m/s <sup>2</sup> ]	constant gravitation vector with $ \mathbf{g}  = 9.81$ m/s <sup>2</sup>
$\mathbf{g}(s), \mathbf{h}(s)$	[-]	vector of inequality and equality constrains
$\mathbf{g}_W$	[-]	<i>Active set</i> of inequality constrains
$\mathbf{h}(\alpha_i)$	[-]	hardening functions of the plastic hardening parameters $\mathbf{p}$ governed by the internal plastic hardening variables $\alpha_i$
$\hat{\mathbf{h}}^\alpha$	[MPa]	volume-specific total angular momentum production of $\varphi^\alpha$
$\hat{\mathbf{m}}^\alpha$	[MPa]	volume-specific direct angular momentum production of $\varphi^\alpha$
$\mathbf{n}$	[-]	outward oriented unit surface normal vector

$\mathbf{p}$	[ - ]	vector of plastic hardening parameter of $F$
$\mathbf{p}^{vG}$	[ - ]	vector of <i>van Genuchten</i> model parameters
$\hat{\mathbf{p}}^\alpha$	[ N/m <sup>3</sup> ]	volume-specific direct momentum production of $\varphi^\alpha$
$\mathbf{q}, \mathbf{q}^\alpha$	[ J/m <sup>2</sup> s ]	heat influx vector of $\varphi$ and $\varphi^\alpha$
$\mathbf{q}$	[ - ]	column vector of all internal variables of the FE mesh
$\mathbf{s}$	[ - ]	vector collects the optimisation material parameters
$\hat{\mathbf{s}}^\alpha$	[ N/m <sup>3</sup> ]	volume-specific total momentum production of $\varphi^\alpha$
$\mathbf{t}, \mathbf{t}^\alpha$	[ MPa ]	surface traction vector acting on $\partial\mathcal{B}$ and $\partial\mathcal{B}^\alpha$
$\bar{\mathbf{t}}$	[ MPa ]	external load vector acting on the boundary $\Gamma_t$
$\mathbf{u}, \delta\mathbf{u}$		DOF column vector of the primary variables $\mathbf{u} = [\mathbf{u}_S^T, p^{WR}, p^{AR}]^T$ of the FE mesh and its test function
$\mathbf{u}_S$	[ m ]	solid displacement vector (primary variable)
$\mathbf{w}_\beta, \mathbf{w}_{\beta R}$	[ m/s ]	filter and seepage velocity vector of the fluid components $\varphi^\beta$
$\delta\mathbf{W}_{\mathbf{u},ext}, \delta\mathbf{W}_{\mathbf{u},int}$	[ Nm ]	external and internal virtual work vector of $\mathcal{G}_{\mathbf{u}_S}$
$\delta\mathbf{W}_{\mathbf{u},ext}^e, \delta\mathbf{W}_{\mathbf{u},int}^e$	[ Nm ]	external and internal virtual work vector of an element
$\mathbf{x}$	[ m ]	actual position vector
$\dot{\mathbf{x}}$	[ m/s ]	aggregate (barycentric) velocity vector
$\overset{'}{\mathbf{x}}_\alpha = \mathbf{v}_\alpha$	[ m/s ]	constituent velocity vector
$\ddot{\mathbf{x}}$	[ m/s ]	aggregate (barycentric) acceleration vector
$\overset{''}{\mathbf{x}}_\alpha = \mathbf{v}_\alpha$	[ m/s ]	constituent acceleration vector
$\mathbf{X}_\alpha = \mathbf{x}_{0\alpha}$	[ m ]	reference position vector of $P^\alpha$
$\mathbf{y}$		vector of all global and local variables of the FE mesh
$\mathbf{A}_S$	[ - ]	<i>Almansi</i> solid strain tensor
$\mathbf{B}_S$	[ - ]	left <i>Cauchy-Green</i> solid deformation tensor
$\mathbf{C}_S$	[ - ]	right <i>Cauchy-Green</i> solid deformation tensor
$\overset{4}{\mathbf{C}}^{Se}$	[ MPa ]	4-th order elasticity tensor ( $\mathbb{C}^{Se} := \overset{4}{\mathbf{C}}^{Se}$ )
$\mathbf{D}_\alpha$	[ 1/s ]	strain rate tensor of $\varphi^\alpha$
$\mathbf{E}_S$	[ - ]	<i>Green-Lagrangean</i> solid strain tensor
$\mathbf{F}_\alpha$	[ - ]	material deformation gradient tensor of $\varphi^\alpha$
$\mathbf{H}$	[ - ]	<i>Hessian</i> matrix
$\mathbf{I}, \overset{4}{\mathbf{I}}$	[ - ]	2-nd and 4-th order identity tensor (fundamental tensor)
$\overset{4}{\mathbf{I}}^D$	[ - ]	4-th order deviatoric projection tensor
$\mathbf{J}, \mathbf{J}_G, \mathbf{J}_L$	[ - ]	entire, global and local <i>Jacobian</i> matrix
$\mathbf{L}_\alpha$	[ 1/s ]	spatial velocity gradient tensor of $\varphi^\alpha$
$\mathbf{P}^\alpha$	[ MPa ]	1-st <i>Piola-Kirchhoff</i> stress tensor of $\varphi^\alpha$

$\mathbf{Q}_S$	$[-]$	proper orthogonal tensor
$\mathbf{S}^\alpha$	$[\text{MPa}]$	2-nd <i>Piola-Kirchhoff</i> stress tensor of $\varphi^\alpha$
$\mathbf{T}^\alpha$	$[\text{MPa}]$	<i>Cauchy</i> stress tensor of $\varphi^\alpha$
$\mathbf{W}_\alpha$	$[1/\text{s}]$	spin or vorticity tensor of $\varphi^\alpha$

## Calligraphic letters

Symbol	Unit	Description
$\mathcal{B}, \mathcal{B}^\alpha$		aggregate body and partial constituent body
$\mathcal{D}_{\text{int}}$	$[\text{J}/\text{m}^3 \text{s}]$	entire volume-specific internal dissipation
$\mathcal{D}_{S \text{int}}, \mathcal{D}_{F \text{int}}$	$[\text{J}/\text{m}^3 \text{s}]$	volume-specific internal solid and fluid dissipation
$\mathcal{G}, \partial \mathcal{G}$		elastic domain and boundary of $\mathcal{G}$
$\mathcal{F}_D$		deviatoric part of the multiplicative split of $F$
$\mathcal{F}_H$	$[\text{MPa}]$	hydrostatic part of the multiplicative split of $F$
$\mathcal{P}$	$[\text{MPa}]$	<i>Lagrangean</i> multiplier representing the pore air pressure $p^{AG}$
$\mathcal{S}_u(t), \mathcal{T}_u$		trial and test space of $\mathbf{u}$
$\mathcal{V}^3$		proper <i>Euclidean</i> vector space
$\mathcal{F}$		vector including the global and local system of equations
$\mathcal{G}_{u_s}$		abstract function containing all global weak forms
$\mathbf{v}$		vector of internal and hardening variables $\mathbf{q}$ and $\mathbf{p}$
$\mathcal{L}$		<i>Lagrange</i> function of the constrained optimisation problem
$\mathcal{L}_i$		abstract function containing all local equations of viscoplasticity with isotropic hardening
$\mathcal{S}_D, \mathcal{S}_H$		sets of plastic parameters controlling the shape of $F$ in the deviatoric and hydrostatic principle stress plane
$\mathcal{W}$		<i>Active Set</i> of inequality constrains $\mathbf{g}(\mathbf{s})$

## Selected acronyms

Symbol	Description
BFGS	Broyden-Fletcher-Goldfarb-Shanno
CT	Computed Tomography
DAE	Differential-Algebraic Equation
DOF	Degrees of Freedom
FEM	Finite Element Method
f-s (n-c)	failure surface of the new concept

---

f-s (o-c)	failure surface of the old concept
GDS	Grain Size Distribution
IBVP	Initial Boundary Value Problem
LBB	Ladyshenskaya-Bauška-Brezzi
ODE	Ordinary-Differential Equation
PANDAS	<b>P</b> orous Media <b>A</b> ddaptive <b>N</b> onlinear Finite Element Solver based on <b>D</b> ifferential <b>A</b> lgebraic <b>S</b> ystems
PDE	Partial-Differential Equation
REV	Representative Elementary Volume
SQP	Sequential Quadratic Programming
TM	Theory of Mixtures
TPM	Theory of Porous Media
VEGAS	Versuchseinrichtung zur Grundwasser- und Altlastensanierung - Research Facility for Subsurface Remediation
y-s	yield surface



# Chapter 1:

## Introduction and Overview

The soil on which a building is constructed carries the complete load of the building including wind loads acting on the building. The sum of these loads is transferred to the soil by the foundations. Accordingly, the soil is the main link in the chain of stability of the entire construction. The absorption of loads has to take place with minor soil deformations. Otherwise, there is a risk to slope or foundation failure. This would lead to an unstable building associated with the danger of collapse of the building. Moreover, soil failure induced by heavy precipitation events or earthquakes can trigger landslides or failure of embankment dams and which in turn may wreak havoc on human and nature. Before the destructive failure is triggered, various physical processes within the soil such as the initiation of localisation zones with plastic deformations lead to a sudden decrease of the load carrying capacity of the soil. By virtue of the fact that the soil consists mainly of a solid grain matrix, in which the load is carried by normal and friction forces between the grains, irreversible plastic deformations of the grain structure almost occur with any increase of load conditions. Additionally, the soil deformation behaviour is strongly influenced by the pore fluids like water and air streaming within the matrix. Thus, due to strongly coupled deformation and flow processes, the experimental investigation and the theoretical modelling of the partially saturated soil behaviour is a huge challenge for engineers and scientists. Only on the basis of a detailed study of the soil behaviour, it is possible to give realistic predictions of failure situations of landslides or embankments. For the realisation of this ambitious goal, advanced soil models as well as efficient and robust numerical computing methods are necessary. The application of computer simulations is more and more important, because, therewith, a better understanding of the ongoing complex physical processes of the constructions can be reached.

### 1.1 Motivation

In recent years, the increasing number of landslides occurrences caused by long-lasting heavy precipitation events has been observed all over the world. For instance, a landslide happened in Nachterstedt (Germany) in the year 2009 where approximately 1 million cubic meters soil slid down to the Concordia Lake, cf. Figure 1.1 (left). This lake was laid out artificially by a controlled flooding of the disused mine through an increase of the groundwater level, which finally caused the landslide. In contrast to this landslide, the motion of the natural *Heumös* hillslope situated in Ebnet near Dornbirn (Austria) is slow and discontinuous, cf. Figure 1.1 (right). In some regions, the *Heumös* hillslope is creeping approximately 10 cm per year still without any indication of a sudden landslide. Hence, it is particularly of interest to determine the hazard potential of hillslopes before actual the failure happens. On that point, computer analysis can give a good contribution towards the prediction of possible motion situations of the slope.



**Figure 1.1:** (left) Landslide (2009) in Nachterstedt, Germany, (<http://i418.photobucket.com/albums/pp263/glenlatterach/>) and (right) creeping Heumös hillslope in Ebnet, Austria (<http://www.grosshang.de>).

In the face of more frequently occurring flood water events, densely populated regions close to rivers and lakes are always exposed to danger. The protection of these regions by embankment dams or dikes will become more and more important. Furthermore, the global climate warming leads to a melting of the polar ice caps with the additional devastating effect that the global sea level is rising. Beside the protective function against high flood, dams are more and more built for the production of renewable energy by using the water force of the dammed-up river to run turbines. The large amount of dammed water constitutes a huge destructive force against human life and nature in case of a dam failure as happened for example at the Teton Dam (1976) or the Taum Sauk reservoir (2005), cf. Figure 1.2. In both cases, the failure was triggered by the internal soil erosion, during which the soil grains are detached from the solid grain structure by the seepage force of the streaming pore water. Thereby, the porosity of the soil increases continuously with the consequence that the dam gradually loses its bearing capacity until it fails. Therefore, it is important to detect weak zones of the dam as early as possible in order



**Figure 1.2:** (left) The Teton Dam (1976) near Rexburg, Idaho, USA ([http://web.mst.edu/rogersda/teton\\_dam/](http://web.mst.edu/rogersda/teton_dam/)) and (right) the Taum Sauk reservoir (2005) in Lesterville, Missouri, USA (Figure is taken from the United States Geological Survey published in Wikipedia).

to take necessary and precautionary measures. Concerning this, computer simulations of dams can help to detect weak zones of construction.



## 1.2 State of the Art

The accurate numerical simulations of complex geotechnical problems are becoming more and more important. In particular, this addresses the well-founded prediction of the stress-strain behaviour of frictional granular material subjected to a frequent change of mechanical and hydraulic loading conditions. Therefore, there is a need for suitable mathematical models, which are able to realistically predict the deformation behaviour of partially saturated soils. In the following, an overview of some important research fields treated in this thesis is given.

### *Constitutive modelling of partially saturated soils*

Partially saturated frictional soils are commonly described by a triphasic model, where the individual phases are the materially incompressible, elasto-plastic or elasto-viscoplastic solid skeleton and the two pore fluids, namely, the materially incompressible pore water and the materially compressible pore air. Based on a continuum-mechanical approach, Ehlers and Blome [58] or Ehlers et al. [64] derived a triphasic model in a thermodynamically consistent manner in the framework of the Theory of Porous Media (TPM). The TPM is the Theory of Mixtures (TM) extended by the Concept of Volume Fractions in order to take into account the micro-structural information of the porous material in a homogenised fashion. In contrast, the TM is commonly used in chemical-engineering applications for describing mixtures consisting of miscible chemically reacting constituents, like gases, where the micro-structural information of the mixture is irrelevant. The main developments of the TM go back to the works of Truesdell and Toupin [163], Bowen [19] or to a later work of Truesdell [161]. The general fundamental approaches and derivations of the TPM can be found in Bowen [20, 21], de Boer [13, 14], de Boer and Ehlers [15, 16] or Ehlers [46, 46, 47, 52, 53] and in the citations therein. To describe partially saturated soils, the TPM builds the main theoretical framework, while the material specific informations of the soil have to be introduced via constitutive equations.

The challenging task in the field of geomechanics is the determination of the very complex stress-strain behaviour of cohesionless granular materials such as sand. In order to describe the plastic material behaviour numerically, various yield functions for soils have been developed during the last six decades, compare, for example, [12, 32, 38, 39, 96, 100, 121, 128]. The assets and drawbacks of some of these yield functions are discussed in [49]. In these contributions, the single-surface yield criterion introduced by Ehlers [48] is used, which is downward compatible to other plasticity models, such as the well-known *Drucker-Prager* criterion [45] or the *von Mises* criterion [116] for non-porous solids. Moreover, granular materials show with the first loading a materially non-linear coupled elastic-plastic deformation behaviour. The hardening behaviour is described by the evolution of the yield surface and is governed by either the plastic work [66] or the plastic strain [67]. However, it is known from Desai [40] (pp. 181) that using the plastic strain provides a more consistent formulation than using the plastic work. It is possible to model the isotropic hardening and softening behaviour in a simple and efficient way by the separation of the plastic strain into a volumetric and a deviatoric part, cf. Krenk [96], Desai [40] (pp. 181) and Scholz [137]. However, the increase (hardening) of the yield

surface is limited. This yield limit is commonly defined by a constant failure surface, which is reached at the deviatoric limit stress. This assumption has been experimentally examined by Ehlers and Avcı [56]. They found out that the failure surface is variable and depends strongly on the stress state. This means that starting from an initial small failure surface of the unloaded granular material, the failure surface is adapted to the current stress state. As a consequence, Ehlers and Avcı [56] have introduced a variable limit of the yield surface controlled by a hydrostatic stress dependent failure surface as it is essential for accurate modelling of the soil behaviour as well as initial-boundary-value problems (IBVP). This particular characteristic of granular materials will be discussed with respect to experimental studies on sand and the constitutive modelling in detail in this contribution.

In order to take the special properties of partially saturated soil into account, Alonso et al. [1], Bolzon et al. [18] and Laloui and Nuth [102] postulated that the yield surface within the elasto-plastic theory is a function of the stress state as well as of the pore-water saturation. Proceeding from the triphasic model ([58, 64]) based on the effective stress concept (Skempton [146]), the influence of the capillary property of the unsaturated zone of the soil on the elasto-plastic solid behaviour is already considered. Thereby, the effective solid stress is reduced by the resulting negative fluid pressure, which corresponds to the capillary pressure. As a consequence, the constitutive modelling of the plastic and saturation behaviour of soil is decoupled and, therewith, experimental investigations of the material properties are also simplified. Concerning this, Ehlers et al. [57] could show the slope stiffening through the capillary effect by numerical studies of slope failure problems.

### *Experimental Investigation*

Based on the property of immiscible materials together with the *principle of phase separation* (Ehlers [46]), the mechanical and hydraulic behaviours of partially saturated soils can be studied in a decoupled fashion such that only one of the two processes is ever active, and put together later by adding the coupling mechanisms. Therewith, the experimental investigation and theoretical modelling of soil are significantly simplified. Proceeding from this approach, the stress-strain characteristics of the solid skeleton of the partially saturated soil are determined from triaxial tests performed with fluid saturated (with pore air or water) soils under homogeneous loading conditions. To describe the material properties of the individual fluid components of the multiphasic material such as material compressibility or viscosity, etc., the constitutive approaches derived for a single material can be used for the fluid constituents, e. g., ideal gas law (for compressible gas), *Newtonian* fluids (viscous fluid stress), etc. In the next step, the motion characteristics (hydraulic properties) of the pore fluids, such as the permeability properties of the soil, the mobility of the pore fluids within the partially saturated zone, etc., can be measured with deformation-free experiments without any external mechanical load onto the specimen, cf. Ehlers et al. [57].

Cohesionless frictional granular materials such as sand are only statically stable if they are under a hydrostatic pressure state. Therefore, the material behaviour of sand is determined via triaxial experiments, while the sand specimen positioned in the triaxial

cell is confined with degassed water. The pressure on the specimen is regulated by a volume-pressure controller. The central challenge of performing triaxial experiments is in the exact measurement of the deforming specimen. Concerning this, several methods have been proposed in the related literature with different demands on the volume measurement accuracy depending on the specific problem under study. Most of these methods were documented by Alva-Hurtado and Selig [2] or by Geiser et al. [74], whereas Alva-Hurtado and Selig [2] differentiate the measuring methods in three categories. The first category is the measurement of the outflow and the inflow of cell water caused by the deforming specimen. The second one measures the pore volume change through out- and inflow of the pore water. However, this is only feasible on saturated specimens and drained boundary conditions. In contrast to this, the third category measures directly the volume change on the specimen.

Within this thesis, the focus is on triaxial tests with homogeneous and drained conditions. Thus, all three categories of the measurement techniques are qualified. Nevertheless, the simplest and most straightforward way to measure the volume change of the specimen is carried out by the first category. Therein, the stiffness and the volume capacity of the triaxial cell are particularly important. Leong et al. [105] investigated the measuring error of different standard triaxial cells built of acrylic glass, steel or double-wall cell systems. These investigations showed that the cell deformation and the volume capacity of the cell yield the major parts of the measuring error. To avoid these disadvantages, a new stiff triaxial aluminium cell with an appropriate cell-water capacity was constructed. Moreover, the cell is well adapted for the volume deformation of the specimen, such that the absolute volume-deformation measuring error of the test setup could be minimised, cf. Ehlers et al. [57].

For the calibration of the constitutive approaches for the solid stress-strain behaviour of the investigated material, quite a few triaxial experiments on dry sand using compact cylindrical specimen under homogeneous and drained conditions have been performed. This set of experiments consists of hydrostatic-compression, shear-compression and shear-extension tests with different confining pressures to investigate the dependency of the stress-strain response on the isotropic stress state. An important yielding and failure behaviour of sand could be detected via stress-path-dependent triaxial experiments. This is discussed in detail later in this thesis.

### *Parameter Identification*

Due to improved experimental techniques, the knowledge of the physical behaviour of soil is increasing, whereas more and more sophisticated material laws have been developed with the drawback that the number of material parameters increases. Consequently, the determination of these material parameters becomes more and more difficult. Therefore, the use of optimisation methods is inevitable for their identification. The parameter identification process is realised by a numerical inverse computation of the experiments, whereas the computation is iterated with always improved parameters by use of gradient-based optimisation methods. The iteration process is performed until the optimal parameter set is found by which the experimental results are best approximated. Proceeding from this consideration, the optimisation task (object function) is defined by the squared dif-

ferences of the approximation error, which has to be minimised. This procedure is called the *Least-Squares* method.

The solution strategies of the optimisation methods to evaluate the object functions are differentiated between deterministic (reproducible) methods (Luenberger and Ye [109], Bertsekas [8] and Spellucci [147]) and stochastic (non-reproducible) methods (Bäck and Schwefel [4] and Schwefel [142]). The first group can be subdivided into two categories of gradient-based and gradient-free methods. To the first category of gradient-based methods, the *Newton*-like methods belongs to. In contrast to the *Newton* method, the most popular *Quasi-Newton* methods, such as the *Gauss-Newton* method, the *Levenberg-Marquardt* method or the very famous BFGS (*Broyden-Fletcher-Goldfarb-Shannon*) method, approximate the computationally intensive *Hessian* matrix, the second derivative of the *Least Squares* object function. The category of gradient-free methods is a huge group and comprises also two categories of deterministic *simplex*-based methods, cf. Nelder and Mead [119], and the stochastic methods. An overview of the most important optimisation methods can be found in Rao [129].

By the reason of the high number of parameters, solving the optimisation problem is not unique. Therefore, the goal is to find an optimal combination of the parameters, which represents the global minimum with many local minima. However, not each optimisation method, which solves the parameter-identification problem, obviously determines the optimal material parameter set with the best fit to experimental results. To decide which method is the most suitable one for solving the considered problem depends on the requirements of the optimisation problem. For example, the quality of the solution of gradient-based methods strongly depends on the initial parameter set, because each new set of parameters is determined by the steepest descent of the object function. Accordingly, the optimisation procedure almost always finishes at a local minimum. In contrast, evolution strategies screen a large region of minima, where the probability to find the global minimum is much greater, but it requires a high number of computations of the object function, especially, optimisation problems with quite a few number of parameters (Mahnken [111]).

### *Numerical Investigations of Landslides*

Numerical analyses of natural slopes using the Finite-Element Method (FEM) are getting increasingly important. On the one hand, by numerical stability investigations of existing but endangered slopes, possible failure prognoses can be given, and, on the other hand, by simulation of already happened landslides, the capability of the used model can be verified. For example, Ferrari et al. [72] simulated the Steinernase landslide (Switzerland), proceeding from a weak coupling of the hydrological and mechanical modelling tools by repeatedly updating the respective boundary conditions. The included model parameters were identified on the basis of long-term field measuring data. On the other hand, Ehlers et al. [57] numerically investigated the Heumös hillslope (Austria) along idealised cross sections on the basis of a fully-coupled mechanical-hydraulic soil model, wherein the analysed cross sections have been determined by Lindenmaier [107]. However, if more sophisticated models are used for the description of the slope material and the apparent influence of the mutual interaction between hydrological and mechanical processes is of

particular interest, it is common practice to revert to idealised but well-defined slope geometries (Darve and Laouafa [35], Tsaparas et al. [164], Ehlers et al. [57, 64], Klubertanz et al. [94]). Admittedly, reliable predictions of the stability behaviour of slopes on the basis of FEM analyses demand a high spatial resolution of localisation zones of plastic deformations. In this regard, Ehlers et al. [64] applied space-adaptive methods for an adequate determination of shear bands in partially saturated soil in two-dimensional simulations of embankment scenarios. Three-dimensional investigations of excavation problem have been computed on a multiprocessor system by Wieners et al. [177], Ammann [3] and Graf [78]. However, these simulations have been carried out without taking into account the plastic soil hardening and softening behaviour.

### *Simulation of Internal Erosion*

The detachment of grains from the soil matrix and, subsequently, the transport of these grains through the pore-channel network driven by the pore water seepage flow is denoted as the internal erosion of soil. Concerning this, Ziemers [183] distinguished between internal erosion and internal suffusion. The difference is that the suffusion process involves only the detachment and transport of the fine grain content of the soil, while the coarse grains, building up the main structure of the soil, remain unaffected by the suffusion. In contrast, during an erosion process, where all grains are affected, the coarse grains can burst from the main grain structure. Following this, an erosion pipe can be gradually developed through the soil with adverse reactions to the load-bearing capacity of e.g., dams, cf. Bendahmane et al. [6], Wan and Fell [170] and Indraratna et al. [90]. In this sense, the suffusion is denoted as a special case of erosion driven at low seepage forces. However, in this thesis, only internal suffusion processes are treated, although it is called internal erosion.

A continuum-mechanical description of erodible saturated soils has been proposed by Vardoulakis et al. [168] and Wang and Wan [173]. They extended a common biphasic model consisting of a solid and a fluid phase by an erosion phase representing the amount of fluidised grains, which are in motion within the pore fluid. Based on this, Steeb and Diebels [151] derived an erodible-soil model in the framework of the TPM in a thermodynamically consistent representation. Within the TPM, the fluidising process of grain structure is described by the mass exchange or mass production between the solid and the erosion phases. The driving force of the mass production is the seepage velocity of the pore fluid, cf. Vardoulakis et al. [168] and Steeb et al. [153], or the pore gas, cf. Steeb [150]. Due to the fact that the suffusion is limited only to the fine grain content of the soil, Steeb et al. [153] have separated the solid grains in a stable grain part, which characterises the unerodible main matrix of large grains, and an unstable erodible fine grain part. However, this leads to a larger set of balance equations governing the continuum-mechanical system.

The mechanical behaviour of the soil is only affected by the suffusion process, when the soil consists of less than 70 % of large grains. This property of soils has been investigated by Vallejo [165] via triaxial tests on samples made up with glass beads using different compositions only of a large and a small bead size. He has detected that the maximal strength of a sample is obtained at the minimum porosity defined by the optimal ratio between the small and the large bead content. The large beads build the main stiff matrix

of the soil. Proceeding from the minimal porosity at which both bead groups sharing the applied load, the mechanical properties are reduced by a variation of the fine bead content due to the increase of the porosity. Similar behaviour was also observed in sand-clay soil mixtures (Vallejo et al. [166] and Sterpi [154]). Relating these results to internal suffusion, the loss of the fine grains leads to an increase of the porosity with the consequence that the stiffness and the strength are reduced. Thus, the resistance of the soil against friction forces is decreasing with the result of increasing deformations under the current load.

Due to the internal erosion, the strength and stiffness of the soil is degraded by the increase of the soil porosity. Proceeding from this, Papamichos and Vardoulakis [124] or Wood et al. [179] have reduced the yield surface in dependence of growing porosity like the behaviour of material softening. Moreover, Steeb et al. [153] have presented an approach to reduce the elastic parameters by introducing a damage variable as it is a common practise in modelling of damage-behaviour of brittle materials, cf. Kachanov [91] or of damage in multiphase materials, cf. Rempler [130]. In this context, the principle challenge of this thesis is the integration of the internal erosion process into a closed soil model with the goal to investigate physically sophisticated geotechnical issues by numerical methods. Nevertheless, due to the complexity of the internal erosion process, some simplifications must be made, e.g., concerning the modelling approach and the constitutive description.

### 1.3 Aims and Scopes

In order to numerically investigate realistic IBVP, the IBVP has to be firstly analysed with regard to the material behaviour, the loading and the boundary conditions. The loading conditions of the real problem, that means whether it is a static, a dynamic or a cyclic loading, etc., constitute how the used material of the IBVP has to be experimentally investigated for determining the material characteristics such as elastic, elasto-(visco)plastic, viscoelastic behaviour, etc. Concerning this, appropriate testing methods have to be chosen. Proceeding from the results of these calibration experiments\*, the constitutive material model is developed, or the most appropriate one from already available material laws is picked up. Referring this to the objective of this thesis, the material of the real problem is partially saturated sand, which can be found in almost all geomechanical problems. Thus, the goal is to simulate the deformation and flow processes of the partially saturated sand as accurately as possible in order to get the basis for a realistic simulation of complex IBVP. Concerning this, based on the triphasic soil model, the used constitutive models are tested and improved, cf. [57], in particular, the modelling of the stress-strain behaviour. For this purpose, several experiments have been carried out in order to verify and to validate the applied constitutive models, cf. [56, 57].

Following the process of the soil-model investigation, the task field can be roughly sub-

---

\*Calibration experiments are elementary tests, which are particularly characterised by their simple loading and boundary conditions. By the simplicity of the system conditions, a homogeneous stress-strain distribution within the specimen as well as the reproducibility of the experiments is ensured. These experiments mainly represent the pure material behaviour and they are used for the calibration of the constitutive equations or for the identification of the constitutive material parameters, respectively.

divided into three task fields of *Experimental Investigation*, *Constitutive Modelling* and *Parameter Identification*. They are illustrated in Figure 1.3 by a circular loop representing the mutual dependency, whereas the calibrated material model is validated by simulations of additional experiments or by numerical investigations of IBVP. Therewith, the other fields are directly or indirectly proved. Hence, the *Model Validation* is located in the centre of the circle loop of the material modelling procedure, cf. Figure 1.3. The content of the individual task fields can be roughly summarised as follows:

**Experimental Investigation.** Depending on the type of the loading condition of the real problem, the experimental investigation of the soil material is carried out either under quasi-static or dynamic loading conditions. However, granular materials under dynamic loading strongly tend to soil liquefaction accompanied by an abrupt loss of the soil stiffness. Modelling such a material behaviour demands a different theoretical approach ([26, 28, 86, 132]) as the soil behaviour of quasi-static loading conditions, which is treated in this contribution. In general, soils exhibit isotropic (enlargement of the yield surface) as well as kinematic (translational shift of the centre of the yield surface) hardening. The kinematic hardening process occurs during cycle loads from compression to extension and vice versa (*Bauschinger* effect). However, kinematic hardening can be excluded from the experimental and theoretical investigations of the test material if cyclic-loading paths are not provided for the real problem investigated in this thesis. Nevertheless, all detected material properties by the experiments, which may be relevant for the real problem, have to be reproduced by the constitutive models.

**Constitutive Modelling.** For the numerical modelling of the material behaviour, mathematical models have to be developed based on experimental results. Concerning this, different mathematical approaches are available as empirical, rheological or constitutive models. Following Mahnken [111], the empirical and rheological models do not necessarily fulfil the 2-nd law of thermodynamics in contrast to the constitutive models. Empirical models have only the task to approximate the experimental data preferably by

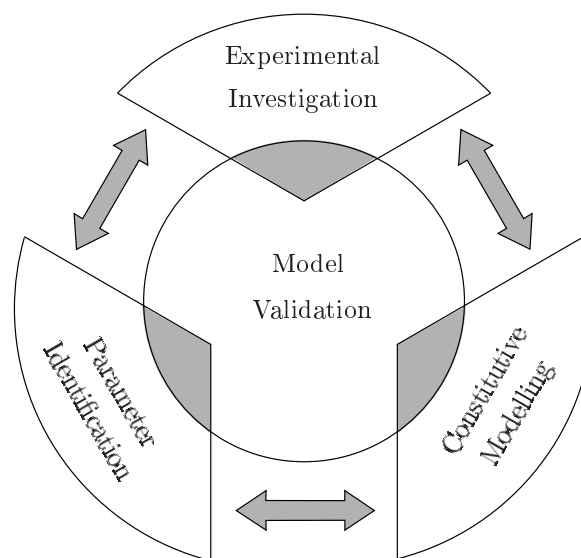


**Figure 1.3:** Illustration of the individual task-field dependencies of the material modelling procedure.

few parameters and without pursuing stringently any physical restriction. Rheological models are able to describe complex material behaviour by combination of basic elements such as spring, dashpot and friction types. The disadvantage, however, is that the number of material parameters is increasing with advancing model complexity. In contrast to these approaches, thermodynamically consistent models are formulated within the framework of a classical continuum-mechanics theory. They base on the phenomenological description of the thermodynamic process of the material under consideration, which are experimentally determinable and measurable (observable). In this thesis, the phenomenological approach of constitutive material formulation is pursued.

**Parameter Identification.** In order to solve constrained optimisation problems consisting of a main problem and secondary constraints of equality and inequality conditions fast and efficiently, the *Sequential-Quadratic-Programming* (SQP) ([17, 87, 135, 136, 149]) method is a proper choice. The SQP method belongs to the group of gradient-based methods and solves the optimisation problem in a *Lagrangian* formulation. Despite the fact that gradient-based deterministic methods only find the local solution, the SQP method is well established in the engineering field of parameter optimisation. Since the choice of the initial parameter set has a great impact on the results of this method, however, the user of this method needs a good knowledge of the material behaviour and the constitutive laws used in the material model. Moreover, the gradient of the object function requires an extensive sensitivity analysis of the optimised parameters related to the matched physical quantities.

**Model Validation.** The calibrated material model is validated by numerical computations of additional experiments. These experiments must be independent from those used for the model calibration, and they should exhibit an inhomogeneous deformation distribution and a localisation of plastic deformation zones. With such experiments, the modelling quality of the plastic material behaviour can be proven. In case that the validation of the material model is not successful, although the material model matched the elementary tests well, the problem has to be searched within the other three task fields of the material identification process (Figure 1.3). The potential reason for this may be, for instance, that the material behaviour is not completely covered by the present elementary tests, and particular physical properties of the material are only activated during the validation experiments. To capture these properties, further elementary tests have to be carried out. Accordingly, the constitutive model has to be extended. However, the inaccuracy of the numerical computation of the validation experiment could also be caused directly by the numerical method, e. g., the mesh dependency of the numerical solution. The resulting numerical error can be analysed by convergence studies using more refined discretisation levels of the finite-element mesh (FE mesh). Finally, the parameter identification procedure is finished if the model validation procedure is successfully completed.

**Simulation of IBVP.** Proceeding from a successfully calibrated and validated soil model, numerical analyses of realistic IBVP using this material model can be carried out.



## 1.4 Outline of the Thesis

Starting with **Chapter 2**, the fundamental concept of the Theory of Porous Media developed for the description of multiphasic porous materials is briefly outlined. Therein, the kinematic relations of the individual constituents and the mechanical balance equations of the multiphasic materials are presented. The complex coherences of multiphasic porous material consisting of a solid matrix and one or more pore-fluid components are explained in the frame of the well-known continuum mechanics of single-phase materials.

The porous material investigated in this thesis is the GEBA<sup>†</sup> sand. Its mechanical behaviour is determined via triaxial experiments. Concerning this, the required experimental equipment as well as the elimination of the measuring error of the test system are presented in **Chapter 3**. Furthermore, the fundamental triaxial loading paths in the principle stress space are illustrated and the complex stress-strain behaviour of dense compacted sand is discussed in detail. Therein, the newly observed yielding and failure behaviour is highlighted.

Based on the experimental results from the triaxial tests and using the TPM, the constitutive relations for the partially saturated soil are derived in **Chapter 4** in a thermodynamically consistent manner with regard to the interactions between the individual constituents. For the materially incompressible solid matrix, a non-linear elastic material law and a plastic hardening and softening approach for the yielding behaviour is formulated. For the pore air (pore gas), a well-known constitutive relation is derived, while the pore water is assumed to be incompressible.

The numerical treatment of the triphasic model – discretisation of the governing balance equations in space and time – under consideration of constitutive relations is presented in **Chapter 5** within the frame of the FEM. Furthermore, the solution procedure of non-linear optimisation problems, such as the parameter identification, is discussed using the gradient-based SQP method with a semi-analytically computation of the sensitivities.

In **Chapter 6**, the results of the calibration and the validation procedure of the triphasic model for the GEBA sand are presented. The calibration of the solid matrix is carried out using triaxial experiments, while the model validation is obtained by numerical computation of small-scale failure experiments. Moreover, the constitutive models for the saturation behaviour of the sand are fitted on the basis of deformation-free hydraulic experiments. Following this, the complete calibrated triphasic model is numerically validated by simulations of slope failure scenarios at the technical scale, where the loading conditions of the slope are driven by mechanical as well as by hydraulic forces.

Proceeding from the validated soil model, the numerical analysis of the still creeping real Heumös hillslope is carried out in **Chapter 7**. The Heumös hillslope occupies a highly complex deformation and flow behaviour. This complexity based not only on the heterogeneities of the slope material, but also because of the intricate topology and substructure of the slope. For the success of this numerical investigation, the Research Unit 581 ‘Grosshang’ funded by the Deutsche Forschungsgemeinschaft (DFG) decisively contributed.

---

<sup>†</sup>sand from the Gebenbacher sand pit (trade name GEBA, Dorfner, Hirschau, Germany)

In **Chapter 8**, the modelling approach of an internal erosion process of soil is described. Concerning this matter, the triphasic model is further extended by taken into account the porosity development via detaching fine grains from the solid skeleton. Using the soil erosion model, some typical erosion soil problems are numerically investigated in this chapter.

In the Conclusion, **Chapter 9**, a brief summary of the investigated topics und some remarks to future work in these fields are presented. Subsequently, in the **Appendix**, required information and elaborations to some selected issues are given in order to facilitate the understanding of the thesis.

# Chapter 2:

## Continuum-Mechanical Fundamentals of the Theory of Porous Media

This chapter is based on previous work by Ehlers [47, 48, 50, 52–54] and citations therein. It is subdivided in three fundamental parts of the TPM. In the first part, the general basis of the TPM are discussed followed by the second part the kinematic relations of multiphasic materials. Additionally, the mechanical and thermodynamical balance laws are briefly presented in the third part. Therein, the local forms of the balance laws of a constituent as well as for the overall aggregate of multiphasic materials are presented. The main focus within the formulations is addressed on the production terms describing the exchange of physical quantities between the constituents. These production terms have to vanish in regard to the overall aggregate of a closed system where no material can enter or leave the system from the outside of the body.

**Remark:** In this chapter as well as in the following ones, tensorial operations based on the tensor calculus of de Boer [11] and of the lecture notes on vector and tensor calculus of Ehlers [55] are used.

### 2.1 Theoretical Basis

The individual constituents of a heterogeneously constituted porous material are in a state of ideal disarrangement and, therefore, each individual constituent is statistically homogeneously distributed over the Representative Elementary Volume (REV) of the overall aggregate  $\varphi$ . Based on continuum-mechanical consideration of the multiphasic material, the micro-scale informations of the overall aggregate  $\varphi$  and its constituents  $\varphi^\alpha$  are homogenised to macro-scale quantities. This is achieved by real or virtual averaging processes over the REV described by average functions. This homogenisation process leads to a smeared model  $\varphi$  of superimposed and interacting continua  $\varphi^\alpha$ :

$$\varphi = \bigcup_{\alpha=1}^k \varphi^\alpha. \quad (2.1)$$

Therein,  $\alpha = 1, \dots, k$  indicate the different constituents.

The geometrical and physical properties of the constituents are described by mathematical field functions defined over the entire aggregate  $\varphi$ . Thereby, the effective values of the constituents are smeared out over the REV applying a volumetric homogenisation procedure. Introducing the concept of volume fractions, the homogenised micro-structural information of the REV are virtually separated by the individual volume fractions of  $\varphi^\alpha$ . Based on a saturated soil problem which is idealised by a biphasic model, the volumetric

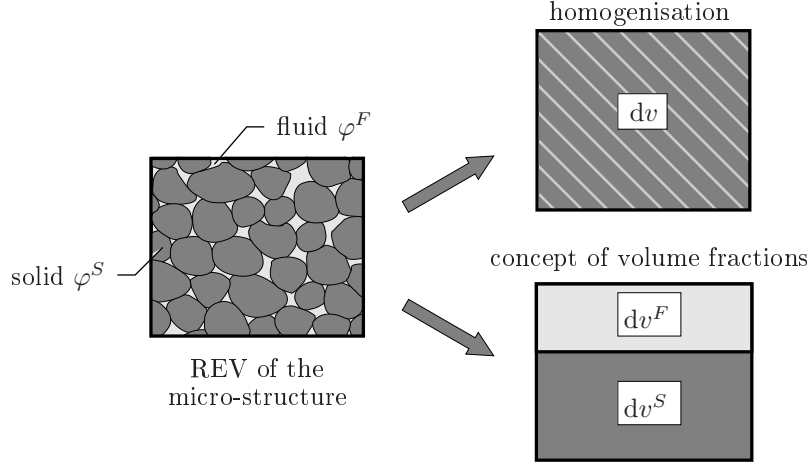


**Figure 2.1:** REV of the qualitative micro-structure of a fluid saturated porous material (left), multi-component TPM macro model obtained by a volumetric homogenisation process, (right).

homogenisation procedure is schematically illustrated in Figure 2.1. Therein, the micro-structure of the soil is built by the grain matrix mainly stabilised by normal and friction forces between the grains. Furthermore, the pore spaces are consisting of filled with one or more pore fluids  $\varphi^\beta$  summarising to the overall fluid phase  $\varphi^F$ . Thereby,  $\beta$  denotes the fluid components.

Concerning the overall aggregate  $\varphi$ , the volume of the multiphasic body  $\mathcal{B}$  is determined by the sum over all volume parts  $V^\alpha$  of the constituents:

$$V = \int_{\mathcal{B}} dv = \sum_{\alpha=1}^k V^\alpha, \quad \text{where} \quad V^\alpha = \int_{\mathcal{B}} dv^\alpha =: \int_{\mathcal{B}} n^\alpha dv. \quad (2.2)$$

Herein,  $n^\alpha$  represent the volume fractions of the constituents at a local material point  $P^\alpha$  and is introduced as the local ratio of the partial volume element  $dv^\alpha$  of  $\varphi^\alpha$  with respect to the bulk volume element  $dv$  of  $\varphi$ , while the sum over all volume fractions leads to the saturation condition of the overall aggregate  $\varphi$ :

$$n^\alpha = \frac{dv^\alpha}{dv} \quad \text{and} \quad \sum_{\alpha=1}^k n^\alpha = 1. \quad (2.3)$$

Following the case of several fluid constituents  $\varphi^\beta$ , the volume fraction  $n^F$  of the overall fluid phase is composed of the volume parts of  $n^\beta$ :

$$n^F = \sum_{\beta=1}^l n^\beta = 1 - n^S. \quad (2.4)$$

Therein,  $l = k - 1$  is the number of the pore-fluid components  $\varphi^\beta$ . The ratio of the volume fractions  $n^\beta$  of the fluid components with regard to the fluid volume fraction  $n^F$  yields the saturation  $s^\beta$  of the fluid components. Thus,

$$s^\beta = \frac{n^\beta}{n^F} \quad \text{where} \quad \sum_{\beta=1}^l s^\beta = 1 \quad (2.5)$$

represents the fluid saturation condition.

For  $\varphi^\alpha$ , two different density functions can be introduced, viz.

$$\rho^{\alpha R} = \frac{dm^\alpha}{dv^\alpha} \quad \text{and} \quad \rho^\alpha = \frac{dm^\alpha}{dv}. \quad (2.6)$$

Therein, the material density  $\rho^{\alpha R}$ , which represents the realistic or the effective local averaged density of  $\varphi^\alpha$ , relates the partial mass element  $dm^\alpha$  to the partial volume element  $dv^\alpha$ , while the partial (global or bulk) density  $\rho^\alpha$  relates the same mass element to the bulk volume element  $dv$ . By use of the definition of the volume fraction in equation (2.3), the material and the partial densities are related to each other as follows:

$$\rho^\alpha = n^\alpha \rho^{\alpha R}. \quad (2.7)$$

Excluding thermal loads, the partial density  $\rho^\alpha$  varies through the realistic density  $\rho^{\alpha R}$  and the volume fraction  $n^\alpha$ . This implies that even if the constituent  $\varphi^\alpha$  is materially incompressible by  $\rho^{\alpha R} = \text{const.}$ , the partial density  $\rho^\alpha$  is changed by varying  $n^\alpha$ .

## 2.2 Kinematical relations

### 2.2.1 Motion function

Following superimposed and interacting continua of multiphasic materials within the framework of the TPM, the overall body  $\mathcal{B}$  consists of a coherent manifold of material points  $P^\alpha$  of all constituent  $\varphi^\alpha$ . Thereby, the material point  $P^\alpha$  of each constituent  $\varphi^\alpha$  in the reference configuration at time  $t_0$  is defined by the reference position vector  $\mathbf{X}_\alpha$ , cf. Figure 2.2. The motion of a constituent  $\varphi^\alpha$  is given by the individual motion function  $\chi_\alpha$ . Hence, the actual position vector  $\mathbf{x}$  at time  $t$  in the *Lagrangian* description reads

$$\mathbf{x} = \chi_\alpha(\mathbf{X}_\alpha, t), \quad \dot{\mathbf{x}}_\alpha = \frac{d}{dt} \chi_\alpha(\mathbf{X}_\alpha, t) \quad \text{and} \quad \ddot{\mathbf{x}}_\alpha = \frac{d^2}{dt^2} \chi_\alpha(\mathbf{X}_\alpha, t). \quad (2.8)$$

Herein,  $\dot{\mathbf{x}}_\alpha$  is the velocity and  $\ddot{\mathbf{x}}_\alpha$  is the acceleration field. The inverse motion  $\chi_\alpha^{-1}$  of  $\varphi^\alpha$  exist only if the *Jacobians* determinants  $J_\alpha$  are non-zero:

$$\mathbf{X}_\alpha = \chi_\alpha^{-1}(\mathbf{x}, t), \quad \text{if} \quad J_\alpha = \det \frac{\partial \chi_\alpha}{\partial \mathbf{X}_\alpha} \neq 0. \quad (2.9)$$

Inserting the inverse motion function of equation (2.9) in (2.8)<sub>1</sub>, the *Eulerian* representation of the motion of  $\varphi^\alpha$  in regard to the position vector  $\mathbf{x}$  of the current configuration yields

$$\dot{\mathbf{x}}_\alpha = \dot{\mathbf{x}}_\alpha[\chi_\alpha^{-1}(\mathbf{x}, t), t] = \dot{\mathbf{x}}_\alpha(\mathbf{x}, t) \quad \text{and} \quad \ddot{\mathbf{x}}_\alpha = \ddot{\mathbf{x}}_\alpha(\mathbf{x}, t). \quad (2.10)$$

The velocity of the overall aggregate results from the sum of the partial velocities weighted with their corresponding densities  $\rho^\alpha$  and is introduced as the barycentric velocity

$$\dot{\mathbf{x}} = \frac{1}{\rho} \sum_{\alpha=1}^k \rho^\alpha \dot{\mathbf{x}}_\alpha. \quad (2.11)$$

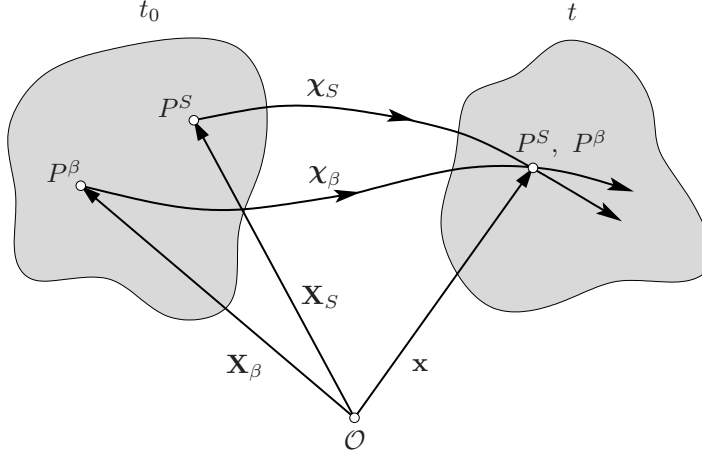


**Figure 2.2:** Motion of a superimposed multiphasic porous material with  $\varphi^S$  as the solid skeleton and  $\varphi^\beta$  as the fluid components where the solid and the fluids follows their own individual motion function.

The material and total time derivatives of an arbitrary, steady and sufficiently steady differentiable scalar and vectorial field function  $(\Gamma)'_\alpha$  and  $(\mathbf{\Gamma})'_\alpha$  of a constituent  $\varphi^\alpha$  read

$$\begin{aligned} (\Gamma)'_\alpha &= \frac{d_\alpha}{dt} \Gamma(\mathbf{x}, t) = \frac{\partial \Gamma}{\partial t} + \text{grad } \Gamma \cdot \dot{\mathbf{x}}_\alpha, \\ (\mathbf{\Gamma})'_\alpha &= \frac{d_\alpha}{dt} \mathbf{\Gamma}(\mathbf{x}, t) = \frac{\partial \mathbf{\Gamma}}{\partial t} + (\text{grad } \mathbf{\Gamma}) \dot{\mathbf{x}}_\alpha. \end{aligned} \quad (2.12)$$

Therein, the first part represents the local time derivative, while the second part is the so-called convective part, which denotes the change of the field function by the differential operator  $\text{grad}(\cdot) = \partial(\cdot)/\partial \mathbf{x}$  in the actual configuration  $\mathbf{x}$  and the velocities  $\dot{\mathbf{x}}_\alpha$  of the constituents  $\varphi^\alpha$ .

Proceeding from the reference configuration, the porous solid structure is at any time known in contrast to the fluid phase. Therefore, the kinematics of the solid phase generally proceed from a *Lagrangean* description using the displacement vector  $\mathbf{u}_S$ , while the pore-fluid flow is better described by the *Eulerian* description by the seepage velocities  $\mathbf{w}_\beta$ , which is defined by the relative relation of fluid and solid velocities:

$$\mathbf{u}_S = \mathbf{x} - \mathbf{X}_S, \quad \mathbf{w}_\beta = \dot{\mathbf{x}}_\beta - \dot{\mathbf{x}}_S, \quad \text{where} \quad (\mathbf{u}_S)'_S = \dot{\mathbf{x}}_S. \quad (2.13)$$

Moreover, two diffusion velocities are introduced. The first one is defined by the difference of the velocity of a constituent  $\varphi^\alpha$  with respect to the barycentric velocity  $\dot{\mathbf{x}}$ , while the second one is related to the fluid velocity  $\dot{\mathbf{x}}_F$ :

$$\mathbf{d}_\alpha = \dot{\mathbf{x}}_\alpha - \dot{\mathbf{x}} \quad \text{and} \quad \mathbf{d}_{\beta F} = \dot{\mathbf{x}}_\beta - \dot{\mathbf{x}}_F. \quad (2.14)$$

Regarding the whole aggregate and the fluid phase, the diffusion velocities have to vanish:

$$\sum_{\alpha=1}^k \rho^\alpha \mathbf{d}_\alpha = \mathbf{0} \quad \text{and} \quad \sum_{\beta=1}^l \rho^\beta \mathbf{d}_{\beta F} = \mathbf{0}. \quad (2.15)$$

To note that the superscript  $(\cdot)^\alpha$  denotes the single constituent, while the subscript  $(\cdot)_\alpha$  characterises the motion of the physical quantity, which depends on the kinematic quantity of the constituent  $\alpha$ .

### 2.2.2 Deformation and strain measures

The local deformation of a material point is measured by the deformation gradient  $\mathbf{F}_\alpha$ , which interconnects the undeformed state of a body with the deformed state. Thus,  $\mathbf{F}_\alpha$  transports the line element  $d\mathbf{X}_\alpha$  of the reference configuration to the line element  $d\mathbf{x}$  of the current configuration via

$$d\mathbf{x} = \mathbf{F}_\alpha d\mathbf{X}_\alpha \quad \text{and} \quad d\mathbf{X}_\alpha = \mathbf{F}_\alpha^{-1} d\mathbf{x}. \quad (2.16)$$

Considering a natural basis system,  $\mathbf{F}_\alpha$  is a so-called two-field tensor\*:

$$\mathbf{F}_\alpha = \text{Grad}_\alpha \mathbf{x} = \frac{\partial \mathbf{x}}{\partial \mathbf{X}_\alpha} \quad \text{and} \quad \mathbf{F}_\alpha^{-1} = \text{grad} \mathbf{X}_\alpha = \frac{\partial \mathbf{X}_\alpha}{\partial \mathbf{x}}. \quad (2.17)$$

Therefore, the transport mechanism of the line elements in  $(2.16)_1$  is the so-called covariant push-forward operation, while the inverse transport is the covariant pull-back operation. Further geometrical transport mechanisms are the contravariant push-forward transport of the reference quantities of the oriented area elements  $d\mathbf{A}_\alpha$  and the transport of the volume elements  $dV_\alpha$  to the corresponding current quantities  $d\mathbf{a}$  and  $dv$ , respectively:

$$d\mathbf{a} = (\det \mathbf{F}_\alpha) \mathbf{F}_\alpha^{T-1} d\mathbf{A}_\alpha \quad \text{and} \quad dv = (\det \mathbf{F}_\alpha) dV_\alpha. \quad (2.18)$$

The determinant of the deformation gradient,  $\det \mathbf{F}_\alpha$ , is also called the *Jacobian*  $J_\alpha$ , which describes the volume change of a physical body, is constrained to positive values because the body cannot be compressed to zero volume. Thus,

$$\det \mathbf{F}_\alpha = J_\alpha > 0, \quad \text{where} \quad \det \mathbf{F}_\alpha(t_0) = 1 \quad (2.19)$$

is the undeformed state at the initial time  $t_0$ . Proceeding from the differences of the squares of the current and the reference line elements

$$\begin{aligned} ||d\mathbf{x}||^2 - ||d\mathbf{X}_\alpha||^2 &= d\mathbf{X}_\alpha \cdot \mathbf{C}_\alpha d\mathbf{X}_\alpha - d\mathbf{X}_\alpha \cdot d\mathbf{X}_\alpha = d\mathbf{X}_\alpha \cdot (\mathbf{C}_\alpha - \mathbf{I}) d\mathbf{X}_\alpha, \\ ||d\mathbf{x}||^2 - ||d\mathbf{X}_\alpha||^2 &= d\mathbf{x} \cdot d\mathbf{x} - d\mathbf{x} \cdot \mathbf{B}_\alpha^{-1} d\mathbf{x} = d\mathbf{x} \cdot (\mathbf{I} - \mathbf{B}_\alpha^{-1}) d\mathbf{x}, \end{aligned} \quad (2.20)$$

further strain tensors  $\mathbf{C}_\alpha$  and  $\mathbf{B}_\alpha$  are introduced, where  $\mathbf{C}_\alpha = \mathbf{F}_\alpha^T \mathbf{F}_\alpha$  is the right *Cauchy-Green* deformation tensor, while  $\mathbf{B}_\alpha = \mathbf{F}_\alpha \mathbf{F}_\alpha^T$  is the left *Cauchy-Green* deformation tensor. Based on (2.20), the *Green-Lagrangean*  $\mathbf{E}_\alpha$  and the *Almansi*  $\mathbf{A}_\alpha$  strain tensors are defined by

$$\mathbf{E}_\alpha = \frac{1}{2}(\mathbf{C}_\alpha - \mathbf{I}) \quad \text{and} \quad \mathbf{A}_\alpha = \frac{1}{2}(\mathbf{I} - \mathbf{B}_\alpha^{-1}). \quad (2.21)$$

---

\*The first basis system of the two field tensor  $\mathbf{F}_\alpha = \mathbf{a}_{\alpha i} \otimes \mathbf{h}_\alpha^j$  is covariant and located in the actual configuration  $\mathbf{a}_{\alpha i}$ , while the second contravariant basis system is located in the reference configuration  $\mathbf{h}_\alpha^j$ . The co- and contravariant basis systems of the inverse of  $\mathbf{F}_\alpha$  are vice versa as well as the positions are transposed,  $\mathbf{F}_\alpha^{-1} = \mathbf{h}_{\alpha j} \otimes \mathbf{a}_\alpha^i$ , cf. Ehlers [47] and Markert [114].

The basis systems of both strain tensors are contravariant, while the metric is covariant. Applying a contravariant transport mechanism on either of the strain tensors, the other one can be computed via

$$\mathbf{A}_\alpha = \mathbf{F}_\alpha^{T-1} \mathbf{E}_\alpha \mathbf{F}_\alpha^{-1} \quad \text{and} \quad \mathbf{E}_\alpha = \mathbf{F}_\alpha^T \mathbf{A}_\alpha \mathbf{F}_\alpha. \quad (2.22)$$

The deformation tensors  $\mathbf{C}_\alpha$  and  $\mathbf{B}_\alpha$  at the undeformed initial state (time  $t_0$ ) correspond to the identity tensor  $\mathbf{C}_\alpha(t = t_0) = \mathbf{B}_\alpha(t = t_0) = \mathbf{I}$ , whereas the strain tensors  $\mathbf{E}_\alpha$  and  $\mathbf{A}_\alpha$  are equivalent to the  $\mathbf{0}$ -tensor.

In case of a small-strain consideration of the solid phase, the geometrical linearisation of the solid strain tensors  $\mathbf{E}_\alpha$  and  $\mathbf{A}_\alpha$  reads:

$$\text{lin } \mathbf{E}_S = \text{lin } \mathbf{A}_S =: \boldsymbol{\varepsilon}_S = \frac{1}{2} [\text{Grad}_S \mathbf{u}_S + (\text{Grad}_S \mathbf{u}_S)^T], \quad (2.23)$$

wherein  $\boldsymbol{\varepsilon}_S$  is the linear well-known *Hookean* strain tensor. For the computation of strain rates, the time derivative of the deformation tensor  $\mathbf{F}_\alpha$  is introduced by

$$(\mathbf{F}_\alpha)'_\alpha = \mathbf{L}_\alpha \mathbf{F}_\alpha, \quad \text{where} \quad \mathbf{L}_\alpha = (\mathbf{F}_\alpha)'_\alpha \mathbf{F}_\alpha^{-1} = \text{grad } \dot{\mathbf{x}}_\alpha \quad (2.24)$$

is the spatial velocity gradient of the constituent  $\varphi^\alpha$ .  $\mathbf{L}_\alpha$  can be uniquely decomposed into a symmetric (strain tensor rate) and a skew-symmetric (spin tensor) part,  $\mathbf{D}_\alpha$  and  $\mathbf{W}_\alpha$ , respectively,

$$\mathbf{L}_\alpha = \mathbf{D}_\alpha + \mathbf{W}_\alpha, \quad \text{where} \quad \begin{cases} \mathbf{D}_\alpha &= \frac{1}{2} (\mathbf{L}_\alpha + \mathbf{L}_\alpha^T) \\ \mathbf{W}_\alpha &= \frac{1}{2} (\mathbf{L}_\alpha - \mathbf{L}_\alpha^T) \end{cases}. \quad (2.25)$$

### 2.2.3 Stress measures

At each material point  $P^\alpha$  of a deformed body  $\mathcal{B}$  exists a three-dimensional(3-d) spacial information of the stress-strain state in the proper *Euclidean* vector space  $\mathcal{V}^3$ <sup>†</sup> caused by acting of external mechanical contact forces  $\mathbf{t}^\alpha$  or gravitation forces  $\mathbf{b}^\alpha$ . By use of the mechanical cutting principle of *Euler*, the internal forces in the body  $\mathcal{B}$  can be illustrated through a virtual cut through the body. The stress vectors  $\mathbf{t}^\alpha$  acting on both cutting planes of the body  $\mathcal{B}$  at the material point  $P^\alpha$  are equal and outward oriented,  $\mathbf{t}(\mathbf{x}, \mathbf{n}, t) = -\mathbf{t}(\mathbf{x}, -\mathbf{n}, t)$ , where  $\mathbf{n}$  is the unit vector. This is referred to as the *Cauchy* lemma. Introducing the *Cauchy* theorem,

$$\mathbf{t}^\alpha(\mathbf{x}, t, \mathbf{n}) = \mathbf{T}^\alpha(\mathbf{x}, t) \mathbf{n}, \quad (2.26)$$

the stress vector  $\mathbf{t}^\alpha$  is mapped by a linear projection of the *Cauchy* stress tensor  $\mathbf{T}^\alpha$  in direction to  $\mathbf{n}$ . Geometrically expressed,  $\mathbf{T}^\alpha$  is also called the true stress tensor while  $\mathbf{t}^\alpha$  is acting on the oriented current area element  $d\mathbf{a}$ :

$$d\mathbf{f}^\alpha = \mathbf{t}^\alpha da = (\mathbf{T}^\alpha \mathbf{n}) da = \mathbf{T}^\alpha (\mathbf{n} da) = \mathbf{T}^\alpha d\mathbf{a}. \quad (2.27)$$

---

<sup>†</sup>In general,  $\mathcal{V}^n$  is a  $n$ -dimensional vector space, wherein the elementary vector calculus is valid and, additionally, the scalar product must be positive,  $|\mathbf{v}|^2 = \mathbf{v} \cdot \mathbf{v} > 0 \forall \mathbf{v} \neq \mathbf{0}$ . The *Euclidean* vector space is a physical space and it is restricted in  $n = 3$  dimension. Hence, the vector  $\mathbf{v}$  has three linear independent basis vectors, cf. de Boer [11] and Ehlers [55].



Accordingly, the actual force vector  $d\mathbf{f}^\alpha$  can be also expressed with other stress tensors relating to the weighted area element  $d\bar{\mathbf{a}}_\alpha = (\det \mathbf{F}_\alpha)^{-1} d\mathbf{a}$  or to the reference area element  $d\mathbf{A}_\alpha$ :

$$d\mathbf{f}^\alpha = \boldsymbol{\tau}^\alpha d\bar{\mathbf{a}}_\alpha = \mathbf{P}^\alpha d\mathbf{A}_\alpha. \quad (2.28)$$

Herein,  $\boldsymbol{\tau}^\alpha$  is the *Kirchhoff* stress tensor (or weighted *Cauchy* stress tensor) and  $\mathbf{P}^\alpha$  is the first *Piola-Kirchhoff* stress tensor. They are related to each other as follows:

$$\mathbf{T}^\alpha = (\det \mathbf{F}_\alpha)^{-1} \boldsymbol{\tau}^\alpha = (\det \mathbf{F}_\alpha)^{-1} \mathbf{P}^\alpha \mathbf{F}_\alpha^T = (\det \mathbf{F}_\alpha)^{-1} \mathbf{F}_\alpha \mathbf{S}^\alpha \mathbf{F}_\alpha^T. \quad (2.29)$$

Therein,  $\mathbf{P}^\alpha$  is a two field-tensor, because the first basis system is in the current configuration, while the second one is located in the reference configuration. Furthermore, the second *Piola-Kirchhoff* stress tensor  $\mathbf{S}^\alpha = \mathbf{F}_\alpha^{-1} \mathbf{P}^\alpha$  is determined by mapping the first basis system of  $\mathbf{P}^\alpha$  to the reference configuration by applying the covariant pull-back transport theorem. All presented stress tensors exist in the finite theory of large deformations. Considering only a geometrically linear approach to the displacement of the solid phase (small deformations) (2.23), all stress tensors coincide to the geometrical linear stress tensor  $\boldsymbol{\sigma}^S$ :

$$\boldsymbol{\sigma}^S : \approx \mathbf{S}^S \approx \mathbf{P}^S \approx \boldsymbol{\tau}^S \approx \mathbf{T}^S. \quad (2.30)$$

## 2.3 Balance relations

The deformation and thermal processes of a continuum mechanical body  $\mathcal{B}$  are described by fundamental balance relations. These balances of mass, momentum, moment of momentum, energy (1-st law of thermodynamics) and entropy (2-nd law of thermodynamics) are axiomatically introduced, i.e., they are derived by observation of physical processes. Regarding a constituent within a mixture, the own physical regularities as well as the effect resulting from the mutual interactions between the other constituents have to be considered. These interrelationships demand additional production terms of mass, moment, energy, etc., according to each individual constituent, whereas the overall aggregate itself behaves like a single-phase material. This implies that the production quantities have to annul each other. For the mathematical description of multiphasic materials, Truesdell [161] introduced the fundamental statements of mixtures, the so-called ‘metaphysical principles’:

### *Truesdell’s metaphysical principles*

1. *All properties of the mixture must be mathematical consequences of properties of the constituents.*
2. *So as to describe the motion of a constituent, we may in imagination isolate it from the rest of the mixture, provided we allow properly for the actions of the other constituents upon it.*
3. *The motion of the mixture is governed by the same equations as is a single body.*

(2.31)

This principle implies that a single constituent of a mixture can be described as if the other phases were not existing, namely, like a single-phase material. But the mutual interactions must be considered by production terms for which additional constitutive equations have to be formulated. Based on these principles, the constitutive modelling of multiphasic materials can be further simplified through extension by the *principle of phase separation*, cf. Ehlers [46], which predicates that each constituent depends only on its own process variables as a single-phase material, cf. Chapter 4.

### 2.3.1 General structure of the balance relations

All fundamental balance relations can be generally expressed by the master balance (Haupt [84]). Using this abstract shape in its global representation, a general structure of a volume-specific scalar  $\Psi$  and vector-valued  $\mathbf{\Psi}$  mechanical quantity of the overall aggregate with respect to the whole body  $\mathcal{B}$  can be introduced via

$$\begin{aligned} \frac{d}{dt} \int_{\mathcal{B}} \Psi \, dv &= \int_{\partial \mathcal{B}} (\boldsymbol{\phi} \cdot \mathbf{n}) \, da + \int_{\mathcal{B}} \sigma \, dv + \int_{\mathcal{B}} \hat{\Psi} \, dv, \\ \frac{d}{dt} \int_{\mathcal{B}} \mathbf{\Psi} \, dv &= \int_{\partial \mathcal{B}} (\mathbf{\Phi} \mathbf{n}) \, da + \int_{\mathcal{B}} \boldsymbol{\sigma} \, dv + \int_{\mathcal{B}} \hat{\mathbf{\Psi}} \, dv. \end{aligned} \quad (2.32)$$

Therein,  $\boldsymbol{\phi} \cdot \mathbf{n}$  and  $\mathbf{\Phi} \mathbf{n}$  represent the efflux of physical quantities over the surface  $\partial \mathcal{B}$  of the aggregate  $\mathcal{B}$  (external vicinity), whereas the supply of the volume-specific physical quantities,  $\sigma$  and  $\boldsymbol{\sigma}$ , results from distance activities (external source). The last term is the volume-specific productions  $\hat{\Psi}$  and  $\hat{\mathbf{\Psi}}$ , which allow the production of the physical represents quantities  $\Psi$  and  $\mathbf{\Psi}$  proceeding from opened systems. Applying the material time derivative on the mechanical quantities and the *Gauss* theorem on (2.32) (transferring the surface integral on  $\partial \mathcal{B}$  into the volume integral over  $\mathcal{B}$ ), the local representation of the master balance reads

$$\begin{aligned} \dot{\Psi} + \Psi \operatorname{div} \dot{\mathbf{x}} &= \operatorname{div} \boldsymbol{\phi} + \sigma + \hat{\Psi}, \\ \dot{\mathbf{\Psi}} + \mathbf{\Psi} \operatorname{div} \dot{\mathbf{x}} &= \operatorname{div} \mathbf{\Phi} + \boldsymbol{\sigma} + \hat{\mathbf{\Psi}}, \end{aligned} \quad (2.33)$$

which is valid at any material point  $P$  of  $\mathcal{B}$ . The individual balances can be derived by inserting for  $\Psi$  (or  $\mathbf{\Psi}$ ) the corresponding quantities for the mass, momentum, moment of momentum (m. o. m.), energy and entropy balances:

	$\Psi, \mathbf{\Psi}$	$\boldsymbol{\phi}, \mathbf{\Phi}$	$\sigma, \boldsymbol{\sigma}$	$\hat{\Psi}, \hat{\mathbf{\Psi}}$
mass	$\rho$	$\mathbf{0}$	$0$	$0$
momentum	$\rho \dot{\mathbf{x}}$	$\mathbf{T}$	$\rho \mathbf{b}$	$\mathbf{0}$
m. o. m.	$\mathbf{x} \times (\rho \dot{\mathbf{x}})$	$\mathbf{x} \times \mathbf{T}$	$\mathbf{x} \times (\rho \mathbf{b})$	$\mathbf{0}$
energy	$\rho \varepsilon + \frac{1}{2} \dot{\mathbf{x}} \cdot (\rho \dot{\mathbf{x}})$	$\mathbf{T}^T \dot{\mathbf{x}} - \mathbf{q}$	$\dot{\mathbf{x}} \cdot (\rho \mathbf{b}) + \rho r$	$0$
entropy	$\rho \eta$	$\boldsymbol{\phi}_\eta$	$\sigma_\eta$	$\hat{\eta} \geq 0$

(2.34)

Herein,  $\rho \dot{\mathbf{x}}$  denotes the momentum of the overall aggregate and  $\mathbf{x} \times (\rho \dot{\mathbf{x}})$  is the corresponding moment of momentum, where the cross sign denotes the outer vector product. Further physical quantities of the energy balance in (2.35) are the internal energy  $\varepsilon$ , the heat influx vector  $\mathbf{q}$  and the external heat supply  $r$ , whereas the entropy balance consists by the entropy  $\eta$ , the efflux of the entropy  $\phi_\eta$ , the external entropy supply  $\sigma_\eta$  and the entropy production  $\hat{\eta}$ . The balance equations of the overall aggregate in (2.34) is constrained to closed systems, i. e., from the surrounding of the body  $\mathcal{B}$  no supply of physical quantities are admitted. Therefore, the production terms  $\hat{\Psi}$  (or  $\hat{\Psi}$ ) are zero for all balances except of  $\hat{\eta}$ , which is the measure for the irreversibility of the thermodynamical process. The thermodynamical process is irreversible, if the entropy production  $\hat{\eta}$  is positive, otherwise, it is zero (reversible process), but never negative. Evaluating the local master balance (2.33) for the individual balances in (2.34), the specific well-known mechanical balance laws in the local form of the overall aggregate result in:

Balance equations of the overall aggregate	
mass:	$\dot{\rho} + \rho \operatorname{div} \dot{\mathbf{x}} = 0$
momentum:	$\rho \ddot{\mathbf{x}} = \operatorname{div} \mathbf{T} + \rho \mathbf{b}$
m. o. m.:	$\mathbf{0} = \mathbf{I} \times \mathbf{T} \longrightarrow \mathbf{T} = \mathbf{T}^T$
energy:	$\rho \dot{\varepsilon} = \mathbf{T} \cdot \mathbf{L} - \operatorname{div} \mathbf{q} + \rho r$
entropy:	$\rho \dot{\eta} \geq \operatorname{div} \phi_\eta + \sigma_\eta$

(2.35)

The structure of the master balance of the constituent  $\varphi^\alpha$  is equivalent to (2.32), however, with the difference that according to *Truesdell's* principles, the production terms have to be taken into account for each balance in order to consider the mutual exchange of physical quantities. Hence, the master balance of  $\varphi^\alpha$  reads

$$\begin{aligned}
 \frac{d_\alpha}{dt} \int_{\mathcal{B}} \Psi^\alpha dv &= \int_{\partial \mathcal{B}} (\phi^\alpha \cdot \mathbf{n}) da + \int_{\mathcal{B}} \sigma^\alpha dv + \int_{\mathcal{B}} \hat{\Psi}^\alpha dv, \\
 \frac{d_\alpha}{dt} \int_{\mathcal{B}} \Psi^\alpha dv &= \int_{\partial \mathcal{B}} (\Phi^\alpha \mathbf{n}) da + \int_{\mathcal{B}} \sigma^\alpha dv + \int_{\mathcal{B}} \hat{\Psi}^\alpha dv,
 \end{aligned}
 \tag{2.36}$$

and, analogously to (2.33), the local form of the master balance of an individual constituent  $\varphi^\alpha$  yields

$$\begin{aligned}
 (\Psi^\alpha)'_\alpha + \Psi^\alpha \operatorname{div} \dot{\mathbf{x}}_\alpha &= \operatorname{div} \phi^\alpha + \sigma^\alpha + \hat{\Psi}^\alpha, \\
 (\Psi^\alpha)'_\alpha + \Psi^\alpha \operatorname{div} \dot{\mathbf{x}}_\alpha &= \operatorname{div} \Phi^\alpha + \sigma^\alpha + \hat{\Psi}^\alpha.
 \end{aligned}
 \tag{2.37}$$

Referring (2.37) to the overall aggregate with regard to the barycentric kinematics (2.11) of the mixture, the master balance (2.34) of a single-phase material has to result. For the

individual physical quantities of  $\varphi^\alpha$ , this leads to the following conditions:

	scalar-value	vector-value
physical quantity	$\Psi = \sum_{\alpha} \Psi^\alpha$	$\mathbf{\Psi} = \sum_{\alpha} \mathbf{\Psi}^\alpha$
efflux	$\phi \cdot \mathbf{n} = \sum_{\alpha} (\phi^\alpha - \Psi^\alpha \mathbf{d}_\alpha) \cdot \mathbf{n}$	$\mathbf{\Phi} \mathbf{n} = \sum_{\alpha} (\mathbf{\Phi}^\alpha - \mathbf{\Psi}^\alpha \otimes \mathbf{d}_\alpha) \mathbf{n}$
supply	$\sigma = \sum_{\alpha} \sigma^\alpha$	$\boldsymbol{\sigma} = \sum_{\alpha} \boldsymbol{\sigma}^\alpha$
production	$\hat{\Psi} = \sum_{\alpha} \hat{\Psi}^\alpha$	$\hat{\mathbf{\Psi}} = \sum_{\alpha} \hat{\mathbf{\Psi}}^\alpha$

(2.38)

Evaluating (2.38) for each balance equation analogously to the overall aggregate in (2.34), the individual physical quantities of a constituent  $\varphi^\alpha$  are constituted as follows:

	$\Psi^\alpha, \mathbf{\Psi}^\alpha$	$\phi^\alpha, \mathbf{\Phi}^\alpha$	$\sigma^\alpha, \boldsymbol{\sigma}^\alpha$	$\hat{\Psi}^\alpha, \hat{\mathbf{\Psi}}^\alpha$
mass	$\rho^\alpha$	$\mathbf{0}$	$0$	$\hat{\rho}^\alpha$
momentum	$\rho^\alpha \dot{\mathbf{x}}_\alpha$	$\mathbf{T}^\alpha$	$\rho^\alpha \mathbf{b}^\alpha$	$\hat{\mathbf{s}}^\alpha$
m. o. m.	$\mathbf{x} \times (\rho^\alpha \dot{\mathbf{x}}_\alpha)$	$\mathbf{x} \times \mathbf{T}^\alpha$	$\mathbf{x} \times (\rho^\alpha \mathbf{b}^\alpha)$	$\hat{\mathbf{h}}^\alpha$
energy	$\rho^\alpha \varepsilon^\alpha + \frac{1}{2} \dot{\mathbf{x}}_\alpha \cdot (\rho^\alpha \dot{\mathbf{x}}_\alpha)$	$(\mathbf{T}^\alpha)^T \dot{\mathbf{x}}_\alpha - \mathbf{q}^\alpha$	$\dot{\mathbf{x}}_\alpha \cdot (\rho^\alpha \mathbf{b}^\alpha) + \rho^\alpha r^\alpha$	$\hat{e}^\alpha$
entropy	$\rho^\alpha \eta^\alpha$	$\phi_\eta^\alpha$	$\sigma_\eta^\alpha$	$\hat{\eta}^\alpha$

(2.39)

Therein,  $\hat{\rho}^\alpha$  is the mass production,  $\hat{\mathbf{s}}^\alpha$  is the total momentum production,  $\hat{\mathbf{h}}^\alpha$  is the total production of angular momentum,  $\hat{e}^\alpha$  denotes the total energy production and  $\hat{\eta}^\alpha$  is the total entropy production of the constituent  $\varphi^\alpha$ . These total production terms consist of two parts. The first part is the direct production term and the other one results from the productions of the lower balances:

total production	=	direct production	+	additional terms
$\hat{\mathbf{s}}^\alpha$	=	$\hat{\mathbf{p}}^\alpha$	+	$\hat{\rho}^\alpha \dot{\mathbf{x}}_\alpha$
$\hat{\mathbf{h}}^\alpha$	=	$\hat{\mathbf{m}}^\alpha$	+	$\mathbf{x} \times (\hat{\mathbf{p}}^\alpha + \hat{\rho}^\alpha \dot{\mathbf{x}}_\alpha)$
$\hat{e}^\alpha$	=	$\hat{\varepsilon}^\alpha$	+	$\hat{\mathbf{p}}^\alpha \cdot \dot{\mathbf{x}}_\alpha + \hat{\rho}^\alpha (\varepsilon + \frac{1}{2} \dot{\mathbf{x}}_\alpha \cdot \dot{\mathbf{x}}_\alpha)$
$\hat{\eta}^\alpha$	=	$\hat{\zeta}^\alpha$	+	$\hat{\rho}^\alpha \eta^\alpha$

(2.40)

Herein, the direct moment production  $\hat{\mathbf{p}}^\alpha$  expresses the volume-specific force interaction of the constituent  $\varphi^\alpha$  with the other constituents in  $\varphi$ , the direct moment of momentum production  $\hat{\mathbf{m}}^\alpha$  denotes the angular momentum coupling between the constituents,

and the quantities  $\hat{\varepsilon}^\alpha$  and  $\hat{\zeta}^\alpha$  are the direct energy and entropy productions. According to the *Truesdell's* principles for the overall aggregate  $\varphi$ , the sum of the production terms of a multiphasic material within a closed system must vanish expecting the entropy production, which can also be greater than zero:

$$\sum_{\alpha} \hat{\rho}^\alpha = 0, \quad \sum_{\alpha} \hat{\mathbf{s}}^\alpha = \mathbf{0}, \quad \sum_{\alpha} \hat{\mathbf{h}}^\alpha = \mathbf{0}, \quad \sum_{\alpha} \hat{\varepsilon}^\alpha = 0, \quad \sum_{\alpha} \hat{\eta}^\alpha \geq 0. \quad (2.41)$$

Proceeding from the general formulation and the substitution of total production terms by the direct ones with (2.40), the balance equations of the individual constituents  $\varphi^\alpha$  yield:

Constituent balance equations	
mass:	$(\rho^\alpha)'_\alpha + \rho^\alpha \operatorname{div} \dot{\mathbf{x}}_\alpha = \hat{\rho}^\alpha$
momentum:	$\rho^\alpha \ddot{\mathbf{x}}_\alpha = \operatorname{div} \mathbf{T}^\alpha + \rho^\alpha \mathbf{b}^\alpha + \hat{\mathbf{p}}^\alpha$
m. o. m.:	$\mathbf{0} = \mathbf{I} \times \mathbf{T}^\alpha + \hat{\mathbf{m}}^\alpha$
energy:	$\rho^\alpha (\varepsilon^\alpha)'_\alpha = \mathbf{T}^\alpha \cdot \mathbf{L}_\alpha - \operatorname{div} \mathbf{q}^\alpha + \rho^\alpha r^\alpha + \hat{\varepsilon}^\alpha$
entropy:	$\rho^\alpha (\eta^\alpha)'_\alpha = \operatorname{div} \left( -\frac{1}{\theta^\alpha} \mathbf{q}^\alpha \right) + \frac{1}{\theta^\alpha} \rho^\alpha r^\alpha + \hat{\zeta}^\alpha$

(2.42)

Therein, for the entropy efflux  $\phi_\eta^\alpha$  and the entropy supply  $\sigma_\eta^\alpha$ , a-priori constitutive assumptions corresponding to a single-phase material have been used, viz.

$$\phi_\eta^\alpha = -\frac{1}{\theta^\alpha} \mathbf{q}^\alpha \quad \text{and} \quad \sigma_\eta^\alpha = \frac{1}{\theta^\alpha} \rho^\alpha r^\alpha, \quad (2.43)$$

where, for each  $\varphi^\alpha$ , an individual absolute *Kelvin's* temperature field  $\theta^\alpha > 0$  is allowed.

Furthermore, standard *Cauchy* materials possess a symmetric *Cauchy* stress tensor  $\mathbf{T} = \mathbf{T}^T$  in consequence of  $\mathbf{I} \times \mathbf{T} = \mathbf{0}$ , which is the result of the angular momentum balance. Considering the mixture theory, the individual stress tensors  $\mathbf{T}^\alpha$  is not generally symmetric due to the skew-symmetric moment of momentum coupling tensor  $\hat{\mathbf{M}}^\alpha$  (cf. Ehlers [54]):

$$\mathbf{T}^\alpha = (\mathbf{T}^\alpha)^T - \hat{\mathbf{M}}^\alpha \quad \text{with} \quad \hat{\mathbf{m}}^\alpha = \frac{1}{2}(\mathbf{I} \times \hat{\mathbf{M}}^\alpha). \quad (2.44)$$

However, by evaluating the sum of  $\hat{\mathbf{h}}^\alpha$  in (2.41)<sub>3</sub> over the overall aggregate, the sum of  $\hat{\mathbf{M}}^\alpha$  must vanish. Thus, the stress tensor  $\mathbf{T}$  of the overall aggregate is symmetric. Proceeding from mixture materials with immiscible constituents, where the individual constituents are of a *Cauchy*-material typ, the stress tensor  $\mathbf{T}^\alpha$  of each constituent  $\varphi^\alpha$  is symmetric at the micro scale. Hence, the symmetric micro-stress property of the constituents is preserved after the homogenisation procedure over the micro structure, and the individual direct moment of momentum productions  $\hat{\mathbf{m}}^\alpha$  is not existing (Hassanizadeh and Grey [82] and Ehlers [52]):

$$\mathbf{T}^\alpha = (\mathbf{T}^\alpha)^T \quad \longrightarrow \quad \hat{\mathbf{m}}^\alpha \equiv \mathbf{0}. \quad (2.45)$$

In contrast to mixture materials, granular materials, wherein the individual grains can rotate, belong to the group of micro-polar materials. In order to take the micro-rotations of the particles into consideration, the rotational degree of freedom has to be regarded, which implies an unsymmetric stress tensor  $\mathbf{T}^\alpha \neq (\mathbf{T}^\alpha)^T$ . The idea of the extended continuum theory on rotational kinematics for granular materials goes back to the *Cosserat* brothers [31], why these materials are also called *Cosserat* continua. Treating the *Cosserat* theory in the framework of the TPM, the interested reader is referred to the works of, e.g., [42, 43, 68, 69, 137].

Moreover, the balance relations (2.34) of the overall aggregate  $\varphi$  and of the individual constituent  $\varphi^\alpha$  (2.42) are in relation to each other by the sum over all constituents referred to the barycentric motion of  $\varphi$ . Carrying out this procedure, some restrictions result:

$$\begin{aligned}
 \rho &= \sum_{\alpha} \rho^{\alpha} & ; \rho \mathbf{b} &= \sum_{\alpha} \rho^{\alpha} \mathbf{b}^{\alpha} \\
 \rho \dot{\mathbf{x}} &= \sum_{\alpha} \rho^{\alpha} \dot{\mathbf{x}}_{\alpha} & ; \rho \ddot{\mathbf{x}} &= \sum_{\alpha} [\rho^{\alpha} \ddot{\mathbf{x}}_{\alpha} - \operatorname{div} (\rho^{\alpha} \mathbf{d}_{\alpha} \otimes \mathbf{d}_{\alpha}) + \hat{\rho}^{\alpha} \dot{\mathbf{x}}_{\alpha}] \\
 \mathbf{T} &= \sum_{\alpha} (\mathbf{T}^{\alpha} - \rho^{\alpha} \mathbf{d}_{\alpha} \otimes \mathbf{d}_{\alpha}) & ; \mathbf{q} &= \sum_{\alpha} [\mathbf{q}^{\alpha} - (\mathbf{T}^{\alpha})^T \mathbf{d}_{\alpha} + \rho^{\alpha} \varepsilon^{\alpha} \mathbf{d}_{\alpha} + \frac{1}{2} (\mathbf{d}_{\alpha} \cdot \mathbf{d}_{\alpha}) \mathbf{d}_{\alpha}] \\
 \rho r &= \sum_{\alpha} \rho^{\alpha} (r^{\alpha} + \mathbf{b}^{\alpha} \cdot \mathbf{d}_{\alpha}) & ; \rho \varepsilon &= \sum_{\alpha} \rho^{\alpha} (\varepsilon^{\alpha} + \frac{1}{2} \mathbf{d}_{\alpha} \cdot \mathbf{d}_{\alpha})
 \end{aligned} \tag{2.46}$$

The caloric primary variable entropy  $\eta^\alpha$  of the internal energy  $\varepsilon^\alpha$  is not suited for describing temperature dependent material behaviour in contrast to the conjugated caloric primary variable temperature  $\theta^\alpha$ . This is why  $\theta^\alpha$  is measurable or observable during the natural processes compared to  $\eta^\alpha$ . Therefore, the mass-specific constituent *Helmholtz* free energy  $\psi^\alpha$  is introduced via the *Legendre* transformation,

$$\psi^\alpha = \varepsilon^\alpha - \theta^\alpha \eta^\alpha, \tag{2.47}$$

which is a function of the primary variables of the caloric quantities  $\theta$  and of the mechanical-strain quantities. Therewith, the entropy inequality (2.42) is rewritten to

$$\begin{aligned}
 \hat{\eta} = \sum_{\alpha} \hat{\eta}^{\alpha} &= \sum_{\alpha} \frac{1}{\theta^{\alpha}} \{ \mathbf{T}^{\alpha} \cdot \mathbf{L}_{\alpha} - \rho^{\alpha} [(\psi^{\alpha})'_{\alpha} + (\theta^{\alpha})'_{\alpha} \eta^{\alpha}] - \hat{\mathbf{p}}^{\alpha} \cdot \dot{\mathbf{x}}_{\alpha} - \\
 &\quad - \hat{\rho}^{\alpha} (\psi^{\alpha} + \frac{1}{2} \dot{\mathbf{x}}_{\alpha} \cdot \dot{\mathbf{x}}_{\alpha}) - \frac{1}{\theta^{\alpha}} \mathbf{q}^{\alpha} \cdot \operatorname{grad} \theta^{\alpha} + \hat{\varepsilon}^{\alpha} \} \geq 0.
 \end{aligned} \tag{2.48}$$

In this contribution, only isothermal IBVP with a constant and single temperature for all constituents are investigated ( $\theta^\alpha \equiv \theta \equiv \text{const.}$ ). Hence, the entropy inequality (2.48) is transferred to the so-call *Clausius-Planck* inequality

$$\mathcal{D}_{\text{int}} = \sum_{\alpha=1}^k [\mathbf{T}^{\alpha} \cdot \mathbf{D}_{\alpha} - \rho^{\alpha} (\psi^{\alpha})'_{\alpha} - \hat{\mathbf{p}}^{\alpha} \cdot \dot{\mathbf{x}}_{\alpha} - \hat{\rho}^{\alpha} (\psi^{\alpha} + \frac{1}{2} \dot{\mathbf{x}}_{\alpha} \cdot \dot{\mathbf{x}}_{\alpha})] \geq 0. \tag{2.49}$$

Therein,  $\mathcal{D}_{\text{int}}$  represents the internal dissipation of the mechanical energy. For  $\mathcal{D}_{\text{int}} = 0$ , reversible mechanical processes of the considered material are described, while, for  $\mathcal{D}_{\text{int}} > 0$ , dissipative processes are identified as irreversible processes of plastic, viscoelastic or viscoplastic deformations of the solid skeleton or the motion of viscous pore fluids with mutual momentum interactions between the constituents or mass production processes of internal erosion (Steeb and Diebels [151]) or of growing biological tissues (Ehlers et al. [65]). Moreover, proceeding from non-polar material properties, the symmetric *Cauchy* stress tensor  $\mathbf{T}^\alpha = (\mathbf{T}^\alpha)^T$  refers only to the symmetric part of the deformation velocity gradient  $\mathbf{L}_\alpha = \mathbf{D}_\alpha$ , cf. (2.25).





# Chapter 3:

## Triaxial Experimental Investigations of Granular Materials

The stress-strain behaviour of materials is commonly investigated by elementary experiments. The results of these experiments uniquely describe the general material behaviour, and they are used for the constitutive modelling and the model calibration. However, for that purpose, elementary deformation experiments on partially saturated soils are not particularly suited due to the strongly coupled deformation and flow processes. Thus, the detected physical properties cannot be uniquely mapped to the individual phases. Proceeding from *the principle of phase separation* (Ehlers [46]), the experimental investigation of a partially saturated sand are split into deformation-governed experiments and non-deformation-governed hydraulic experiments. Based on drained triaxial tests, the deformation behaviour of the solid skeleton with vacant pore spaces (dry sand) is examined in the current chapter, while the experimental study of the hydraulic sand properties is discussed in Section 6.2. Prior to this study, the triaxial equipments and the error analysis of the triaxial test setup as well as the basics of experimental mechanics of triaxial testing are discussed. Then, the complex stress-strain behaviour of dense sand is demonstrated on the basis of monotonic and non-monotonic stress-path-depending triaxial experiments, whereas, in particular, new experimental observations to the yielding and failure behaviour of dense sand are illustrated.

### 3.1 Triaxial experimental

The stress-strain behaviour of granular materials is very complex and demands spatial experimental investigations. A complete 3-d information of the mechanical loading behaviour is obtained by a *true triaxial apparatus* using cubical specimens, where all three principle loading directions can be individually controlled. The pioneering work on constructions of such triaxial apparatus was made, e.g., by Ko and Scott [95], Pearce [125] and Lade and Duncan [99] and also the researchers referred therein. Despite of the complexity of this apparatus in operating, they are significant for investigations of particular behaviour of granular materials.

Concerning to true triaxial results, Lade and Wang [174] have shown that shear bands occur when all three principle stresses differs from each other. However, evolving of shear bands are always associated with a strong decrease of the shear stress and an inhomogeneous stress-strain distribution within the specimen. But, for calibration of the constitutive models, a homogeneous stress-strain relation is required, i.e., the boundary conditions have to be chosen in such a way that the homogeneous development of the stresses and strains is not disturbed. For the true triaxial experiments, this is obtained by coupling the stresses of two principle stress directions. Therewith, shear bands may

be developed only at a very large strain state, which is clearly initiated after the peak shear stress has been passed. This is automatically fulfilled by drained triaxial tests using cylindrical specimens and applying a homogeneous load and homogeneous boundary conditions (elementary tests), cf. Appendix A. The homogeneous boundary conditions are obtained by lubrication of the endplates. Therewith, the shear stresses at the top and the bottom of the specimen are minimised to zero, otherwise, the specimen bulges because the influence of the boundaries on the stress-strain relation, where the volume extensions of the specimen are impeded, gradually declines away from the boundaries. As a consequence, shear bands through the specimens are developed and the specimen owns no more homogeneous stress-strain relation.

In general, the material characteristics of granular materials are investigated by cylindrical specimens, where the specimen is permanently under a surrounding cell-water pressure within the triaxial cell. The cell pressure controls the radial and tangential stresses of the specimen,  $\sigma_2 = \sigma_3 = -p$ , whereas the axial force  $\sigma_1$  is driven by the load piston. Despite of the two coupled stress directions, almost the complete characteristics of the material can be determined, which are required for the model calibration (Müllerschön [118]). Furthermore, compared to the *true triaxial apparatus*, the handling is much easier.

However, triaxial tests using rotational symmetric specimens have some specific difficulties to perform ‘error-free’ experiments. The most difficulties are the elimination of the errors resulting from the cell deformation, the measuring instruments or air bubbles within the cell and pipes, cf. Leong [105]. These essential issues will be discussed next.

### 3.1.1 Triaxial cell

As mentioned in the introduction, one difficulty of triaxial testing is the correct volume measurement, particularly, if small contraction or dilatation specimen deformations must be accurately resolved. Because of the comparably large cell deformation of conventional acrylic glass cells, different kinds of double-wall cell systems were developed, which eliminate the cell deformation by controlling the pressure in the inner and the outer cell. The price to pay is the high complexity of the test system and the circumstantial handling of the specimen setup. For these reasons, a new triaxial cell had to be developed, which is illustrated in Figure 3.1 in the assembled state (left) and as the individual parts of the cell (middle), while the right figure shows the cell cover for extension tests with a larger diameter of the load piston ( $\varnothing 10$  cm). The triaxial cell presented in Figure 3.1 retains its simplicity but reduces unwanted volume deformations to a minimum.

The cell was constructed of a massive aluminium pipe (A) with 2.5 cm thick cell wall, which has been specially anodised to avoid air bubble adhesion, such that the cell deformation could be almost eliminated. In order to remove preferable all air bubbles within the cell, the inner surface of the cell cover (E) has a convex shape, where the highest two points are positioned at the two air-bleed vents at top of the cell, respectively. Therewith, the air bubbles can freely ascend along the plane surface to the air-bleed vents. The counterpart (D) is only for the purpose to fill the inner space of the cell in order to reduce the amount of required cell water. Furthermore, two different diameters of the load piston can be installed depending on whether compression or extension tests are intended to be

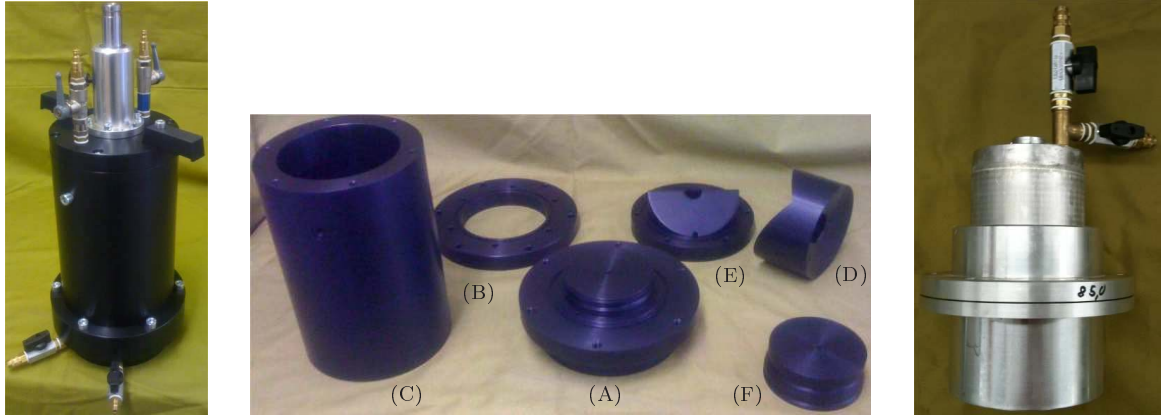


**Figure 3.1:** (left) Assembled aluminium cell with a load piston of  $\varnothing 2.5$  cm, (middle) disassembled parts, which are assembled in alphabetical order (A)-(E) where (F) is the socket of the specimen laying on (A) and (right) the top cell cover with the load piston of  $\varnothing 10$  cm for extension tests.

performed. For the compression loading, a load piston of  $\varnothing 2.5$  cm is used, cf. in Figure 3.1 (left). However, this load piston cannot be applied for extension tests. Hence, no axial force on the load piston during the hydrostatic loading path is building up, which can be subsequently reduced for the extension loading, because the confined water pressure is acting on the complete sample as well as on the top of the specimen. Therefore, a load piston with the same diameter as the specimen ( $\varnothing 10$  cm) has been constructed by which the complete axial load is applied. Thus, according to the intended tests of compression or extension loading, the top cell cover (E) together with (D) and the load piston with  $\varnothing 2.5$  cm can be exchanged with the top cell cover with the load piston of  $\varnothing 10$  cm (Figure 3.1). A further measure to rid the cell from air bubbles is to flood the cell with  $\text{CO}_2$  before it is filled with degassed water.

Proceeding from a homogeneous deformation of compact specimens, their volumetric deformation can be easily measured via in- and outflow of the degassed confined cell water. Due to the fact that the main error source in calibration of the volume measuring of the triaxial experiment is the amount of water in the system, it is very important to reduce it to a minimum. Following this, the new system, which is made up of the new cell (Figure 3.1), pipes and the volume-pressure device (Figure 3.2), requires only a total water volume of  $\approx 1100 \text{ cm}^3$  using a cylindrical specimen with a volume of  $785 \text{ cm}^3$  (diameter and height of 10 cm). This is a very low value of confined cell water and, therewith, the volume measuring error has been reduced significantly. Unfortunately, the aluminium cell has one obvious disadvantage, namely, it is not possible to look inside the cell to observe the deforming specimen during the experiment. However, it is not indispensably necessary for investigation of homogeneously deforming specimens (elementary tests).

### 3.1.2 Volume-change monitoring

The variation of the amount of cell water representing the volume change of the specimen is very few, in particular, during hydrostatic compression tests. Therefore, a precise measuring device including a setup with few calibration errors is essential for a good

quality of the experimental results.

For controlling the in-/outflow of the confined cell water, the pressure-volume controller (p-v controller), which is shown in Figure 3.2, from the company Wille GmbH (Willsdruff, Germany) is applied. The maximal pressure limit of the screw-driven p-v controller is at 950 kPa and the water tank capacity is 200 cm<sup>3</sup>. However, calibration tests of the p-v controller pointed out that some modifications on the controller have to be made in order to reduce the measuring error. The water tank capacity of the p-v controller is too huge for standard triaxial testing of sand and, additionally, the construction of the tank is not stiff enough. The extension of the tank amounts 2.8 cm<sup>3</sup> at the maximal pressure state. By installing a new stiffer tank with only 50 cm<sup>3</sup> capacity, the systematic error could be reduced to 0.3 cm<sup>3</sup>.



**Figure 3.2:** *P-v controller: (left) plunger cylinder on which a water tank capacity of 50 cm<sup>3</sup> is attached and (right) the p-v controller device.*

The p-v controller computes the volume change by the rotational movement of the gear. Due to the gear backlash of the screw-driven p-v controller, it is important to verify the resulting volume measuring error of the p-v controller. The play of the gear becomes evident through the following tests, where the results are illustrated in Figure 3.3. Concerning this, the triaxial cell is filled with degassed water and is confined until 100 kPa.

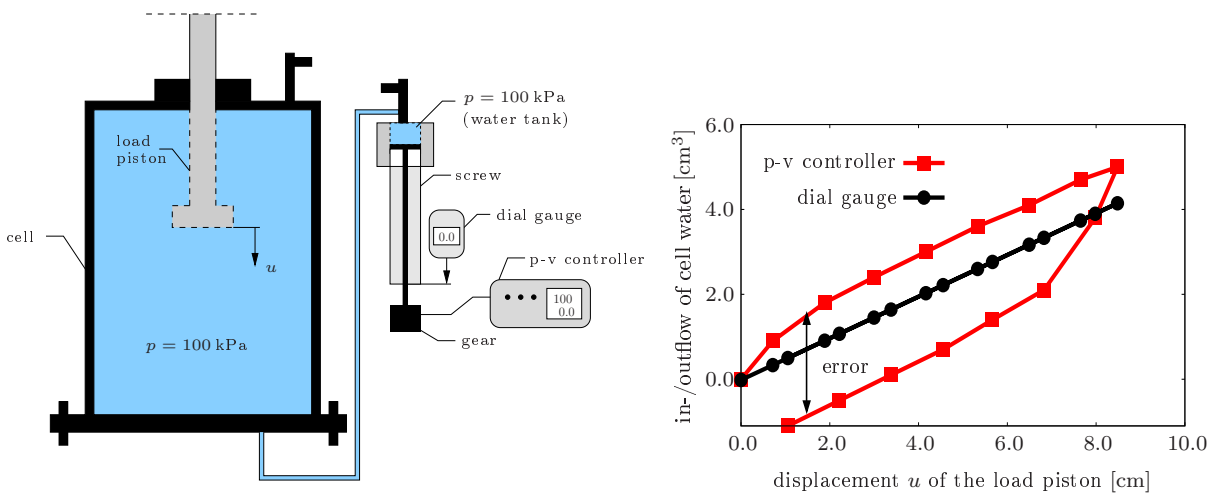


**Figure 3.3:** *(left) The controller test by which the load piston is driven down and up at constant cell pressure of 100 kPa and (right) the results of in-/outflow of cell water during the piston motion – comparison of measured data received by the p-v controller (the red curve with square dots) and the real motion of the plunger cylinder recorded by the dial gauge (the black curve with circle dots).*

Thereafter, the load piston ( $\varnothing 2.5$  cm) is slowly moved into the cell and back to the starting point, while the cell pressure is kept constant through in- and outflow of confined cell water. Figure 3.3 (right) shows the volume change of the cell water measured with the p-v controller (red curve with square points), whereas the black curve with points represents the volume change converted from the real motion of the screw, which is measured with a digital distance indicator over the load-piston displacement  $u$ . The results show a clear measuring error of more than  $3 \text{ cm}^3$ , which additionally varies with the cell pressure. Proceeding from this test, only the measured data taken from the digital distance indicator is used for further applications.

After the individual error has been minimised best as possible, the remaining systematic error is identified. Thereby, hydrostatic tests with a steel dummy owning the same dimensions as the specimen have been carried out. In order to ensure that almost the same systematic error is reproduced, the identical testing procedure is exactly performed for

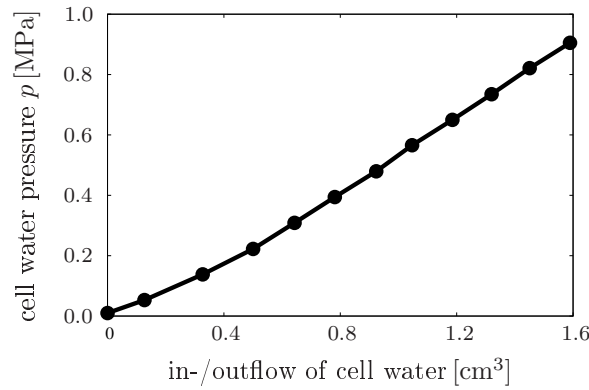


**Figure 3.4:** Systematic volume calibration error of the complete triaxial system.

the sand tests. The results are shown in Figure 3.4. For instance, a systematic error at the maximal pressure amounts  $1.6 \text{ cm}^3$ , which corresponds only about 0.2 % volume of the tested specimen.

Besides this, further systematic error sources as bedding error, membrane penetration or friction force of the load piston has been also considered, whereas, for the tested material, these error sources are not so significant compared with the presented ones. Nevertheless, they have to be taken into account.

### 3.1.3 Homogeneous standard triaxial tests

Proceeding from a homogeneous stress-strain distribution, only the principle stress directions of the geometrically linear second-order stress tensor  $\boldsymbol{\sigma}$  (2.30) are activated, cf. Appendix A.2. Therewith,  $\boldsymbol{\sigma}$  can be also expressed as a vector  $\boldsymbol{\sigma} = \sigma_i \mathbf{e}_i$ , wherein  $\sigma_i$  are the principle stresses and  $\mathbf{e}_i$  the corresponding orthonormal eigenvectors. For graphical illustrations, the principle stresses are spanning a vector space, which is better described by the cylindrical coordinate system with the *Reuss* variables  $I_\sigma$ ,  $R$  and  $\Theta$ . Thereby, the first principle stress invariant  $I_\sigma$  of the stress tensor  $\boldsymbol{\sigma}$  represents the hydrostatic axis and  $R$  and  $\Theta$  describe the deviatoric stress space, where  $R$  is the radius and  $\Theta$  denotes the

Lode angle:

$$I_\sigma = \boldsymbol{\sigma} \cdot \mathbf{I}, \quad R := \sqrt{2 \mathbb{II}_\sigma^D} \quad \text{and} \quad \Theta := \frac{1}{3} \arcsin \left( \frac{\sqrt{27}}{2} \frac{\mathbb{III}_\sigma^D}{(\mathbb{II}_\sigma^D)^{3/2}} \right). \quad (3.1)$$

Therein,  $R$  and  $\Theta$  depend on the (negative) second and the third principal deviatoric invariants  $\mathbb{II}_\sigma^D$  and  $\mathbb{III}_\sigma^D$  of  $\boldsymbol{\sigma}$ :

$$\mathbb{II}_\sigma^D = \frac{1}{2} \boldsymbol{\sigma}^D \cdot \boldsymbol{\sigma}^D \quad \text{and} \quad \mathbb{III}_\sigma^D = \frac{1}{3} \boldsymbol{\sigma}^D \boldsymbol{\sigma}^D \cdot \boldsymbol{\sigma}^D, \quad (3.2)$$

where  $\boldsymbol{\sigma}^D = (\boldsymbol{\sigma} - 1/3 \boldsymbol{\sigma} \cdot \mathbf{I}) \mathbf{I}$  is the deviatoric stress tensor. Based on these important relations, the loading path progression within the principle stress space of two standard triaxial compression tests will be discussed in the following. Above all, the *Reuss* variables are particularly used for the constitutive modelling of the plastic behaviour, see Section 4.2.2.

By way of illustration, Figures 3.5 and 3.6 show the loading stress paths of two compression tests in the principle stress space. Firstly, in both cases, the test is isotropically driven by the hydrostatic stress  $\sigma^H$  along the hydrostatic axis  $I_\sigma$  until point H. Afterwards, in Figure 3.5, the axial load  $\sigma_1$  is increased along the path  $\overline{HP}$ , while the other both principle stress directions  $\sigma_2$  and  $\sigma_3$  are kept constant, whereas in Figure 3.6,  $I_\sigma$  stays constant by reducing  $\sigma_2$  and  $\sigma_3$  from H to  $P'$  (or its projection  $\overline{HP''}$  in the  $\sigma_2$ - $\sigma_3$  plane) during the

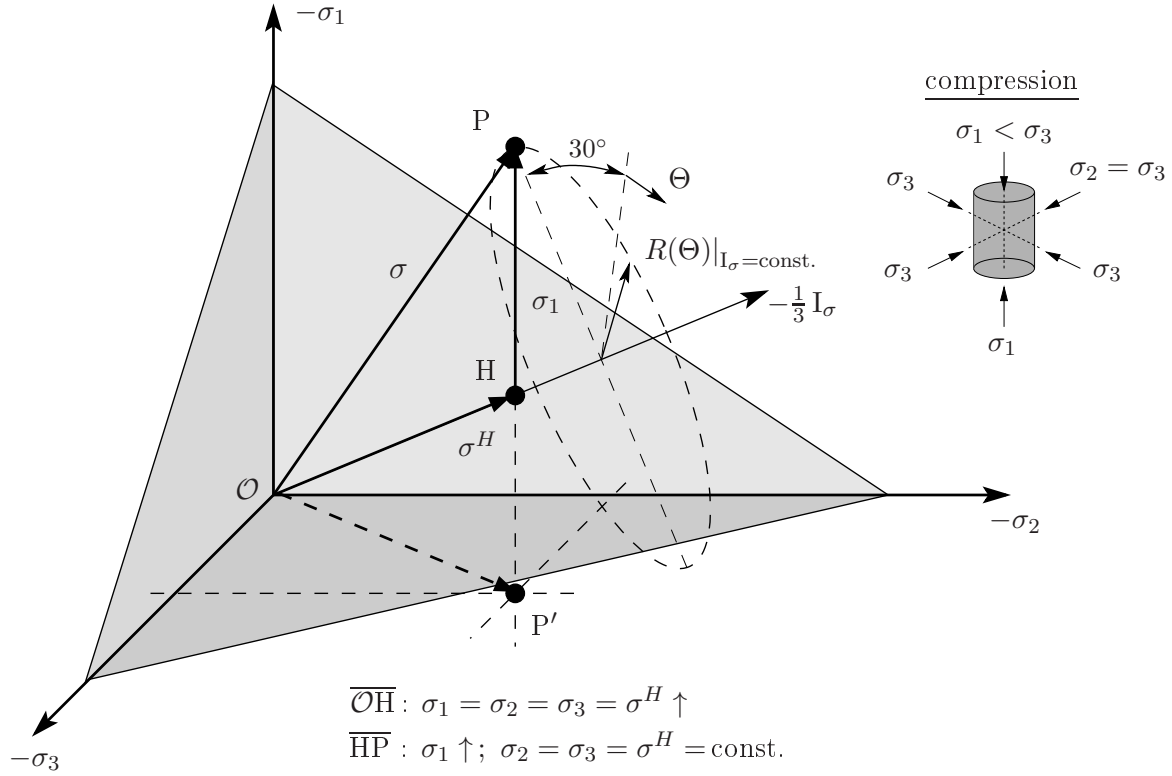


**Figure 3.5:** Illustration of the stress path of a standard compression test with the confining pressure  $\sigma^H = -p = \text{const.}$  in the principle stress space.

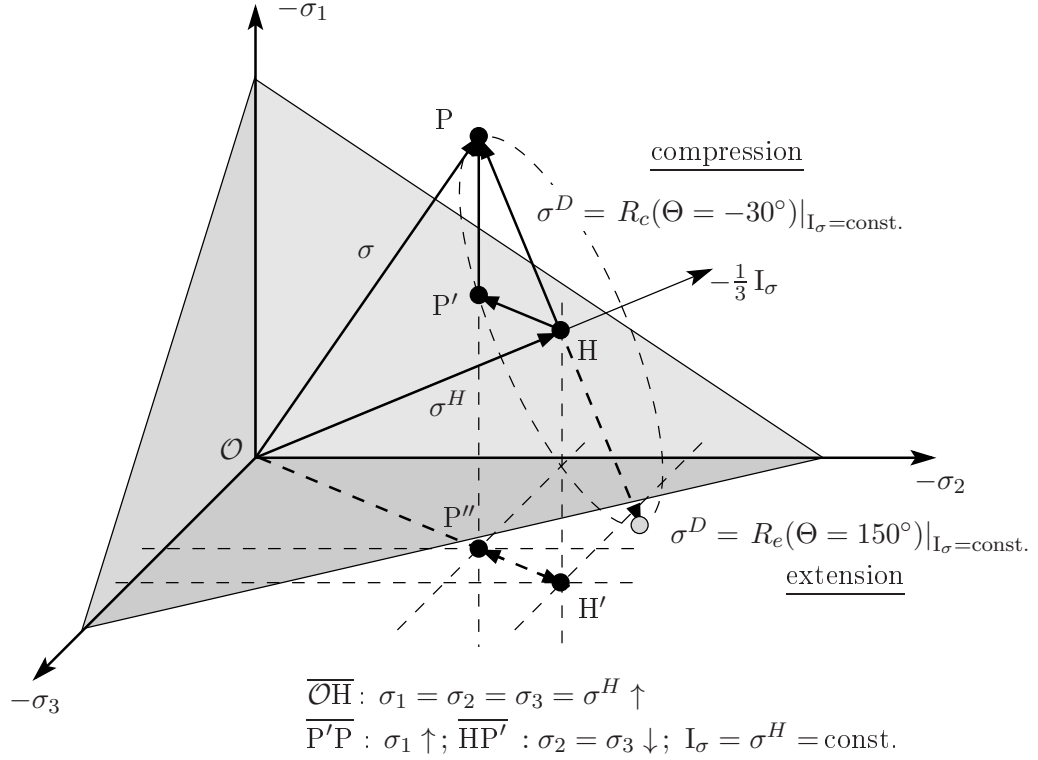


**Figure 3.6:** Illustration of the stress path of a standard compression test with  $I_\sigma = \text{const.}$  in the principle stress space.

increase of  $\sigma_1$  from  $\overline{P'P}$ , where the amount of  $\sigma_2$  and  $\sigma_3$  corresponds to  $\sigma_1$ . This load path is defined as a pure deviatoric stress loading  $\sigma^D$ .

Furthermore, in these Figures, the dashed circle represents the deviatoric or the octahedral plane, which is perpendicular to the hydrostatic axis  $I_\sigma$ . Therein, the load direction within this deviatoric plane is defined by the radius  $R$  and the *Lode* angle  $\Theta$ . In contrast to *true triaxial apparatus*, where arbitrary *Lode* angles can be derived, cf. [174, 181], cylindrical triaxial tests are restricted only to compression shear tests  $R_c = R(\Theta = -30^\circ)$  and extension shear tests  $R_e = R(\Theta = 150^\circ)$ . However, the simple shear loading is defined by  $R_s = R(\Theta = 0)$ . The compression and extension points are regularly repeated within the deviatoric plane and occur at each  $120^\circ$ , while the shear load points follow the sequences of every  $60^\circ$ .

Figure 3.7 represents the stress paths in the principle hydrostatic and in the deviatoric stress plane, whereas triaxial stress paths are commonly discussed at the hydrostatic plane. Therein, three types of possible monotonic loading paths A, B and C are illustrated. They are driven as follows:

- A :=  $\sigma_1 \uparrow \downarrow; \sigma_2 = \sigma_3 = \text{const.}$       • B :=  $\sigma_1 \downarrow \uparrow; \sigma_2 = \sigma_3 \uparrow \downarrow; I_\sigma = \text{const.}$
- C :=  $\sigma_2 = \sigma_3 \downarrow \uparrow; \sigma_1 = \text{const.}$

The monotonic stress paths in the parentheses in Figure 3.7 have been not carried out in the framework of this contribution.

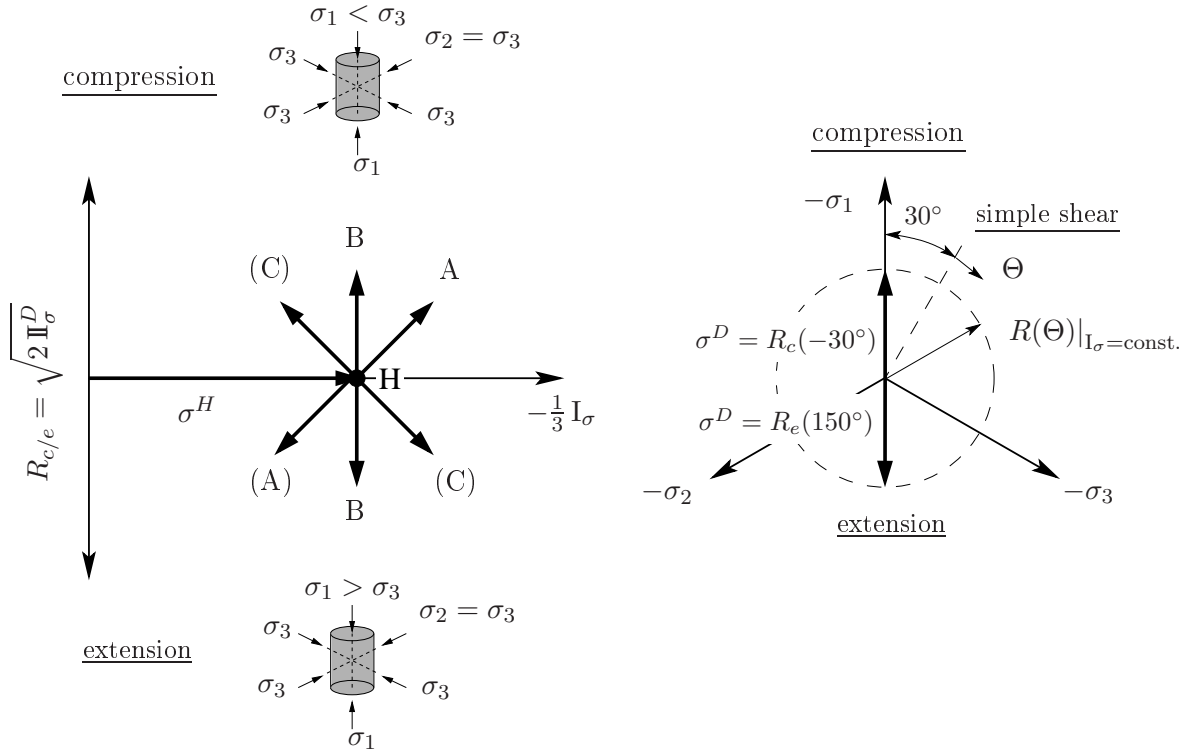


**Figure 3.7:** Standard cylindrical triaxial compression and extension loading paths presented in the hydrostatic (left) and deviatoric (right) stress planes.

## 3.2 Experimental observations of yielding and failure behaviour of sand

Investigating dry sand, the pore content is air, which has, especially under drained conditions, no physical influence on the solid behaviour and can thus be neglected. Furthermore, as the sand grains are incompressible and widely uncrushable, the dilatation and compression behaviour of sand only results from a change of the pore volume or from the compactness of the packing, respectively. However, concerning this, Yamamuro and Lade [182] experimentally investigated the influence of crushing grains on the material behaviour. Therefore, they carried out triaxial compression tests with different confining pressures and observed the onset of crushing of particles at a confining pressure of approximately 2.1 MPa, while the influence of crushing on the stress-strain behaviour ended around a confining pressure of 4 MPa. During grain crushing, the stress-strain curves are flattening as well as the stiffness and strength of the granular material decreases. However, confining pressures higher than 2.1 MPa can only be found at very special geotechnical problems, while, in general, pressures occurring in practice are clearly located below the significant limit of particle crushing. In further consideration of grain properties in this contribution, they are assumed to be incompressible and uncrushable within the applied range of moderate pressures.

Concerning the description of an elasto-plastically deforming solid skeleton consisting of



granular matter, the most difficult part is the description of the evolution of the plastic yield surface with its associated hardening and softening behaviour. In case of frictional granular material, the yielding behaviour was experimentally investigated in the late sixties of the last century, for example, by Poorooshasb et al. [127, 128] and by Tatsuoka and Ishihara [155]. These investigators carried out triaxial stress-path-depending compression tests including unloading and reloading cycles, where the shear stress was properly kept below the peak value in order to detect the restarting points of yielding at various confining pressures. These points were identified as loci on a yield surface. Lade and Kim [100] assumed that yield points with the same plastic work uniquely belong to the same contour of a yield surface evolving independently from the stress path or the stress level until the failure surface is reached. As a consequence, the standard failure behaviour was described by only one fixed failure surface. In contrast to this, it was detected from the stress-path-dependent experiments on dry sand presented in the following that there must exist an individual failure surface at each stress level at the failure state, cf. Ehlers and Avcı [56]. This led to the conclusion that the failure surface is not fixed, but depends on the stress level, instead. Similar experiments were carried out by Lade and Prabucki [101], where they found the same results, namely, that preshearing until the peak failure state increases the failure strength of lower stress levels. To explain this material behaviour, consider the differences of granular matter in comparison to standard solid materials like, for instance, metallic polycrystals. In metal plasticity, the hardening process irreversibly changes the internal structure of the material, thus extending the elastic domain in the principal stress space, when isotropic hardening was assumed. Increasing the external load continues the hardening process until the material fails and the corresponding failure surface is reached. Close to the failure surface, unloading and reloading cycles exhibit an elastic material up to the failure state. In contrast to metals, where the yield and failure functions do not depend on the hydrostatic stress (plastic incompressibility), the solid behaviour of granular material crucially depends on it through the confining pressure. As a result, the loading paths of triaxial experiments start by applying a hydrostatic stress up to a certain value of the confining pressure continued by a shear loading both accompanied by elasto-plastic deformations. The application of the hydrostatic stress leads to a certain densification of the grain packing. During shear loading, this packing is firstly furthermore densified and then loosened at higher shear-stress levels. The densification and dilatation process coming along with a structural interlock of the particles finally defines the corresponding failure surface, namely, when the peak shear stress is reached. After shear unloading and reducing the confining pressure to a smaller value, one observes the intergranular structure unchanged. If the shear stress is increased again, one firstly obtains a shear-stress value higher than that obtained during monotonic loading at the smaller confining pressure. However, any ongoing displacement-controlled loading immediately reduces the shear-stress level to that smaller value belonging to a monotonic loading path at the smaller confining pressure. At the microstructure of the sand grains, this behaviour is due to the fact that the particles change their structure towards a looser packing, while the loading process is continued and the particles partly lose their mutual interlock. This state approximately belongs to a new but smaller failure surface with a corresponding peak shear stress.

### 3.2.1 Test-sand properties

The granular material under study is a GEBA fine sand with an effective density (grain density) of  $\rho^{SR} = 2.65 \text{ g/cm}^3$ . All experiments were performed under dry conditions with an initial partial density (assembly density) of  $\rho_{0S}^S = n_{0S}^S \rho^{SR} = 1.55 \text{ g/cm}^3$  corresponding to a volume fraction of  $n_{0S}^S = 0.585$  and a \*void ratio of  $e = 0.709$ . The assembly density of the sand can be adjusted between  $\rho_{0S}^S = 1.37 \text{ g/cm}^3$  in the loosest case with a maximum void ratio of  $e = 0.934$  to  $\rho_{0S}^S = 1.66 \text{ g/cm}^3$  in the densest case with a void ratio of  $e = 0.596$ . Moreover, the †Density Index  $I_D = 0.67$  of the tested specimens corresponds to dense sand with grain sizes ranging between 0.06 mm and 0.3 mm with a sieve retention of  $d_{10} = 0.09 \text{ mm}$  and  $d_{60} = 0.11 \text{ mm}$ , cf. the grain size distribution curve in Figure 3.8. A uniformity coefficient of  $C_u = 1.22$  classifies the GEBA sand as well-graded with roundly shaped particles.

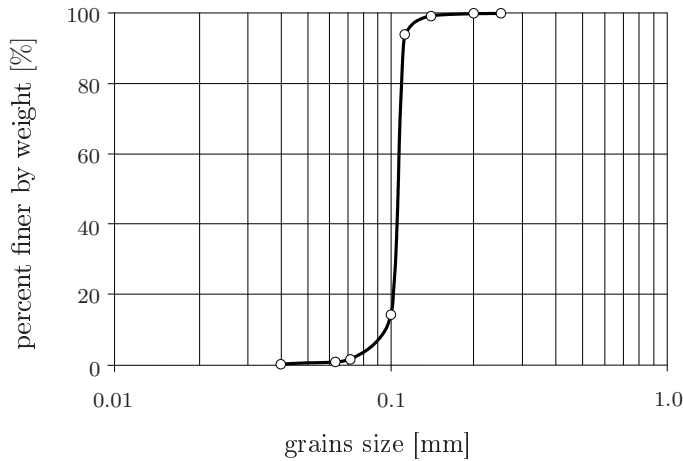


**Figure 3.8:** Grain size distribution (GSD) of the GEBA fine sand (Germer and Braun [77]).

The triaxial experiments have been carried out with a uniform cylindrical shape of the specimen of 10 cm both in height and diameter. Furthermore, the endplates were lubricated by latex rubber sheets with thin layers of silicone grease to ensure a homogeneous strain field of the specimen during the deformation. The specimen is drained through a porous stone ( $\varnothing 1 \text{ cm}$ ), which is worked into the middle of the bottom plate. Therewith, no pore pressure can be developed during the deformation procedure, cf. Appendix A.

### 3.2.2 Characteristics of homogeneous test conditions

In this section, the general behaviour of compact sand determined via monotonic triaxial tests as well as the aforementioned new observations made on non-monotonic stress-path-dependent tests will be presented. Then, on the basis of these experiments, the modelling approach for the yielding and failure behaviour of compact sand with the old failure concept using a fixed failure surface and the new failure concept with a variable failure surface will be discussed, whereas the constitutive modelling is presented in Section 4.2.2.

---

\* $e = (1 - n_{0S}^S)/n_{0S}^S$

† $I_D = (e_{max} - e)/(e_{max} - e_{min})$

### Drained monotonic loading condition

Figure 3.9 shows a drained triaxial compression test on a dry dense sand specimen with a height-to-diameter rate of  $h/d = 1$  under a constant confining pressure (cell pressure) of  $\sigma_3 = 0.2$  MPa. During the loading process, the volume deformation changed from a small contraction to dominant dilatation behaviour. Over the whole monotonic loading path, the material response showed a non-linear progression of the stress-strain behaviour, which was almost governed by plastic hardening. However, the continuous increase of

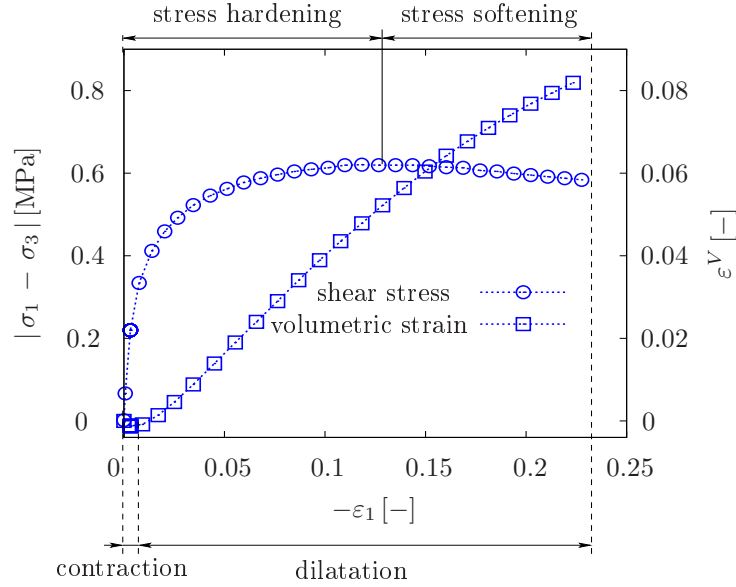


**Figure 3.9:** Triaxial compression test with a constant confining pressure of  $\sigma_3 = 0.2$  MPa.

loosening the grain structure led to a smooth stress softening. This is a consequence of the volumetric dilatation and not of a localisation of plastic strains towards shear bands. Through computer tomography (CT), Desrues et al. [41] illustrated that shear band structures inside the sample are only initiated when imperfections either disturb the axial symmetry or the homogeneity of the specimen, for example, by an eccentric application of the external load or by poorly prepared samples. Small imperfections, which are generally unpreventable, only have a marginal impact on the stress-strain behaviour and may only become dominant at very large strains of  $\varepsilon_1 > 25\%$ . Nevertheless, internal shear bands are generally invisible at the surface of the sample.

In contrast to Desrues' choice of samples with a height-to-diameter rate of  $h/d = 1$ , Lade [98] used slender specimens of  $h/d = 2.66$  for his triaxial experiments. On the basis of his results, he postulated that the initiation of shear bands appears with diminishing the dilatation rate, while, in contrast, Desrues et al. [41] could not detect any pronounced shear-banding effect by CT scans of compact specimens with  $h/d = 1$ . Shear banding preferably occurs when slender specimens are tested, which strongly tend to load imperfections with increasing deformations, therewith encouraging the development of localisation zones of plastic strains. In general, a shear band is characterised by a local increase of voids. Desrues et al. [41] compared the change of voids at a local point within an evolving shear band with the average value of the considered cross section, which represents the global

behaviour. In case of slender specimens or specimens with non-lubricated boundary conditions, the void ratios between local and global values showed sharp distinctions, while compact specimens under ideal test conditions exhibited only marginal differences. The differences between local and global void ratios did not start before an axial strain  $\varepsilon_1$  of more than approximately 20 % was reached. This value is clearly located after the peak stress. Therefore, the poor distinct shear-band pattern inside of drained lubricated compact specimens, which may develop at a very high deformation state, has no significant influence on the global material behaviour and cannot be the reason of stress softening.

### Drained non-monotonic loading condition

The plastic hardening, softening and failure behaviour of sand strongly depends on the stress level and is described by the sophisticated shape of the yield surface explained in detail in Section 4.2.2. In the framework of cohesive-frictional materials, the characteristic contour of yield surfaces was experimentally determined by Tatsuoka and Ishihara [155]. In particular, they carried out complex triaxial stress-path-depending compression tests by applying different stress levels during reloading, while repeatedly changing the confining pressures after unloading. In Figure 3.10, such a stress path in the hydrostatic plane is illustrated, where the points P1-P12 denote the stress points at which the loading path is changed. Therein,  $\overline{P_0P_1}$ ,  $\overline{P_3P_4}$ ,  $\overline{P_6P_7}$  and  $\overline{P_9P_{10}}$  are the hydrostatic loading paths, whereas  $\overline{P_1P_2}$ ,  $\overline{P_4P_5}$ ,  $\overline{P_7P_8}$  and  $\overline{P_{10}P_{11}}$  are the compression loading paths. Furthermore,  $\overline{P_2P_3}$ ,  $\overline{P_5P_6}$ ,  $\overline{P_8P_9}$  and  $\overline{P_{11}P_{12}}$  represent the unloading paths. Thereby, the stress level during unloading is chosen well below the failure load in order to detect yield loci by the onset of hardening during the reloading path. At the unloading path, the plastic deformation is frozen and only elastic deformations are occurring. Immediately after reaching the elastic limit at the higher stress state, the plastic yielding process starts again. The yield locus at the reloading path is detected through the stress-strain (Poorooshasb

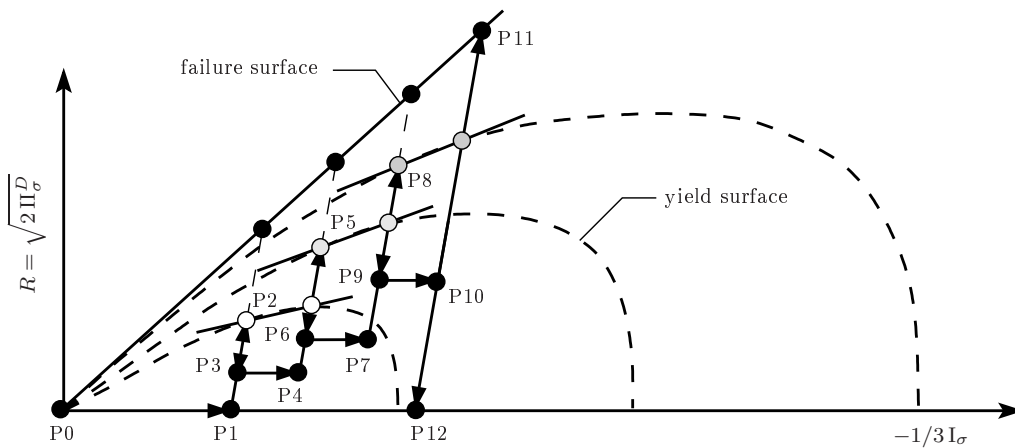


**Figure 3.10:** Generic sketch of one of the triaxial stress path test for the determination of the contour of yield surfaces and the hardening behaviour presented (Tatsuoka and Ishihara [155]).

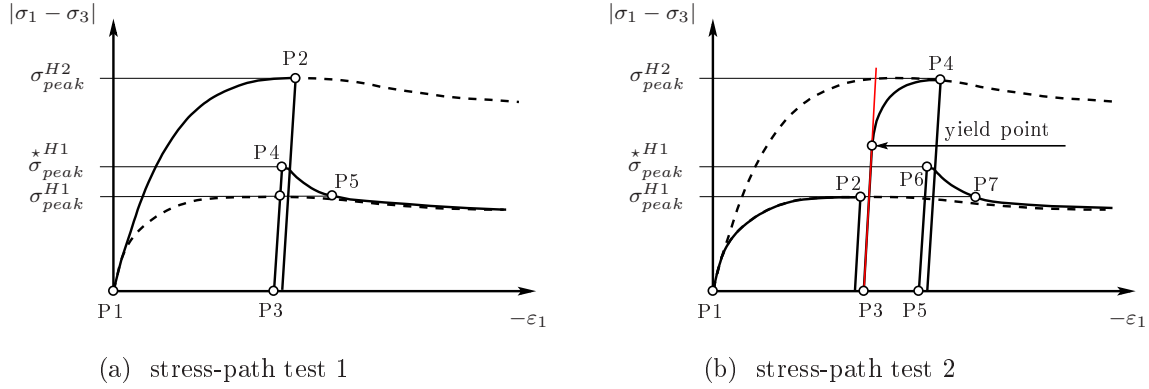
et al. [127]) or axial-volume strain (Tatsuoka and Ishihara [155]) behaviour, while the progression switches from a linear to a non-linear behaviour. The yield loci of the restart

of yielding and those of the lower stress level are marked in Figure 3.10 by the same shade of grey level. Accordingly, Lade and Kim [100] have assumed that such a pair of yield loci with the same grey-level owns the same plastic work. Proceeding from an infinite number of the yield loci with the same plastic work, the contour of one yield surface is characterised, cf. [66, 100]. In Figure 3.10, such contours of yield surfaces are illustrated by dashed lines, respectively. Proceeding from the lowest yield surface to the higher ones, a hardening process takes place, which is governed by the plastic work. Accordingly, on the basis of these experiments, it was concluded that the evolution of the yield surface ends at the failure surface independent from the stress path (Ehlers and Müllerschön [66]). It was assumed that the failure surface (black line) in Figure 3.10 is the approximation of the black points representing the peak shear stresses with respect to the confining pressures. This assumption led to a fixed failure surface with an unchangeably large size and to an almost linear relation with minimal curvature at lower stresses. To overcome this problem, Lade and Kim [100] have introduced an additional failure surface differing from the shape of the yield function to improve the approximation of the failure states of monotonically loaded experiments. Within this approach, the failure state is defined by the intersection point between the evolving yield surface and the fixed failure surface at the current stress state.

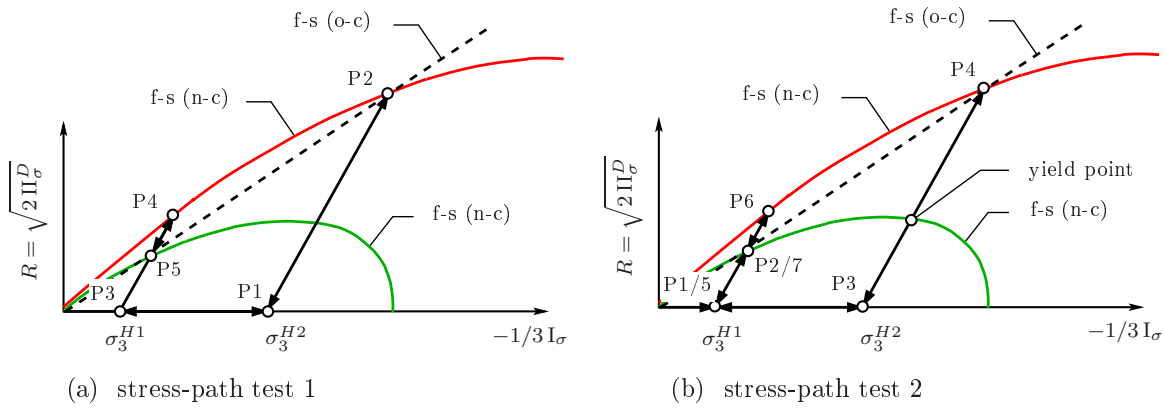
To clarify the assumption of a fixed failure surface, three stress-path-depending triaxial experiments have been performed, while the standard monotonic tests serve as reference solutions to detect differences in the stress-strain progression. A sketch of the stress-strain progression of these stress-path tests is given in Figures 3.11 and 3.13 (left), while the corresponding stress paths in the hydrostatic stress plane are shown in Figures 3.12 and 3.13 (right). Based on these experiments, it could be observed that the failure surface is not fixed. It is varying with the stress level. As a consequence, a new failure concept with a variable failure surface has been developed.

Figure 3.11 illustrates the stress-strain procedure of the stress-path tests 1 and 2 and also includes the order of the applied loading and unloading steps indicated by the stress points P1–P5 and P1–P7. By comparing the peak stress  $\sigma_{peak}^{H1}$  of the reference test with the peak stress  $\sigma_{peak}^{*H1}$  of the presheared test in the points P4 and P6 in Figure 3.11 (a) and (b), respectively, a distinct increase of the peak shear stress could be observed. Moreover, during the load path  $\overline{P3P4}$  in Figure 3.11 (b), the stress-strain progression changes from a linear to a non-linear behaviour, although it was presheared at the lower stress level until  $\sigma_{peak}^{H1}$  (P2). That means that the shear stress exceeds the elastic domain and the hardening process is restarted. In contrast, the old failure concept with the fixed failure surface can only predict a linear elastic approach after preshearing until the peak stress.

Proceeding from the observed stress-strain behaviour of the stress-path tests 1 and 2 (Figure 3.11), a new failure concept illustrated in Figure 3.12 by a sketch of both tests in the hydrostatic stress plane has been developed. Therein, two failure surfaces indicated by f-s(n-c) are sketched, where n-c denotes the new failure concept. The failure surfaces are depicted by a green and a red solid curve corresponding to triaxial compression tests under different confining pressures  $\sigma_3^{H1}$  and  $\sigma_3^{H2}$ , respectively, and two different values of the maximally applied hydrostatic stress expressed by  $I_\sigma$ . However, it should be noted that the failure surface is an imaginary limit of the evolving yield surface basically governed



**Figure 3.11:** Sketch of the observed stress-strain behaviour of stress-path test 1 (a) and 2 (b).



**Figure 3.12:** Different types of stress-path experiments and evolution of the failure surfaces  $f-s(n-c)$  of the new concept and  $f-s(o-c)$  of the old concept, respectively.

by the applied hydrostatic pressure. On the other hand, the fixed failure surface of the old failure concept  $f-s(o-c)$  indicated by the dashed black lines, which illustrates the failure surface introduced by Lade and Kim [100], has to approximate all possible peak shear stresses independently from how the stress path is driven up to peak-stress values. Obviously, this triggers a larger size of the failure surface compared with the new failure concept.

Furthermore, the stress-path test in Figure 3.13 exhibits the effect of a previous hydrostatic consolidation up to the limit of our triaxial device and applied to the specimen before shear-stress loading. In Figure 3.13 (right), the green curve represents the yield surface at the end of the preconsolidation process. However, the yield surface has not yet reached the failure surface in direction to the deviatoric stress loading. Therefore, the stress-strain behaviour is only marginally influenced by the preconsolidation. Only a short part at the beginning of the shear stress behaves linearly elastic, whereas the failure behaviour is not affected compared to the reference compression test without preconsolidation.

The modelling of the continuously changing failure behaviour is realised by a variable failure surface depending on the hydrostatic pressure state as illustrated in Figure 3.12. In contrast, Lade and Prabucki [101] modelled this effect, which is known as the so-called

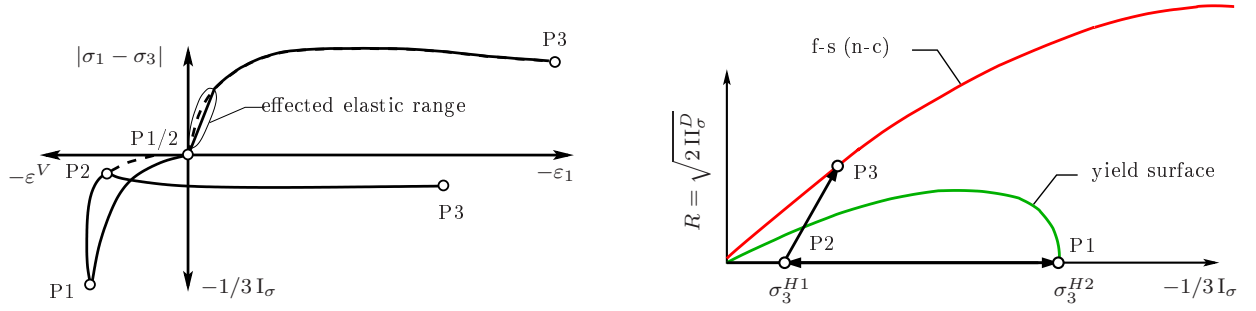


**Figure 3.13:** Stress-path test 3: (left) the observed stress-strain behaviour and (right) the yielding behaviour.

preshearing of sand, by interpreting the yield surface  $f-s(n-c)$  (red solid curve) as the actual failure surface up to the intersection point with the fixed failure surface  $f-s(o-c)$  (dashed black line) followed by the failure surface  $f-s(o-c)$ . As a result, one obtains a discontinuous shape of the failure surface, which can be avoided by introducing the stress-dependent failure concept presented in Section 4.2.2. Experimental results and numerical simulations using the old concept with a fixed failure surface and, on the other hand, the new concept with a variable failure surface are given in Section 6.1.2. Additionally, in that chapter, differences of both concepts are more precisely discussed. It will be shown that these experimentally observed properties of granular materials are crucial for correct matching their failure behaviour.





## Chapter 4:

# Constitutive Modelling

Proceeding from a multiphasic porous material with isothermal conditions ( $\theta^\alpha \equiv \theta \equiv \text{const.}$ ), the primary kinematic field variables of the individual constituents are the known physical quantities of the balance laws of mass, momentum and entropy. The energy balance is not required because of the assumption of a constant temperature. However, the resulting system of balance equations is indeterminate. To complete the system of equations, the unknown quantities of the balance equations have to be identified and, subsequently, for these quantities, constitutive equations have to be formulated on the basis of experimental observations of the considered material. This procedure is also known as the so-called closure problem of continuum mechanics, cf., e.g. [52, 85, 162, 163]. Moreover, for a thermodynamically consistent derivation of constitutive equations, the principles of Rational Thermodynamics (Truesdell [160]) have to be satisfied, which prevent non-physical assumptions for the constitutive modelling of the material behaviour. In the current chapter, the procedure of the constitutive setting for the triphasic model is presented, cf. [53, 64]. The experimental observed stress-strain behaviour of the solid skeleton discussed in Chapter 3 is incorporated into the constitutive modelling approaches.

### 4.1 Triphasic model for partially saturated sand

The fundamental constituent of the partially saturated soil is the solid skeleton, which is assumed as a materially incompressible solid phase  $\alpha = S$ , whereas the pore spaces of the solid structure are filled by the materially compressible pore air  $\alpha = A$  and the materially incompressible pore water  $\alpha = W$ . In Table 4.1, the triphasic model is summarised:

<b>Triphasic Soil Model</b>	
overall aggregate:	$\varphi = \varphi^S \cup \varphi^F \quad \text{where} \quad \varphi^F = \varphi^W \cup \varphi^A$
saturation of $\varphi$ :	$n^S + n^F = 1, \quad n^F = 1 - n^S = n^W + n^A$
fluid saturation of $\varphi^F$ :	$s^W = \frac{n^W}{n^F}, \quad s^A = \frac{n^A}{n^F}$
volume fractions:	$n^W = s^W(1 - n^S), \quad n^A = (1 - s^W)(1 - n^S)$
effective densities:	$\rho^{SR} = \text{const.}, \quad \rho^{WR} = \text{const.}, \quad \rho^{AR} \neq \text{const.}$

(4.1)

### Balance of mass

Excluding the mass exchange between the constituents,  $\hat{\rho}^\alpha \equiv 0$ , the local mass balance in (2.42) is reduced to

$$(\rho^\alpha)'_\alpha + \rho^\alpha \operatorname{div} \dot{\mathbf{x}}_\alpha = 0. \quad (4.2)$$

Evaluating (4.2) for the materially incompressible solid phase  $\varphi^S$ , the volume balance results

$$(n^S)'_S + n^S \operatorname{div} \dot{\mathbf{x}}_S = 0. \quad (4.3)$$

An integration of (4.3) over time yields

$$n^S = n_{0S}^S (\det \mathbf{F}_S)^{-1}, \quad (4.4)$$

where  $n_{0S}^S$  characterises the solidity in the solid reference configuration at time  $t_0$  and  $\mathbf{F}_S$  is the solid deformation gradient.

Using the transformation of the material time derivative of the fluid volume fraction  $n^\beta$  with regard to the solid motion

$$(n^\beta)'_S = (n^\beta)'_\beta - \operatorname{grad} n^\beta \cdot \mathbf{w}_\beta, \quad (4.5)$$

the volume balance of the materially incompressible pore water  $\varphi^W$  and the mass balance of the materially compressible pore air phase  $\varphi^A$  are obtained as

$$\begin{aligned} 0 &= (n^W)'_S + n^W \operatorname{div} (\mathbf{u}_S)'_S + \operatorname{div} (n^W \mathbf{w}_W), \\ 0 &= n^A (\rho^{AR})'_S + \rho^{AR} (n^A)'_S + n^A \rho^{AR} \operatorname{div} (\mathbf{u}_S)'_S + \operatorname{div} (n^A \rho^{AR} \mathbf{w}_A). \end{aligned} \quad (4.6)$$

### Balance of momentum

In this contribution, the investigated IBVP are only restricted to quasi-static problems. Therewith, the acceleration of the individual constituents is neglected,  $\ddot{\mathbf{x}}_\alpha \equiv \mathbf{0}$ , whereas the barycentric acceleration  $\ddot{\mathbf{x}}$  in (2.46) is not implicitly zero. Excluding therein the mass production,  $\hat{\rho}^\alpha \equiv 0$ , the barycentric acceleration  $\ddot{\mathbf{x}}$  leads to

$$\rho \ddot{\mathbf{x}} = - \sum_{\alpha=1}^k \operatorname{div} (\rho^\alpha \mathbf{d}_\alpha \otimes \mathbf{d}_\alpha). \quad (4.7)$$

The diffusion processes within the partially saturated soil are very slow and, thus, the gradient of the diffusion velocities is negligibly small, cf. Ehlers [53]. Therefore, the barycentric acceleration can be ignored:  $\ddot{\mathbf{x}} = \mathbf{0}$ . As consequence, the total *Cauchy*-stress tensor in (2.46) is only composed by the sum of the individual stress components,  $\mathbf{T} = \sum_{\alpha=1}^k \mathbf{T}^\alpha = \mathbf{T}^S + \mathbf{T}^W + \mathbf{T}^A$ . Hence, the overall momentum balance reads

$$\mathbf{0} = \operatorname{div} (\mathbf{T}^S + \mathbf{T}^W + \mathbf{T}^A) + \rho \mathbf{g}, \quad (4.8)$$

wherein  $\rho \mathbf{g}$  is the constant gravitation force, which is a constitutive assumption for  $\mathbf{b}^\alpha = \mathbf{b} \equiv \mathbf{g}$ , while  $\rho$  is the density of the overall aggregate built by the sum of the individual

densities  $\rho = n^S \rho^{SR} + n^W \rho^{WR} + n^A \rho^{AR}$ , cf. (2.46). Moreover, based on (2.40)<sub>1</sub> with (2.41)<sub>2</sub> and  $\hat{\rho}^\alpha \equiv 0$ , the sum over the direct momentum productions  $\hat{\mathbf{p}}^\alpha$  must vanish and, thus, the solid momentum production  $\hat{\mathbf{p}}^S$  can be expressed by terms of the pore fluids:

$$\sum_{\alpha=1}^k \hat{\mathbf{p}}^\alpha = \hat{\mathbf{p}}^S + \hat{\mathbf{p}}^W + \hat{\mathbf{p}}^A = \mathbf{0} \quad \rightarrow \quad \hat{\mathbf{p}}^S = -(\hat{\mathbf{p}}^W + \hat{\mathbf{p}}^A). \quad (4.9)$$

### Thermodynamical restrictions

Evaluating (2.49) for the partially saturated soil model with  $\hat{\rho}^\alpha \equiv 0$ , the following expression of the entropy inequality can be found:

$$\begin{aligned} 0 \leq & \underbrace{(\mathbf{T}^S + n^S \mathcal{P} \mathbf{I})}_{\mathbf{T}_E^S} \cdot \mathbf{D}_S + \underbrace{(\mathbf{T}^W + n^W \mathcal{P} \mathbf{I})}_{\mathbf{T}_E^W} \cdot \mathbf{D}_W + \underbrace{(\mathbf{T}^A + n^A \mathcal{P} \mathbf{I})}_{\mathbf{T}_E^A} \cdot \mathbf{D}_A - \\ & - [\rho^S (\psi^S)'_S + \rho^W (\psi^W)'_W + \rho^A (\psi^A)'_A] + \mathcal{P} \frac{n^A}{\rho^{AR}} (\rho^{AR})'_A - \\ & - \underbrace{(\hat{\mathbf{p}}^W - \mathcal{P} \operatorname{grad} n^W)}_{\hat{\mathbf{p}}_E^W} \cdot \mathbf{w}_W - \underbrace{(\hat{\mathbf{p}}^A - \mathcal{P} \operatorname{grad} n^A)}_{\hat{\mathbf{p}}_E^A} \cdot \mathbf{w}_A. \end{aligned} \quad (4.10)$$

Therein, the constraint of the local composition of the multiphasic material is included. This constraint is derived by the material time derivative of the saturation condition of the overall aggregate  $\varphi$  (4.1), which implies that the sum of the temporal change of volume fractions has to vanish:

$$\begin{aligned} 0 &= (n^S + n^W + n^A)'_S = (n^S)'_S + (n^W)'_S + (n^A)'_S \\ &= \mathcal{P} [n^S \operatorname{div} \dot{\mathbf{x}}_S + n^W \operatorname{div} \dot{\mathbf{x}}_W + n^A \operatorname{div} \dot{\mathbf{x}}_A + \\ &\quad + \operatorname{grad} n^W \cdot \mathbf{w}_W + \operatorname{grad} n^A \cdot \mathbf{w}_A + \frac{n^A}{\rho^{AR}} (\rho^{AR})'_A], \end{aligned} \quad (4.11)$$

wherein the relation in (4.5) is applied, and  $\mathcal{P}$  is the *Lagrangean* multiplier, which has to be identified yet. Proceeding from the symmetric deformation tensor  $\mathbf{D}_\alpha$  (2.25), the relations  $\operatorname{div} \dot{\mathbf{x}}_\alpha = \mathbf{D}_\alpha \cdot \mathbf{I}$  are used in (4.11) and (4.10), respectively. Furthermore, in (4.10), the power resulting from the momentum production of the solid phase  $\hat{\mathbf{p}}^S$  is substituted using (4.9) and (2.13)<sub>2</sub>:

$$\hat{\mathbf{p}}^S \cdot \dot{\mathbf{x}}_S + \hat{\mathbf{p}}^W \cdot \dot{\mathbf{x}}_W + \hat{\mathbf{p}}^A \cdot \dot{\mathbf{x}}_A = \hat{\mathbf{p}}^W \cdot \mathbf{w}_W + \hat{\mathbf{p}}^A \cdot \mathbf{w}_A. \quad (4.12)$$

Based on the *principle of effective stress concept* (Bishop [9] and Skempton [146]), the expressions in the parentheses in (4.10) are summarised to the effective or extra quantities  $(\cdot)_E^\alpha$  for which constitutive equations have to be found, cf. de Boer and Ehlers [16].

### Constitutive variables and conditions

From the continuum-mechanical point of view, the initial values of the individual quantities (motion, densities, volume fractions, temperatures) and the total state-field quantities (motion and temperature) of a general IBVP are assumed to be given. However, the temperature field is excluded in this contribution because of treating only isothermal processes, whereas temperature-dependent deformable partially saturated soil problems have been treated, e. g., by Graf [78]. For the general procedure, cf. Ehlers [47], all quantities, which are not directly determinable by the given total motion field  $\mathbf{x} = \boldsymbol{\chi}_\alpha(\mathbf{X}_\alpha, t)$  and the balance relations, are summarised into the response functional  $\mathcal{R}$ , viz.

$$\mathcal{R} = \{ \psi^\alpha, \mathbf{T}_E^\alpha, \hat{\mathbf{p}}_E^\beta \}. \quad (4.13)$$

Hence,  $\mathcal{R} = \mathcal{R}(\mathcal{V})$  includes material-dependent quantities and is governed by the independent set of process or constitutive variables  $\mathcal{V} = \mathcal{V}(\mathbf{x}, t)$ , which are defined by the actual position  $\mathbf{x}$  at time  $t$  and are known by the motion functions  $\boldsymbol{\chi}_\alpha$ . In order to enable the fulfilment of the entropy inequality in (4.10), the constitutive functions in  $\mathcal{R}$  can be derived from the material time derivatives of the *Helmholtz* free energies  $\psi^\alpha$ . Thereby, in order to avoid an arbitrariness of the constitutive modelling, they have to fulfil the fundamental thermodynamical principles of *equipresence*, *determinism*, *local action*, *frame indifference* and *dissipation* (Truesdell [160], Noll [120], Coleman and Noll [30]). First of all, following the *principle of equipresence*, the response functions  $\mathcal{R}$  of multiphasic materials are postulated to depend by the basic set of process variables  $\mathcal{V}$ ,

$$\mathcal{V} = \{ n^\alpha, \text{grad } n^\alpha, \rho^{\alpha R}, \text{grad } \rho^{\alpha R}, \mathbf{F}_S, \text{grad } \mathbf{F}_S, \dot{\mathbf{x}}_\beta, \text{grad } \dot{\mathbf{x}}_\beta, \mathbf{X}_\alpha \}, \quad (4.14)$$

which results from the thermodynamical process. Multiphasic materials depending on the given set of parameters in (4.14), which includes the basic form of the process variables as well as their gradients (Ehlers [47]), are called *second-grade materials*. Following the statement of Bowen [20, 21], the *second-grade* character of these materials is only influenced by the production terms concerning the coupling effects of physical processes between the constituents  $\varphi^\alpha$ . In contrast, *first-grade materials* or *simple materials* (Truesdell and Noll [162]) depend only on the local material point  $P^\alpha$  and its immediate neighbourhood (*principle of local action*). Therefore, the gradients of the process variables are removed from (4.15). For partially saturated soil, the set of process variables yields

$$\mathcal{V}^1 = \{ s^W, \rho^{AR}, \mathbf{F}_S, \mathbf{w}_\beta, \mathbf{D}_\beta \}, \quad \text{where } \mathcal{V}^1 \subset \mathcal{V} \quad (4.15)$$

is the subset of the process variables in (4.14). In (4.15), a homogeneous distribution of the material quantities at the reference configuration is assumed, such that  $\mathbf{X}_\alpha$  has been dropped. Based on the *principle of frame indifference* (Ehlers [54]), the fluid motions  $\dot{\mathbf{x}}_\beta$  can be substituted by the seepage velocities  $\mathbf{w}_\beta$  (2.13)<sub>2</sub> due to  $\mathbf{w}_\beta$  is frame indifferent to an arbitrary change of the observer position. Furthermore, only the symmetric part of the deformation gradient  $\mathbf{L}_\beta = \text{grad } \dot{\mathbf{x}}_\beta$  is frame indifferent and, therefore,  $\mathbf{L}_\beta$  is substituted by the symmetric deformation velocity tensor  $\mathbf{D}_\beta$ , which governs the extra stress  $\mathbf{T}_E^\beta$  (friction stress) describing viscous properties of fluids. Moreover, in (4.15), both fluid volume

fractions,  $n^W$  and  $n^A$ , are substituted by the water saturation  $s^W$  with the expression in (4.1)<sub>3</sub>, while  $n^S$  is determined by (4.4) and  $n^F$  by the saturation condition (4.1)<sub>2</sub>. Therefore,  $n^\alpha$  is no more an independent variable and can be removed from the general set of  $\mathcal{V}$ .

Applying the *principle of phase separation* (Ehlers [46]), the set of  $\mathcal{V}^1$  can be separated in parts corresponding to the individual constituent. Thereby, it is assumed that each constituent  $\varphi^\alpha$  depends only on its own set of process variables and, additionally, a further meaningful reduction of the process variables is allowed regarding the considered material properties. Hence, the corresponding dependencies of the *Helmholtz* free energies result in

$$\psi^S = \psi^S(\mathbf{F}_S), \quad \psi^W = \psi^W(s^W), \quad \psi^A = \psi^A(\rho^{AR}). \quad (4.16)$$

The dependency of  $\psi^S$  can be also expressed by  $\mathbf{C}_S$  or  $\mathbf{B}_S$  as well as  $\mathbf{E}_S$  or  $\mathbf{A}_S$ , which results by the evaluation of the *principle of frame indifference*. This statement is based on the property that each deformation tensor owns the same principle invariants, which are indifferent to the transformation with the so-called proper orthogonal rotation tensor  $\mathbf{Q}_S^*$ .

For the modelling of finite elasto-plastic material behaviour (Lee [103], Haupt [83], Ehlers [48]), the deformation gradient  $\mathbf{F}_S$  can be multiplicatively decomposed in an elastic part  $\mathbf{F}_{Se}$  and a plastic part  $\mathbf{F}_{Sp}$ :

$$\mathbf{F}_S = \mathbf{F}_{Se} \mathbf{F}_{Sp}. \quad (4.17)$$

Thereby, a stress-free intermediate configuration is introduced. This configuration is geometrically incompatible concerning to the pure unloading step of the external forces. Because within the body  $\mathcal{B}$ , additional elastic stresses remain after unloading, which are released by virtually cutting of  $\mathcal{B}$  into finite stress-free pieces. The reversal of the residual stresses is connected by additional elastic deformations, which leads to the geometrically incompatible plastic intermediate configuration. In case of a homogeneous deformation state, the intermediate configuration is geometrically compatible with respect to the unloading step. Thus, no elastic stresses remain after the unloading step because the reversed elastic strains are completely related to the elastic stresses (Kleiber [93], Haupt [83] and Ehlers [46]).

Inserting the multiplicative split of  $\mathbf{F}_S$  (4.17) in (2.21), the *Green-Lagrangean* deformation tensor  $\mathbf{E}_S$  can be additively decomposed into an elastic and a plastic part, viz.

$$\mathbf{E}_S = \mathbf{E}_{Se} + \mathbf{E}_{Sp} \quad \text{where} \quad \begin{cases} \mathbf{E}_{Se} &= \mathbf{F}_{Sp}^T \hat{\mathbf{\Gamma}}_{Se} \mathbf{F}_{Sp} = \frac{1}{2} (\mathbf{C}_S - \mathbf{C}_{Sp}), \\ \mathbf{E}_{Sp} &= \frac{1}{2} (\mathbf{C}_{Sp} - \mathbf{I}), \\ \hat{\mathbf{\Gamma}}_{Se} &= \frac{1}{2} (\hat{\mathbf{C}}_{Se} - \mathbf{I}). \end{cases} \quad (4.18)$$

Therein,  $\hat{\mathbf{\Gamma}}_{Se}$  is the elastic strain measures at the intermediate configuration and is expressed by the elastic intermediate right *Cauchy-Green* deformation tensor  $\hat{\mathbf{C}}_{Se}$ . The topscript  $(\hat{\cdot})$  characterises the quantities of the intermediate configuration. Applying this to  $\hat{\mathbf{\Gamma}}_{Se}$  a contravariant pull-back transport mechanism,  $\mathbf{F}_{Sp}^T(\cdot)\mathbf{F}_{Sp}$ , the elastic *Green-Lagrangean* deformation tensor  $\mathbf{E}_{Se}$  in terms of the reference configuration is obtained,

---

\* $\mathbf{Q}_S$  is properly orthogonal, such that  $\mathbf{Q}_S \mathbf{Q}_S^T = \mathbf{I}$  and  $\det \mathbf{Q}_S = 1$ , (Ehlers [48] and Haupt [85]).

cf. Ehlers [48, 54] and Markert [114]. Following a geometrically linear approach of the deformations, the reference and actual configurations coincide with each other and, thus, the intermediate configuration is vanishing. Hence, the linearisation of  $\mathbf{E}_S$  leads to the total solid strain tensor  $\boldsymbol{\varepsilon}_S$  (2.23), wherein  $\boldsymbol{\varepsilon}_{Se}$  and  $\boldsymbol{\varepsilon}_{Sp}$  are the elastic and plastic strain parts of solid deformations, respectively:

$$\text{lin } \mathbf{E}_S := \boldsymbol{\varepsilon}_S = \boldsymbol{\varepsilon}_{Se} + \boldsymbol{\varepsilon}_{Sp}. \quad (4.19)$$

In contrast to the elastic strain tensor  $\boldsymbol{\varepsilon}_{Se}$ , the internal history-dependent quantities such as the plastic strains  $\boldsymbol{\varepsilon}_{Sp}$  are determined by the internal dissipation process and cannot be set from the exterior. They are evaluated by evolution equations. This group of internal variables can also consist of several internal scalar-valued hardening parameters  $\alpha_i$ , which control the expansion and the shrinkage of the elastic stress limit. The conjugated stress quantities to the elastic strains  $\boldsymbol{\varepsilon}_{Se}$  and internal variables  $\alpha_i$  are derived by the solid *Helmholtz* free-energy function  $\psi^S$ , which is governed by  $\boldsymbol{\varepsilon}_{Se}$ ,  $\boldsymbol{\varepsilon}_{Sp}$  and  $\alpha_i$ . The *Helmholtz* free-energy function  $\psi^S$  can be additively decomposed in an elastic and a plastic part,  $\psi^{Se}$  and  $\psi^{Sp}$ , respectively:

$$\psi^S(\boldsymbol{\varepsilon}_{Se}, \boldsymbol{\varepsilon}_{Sp}, \alpha_i) = \psi^{Se}(\boldsymbol{\varepsilon}_{Se}) + \psi^{Sp}(\boldsymbol{\varepsilon}_{Sp}, \alpha_i). \quad (4.20)$$

Based on the ideal elasto-plastic material behaviour, the mechanical free energy  $\psi^S$  is only described by the elastic part  $\psi^{Se}$ , which can be assumed to be governed by the elastic strains  $\boldsymbol{\varepsilon}_{Se}$ , Ehlers [47, 54]. For isotropic hardening materials,  $\psi^{Sp}$  is only a function of the internal parameters  $\alpha_i$ , while  $\boldsymbol{\varepsilon}_{Sp}$  is required for the kinematic hardening in order to compute the back-stress tensor, cf. Lubliner [108], Ehlers [48], Wriggers [180] and Simo and Hughes [144]. However,  $\psi^{Sp}$  is only active if the hardening process has been taken place ( $\alpha_i \neq 0$ ). For the case of  $\psi^{Sp}(\alpha_i = 0) = 0$ , only ideal elasto-plasticity is considered. Carrying out the material time derivatives of the *Helmholtz* free-energy functions  $\psi^\alpha$ ,

$$\begin{aligned} \rho_{0S}^S (\psi^S)'_S &= \rho_{0S}^S \frac{\partial \psi^{Se}}{\partial \boldsymbol{\varepsilon}_{Se}} \cdot (\boldsymbol{\varepsilon}_{Se})'_S + \rho_{0S}^S \frac{\partial \psi^{Sp}}{\partial \alpha_i} (\alpha_i)'_S, \\ \rho^W (\psi^W)'_W &= \rho^W \frac{\partial \psi^W}{\partial s^W} (s^W)'_W = \rho_F^W \frac{\partial \psi^W}{\partial s^W} [(s^W n^F)'_W - s^W (n^F)'_W] \\ &= \rho_F^W \frac{\partial \psi^W}{\partial s^W} [(n^W)'_W + s^W (n^S)'_W] \\ &= -\rho_F^W \frac{\partial \psi^W}{\partial s^W} (n^W \mathbf{I} \cdot \mathbf{L}_W + s^W n^S \mathbf{I} \cdot \mathbf{L}_S - s^W \text{grad } n^S \cdot \mathbf{w}_W), \\ \rho^A (\psi^A)'_A &= \rho^A \frac{\partial \psi^A}{\partial \rho^{AR}} (\rho^{AR})'_A, \end{aligned} \quad (4.21)$$

and inserting the results in (4.10) including the decomposition of the rate of the total

strains  $(\boldsymbol{\varepsilon}_S)'_S = (\boldsymbol{\varepsilon}_{Se})'_S + (\boldsymbol{\varepsilon}_{Sp})'_S$ , the entropy inequality yields

$$\begin{aligned}
0 \leq & \underbrace{(\boldsymbol{\sigma}_E^S + \rho_F^W \frac{\partial \psi^W}{\partial s^W} s^W n^S \mathbf{I} - \rho_{0S}^S \frac{\partial \psi^{Se}}{\partial \boldsymbol{\varepsilon}_{Se}})}_{\boldsymbol{\sigma}_{Em}^S} \cdot (\boldsymbol{\varepsilon}_{Se})'_S + \\
& + \boldsymbol{\sigma}_E^S \cdot (\boldsymbol{\varepsilon}_{Sp})'_S - \rho_{0S}^S \frac{\partial \psi^{Sp}}{\partial \alpha_i} (\alpha_i)'_S + \\
& + \underbrace{(\mathbf{T}_E^W + \rho_F^W \frac{\partial \psi^W}{\partial s^W} n^W \mathbf{I})}_{\mathbf{T}_{Em}^W} \cdot \mathbf{D}_W + \mathbf{T}_E^A \cdot \mathbf{D}_A + \\
& + (\mathcal{P} \frac{n^A}{\rho^{AR}} - \rho^A \frac{\partial \psi^A}{\partial \rho^{AR}}) (\rho^{AR})'_A - \hat{\mathbf{p}}_E^A \cdot \mathbf{w}_A - \\
& - \underbrace{(\hat{\mathbf{p}}_E^W + \rho_F^W \frac{\partial \psi^W}{\partial s^W} s^W \text{grad } n^S)}_{\hat{\mathbf{p}}_{Em}^W} \cdot \mathbf{w}_W.
\end{aligned} \tag{4.22}$$

Therein,  $\boldsymbol{\sigma}_{Em}^S$  is the geometrical linear effective solid elastic stress tensor, cf. (2.30), while the fluid extra stresses  $\mathbf{T}_E^A$  and  $\mathbf{T}_{Em}^W$  are the dissipative friction forces of the viscous pore fluids. By evaluating the entropy inequality in (4.22) at the thermodynamical equilibrium state, the internal dissipation is zero and, therewith, the internal variables,  $(\boldsymbol{\varepsilon}_{Sp})'_S = \mathbf{0}$ ,  $(\alpha_i)'_S = 0$  and also  $\mathbf{w}_\beta = \mathbf{0}$ . Thus, the terms within the parentheses in (4.22) have to vanish for arbitrary values of the free variables  $(\boldsymbol{\varepsilon}_{Se})'_S$  and  $(\rho^{AR})'_A$ , whereas the summarised terms in the parentheses indicated with  $(\cdot)_{Em}^\alpha$  denote the pure mechanical extra quantities which consist of the saturation quantities resulting from the *Helmholtz* free energy  $\psi^W$  (4.21)<sub>2</sub> and the extra quantities  $(\cdot)_E^\alpha$ . Proceeding from this argumentation at the thermodynamical equilibrium, the following dependencies result:

$$\begin{aligned}
\boldsymbol{\sigma}_{Em}^S &= \rho_{0S}^S \frac{\partial \psi^{Se}}{\partial \boldsymbol{\varepsilon}_{Se}} = \frac{\partial \Psi^{Se}}{\partial \boldsymbol{\varepsilon}_{Se}}, & \mathcal{P} &= p^{AR} = (\rho^{AR})^2 \frac{\partial \psi^A}{\partial \rho^{AR}}, \\
p^C &:= p^{AR} - p^{WR} = -s^W \rho^{WR} \frac{\partial \psi^W}{\partial s^W}.
\end{aligned} \tag{4.23}$$

Therein,  $\Psi^{Se}$  is the mass-specific elastic free energy and the capillary pressure  $p^C$  is defined as the difference between the effective pressure  $p^{AR}$  of the non-wetting pore air and the effective pressure  $p^{WR}$  of the wetting pore water, cf. Brooks and Corey [25], Ehlers [53] and Graf [78], and the *Lagrangean* multiplier  $\mathcal{P}$  is identified as the effective pore air pressure  $\mathcal{P} = p^{AR}$ . Moreover, the thermodynamical internal stresses  $t_i = t_i(\alpha_i)$  can be introduced via

$$t_i = -\rho_{0S}^S \frac{\partial \psi^{Sp}}{\partial \alpha_i}, \tag{4.24}$$

which is related to the internal hardening variables  $\alpha_i$  (strain-like quantities), cf. Lubliner [108], Wriggers [180] and Simo and Hughes [144]. Thereby, the thermodynamical stresses

$t_i$  or the internal hardening variables  $\alpha_i$ , respectively, are responsible for the evolution of the plastic material parameters describing the yield surface and, therefore, for the increase or decrease of the elastic stress limit of the considered material during the plastic yielding procedure.

Under consideration of the relations in (4.23), the total quantities in the parentheses in (4.22) yield to following expressions after carrying out some transformations, see Appendix B:

<b>Total and Effective Quantities of the Triphasic Soil Model</b>	
$\boldsymbol{\sigma}^S = -n^S p^{FR} \mathbf{I} + \boldsymbol{\sigma}_{Em}^S,$	
$\mathbf{T}^A = -n^A p^{AR} \mathbf{I} + \mathbf{T}_E^A \approx -n^A p^A \mathbf{I} \quad \text{with} \quad \mathbf{T}_E^A \approx \mathbf{0},$	
$\mathbf{T}^W = -n^W p^{WR} \mathbf{I} + \mathbf{T}_{Em}^W \approx -n^W p^W \mathbf{I} \quad \text{with} \quad \mathbf{T}_{Em}^W \approx \mathbf{0},$	(4.25)
$\hat{\mathbf{p}}^A = p^{AR} \text{grad } n^A + \hat{\mathbf{p}}_E^A,$	
$\hat{\mathbf{p}}^W = p^{AR} \text{grad } n^W + p^C s^W \text{grad } n^S + \hat{\mathbf{p}}_{Em}^W,$	
$\quad = p^{WR} \text{grad } n^W + p^C (s^A \text{grad } n^W - s^W \text{grad } n^A) + \hat{\mathbf{p}}_{Em}^W.$	

In (4.25), the fluid pressure components in  $\boldsymbol{\sigma}^S$  are summarised to the effective fluid pressure  $p^{FR}$  using the well-known *Dalton's law*, which is composed by the saturations  $s^\beta$  of the individual pore fluids with their corresponding fluid pressures  $p^{\beta R}$ , viz.

$$p^{FR} = s^W p^{WR} + s^A p^{AR} = s^W p^{WR} + (1 - s^W) p^{AR}. \quad (4.26)$$

By a dimensional analysis of the physical quantities of the soil model, Ehlers et al. [63] has shown that in the frame of geotechnical applications the friction force of the viscous pore fluids  $\mathbf{T}_E^A$  and  $\mathbf{T}_{Em}^W$  can be neglected compared to  $\hat{\mathbf{p}}_E^\beta$  and  $p^\beta$ .

At the thermodynamical equilibrium, where the processes are reversible, the thermodynamic relations of variable pairs can be found. These conjugated variable pairs are  $\{\boldsymbol{\sigma}_{Em}^S, \varepsilon_{Se}\}$ ,  $\{p^{AR}, \rho^{AR}\}$  and  $\{p^C, s^W\}$ . Their relations to each other are derived by the corresponding *Helmholtz* free energies  $\psi^\alpha$ . However, the non-equilibrium part of the dissipative processes in (4.22) remains. These processes are the plastic yielding behaviour resulting from the dissipation of the mechanical work  $\mathcal{D}_{S\text{int}}$  and the dissipation energies  $\mathcal{D}_{F\text{int}}$  follow from friction forces of the percolating pore fluids:

$$\mathcal{D}_{\text{int}} = \underbrace{\boldsymbol{\sigma}_{Em}^S \cdot (\varepsilon_{Sp})'_S + t_i (\alpha_i)'_S}_{\mathcal{D}_{S\text{int}} \geq 0} + \underbrace{\hat{\mathbf{p}}_{Em}^W \cdot \mathbf{w}_W + \hat{\mathbf{p}}_E^A \cdot \mathbf{w}_A}_{\mathcal{D}_{F\text{int}} \geq 0} \geq 0. \quad (4.27)$$

The internal dissipation resulting from plastic yielding  $\mathcal{D}_{S\text{int}}$  takes only place if the current effective solid stress  $\boldsymbol{\sigma}_{Em}^S$  is located at the boundary  $\partial\mathcal{G}$  of the elastic domain  $\mathcal{G}$ , which is defined by the yield function  $F = F(\boldsymbol{\sigma}_{Em}^S, \alpha_i)$  depending on the effective mechanical solid stress tensor  $\boldsymbol{\sigma}_{Em}^S$  and the internal hardening variables  $\alpha_i$ .



Moreover, the percolation of the pore fluids is always associated with a dissipative process  $\mathcal{D}_{F\text{int}} > 0$ . Only in case of stagnant water,  $\mathbf{w}_\beta = \mathbf{0}$ , the fluid is located in a state of thermodynamic equilibrium. For the constitutive approach,  $\hat{\mathbf{p}}_E^\beta$  should proportionally depend on the seepage velocities,  $\hat{\mathbf{p}}_{Em}^W \propto \mathbf{w}_W$  and  $\hat{\mathbf{p}}_E^A \propto \mathbf{w}_A$ , such that a quadratic term of  $\mathbf{w}_\beta$  in  $\mathcal{D}_{F\text{int}}$  governed by positive material parameters can be created. Based on this general procedure for developing thermodynamical consistent constitutive equations, the dissipative restriction of the entropy inequality is still satisfied. This procedure corresponds to the approach used for developing the well-known *Fourier's law* for heat influx of bodies.

## 4.2 Constitutive setting of the solid skeleton

In this section, based on the results of drained triaxial experiments on dry dense sand (see Sections 3.2 and 6.1), the constitutive modelling approach for the elasto-plastic behaviour of the solid skeleton is presented.

### 4.2.1 Elastic behaviour

For modelling the non-linear elastic behaviour of sand, various formulations can be found in the literature. Thereby, the modelling approach of elasticity is generally classified in three basic theoretical categories, namely, in *elasticity*, *hyperelasticity* and *hypoelasticity*, cf. Truesdell and Noll [162], Ciarlet [29] and Müllerschön [118]. In this contribution, the elastic behaviour is modelled by a hyperelasticity formulation using an elastic potential. Following this approach of a conservative relation between stresses and strains, only the elastic response occurs during cycle loading without any dissipation of energy, which is not generally true for the other two elasticity categories, cf. Müllerschön [118].

In the framework of linear elasto-plasticity, the local effective solid stress  $\boldsymbol{\sigma}_{Em}^S$  is obtained from an elastic potential given as a function of the local elastic strain  $\boldsymbol{\varepsilon}_{Se}$ . However, although the material description is based on a geometrically linear theory, the elastic material behaviour of sand is highly non-linear during shear and hydrostatic loading cycles (Ehlers and Müllerschön [66]). Concerning the shear stiffness, the elastic non-linear behaviour occurs within a very small shear strain range  $\varepsilon_{Se}^D < 1 \cdot 10^{-6}$  (Benz [7]) and influences the common sand behaviour marginally compared to the highly elastic non-linear behaviour during hydrostatic loading cycles, which takes place within an elastic volume strain range of about  $\varepsilon_{Se}^V \approx 0.02$ . By this reason, the small non-linearity of the shear module can be assumed to a constant average value, which is acceptable for generally investigations of sand, whereas an accurate modelling of the hydrostatic non-linear stiffness evolution of sand is very important for correct performing the elasto-plastic deformation behaviour.

Under consideration of moderate confining pressures, the hydrostatic non-linear behaviour results from the assumption of rigid and uncrushable grains, where the closest packing at  $n_{max}^S$  defines the so-called point of compaction, cf. Ehlers [46]. However, to reach this point, an infinitely large energy is needed. With this in mind, Ehlers and Scholz [67] introduced a general elastic potential formulated as a volume-specific *Helmholtz* free-energy

function  $\Psi^{Se}$ , which has been modified in order to obtain a better fit of the experimental data observed during hydrostatic loading and unloading loops, cf. Ehlers and Avcı [56]:

$$\begin{aligned} \Psi^{Se} = & \mu^S \boldsymbol{\varepsilon}_{Se}^D \cdot \boldsymbol{\varepsilon}_{Se}^D + \\ & + \frac{1}{2} (k_0^S - k_1^S) (\varepsilon_{Se}^V)^2 - k_1^S (\varepsilon_{Se \text{ crit}}^V)^2 \left[ \ln \left( \frac{\varepsilon_{Se \text{ crit}}^V - \varepsilon_{Se}^V}{\varepsilon_{Se \text{ crit}}^V} \right) + \frac{\varepsilon_{Se}^V}{\varepsilon_{Se \text{ crit}}^V} \right]. \end{aligned} \quad (4.28)$$

Therein,  $\boldsymbol{\varepsilon}_{Se}^D = \boldsymbol{\varepsilon}_{Se} - 1/3 \varepsilon_{Se}^V \cdot \mathbf{I}$  is the elastic strain deviator and

$$\varepsilon_{Se \text{ crit}}^V = 1 - \frac{n_{max}^S}{n_p^S} \quad (4.29)$$

is the critical value of the elastic volume strain belonging to the compaction point given by  $n_{max}^S$ . Based on the assumption of incompressible single grains, the compaction of the solid skeleton is theoretically limited to  $n^S/n_{0S}^S = 1/n_{0S}^S = (\det \mathbf{F}_S)^{-1}$ . Since the pore space between the grains cannot be totally eliminated, the volume fraction  $n^S$  is restricted to  $n^S \leq n_{max}^S < 1$ . Following this,  $n_{max}^S$  defines the maximum solidity reached during the hydrostatic loading, while  $n_p^S$  is the plastic volume fraction formally located in the plastic intermediate configuration. The computation of  $n_p^S$  is derived by the multiplicative split of  $\mathbf{F}_S$  in (4.17) into elastic and plastic parts. Therewith, (4.4) can be reformulated to yield

$$n^S = n_{0S}^S (\det \mathbf{F}_S)^{-1} = n_{0S}^S (\det \mathbf{F}_{Se})^{-1} (\det \mathbf{F}_{Sp})^{-1}. \quad (4.30)$$

In the geometrically linear case of porous media elasto-plasticity, the higher order terms can be neglected, cf. Ehlers and Scholz [67]. Thus, (4.30) reduces to the small-strain expression

$$n^S = n_{0S}^S (1 - \varepsilon_S^V) = n_p^S (1 - \varepsilon_{Se}^V) \quad \text{with} \quad n_p^S = n_{0S}^S (1 - \varepsilon_{Sp}^V). \quad (4.31)$$

Therein,  $\varepsilon_S^V = \boldsymbol{\varepsilon}_S \cdot \mathbf{I}$  is the volumetric part of the linear solid strain  $\boldsymbol{\varepsilon}_S$ , where  $\varepsilon_{Se}^V = \boldsymbol{\varepsilon}_{Se} \cdot \mathbf{I}$  and  $\varepsilon_{Sp}^V = \boldsymbol{\varepsilon}_{Sp} \cdot \mathbf{I}$  are the corresponding volumetric elastic and plastic strains, respectively. It is seen from (4.28) that the deviatoric part of the elastic potential including the first *Lamé* constant or the solid shear modulus  $\mu^S$ , respectively, follows the standard formulation of linear elasticity, while the volumetric part is highly non-linear and proceeds from two bulk material parameters,  $k_0$  and  $k_1$ , where  $k_0$  denotes the initial volumetric stiffness, while  $k_1$  characterises the non-linear stiffness part.

Taking the derivative of (4.28) with respect to  $\boldsymbol{\varepsilon}_{Se}$  yields the effective solid stress

$$\boldsymbol{\sigma}_{Em}^S = \frac{\partial \Psi^{Se}}{\partial \boldsymbol{\varepsilon}_{Se}} = 2 \mu^S \boldsymbol{\varepsilon}_{Se}^D + \left[ k_0^S + k_1^S \left( \frac{\varepsilon_{Se \text{ crit}}^V}{\varepsilon_{Se \text{ crit}}^V - \varepsilon_{Se}^V} - 1 \right) \right] \varepsilon_{Se}^V \mathbf{I}, \quad (4.32)$$

where  $\mu^S$ ,  $k_0$ ,  $k_1$  and  $n_{max}^S$  have to be found from experimental data. According to the strain tensor, the effective stress tensor is also split into a deviatoric stress tensor  $\boldsymbol{\sigma}_{Em}^{SD}$  and a hydrostatic stress tensor  $\boldsymbol{\sigma}_{Em}^{SH}$ , viz.

$$\begin{aligned} \boldsymbol{\sigma}_{Em}^S &= \boldsymbol{\sigma}_{Em}^{SD} + \boldsymbol{\sigma}_{Em}^{SH} = \boldsymbol{\sigma}_{Em}^{SD} + \sigma_{Em}^{SH} \mathbf{I} \\ \text{with: } \sigma_{Em}^{SH} &= \frac{1}{3} \boldsymbol{\sigma}_{Em}^S \cdot \mathbf{I} = \frac{1}{3} \text{I}_\sigma, \quad \boldsymbol{\sigma}_{Em}^{SD} = \boldsymbol{\sigma}_{Em}^S - \sigma_{Em}^{SH} \mathbf{I}. \end{aligned} \quad (4.33)$$

The second derivative of  $\Psi^{Se}$  leads to the fourth-order elasticity stiffness tensor  $\mathbb{C}^{Se} =: \mathbb{C}^{Se}$ :

$$\mathbb{C}^{Se} = \frac{\partial^2 \Psi^{Se}}{\partial \boldsymbol{\varepsilon}_{Se} \otimes \boldsymbol{\varepsilon}_{Se}} = 2\mu^S \mathbf{I}^D + \left[ k_0^S + k_1^S \left( \frac{(\varepsilon_{Se \text{crit}}^V)^2}{(\varepsilon_{Se \text{crit}}^V - \varepsilon_{Se}^V)^2} - 1 \right) \right] \mathbf{I} \otimes \mathbf{I}, \quad (4.34)$$

where  $\mathbf{I}^D$  is the fourth order deviatoric projection tensor  $\mathbf{I}^D = \mathbf{I} - 1/3 \mathbf{I} \otimes \mathbf{I}$  and  $\mathbf{I} =: (\mathbf{I} \otimes \mathbf{I})^T$  is the fourth order identity tensor, cf. Ehlers [55]. The elastic stiffness tensor  $\mathbb{C}^{Se}$  is positive definite for  $\boldsymbol{\varepsilon}_{Se} \neq \mathbf{0}$  by satisfying the condition  $\mathbb{C}^{Se} \cdot (\boldsymbol{\varepsilon}_{Se} \otimes \boldsymbol{\varepsilon}_{Se}) > 0$  and owns the symmetry property  $\mathbb{C}^{Se} = (\mathbb{C}^{Se})^T = (\mathbb{C}^{Se})^{12} = (\mathbb{C}^{Se})^{34}$  based on the symmetries of  $\boldsymbol{\sigma}_{Em}^S = (\boldsymbol{\sigma}_{Em}^S)^T$  and  $\boldsymbol{\varepsilon}_{Se} = (\boldsymbol{\varepsilon}_{Se})^T$ , wherein the numbers over the transpose index  $(\cdot)^T$  denote the exchange of the basis vector positions, e.g., of the first with second basis vector.

## 4.2.2 Plastic behaviour

For the description of the plastic or the viscoplastic part of the material behaviour, respectively, one firstly has to define a yield function  $F(\boldsymbol{\sigma}_{Em}^S)$  enveloping the elastic domain  $\mathcal{G}$ . In order to capture the hydrostatic plastic compressibility and the non-isotropic behaviour at deviatoric loading, the single-surface yield criterion defined by Ehlers [48, 49] is applied, cf. Figure 4.1:

$$\begin{aligned} F(\boldsymbol{\sigma}_{Em}^S) &= \Phi^{1/2} + \beta \mathbf{I}_\sigma + \epsilon \mathbf{I}_\sigma^2 - \kappa = 0, \quad \text{where} \\ \Phi &= \mathbf{II}_\sigma^D (1 + \gamma \mathbf{III}_\sigma^D / (\mathbf{II}_\sigma^D)^{3/2})^m + \frac{1}{2} \alpha \mathbf{I}_\sigma^2 + \delta^2 \mathbf{I}_\sigma^4. \end{aligned} \quad (4.35)$$

This function depends on the first principal invariant  $\mathbf{I}_\sigma$  as well as on the (negative) second and the third principal deviatoric invariants  $\mathbf{II}_\sigma^D$  and  $\mathbf{III}_\sigma^D$  of the effective solid stress  $\boldsymbol{\sigma}_{Em}^S$ , cf. equation (3.2). As many authors do, compare, for example, the paper by Ehlers [48], the constitutive parameters included in (4.35) are summarised in a hydrostatic and a

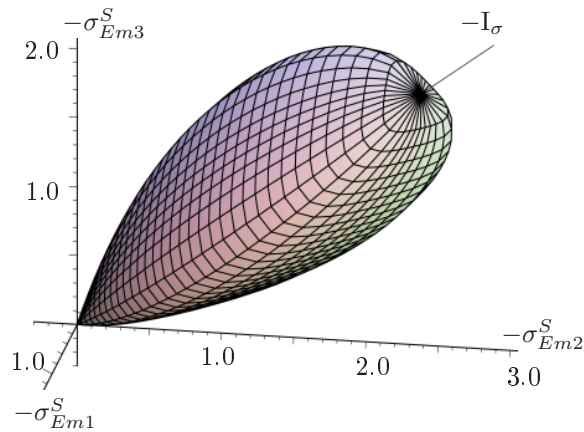


**Figure 4.1:** Limit state described by the fully convex single-surface yield envelope  $F(\boldsymbol{\sigma}_{Em}^S)$ .

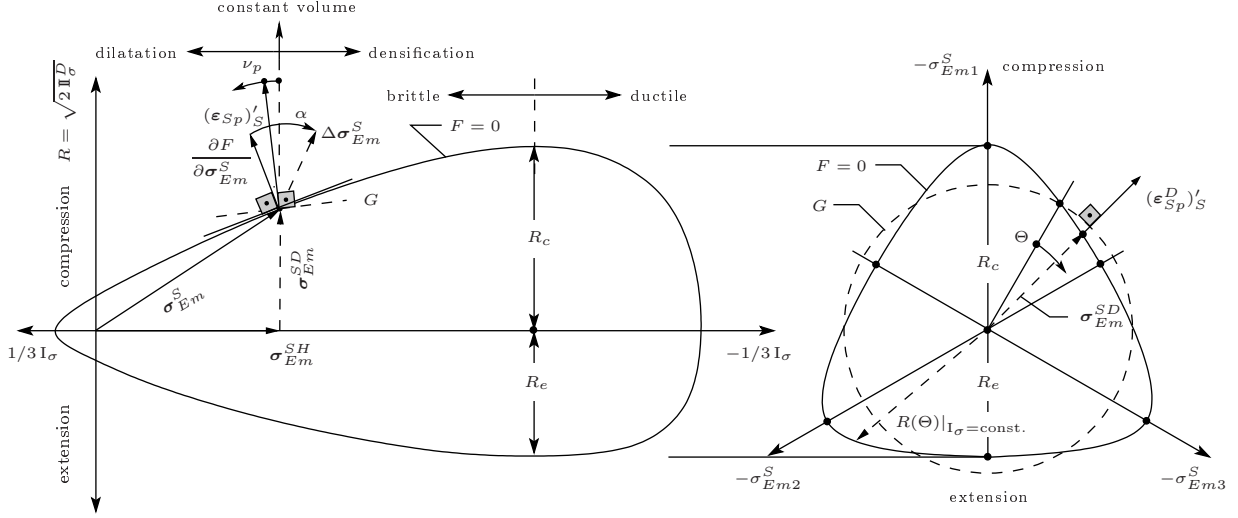


**Figure 4.2:** Illustration of the yield surface characteristics of granular materials and its yielding behaviour: (left) the hydrostatic stress plane and (right) the deviatoric stress plane.

deviatoric set given by

$$\mathcal{S}_H = \{\alpha, \beta, \delta, \epsilon, \kappa\} \quad \text{and} \quad \mathcal{S}_D = \{\gamma, m\} \quad (4.36)$$

depending on whether they control the shape of the yield surface in the hydrostatic ( $\mathcal{S}_H$ ) or in the deviatoric plane ( $\mathcal{S}_D$ ). Ehlers [48] has used the *Reuss* variables given in (3.1) for the reformulation of yield function  $F$ . Therewith, (4.35) can be replaced by

$$R(\Theta, I_\sigma) = \mathcal{F}_D(\Theta) \mathcal{F}_H(I_\sigma), \quad (4.37)$$

where

$$\begin{aligned} \mathcal{F}_D &= [1 + \frac{2}{\sqrt{27}} \gamma \sin(3\Theta)]^{-m/2}, \\ \mathcal{F}_H &= \sqrt{2} [(\epsilon^2 - \delta^2) I_\sigma^4 + 2\beta \epsilon I_\sigma^3 + (\beta^2 - \frac{1}{2} \alpha^2 - 2\epsilon \kappa) I_\sigma^2 - 2\beta \kappa I_\sigma + \kappa^2]^{1/2}. \end{aligned} \quad (4.38)$$

Therein,  $R_s(I_\sigma) = \mathcal{F}_H$  governs the simple shear radius of the yield function in the hydrostatic plane spanned by  $(2\mathbb{I}_\sigma^D)^{1/2}$  and  $I_\sigma$ , while  $\mathcal{F}_D$  yields the deviation of  $\mathcal{F}_H$  towards the compression and extension radii,  $R_c$  and  $R_e$ . Following this, the *Lode* angle  $\Theta$  at any value of the first stress invariant  $I_\sigma$  is zero at simple shear and reaches its maximum value at triaxial compression at  $\Theta = -30^\circ$  yielding  $R_c = R(\Theta = -30^\circ)$  and its minimum value at triaxial extension at  $\Theta = 150^\circ$  yielding  $R_e = R(\Theta = 150^\circ)$ , cf. Section 3.1.3. As a consequence, a typical triangle shape with rounded corners of the yield surface results, cf. Lade and Duncan [99]. For a better understanding and clarification of these coherences, the yield surface is graphically illustrated in Figure 4.2 through two cross sections of the yield surface. The left picture shows the cross section of the yield surface in the hydrostatic stress plane, while the right one represents the shape in the deviatoric stress plane.

Figure 4.2 (left) illustrates the stress path of an arbitrary compression load, where  $\sigma_{Em}^S$  is the current stress state at the yield surface  $F$ , whereas  $\Delta\sigma_{Em}^S$  denotes the direction of its

incremental increase. Moreover,  $\Delta \boldsymbol{\sigma}_{Em}^S$  can be rewritten in term of the temporal change:  $\Delta \boldsymbol{\sigma}_{Em}^S = (\boldsymbol{\sigma}_{Em}^S)'_S \Delta t$ , where  $\Delta t$  is the time increment. In order to assess the elasto-plastic material response, the orientation of the stress change  $(\boldsymbol{\sigma}_{Em}^S)'_S$  has to be evaluated. Based on the geometrical interpretation, the plastic yielding is determined by the angle  $\alpha$ , which is defined between the yielding direction  $\partial F / \partial \boldsymbol{\sigma}_{Em}^S$  (associated plasticity), and the load direction  $(\boldsymbol{\sigma}_{Em}^S)'_S$ . Hence, the following loading/unloading condition yields, viz.

$$\alpha \triangleleft \frac{\partial F}{\partial \boldsymbol{\sigma}_{Em}^S} \cdot (\boldsymbol{\sigma}_{Em}^S)'_S \quad \left\{ \begin{array}{ll} > 0 : \text{plastic loading} & \Rightarrow \Lambda > 0, \\ = 0 : \text{neutral loading} & \Rightarrow \Lambda = 0, \\ < 0 : \text{unloading} & \Rightarrow \Lambda = 0. \end{array} \right. \quad (4.39)$$

In case of plastic loading, the consistency condition  $(F)'_S = 0$  is fulfilled by introducing the consistency parameter or the plastic multiplier  $\Lambda$ . Under numerical consideration of the plastic yielding step within the frame of an elastic-predictor and plastic-corrector step (see following remark and also Chapter 5),  $\Lambda$  maps the trial elastic stress from outside of the yield surface back onto the yield surface such that  $(F)'_S = 0$  is fulfilled again. Thus,  $\Lambda$  is only active if plastic loading occurs, whereas, for an elastic loading step ( $F < 0$ ) or neutral loading,  $\Lambda$  is zero, but never negative.

However,  $\Lambda$  is either computed in the framework of rate-independent elasto-plasticity by the *Kuhn-Tucker* conditions

$$F \leq 0, \quad \Lambda \geq 0, \quad \Lambda F = 0, \quad (4.40)$$

or by use of a viscoplastic approach according to the overstress concept of *Perzyna* [126]:

$$\Lambda = \frac{1}{\eta} \left\langle \frac{F}{\sigma_0} \right\rangle^r \quad \text{or} \quad \eta \Lambda - \left\langle \frac{F}{\sigma_0} \right\rangle^r = 0. \quad (4.41)$$

Herein,  $\eta$  is the relaxation (viscosity) parameter,  $r$  is the viscoplastic exponent,  $\sigma_0$  is an equivalent stress, and  $\langle \cdot \rangle$  are the *Macauley* brackets. Note that for very small values of  $\eta$ , the viscoplastic approach coincides with the plastic description. Proceeding from a computational treatment, the viscoplasticity approach is beneficial as it also regularises the ill-posed plasticity problem during the localisation of shear bands, cf. Simo and Hughes [144], Hartmann et al. [81] and Ehlers et al. [64]. Following this, the assumption of viscoplastic material behaviour will be continued in this thesis by choosing  $\eta$  and  $r$  such that the elasto-viscoplastic model is close to elasto-plasticity.

In contrast to metal plasticity, frictional material is characterised by a dependency of  $F(\boldsymbol{\sigma}_{Em}^S)$  on  $\mathbf{I}_\sigma$ . As a result, it does not follow the concept of associated plasticity, where the yield function  $F(\boldsymbol{\sigma}_{Em}^S)$  coincides with the plastic potential  $G(\boldsymbol{\sigma}_{Em}^S)$  (Hill [88], Lemaitre and Chaboche [104] and Simo and Hughes [144]). Proceeding from an associate flow rule where  $F = G$ , the dilatation behaviour of porous materials is overestimated (Lade [97]). Instead, a separate plastic potential

$$G(\boldsymbol{\sigma}_{Em}^S) = \sqrt{\psi_1 \mathbf{II}_\sigma^D + \frac{1}{2} \alpha \mathbf{I}_\sigma^2 + \delta^2 \mathbf{I}_\sigma^4} + \psi_2 \beta \mathbf{I}_\sigma + \epsilon \mathbf{I}_\sigma^2 \quad (4.42)$$

has been formulated by Ehlers and Müllerschön [66], see also Kim and Lade [92], which is defined as the directional potential for the plastic strain rate:

$$(\boldsymbol{\varepsilon}_{Sp})'_S = \Lambda \frac{\partial G}{\partial \boldsymbol{\sigma}_{Em}^S}. \quad (4.43)$$

Therein, the additional parameters  $\psi_1$  and  $\psi_2$  are required to adjust the dilatation angle  $\nu_p$  to experimental data, which is defined between the deviatoric direction with constant volume changing and the yielding direction,  $(\boldsymbol{\varepsilon}_{Sp}^D)'_S$  and  $(\boldsymbol{\varepsilon}_{Sp})'_S$ , respectively, cf. Figure 4.2 (left). The influence of both parameters on  $\nu_p$  has been numerically studied by Mahnkopf [113]. For the parameter values  $\psi_1 = \psi_2 = 1$ , the non-associated plastic yielding is transferred to the associated plasticity, while for  $\psi_1 \rightarrow \infty$  the associated ideal *Mises* plasticity is approximated. Concerning to experimental studies on sand, Yamada and Ishihara [181] and also Lade and Duncan [99] detected via true triaxial tests that the deviatoric strain increment in the principle deviatoric stress plane shows an almost coaxially flow direction to the origin. Due to this fact, a circle shape in the deviatoric principle stress plane has been chosen for the plastic potential  $G$ , while the third principle stress invariant  $\mathbb{III}_\sigma^D$  in (4.42) is left out, see in Figure 4.2 (right). Therewith, the deviatoric plastic strain  $(\boldsymbol{\varepsilon}_{Sp}^D)'_S$  is always coaxially oriented in the deviatoric stress plane, which is a good approximation for the observed behaviour of Yamada and Ishihara [181].

**Remark:** In the framework of a numerical treatment of the elasto-plastic problem (see Section 5.1.4), a predictor-corrector scheme is pursued based on an incremental procedure. The predictor step is an elastic trial stress, which is located in case of plastic yielding outside the elastic domain. However, this is not allowed by the consistency condition. Therefore, the trial stress has to be directly projected back onto the yield surface. The back projected stress point is numerically determined by an explicit or an implicit *return mapping algorithm* (Simo and Taylor [145] and Simo and Hughes [144]) by solving the local plasticity problem with a set of unknown internal variables. The unique solution of the resulting local system of non-linear equations is guaranteed only if one back stress point at the yield surface exists. For this reason, the yield surface and the plastic potential must be convex functions. However, the local iteration procedure is finished, when the *Kuhn-Tucker* condition is satisfied.

## Modelling of hardening and softening behaviour

The yield function, which is generally formulated by the invariants of the principle effective stresses (4.35), span a 3-d yield surface, cf. Figure 4.1. Following sophisticated yield criteria, the invariants are coupled with the plastic material parameters  $\boldsymbol{\mathcal{S}} = \boldsymbol{\mathcal{S}}_H \cup \boldsymbol{\mathcal{S}}_D$ . Therewith, the shape of the yield surface can be individually formed as is demanded by the investigated material behaviour. In case of ideal material plasticity without plastic hardening, the yield surface is constant. However, in order to correctly model the macroscopically homogeneous stress-strain relation of granular materials, the behaviour of the evolving yield surface must include the densification (hardening) and the loosening (softening) of the solid skeleton. This is accomplished by an isotropic evolution of the yield surface by the change of the plastic material parameters. Thereby, the size of the yielding

surface  $F$  is changed by the amount of  $\Delta F$

$$F(\boldsymbol{\sigma}_{Em}^S, \alpha_i) = F(\boldsymbol{\sigma}_{Em}^S) + \Delta F(\boldsymbol{\sigma}_{Em}^S, \alpha_i),$$

$$\text{where } \Delta F = \sum_{p_j} a_{p_j}(\boldsymbol{\sigma}_{Em}^S) \Delta p_j(\alpha_i) \quad (4.44)$$

is a function of the increment of the hardening material parameters  $\Delta p_j(\alpha_i)$  governed by the internal hardening variables  $\alpha_i$  and of the stress functions  $a_{p_j}(\boldsymbol{\sigma}_{Em}^S)$ , which represent the coupling of the material parameters  $p_j$  with the stress invariants ( $\mathbb{I}_\sigma, \mathbb{II}_\sigma^D, \mathbb{III}_\sigma^D$ ). The initial values of the hardening material parameters  $p_{j0}$  describe the initial size of the yield surface expressed by  $F(\boldsymbol{\sigma}_{Em}^S)$  in (4.44). The changing size of the yield surface governed by  $\Delta F$  is accomplished by formulating isotropic evolution laws for the parameter subset  $\mathbf{p} \subset \mathcal{S}$  of the yield surface, where  $\mathbf{p}$  is the vector of the hardening parameters  $p_j = \{\beta, \delta, \epsilon, \gamma\}$  evaluated by the evolution of  $\alpha_i$ . Thus, the dependencies of the yield criterion  $F$  (4.44) can be reformulated to

$$F(\boldsymbol{\sigma}_{Em}^S, \alpha_i) := F[\boldsymbol{\sigma}_{Em}^S, p_j(\alpha_i)]. \quad (4.45)$$

The actual individual parameters of  $p_j$  are determined through the update prescription

$$p_j(\alpha_i) = p_{j0} + \Delta p_j(\alpha_i) = p_{j0} + \int_t (p_j)'_S d\tilde{t}, \quad (4.46)$$

where  $(p_j)'_S$  is the temporal change of the individual parameters governed by the rate of the internal variables  $(\alpha_i)'_S$ . The evolution of  $p_j$  is computed by applying particular hardening functions  $h_j(\alpha_i)$ .

For the internal hardening variables  $\alpha_i$ , two constitutive approaches are prevalent, viz., the plastic work function  $W^p(\boldsymbol{\varepsilon}_{Sp})$  (e.g., Dafalias and Popov [33], Lade and Kim [100], Ehlers and Müllerschön [66]) or the equivalent plastic strains  $\varepsilon_{vp}(\boldsymbol{\varepsilon}_{Sp})$  (e.g., Simo and Taylor [145], Desai [40], Ehlers [48, 49] and Ehlers and Scholz [67]), whereas Desai [40] argued that a strain hardening provides a more consistent formulation than a plastic work conception. Proceeding from the strain hardening, a volumetric-deviatoric split of the plastic strain rate tensor  $(\boldsymbol{\varepsilon}_{Sp})'_S$  is carried out, which is expressed by the corresponding scalar values of equivalent plastic strains:

$$(\alpha_{vp})'_S \equiv (\varepsilon_{vp})'_S = (\varepsilon_{vp}^V)'_S + (\varepsilon_{vp}^D)'_S = -(\varepsilon_{Sp}^V)'_S + \|(\boldsymbol{\varepsilon}_{Sp}^D)'_S\|, \quad (4.47)$$

wherein  $(\varepsilon_{vp}^V)'_S$  is the equivalent volumetric-plastic strain rate, which is defined positive for the plastic-compression strains and negative for the plastic-dilatation strains, while the equivalent plastic-deviatoric strain rate  $(\varepsilon_{vp}^D)'_S$  is only restricted to positive values (hardening) expressed by the amount of  $(\boldsymbol{\varepsilon}_{Sp}^D)'_S$ . The volumetric-deviatoric split of  $(\varepsilon_{vp})'_S$  as shown in (4.47) is necessary in order to map the volumetric yielding behaviour of sand described in Section 3.2.2 on the basis of a triaxial drained compression test. During such tests, dense sand materials show a plastic volumetric densification behaviour at the hydrostatic loading as well as at the initial shear load until the plastic volume deformation switches to a dilatation behaviour. The ongoing increase of the homogeneous plastic

expansion of the sand grain structure leads to material softening. These important plastic volume properties of sand are considered by the equivalent volumetric-plastic strain rate  $(\varepsilon_{vp}^V)'_S$ .

Based on this approach, the evolution of the hardening parameters,  $(p_j)'_S = h_j(\varepsilon_{vp})$ , described by a linear hardening function  $h_j$  is separated into volumetric and deviatoric parts,  $(p_j^V)'_S$  and  $(p_j^D)'_S$ , which are driven by the corresponding rates of equivalent plastic strains,  $(\varepsilon_{vp}^V)'_S$  and  $(\varepsilon_{vp}^D)'_S$ , cf. Ehlers and Scholz [67]):

$$(p_j)'_S = (p_j^V)'_S + (p_j^D)'_S = p_j^{sat} [C_{p_j}^V (\varepsilon_{vp}^V)'_S + C_{p_j}^D (\varepsilon_{vp}^D)'_S] \quad (4.48)$$

with  $p_j^{sat} = \bar{p}_j^* - p_j$  : hardening saturation .

Therein,  $C_{p_j}^V$  and  $C_{p_j}^D$  are the constant volumetric and deviatoric hardening modulus. The hardening process is limited by the saturation conditions  $p_j^{sat}$ , where  $\bar{p}_j^*$  denote the limit values and  $p_j$  the current values of the individual hardening parameters. The yield surface resulting from  $\bar{p}_j^*$  characterises the maximal reachable size of the current yield surface given by  $p_j$  and is denoted as the failure surface. Accordingly, the evolution of the yield surface stops if the saturation limit is reached by  $p_j^{sat} = 0$ . However, immediately thereafter, the softening process starts with a shrinking of the yield surface by reverse evolutions of the parameters  $p_j$ . Evidently, the deviatoric part of  $(p_j^D)'_S$  in (4.48) only governs the plastic hardening, whereas, in contrast, the volumetric part  $(p_j^V)'_S$  can take positive or negative values according to both hardening and softening process of the yield surface in dependency of the plastic compression,  $(\varepsilon_{vp}^V)'_S > 0$ , and plastic dilatation,  $(\varepsilon_{vp}^V)'_S < 0$ , development.

**Remark:** The hardening parameters  $p_j$  of the yield surface  $F$  have different effects on the shape of the yield surface. For the evolution of the parameters, it can be important to know if the size of the yield surface raises with increasing or decreasing values of  $p_j$ . This depends on the coupling with the stress invariants in  $F$ . A detailed explanation of the meaning of the individual plastic parameters  $\mathcal{S}$  of  $F$  (4.35) is given by Ehlers [48, 49]. For example,  $\beta$  coupled with the first principle stress invariant  $I_\sigma$  as included in the *Drucker-Prager* yield-surface formulation is mainly responsible for the inclination of yield surface  $F$  in the hydrostatic stress plane. Whereas,  $\gamma$  is responsible for the shape of the yield surface in the deviatoric stress plane. By the evolution of  $\gamma$ , the yield surface changes the shape from a circle to the triangle with rounded corners. By evolving  $\beta$  and  $\gamma$  to a higher value, the elastic domain increases. In contrast,  $\epsilon$  and  $\delta$  increase the size of the yield surface with decreasing values due to the coupling with even exponents of  $I_\sigma$ . Hence, both parameters describe the cap of the yield surface in direction of the plastic stress compression, whereas for  $\epsilon = \delta = 0$ , the yield surface is an open cone.

### Stress-dependent evolving failure surface

The experimentally observed stress-path-dependent failure behaviour of sand discussed in Section 3.2.2, has to be theoretically described. This behaviour is characterised by an increase of the material strength at an arbitrary confined stress level by a preshearing



until the peak shear stress at a higher confined stress state. As a consequence, the limit of the yield surface denoted as the failure surface is not constant. Its variation is governed by the current confined stress state. Hence, the evolution of the current yield surface is always guided by the actual failure surface. This model approach is introduced as the new failure concept, whereas, using a fixed failure surface, it is called the old failure concept, cf. Ehlers and Avci [56].

For modelling the stress-path-dependent failure behaviour, the parameters  $\mathbf{p}^*$  describing the failure surface have to be variables. However, a parameter comparison shows that when just the parameter  $\epsilon^*$  taken into account, it is sufficient to perform the stress-path-dependent failure surface. This follows by the fact that  $\epsilon^*$ , which is coupled with the square of  $I_\sigma$  in  $F$  (4.35), increases the size of the failure surface slower at lower stress values, as, for example, the parameter  $\beta^*$  connected only with  $I_\sigma$ . Accordingly, at higher stress values, the failure surface is increased faster by  $\epsilon^*$  as it is required. Thus, the new concept with the variable failure surface governing with the first principle effective stress invariant  $I_\sigma$  is introduced by, cf. Ehlers and Avci [56],

$$\epsilon^*(I_\sigma) = \epsilon_0^* (1 + \bar{C}_\epsilon I_\sigma) \quad \text{with} \quad \epsilon^* \geq \epsilon_{lim}^*, \quad (4.49)$$

while the standard failure surface of the old concept is constant. In (4.49),  $\bar{C}_\epsilon$  is a constant evolution parameter of the failure surface, while  $\epsilon_0^*$  theoretically defines the failure surface for the unloaded virgin material. The initial failure surface is adjusted as small as possible but large enough for the smallest confining pressure of a triaxial experiment. Due to the limited strength of the material by the grain crushing at very high pressure state, the failure surface cannot be increased limitless. In order to avoid unrealistically large size of the failure surface, it is limited by  $\epsilon_{lim}^*$ . Note that for small value of  $\epsilon$  or  $\epsilon^*$ , the yield or failure surface is increasing due to the square of  $I_\sigma$  joint with  $\epsilon$  in the yield surface (4.35). To recapitulate, the yield surface evolving with (4.48) describes the plastic hardening and softening behaviour of sand, whereas the variation of the failure surface described by (4.49) restricts the evolution of the yield surface corresponding to the actual hydrostatic stress state.

The context of the new failure concept is schematically illustrated in Figure 4.3 by the evolution of the yield and failure surfaces in the hydrostatic stress plane. Therein, the unloaded material starts with the initial yield surface  $y\text{-s}(\mathbf{p}_0)$  sketched by the dark grey surface, which is determined by evaluating the yield criterion (4.35) with the initial parameter set  $p_{j0} = \{\beta_0, \delta_0, \epsilon_0, \gamma_0\}$ , whereas the light grey failure surface  $f\text{-s}(\mathbf{p}^*, \epsilon_0^*)$  is represented by the limit parameters  $\mathbf{p}_j^* = \{\beta^*, \delta^*, \epsilon_0^*, \gamma^*\}$ . The evolution of  $y\text{-s}(\mathbf{p})$  driven by (4.48) is limited by  $f\text{-s}(\mathbf{p}^*, \epsilon^*)$  determined by (4.49), which is also bounded by  $f\text{-s}(\mathbf{p}^*, \epsilon_{lim}^*)$ . However, a granular material, which has been shear-preloaded with a high confining pressure until the peak shear stress, can occupy a large size of  $y\text{-s}(\mathbf{p})$  at the lower confining pressure as  $f\text{-s}(\mathbf{p}^*, \epsilon^*)$  computed with the current pressure state. Indeed, the intergranular stability of the grain structure at the peak shear stress with the lower confining pressure is unstable. Hence, a further increase of the load leads to the stress softening with shrinking of  $y\text{-s}(\mathbf{p})$  to  $f\text{-s}(\mathbf{p}^*, \epsilon^*)$ . This behaviour is discussed in more detail in Section 6.1.2, where the simu-

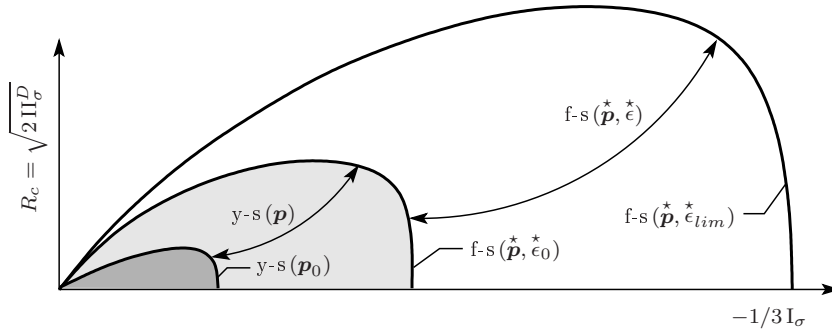


**Figure 4.3:** Sketch of the yield surface ( $y-s$ ) evolution driven by plastic strains and the development of the stress-dependent failure surface ( $f-s$ ) controlled by  $I_\sigma$ .

lations and experiments of stress-path tests are compared with each other. Additionally, the performance of the old concept with using a fixed failure surface is presented in order to illustrate the difference between both model approaches concerning to the yielding and failure behaviour.

### 4.3 Constitutive setting of the mobile pore fluids

Geomechanical problems are often triggered by an increase of the water content within the soil, which may lead to the soil failure triggered by buoyancy forces. On the other hand, the partially saturated zone has a positive effect to the soil stability. Thus, the capillary pressure of the partially saturated zone induces attractive forces between grains, which increase the resistance to soil deformations. For realistic simulation of geomechanical problems, these hydraulic effects resulting from the mobile pore fluids are essential and have to be accurately represented by constitutive models.

Based on the simple percolation experiments on saturated sand with homogeneous material distribution, Darcy [34] has detected a linear laminar flow behaviour and has defined a proportional correlation between the pressure drop and the fluid discharge rate through the soil. However, the mobile pore fluids within the partially saturated zone are triggered by the suction potential of the soil matrix, cf. Figure 4.4. The strength of the matrix potential to suck the water up over the saturated zone depends on the capillary pressure defined by the pressure difference between the non-wetting (air) and the wetting (water) fluids, cf. Brooks and Corey [25], while the relative saturation distribution of the pore water and the pore air within the partially saturated zone is triggered by geometric quantities such as pore and grain size distributions, the shape of grains and the soil texture. The experimental determination of the hydraulic conductivity properties of soil is comprehensively illustrated in Fredlund and Rahardjo [73].

In Figure 4.4, the partially saturated soil idealised by the triphasic model is sketched. Therein, the fully saturated domain,  $s^W = 1$  or  $s^A = 1$ , is percolated by one pore fluid, while the other fluid is not existing or is trapped with its residual saturation  $s_{res}^A$  or  $s_{res}^W$ , respectively. Hence, the saturation limit values yield  $s^W = 1 - s_{res}^A$  or  $s^A = 1 - s_{res}^W$ . In contrast, within the partially saturated zone of the soil lying between the two saturated

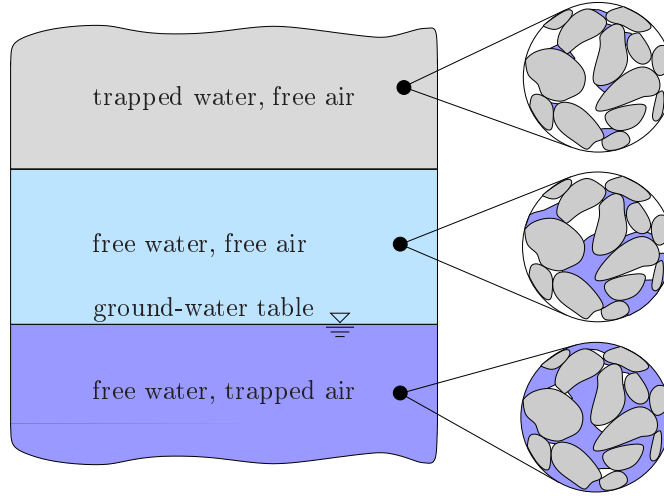


**Figure 4.4:** Illustration of different zones of a partially saturated soil.

domains,  $0 < \{s^W, s^A\} < 1$ , both pore fluids, pore water and pore air, are mobile. However, the hydraulic behaviour of the soil is still changing by the soil deformation (Ehlers and Eipper [60]), which can also lead to irregularities of the pore-channel networks (tortuosity) and causes preferable flow directions (anisotropic flow behaviour), cf. Markert [114]. In this contribution, the fluid motion is restricted only to isotropic flow behaviour.

### Darcy fluid flow

Proceeding from the momentum balance of the pore fluids with the restriction to creeping flow ( $\ddot{\mathbf{x}}_\beta \approx \mathbf{0}$ ) and applying the constitutive approach for the effective momentum productions  $\hat{\mathbf{p}}_E^\beta$  (Ehlers [53]),

$$\hat{\mathbf{p}}_E^\beta = - (n^\beta)^2 \gamma^{\beta R} (\mathbf{K}_r^\beta)^{-1} \mathbf{w}_\beta, \quad (4.50)$$

the seepage velocities  $\mathbf{w}_\beta$  yield

$$\begin{aligned} n^{AR} \mathbf{w}_A &= - \frac{\mathbf{K}_r^A}{\gamma^{AR}} \left[ \text{grad } p^{AR} - \rho^{AR} \mathbf{g} \right], \\ n^{WR} \mathbf{w}_W &= - \frac{\mathbf{K}_r^W}{\gamma^{WR}} \left[ \text{grad } p^{WR} - \rho^{WR} \mathbf{g} - \frac{p^C}{n^W} (s^A \text{grad } n^W - s^W \text{grad } n^A) \right], \end{aligned} \quad (4.51)$$

where  $\gamma^{\beta R}$  is the so-called specific weight of  $\varphi^\beta$ ,  $\mathbf{g}$  is the constant gravitational force and  $\mathbf{K}_r^\beta$  is the relative permeability tensor, which is related to the Darcy permeability tensor  $\mathbf{K}^\beta$  specified at a fully saturated condition ( $s^\beta = 1$ ) through the so-called relative permeability factor  $\kappa_r^\beta$  on the saturation of  $\varphi^\beta$ :

$$\mathbf{K}_r^\beta = \kappa_r^\beta(s^\beta) \mathbf{K}^\beta(n^S). \quad (4.52)$$

Related to the porous solid skeleton,  $\mathbf{K}^\beta$  is rewritten using the specific weights  $\gamma^{\beta R}$  and the effective shear viscosities  $\mu^{\beta R}$  to the intrinsic permeability  $\mathbf{K}^S$  through

$$\mathbf{K}^\beta = \frac{\gamma^{\beta R}}{\mu^{\beta R}} \mathbf{K}^S. \quad (4.53)$$

The solid deformation-dependency of the intrinsic permeability tensor is described by the isotropic distributed intrinsic permeability coefficient  $K^S$  (Ehlers and Eipper [60]):

$$\mathbf{K}^S(n^S) = K^S(n^S) \mathbf{I} = K_{0S}^S \left( \frac{1 - n^S}{1 - n_{0S}^S} \right)^\pi \mathbf{I}. \quad (4.54)$$

Therein,  $\mathbf{K}_{0S}^S = K_{0S}^S \mathbf{I}$  is the initial intrinsic isotropic permeability tensor at an unstressed initial state expressed by the initial intrinsic permeability coefficient  $K_{0S}^S$ , where, analogously to (4.53), the Darcy and the intrinsic permeability coefficients,  $k_{0S}^\beta$  and  $K_{0S}^S$ , are related to  $k_{0S}^\beta = \gamma^{\beta R} / \mu^{\beta R} K_{0S}^S$ . Furthermore,  $\pi \geq 0$  is a material parameter, which governs the exponential development of the permeability by variations of the solidity  $n^S$  induced by volume deformations of the solid skeleton, cf. equation (4.31). An alternative approach to describe the hydraulic conductivity is the *Kozeny-Carman* equation

$$K^S(n^S) = K_{0S}^S \frac{(1 - n^S)^3}{(n^S)^2}, \quad (4.55)$$

which is frequently used in modelling the variation of the permeability during the internal erosion process, where the soil porosity  $n^F$  increases. Moreover, the permeability of soil is much more pronounced by erosion than by the mechanical deformation. Thus, the exponent  $\pi$  in (4.54) is very useful for considering the strongly increase of the permeability with increasing porosity  $n^F = 1 - n^S$ .

Following the argumentation of Fredlund and Rahardjo [73], the fluid flow within the unsaturated soil domain can be treated like the saturated domain, because the air-filled non-conductive pore channels are preventing the water flow. As a result, the capillary-pressure-driven term in  $\mathbf{w}_W$  (4.51) can be neglected, see also Graf [78]. Following this, the Darcy law of the pore water is reduced to

$$n^{WR} \mathbf{w}_W = - \frac{\mathbf{K}_r^W}{\gamma^{WR}} (\text{grad } p^{WR} - \rho^{WR} \mathbf{g}). \quad (4.56)$$

### Partially saturated zone

The pore-fluid mobility within the partially saturated zone is determined via deformation-free water-retention tests on soil samples, cf. Fredlund and Rahardjo [73]. A retention curve is characterised by the effective pore-pressure difference defined as the capillary pressure  $p^C = p^{AR} - p^{WR}$  and the water saturation  $s^W$  (4.23)<sub>3</sub>, which can be derived from the free *Helmholtz* energy of the incompressible pore water  $\psi^W(s^W)$  (Graf [78]). Concerning the description of the retention curves of soil, Brooks and Corey [25], Mualem [117] and van Genuchten [75] have been introduced constitutive relations for the effective water saturation  $s_{eff}^W$  in dependence of  $p^C$  or vice versa (Graf [78]). Thereby,  $s_{eff}^W$  defines the part of the partially saturated zone of the soil, where both pore fluids are mobile, and is bounded by the residual saturations of the pore fluids  $s_{res}^\beta$ . To take these residual properties of soil into account, the formulation of Finsterle (1993) is adopted for  $s_{eff}^W$ :

$$s_{eff}^W := \frac{s^W - s_{res}^W}{1 - s_{res}^W - s_{res}^A}. \quad (4.57)$$

For the computation of  $s_{eff}^W$ , the capillary-pressure-saturation relation of van Genuchten [75] is applied yielding

$$s_{eff}^W(p^C) = [1 + (\alpha_{gen} p^C)^{j_{gen}}]^{-h_{gen}}, \quad (4.58)$$

where  $\mathbf{p}^{vG} = \{\alpha_{gen}, j_{gen}, h_{gen}, \epsilon_{gen}, \gamma_{gen}, h_{gen}\}$  in (4.58) and (4.59) is the set of the *van Genuchten's* hydraulic material parameters. Hence, the water saturation  $s^W$  follows from inserting (4.58) in (4.57) and solving the resulting equation for  $s^W$ . Thus, the relative permeability factor  $\kappa_r^\beta$  in (4.52) depending on  $s_{eff}^W$  is determined by the formulation of the *van Genuchten* model ([75]):

$$\kappa_r^W = (s_{eff}^W)^{\epsilon_{gen}} \{1 - [1 - (s_{eff}^W)^{1/h_{gen}}]^{h_{gen}}\}^2, \quad \kappa_r^A = (1 - s_{eff}^W)^{\gamma_{gen}} [1 - (s_{eff}^W)^{1/h_{gen}}]^{2h_{gen}}. \quad (4.59)$$

### Compressible fluid

For the materially compressible pore air, the constitutive approach of the ideal gas law (*Boyle-Mariotte's* law) is applied, which can be derived from the *Helmholtz* free energy  $\psi^A$ , viz.:

$$\psi^A(\rho^{AR}, \theta) = \bar{R}^A \theta \ln \rho^{AR} + g(\theta) \rightarrow p^{AR}(\rho^{AR}, \theta) = (\rho^{AR})^2 \frac{\partial \psi^A}{\partial \rho^{AR}} = \bar{R}^A \theta \rho^{AR}. \quad (4.60)$$

Therein,  $\bar{R}^A$  denotes the specific gas constant of the pore air, and  $\theta$  is the absolute *Kelvin's* temperature, which is constant in the case of isothermal problems. Reformulating (4.60),  $\rho^{AR}$  can be also given as

$$\rho^{AR} = \frac{p_0 + p^{AR}}{\bar{R}^A \theta}. \quad (4.61)$$



## Chapter 5:

# Numerical Treatment

For the numerical investigation of IBVP in the field of solid mechanics, the finite-element method (FEM) is commonly applied. The FEM is a numerical method embedded within a finite-difference scheme in time for solving systems of partial differential equations (PDE). However, non-linear soil mechanics leads to a system of differential-algebraic equations (DAE) consisting of the PDE of the global balance laws and a secondary system of algebraic constraints of the local problem of plasticity, cf. Ellsiepen [70]. For the numerical treatment of DAE systems of deformable porous materials, efficient numerical solution strategies are required, which have been discussed in, e.g., Ehlers [51, 52, 59, 61, 62], Wieners et al. [176] and Schrefler and coworkers, e.g., [106, 138–140]. Concerning this, in the first part of this chapter, the numerical implementation of the triphasic model within the framework of the FE tool PANDAS (**P**orous **M**edia **A**daptive **N**onlinear **F**inite **E**lement Solver based on **D**ifferential **A**lgebraic **S**ystems) is discussed.

In the second part of this chapter, the numerical optimisation procedure for solving non-linear constraint optimisation problems occurring in the task of parameter identification is illustrated, while the results of the parameter identification process are presented in Chapter 6. To overcome this non-linear optimisation problem, the *Least-Squares* minimisation function of the error between the computed and experimental data is formulated, which is also called the object function. To solve the constraint minimisation problem, gradient-based optimisation methods based on the *Sequential Quadratic Programming* (SQP) algorithm are applied, cf. Spellucci [149], Schittkowski [135] or Boggs and Tolle [17], whereas the required gradients of the object function are determined by semi-analytical computations of the sensitivities. The sensitivities are defined as the deviation of the computed physical quantities with respect to the variation of the optimised material parameters (Mahnken and Stein [112] or Scholz [137]).

### 5.1 Finite-element method

The FEM has nearly unlimited possibilities to investigate complex engineering problems. Its application takes place in different fields, e.g., in automotive, aerospace or civil engineering industries as well as in the scope of university research. Due to the fact of fast increase of computer power within the last two decades, the complexity of the treated problems has been extremely increased. Hence, FEM has become indispensable in the field of engineering. However, the user of FE tools has to be always aware that these methods only approximate the correct solution of complex IBVP, while the correct solution itself is usually unknown. The accuracy of the solution depends on many factors as the approximation of the geometry or the primary field variables of the investigated IBVP as well as the constitutive approach of the material behaviour based on the quality of the experimental investigations of the material. Nevertheless, the FE user has to

ensure that the generated numerical results converge in all probability to the real solution. For detailed information on the FEM and the numerical treatment of non-linear problems of continuum solid mechanics, the interested reader is referred to the works of Bathe [5], Braess [22], Hughes [89], Schwarz [141], Wriggers [180] or Zienkiewicz and Taylor [184, 185].

### 5.1.1 Weak formulation

The local balance equations in (4.6), (4.8)<sub>1</sub> and (4.8)<sub>2</sub>, which are also called the strong formulation of the mechanical balance laws, are continuously fulfilled at each local material point of the continuum mixture body  $\mathcal{B}$ . In contrast, the approximation procedure of the FEM is based on an energetic expression of the mechanical balance laws. Thus, they are satisfied in the global or integral sense over the spatial domain  $\Omega$ . This transformation of the strong local form of the mechanical balance equations into a weak global representation is realised by multiplying them with independent test (weighting) functions  $\delta \mathbf{u}_S$ ,  $\delta p^{WR}$  and  $\delta p^{AR}$  of the primary variables\*  $\mathbf{u}_S$ ,  $p^{WR}$  and  $p^{AR}$  ( $u$ - $p$ - $p$  formulation). This so-called *Galerkin* method is equivalent to the well-known *variational principle of minimum of potential energy* (Zienkiewicz and Taylor [184]). After applying the integration-by-parts rule and the *Gaussian* integral theorem, the weak form of the balance equations can be summarised into the internal and external parts of virtual work,  $\delta W_{int}$  and  $\delta W_{ext}$ , where the former part represents the virtual shape-changing work, while the latter part is the virtual work resulting from the external loads on  $\mathcal{B}$  induced from the vicinity (surface load) and from the distance (gravitation force). For arbitrary variations of the primary variables, the resulting equations of virtual work have to vanish under consideration of the boundary conditions. This conforms to the equilibrium statement of the variational principle:

$$\mathcal{G}_{\mathbf{u}}(\mathbf{u}, \delta \mathbf{u}) = \delta W_{\mathbf{u},int} - \delta W_{\mathbf{u},ext} = \mathbf{0}. \quad (5.1)$$

Therein the primary variables are summarised in the vector  $\mathbf{u} = [\mathbf{u}_S, p^{WR}, p^{AR}]^T$  and  $\mathcal{G}_{\mathbf{u}}$  is the system of the governing balance equations in the variational weak formulation. Note that applying the integration-by-part rule, the order of the differential equation of the strong form is reduced at least by one order. Therefore, the weak representation poses lower requirements for satisfying the global equilibrium of the balance laws as the strong formulations fulfilling the local equilibrium at each material point  $P^\alpha$  of  $\mathcal{B}$ . Hence, the weak form of the momentum balance of the overall aggregate (4.6) yields by weighting with

---

\*In the framework of the numerical treatment of mechanical balance laws, the pore-air pressure  $p^{AR}$  is used as the primary variable instead of the continuum-mechanical kinematic variable of the effective density  $\rho^{AR}$ . In contrast, the effective density  $\rho^{WR}$  of the materially incompressible pore water  $\varphi^W$  is constant and, therewith, the indeterminate pore-water pressure field  $p^{WR}$  is determined from the given boundary condition  $\bar{p}^{WR}$  of the considered problem. Consequently, for the triphasic model, the primary variables  $\mathbf{u}_S$ ,  $p^{WR}$  and  $p^{AR}$  ( $u$ - $p$ - $p$  formulation) are generally used, whereas Graf [78] has also switched the primary variable  $p^{WR}$  with the water saturation  $s^W$  ( $u$ - $s$ - $p$  formulation).



the test function  $\delta \mathbf{u}_S$  and applying the product rule and the *Gaussian* integral theorem

$$\begin{aligned} \mathcal{G}_{\mathbf{u}_S}(\mathbf{u}_S, p^{\beta R}, \delta \mathbf{u}_S) &= \underbrace{\int_{\Omega} (\boldsymbol{\sigma}_{Em}^S - p^{FR} n^F \mathbf{I}) \cdot \text{grad } \delta \mathbf{u}_S \, dv}_{\delta W_{\mathbf{u}_S, \text{int}}} - \\ &\quad - \underbrace{\int_{\Omega} \rho \mathbf{g} \cdot \delta \mathbf{u}_S \, dv}_{\delta W_{\mathbf{u}_S, \text{ext}}} - \underbrace{\int_{\Gamma_t} \bar{\mathbf{t}} \cdot \delta \mathbf{u}_S \, da}_{\delta W_{\mathbf{u}_S, \text{ext}}} = 0, \end{aligned} \quad (5.2)$$

where  $\bar{\mathbf{t}} := \bar{\mathbf{t}}^S + \bar{\mathbf{t}}^W + \bar{\mathbf{t}}^A = (\boldsymbol{\sigma}_{Em}^S - n^F p^{FR} \mathbf{I}) \mathbf{n}$  is the external total stress load vector acting on the *Neumann* boundary  $\Gamma_t$  of the overall medium, and  $\mathbf{n}$  is the outward-oriented unit normal vector on the surface. Therein, the fluid extra stresses  $\mathbf{T}^\beta$  are neglected, cf. (4.25). In case of applying a drained boundary condition for the pore fluids ( $p^{\beta R} = 0 \rightarrow \bar{\mathbf{t}}^{\beta R} = \mathbf{0}$ ),  $\bar{\mathbf{t}}$  corresponds to the stress load of the solid phase  $\bar{\mathbf{t}} := \bar{\mathbf{t}}^S = \boldsymbol{\sigma}_{Em}^S \mathbf{n}$ . Analogously to the overall momentum balance (5.2), the weak form of the volume balance of the materially incompressible pore-water phase (4.8)<sub>1</sub>,

$$\begin{aligned} \mathcal{G}_{pw}(\mathbf{u}_S, p^{WR}, \delta p^{WR}) &= \underbrace{\int_{\Omega} [(n^W)'_S + n^W \text{div}(\mathbf{u}_S)'_S] \delta p^{WR} \, dv}_{\delta W_{pw, \text{int}}} - \\ &\quad - \underbrace{\int_{\Omega} n^W \mathbf{w}_W \cdot \text{grad } \delta p^{WR} \, dv}_{\delta W_{pw, \text{int}}} + \underbrace{\int_{\Gamma_v} \bar{v}^W \delta p^{WR} \, da}_{\delta W_{pw, \text{ext}}} = 0, \end{aligned} \quad (5.3)$$

and of the mass balance of the materially compressible pore air phase (4.8)<sub>2</sub>,

$$\begin{aligned} \mathcal{G}_{pa}(\mathbf{u}_S, p^{AR}, \delta p^{AR}) &= \underbrace{\int_{\Omega} [n^A (\rho^{AR})'_S + \rho^{AR} (n^A)'_S + n^A \rho^{AR} \text{div}(\mathbf{u}_S)'_S] \delta p^{AR} \, dv}_{\delta W_{pa, \text{int}}} - \\ &\quad - \underbrace{\int_{\Omega} n^A \rho^{AR} \mathbf{w}_A \cdot \text{grad } \delta p^{AR} \, dv}_{\delta W_{pa, \text{int}}} + \underbrace{\int_{\Gamma_q} \bar{q}^A \delta p^{AR} \, da}_{\delta W_{pa, \text{ext}}} = 0, \end{aligned} \quad (5.4)$$

are derived by weighting them with the test functions  $\delta p^{WR}$  and  $\delta p^{AR}$  and then applying the product rule and integral theorem. Therein,  $\bar{v}^W = n^W \mathbf{w}_W \cdot \mathbf{n}$  is the efflux of the water volume through the *Neumann* boundary  $\Gamma_v$ , while  $\bar{q}^A = n^A \rho^{AR} \mathbf{w}_A \cdot \mathbf{n}$  is the efflux of the air mass through the *Neumann* boundary  $\Gamma_q$ . Proceeding from quasi-static IBVP, the seepage velocities  $\mathbf{w}_\beta$  are determined by a constitutive assumption, e. g., through the *Darcy* laws

(4.51)<sub>1</sub> and (4.56) governed by the pore-fluid pressures  $p^{\beta R}$ . The resulting expressions of the mechanical quantities  $\bar{\mathbf{t}}$ ,  $\bar{v}^W$  and  $\bar{q}^A$  are acting on the *Neumann* (natural) boundaries  $\Gamma_t$ ,  $\Gamma_v$  and  $\Gamma_q$  of  $\Omega$ , while the primary variables are applied on the *Dirichlet* (essential) boundaries  $\Gamma_{\mathbf{u}_S}$ ,  $\Gamma_{pw}$  and  $\Gamma_{pa}$ . Thus, the boundary  $\Gamma = \partial\Omega$  of the domain  $\Omega$  is divided into a *Neumann* and a *Dirichlet* boundary as follows:

$$\Gamma = \Gamma_{\mathbf{u}_S} \cup \Gamma_t \quad ; \quad \Gamma = \Gamma_{pw} \cup \Gamma_v \quad ; \quad \Gamma = \Gamma_{pa} \cup \Gamma_q, \quad (5.5)$$

where *Dirichlet* and *Neumann* boundaries cannot exist at the same place:

$$\emptyset = \Gamma_{\mathbf{u}_S} \cap \Gamma_t \quad ; \quad \emptyset = \Gamma_{pw} \cap \Gamma_v \quad ; \quad \emptyset = \Gamma_{pa} \cap \Gamma_q. \quad (5.6)$$

In consideration of these boundary conditions defined for each PDE, the unknown primary field variables  $\mathbf{u}_S$ ,  $p^{WR}$  and  $p^{AR}$  governing the PDE are approximated by test functions. To ensure the solution of the PDE, the trial functions must obtain the property of a square-integrability condition on  $\Omega$ . This requirement is satisfied if the trial functions are chosen from the standard *Sobolev* space  $H^1(\Omega)$ ,

$$\begin{aligned} \mathcal{S}_{\mathbf{u}_S}(t) &= \{ \mathbf{u}_S \in H^1(\Omega)^D : \mathbf{u}_S(\mathbf{x}) = \bar{\mathbf{u}}_S(\mathbf{x}, t) \text{ on } \Gamma_{\mathbf{u}_S} \}, \\ \mathcal{S}_{pw}(t) &= \{ p^{WR} \in H^1(\Omega) : p^{WR}(\mathbf{x}) = \bar{p}^{WR}(\mathbf{x}, t) \text{ on } \Gamma_{pw} \}, \\ \mathcal{S}_{pa}(t) &= \{ p^{AR} \in H^1(\Omega) : p^{AR}(\mathbf{x}) = \bar{p}^{AR}(\mathbf{x}, t) \text{ on } \Gamma_{pa} \}, \end{aligned} \quad (5.7)$$

whereas  $\mathcal{S}_{(\cdot)}(t)$  with  $t \in [t_0, T]$  is the shifted Sobolev space by the *Dirichlet* boundaries,  $\bar{\mathbf{u}}_S = \mathbf{u}_S$ ,  $\bar{p}^{WR} = p^{WR}$  and  $\bar{p}^{AR} = p^{AR}$ . The corresponding test functions of  $\delta\mathbf{u}_S$ ,  $\delta p^{WR}$  and  $\delta p^{AR}$  defined in the *Sobolev* space  $\mathcal{T}_{(\cdot)}$ ,

$$\begin{aligned} \mathcal{T}_{\mathbf{u}_S} &= \{ \delta\mathbf{u}_S \in H^1(\Omega)^D : \delta\mathbf{u}_S(\mathbf{x}) = \mathbf{0} \text{ on } \Gamma_{\mathbf{u}_S} \}, \\ \mathcal{T}_{pw} &= \{ \delta p^{WR} \in H^1(\Omega) : \delta p^{WR}(\mathbf{x}) = 0 \text{ on } \Gamma_{pw} \}, \\ \mathcal{T}_{pa} &= \{ \delta p^{AR} \in H^1(\Omega) : \delta p^{AR}(\mathbf{x}) = 0 \text{ on } \Gamma_{pa} \}, \end{aligned} \quad (5.8)$$

fulfil the homogeneous boundary conditions and disappear at the *Dirichlet* boundaries. Therein, the *Sobolev* space  $H^1(\Omega)$  represents functions of which the first derivation still exists in a weak sense (Ellsiepen [70]). The integer variable  $D \in \{1, 2, 3\}$  denotes the dimension in space.

Proceeding from the weak forms in (5.2), (5.3) and (5.4), the objective of the FE problem can be represented in a compact formulation (Ellsiepen [70]):

Find  $\mathbf{u} \in \mathcal{S}_{\mathbf{u}}(t)$  such that  $\mathcal{G}_{\mathbf{u}}(\mathbf{u}, \delta\mathbf{u}; \mathbf{q}, \mathbf{p}) = \mathbf{0} \quad \forall \delta\mathbf{u} \in \mathcal{T}_{\mathbf{u}}, t \in [t_0, T].$

(5.9)

Therein,  $\mathbf{q} := [\boldsymbol{\varepsilon}_{Sp}, \Lambda]^T$  and  $\mathbf{p} := [\beta, \delta, \epsilon, \gamma]^T$  denote all internal (history) variables. The internal variables are separated from the primary variables through a semicolon by the reason that the weak forms depends only indirectly from the local internal variables through the mechanical effective solid stress  $\boldsymbol{\sigma}_{Em}^S$ .

### 5.1.2 Spatial-domain discretisation

The computational spatial domain  $\Omega$  is decomposed in a finite number of contiguous subdomains  $\Omega_e$ :

$$\Omega \approx \Omega^h = \bigcup_{e=1}^E \Omega_e. \quad (5.10)$$

Therein,  $\Omega^h$  is the approximated domain of  $\Omega$  by finite elements building the FE mesh with the total number  $E$  of elements, while  $e$  is the index of an individual finite element  $\Omega_e$ . Depending on the shape function, each element consists of  $N_e$  nodes, while the total number of nodes is denoted by  $N_E$ . Therewith, the continuous or infinite-dimensional trial and test spaces,  $\mathcal{S}_{(\cdot)}(t)$  and  $\mathcal{T}_{(\cdot)}(t)$ , are subdivided to  $N$ -dimensional finite spaces,  $\mathcal{S}_{(\cdot)}^h(t)$  and  $\mathcal{T}_{(\cdot)}^h(t)$ , respectively. Accordingly, the field variables  $\mathbf{u}$  are discretised by the global shape or trial functions  $\phi_{\mathbf{u}}^i$ , additionally taking the *Dirichlet* boundary conditions  $\bar{\mathbf{u}} = [\bar{\mathbf{u}}_S, \bar{p}^{WR}, \bar{p}^{AR}]^T$  into account:

$$\begin{aligned} \mathbf{u}_S(\mathbf{x}, t) &\approx \mathbf{u}_S^h(\mathbf{x}, t) = \bar{\mathbf{u}}_S^h(\mathbf{x}, t) + \sum_{i=1}^{N_{\mathbf{u}_S}} \phi_{\mathbf{u}_S}^i(\mathbf{x}) \mathbf{u}_S^i(t) \in \mathcal{S}_{\mathbf{u}_S}^h(t) \\ p^{WR}(\mathbf{x}, t) &\approx p^{WRh}(\mathbf{x}, t) = \bar{p}^{WRh}(\mathbf{x}, t) + \sum_{i=1}^{N_{pw}} \phi_{pw}^i(\mathbf{x}) p^{WRi}(t) \in \mathcal{S}_{pw}^h(t), \\ p^{AR}(\mathbf{x}, t) &\approx p^{ARh}(\mathbf{x}, t) = \bar{p}^{ARh}(\mathbf{x}, t) + \sum_{i=1}^{N_{pa}} \phi_{pa}^i(\mathbf{x}) p^{ARi}(t) \in \mathcal{S}_{pa}^h(t). \end{aligned} \quad (5.11)$$

Therein,  $N_{\mathbf{u}} = \{N_{\mathbf{u}_S}; N_{pw}; N_{pa}\} \leq N_E$  denotes the set of the total number of nodes of the individual trial functions. For the *u-p-p* formulation, the displacement vector  $\mathbf{u}_S$  is approximated by a quadratic ansatz function, which corresponds to the node number of the FE mesh  $N_{\mathbf{u}_S} = N_E$ , whereas the fluid pressures are commonly linearly interpolated omitting the middle nodes of the finite elements. Thus, the total number of nodes  $N_{p\beta}$  of the ansatz  $\phi_{p\beta}$  is less than  $N_E$ . This discretisation approach of the strongly coupled solid-fluid problem is the so-called mixed finite element formulation<sup>†</sup>. Due to the fact that the position information is given by the trial function  $\phi_{\mathbf{u}}^i$ , the discrete values at the node  $\mathbf{u}^i = [\mathbf{u}_S^i, p^{WRi}, p^{ARi}]^T$  are only time-dependent. Furthermore, the test functions are approximated by ansatz functions based on the well-known approach of the *Bubnov-Galerkin* method, where the same ansatz functions are used as for the trial functions.

---

<sup>†</sup>To solve the solid-fluid problem with a linear ansatz function for the solid displacement  $\mathbf{u}_S$  and the fluid pressures  $p^{\beta R}$ , convergence problems can be encountered. Then, the solid stress over the element is computed with a constant strain progression determined by the gradient of  $\mathbf{u}_S$ , while the fluid pressures are linearly interpolated over the elements. The sum of these different approaches, which have to be carried out in the divergence statement of the balance of momentum, leads to unstable solutions. To overcome this problem, a mixed approximation of the primary variables is used, cf. the argumentation by Graf [78]. This so-called *Taylor-Hood* element fulfils the LBB condition (*Ladyshenskaya-Bauška-Brezzi*), which is an indicator for the stabilisation property of the numerical solution. For detail information the interested reader is to referred to the work of Braess [22], Brezzi and Fortin [24] and Wieners [175].

Hence, the approximation of the variational field quantities yields

$$\begin{aligned}
\delta \mathbf{u}_S(\mathbf{x}) &\approx \delta \mathbf{u}_S^h(\mathbf{x}) = \sum_{i=1}^{N_{u_S}} \phi_{u_S}^i(\mathbf{x}) \delta \mathbf{u}_S^i \in \mathcal{T}_{u_S}^h, \\
\delta p^{WR}(\mathbf{x}) &\approx \delta p^{WRh}(\mathbf{x}) = \sum_{i=1}^{N_{pw}} \phi_{pw}^i(\mathbf{x}) \delta p^{WRi} \in \mathcal{T}_{pw}^h, \\
\delta p^{AR}(\mathbf{x}) &\approx \delta p^{ARh}(\mathbf{x}) = \sum_{i=1}^{N_{pa}} \phi_{pa}^i(\mathbf{x}) \delta p^{ARi} \in \mathcal{T}_{pa}^h.
\end{aligned} \tag{5.12}$$

The gradients of the field quantities,  $\text{grad } \mathbf{u}$ , are derived by the partial derivation of the trial and test functions, respectively,

$$\begin{aligned}
\text{grad } \mathbf{u}^h(\mathbf{x}) &= \sum_{i=1}^{N_u} \text{grad } \phi_u^i(\mathbf{x}) \mathbf{u}^i, \\
\text{grad } \delta \mathbf{u}^h(\mathbf{x}) &= \sum_{i=1}^{N_u} \text{grad } \phi_u^i(\mathbf{x}) \delta \mathbf{u}^i.
\end{aligned} \tag{5.13}$$

Moreover, the geometry of the domain  $\Omega$  is approximated by the basis function  $\phi_{geo}^i$ . To simplify the numerical integration of the weak forms,  $\phi_{geo}^i$  is formulated in local coordinates  $\boldsymbol{\xi} = (\xi_1, \dots, \xi_D)$  within a unit range of  $[-1, 1]$  or  $[0, 1]$ , while the global coordinates  $\mathbf{x} = (x_1, \dots, x_D)$  are obtained by the coordinate transformation

$$\mathbf{x}(\boldsymbol{\xi}) = \sum_{i=1}^{N_e} \phi_{geo}^i(\boldsymbol{\xi}) \mathbf{x}_i, \tag{5.14}$$

which is carried out for each node  $N_e$  of the element  $e$ . The transformation of the differential element  $d\mathbf{x}$  into the local coordinates is performed by the *Jacobian* determinant  $J_e$ , viz.

$$J_e = \left| \det \left( \frac{d\mathbf{x}(\boldsymbol{\xi})}{d\boldsymbol{\xi}} \right) \right|. \tag{5.15}$$

Inserting equations (5.14) and (5.15) into an integral of a function  $f(\mathbf{x})$  given in global coordinates, the following expression can be found:

$$\int_{\Omega_e} f(\mathbf{x}) dv(\mathbf{x}) = \int_{\hat{\Omega}_e} f(\mathbf{x}(\boldsymbol{\xi})) J_e(\boldsymbol{\xi}) d\hat{v}(\boldsymbol{\xi}). \tag{5.16}$$

Therein,  $\hat{\Omega}_e$  is the domain of the reference element and  $d\hat{v}$  is the infinitesimal reference volume. The resulting integral expression represented in local element coordinates can be simply evaluated using the *Gaussian* quadrature:

$$\int_{\Omega_e} f(\mathbf{x}) dv(\mathbf{x}) \approx \sum_{k=1}^K f(\mathbf{x}(\boldsymbol{\xi})) J_e(\boldsymbol{\xi}) w_k. \tag{5.17}$$

Therein,  $w_k$  includes the weighting factors at the integration or *Gauss* point of the element  $\Omega_e$ , respectively. The weighting factors are fixed values depending on the number of *Gauss* points  $K$  and their position. However, the integral solution of a function with a polynomial order of  $2K - 1$  is exactly computed at the *Gauss* points, while beyond the *Gauss* points, the values deviate more or less from the correct solution depending on the approximation accuracy.

The numerical integration of the weak form of the balance laws is carried out element-wise by using the *Gauss* quadrature in (5.17). Thereby, for each degree of freedom (DOF)  $\mathbf{u}^i$  at the element node, test and trial functions are evaluated by setting their values at the considered node to one, whereas the values of the remaining nodes are zero. Analogously, this has to be carried out for each node of the element. Consequently, a system of independent equations results at the element level with the unknown discrete DOF element vector  $\mathbf{u}^e$ . This system of equations is assembled to the global system of equations of the FE mesh applying the assembly operator  $\bigcup_{e=1}^E$ . It includes the position information of each node of the FE mesh and transfers the numbering of the local DOF vector  $\mathbf{u}^e$  of the element  $\Omega_e$  into the global DOF vector  $\mathbf{u}$  of the FE mesh. Following this procedure, the vector of internal and external virtual works  $\mathbf{W}_{\mathbf{u},int}^e$  and  $\mathbf{W}_{\mathbf{u},ext}^e$  at the element level of the balance equations  $\mathcal{G}_{\mathbf{u}}^h$  in (5.2), (5.3) and (5.4), can be rewritten in terms of internal and external nodal force vectors  $\mathbf{f}_{\mathbf{u},int}^e$  and  $\mathbf{f}_{\mathbf{u},ext}^e$ . Assembling the element forces of the FE mesh, the global nodal forces  $\mathbf{f}_{\mathbf{u},int}$  and  $\mathbf{f}_{\mathbf{u},ext}$  of the entire vector of virtual works  $\mathbf{W}_{\mathbf{u},int}$  and  $\mathbf{W}_{\mathbf{u},ext}$  (5.1) result. Furthermore, the virtual DOF vector  $\delta\mathbf{u}^e$  at the element level or  $\delta\mathbf{u}$  of the FE mesh, respectively, is factored out and, therewith, the equilibrium state of the global balance relations in the procedure of the variational principle reads:

$$\begin{aligned} \mathcal{G}_{\mathbf{u}}^h(\mathbf{u}, \delta\mathbf{u}; \mathbf{q}, \mathbf{p}) &= \bigcup_{e=1}^E (\delta\mathbf{W}_{\mathbf{u},int}^e - \delta\mathbf{W}_{\mathbf{u},ext}^e) = \delta\mathbf{u}(\mathbf{f}_{\mathbf{u},int} - \mathbf{f}_{\mathbf{u},ext}) = \mathbf{0} \\ \text{where} \quad \delta\mathbf{u} &= \bigcup_{e=1}^E \delta\mathbf{u}^e, \quad \mathbf{f}_{\mathbf{u},int} = \bigcup_{e=1}^E \mathbf{f}_{\mathbf{u},int}^e, \quad \mathbf{f}_{\mathbf{u},ext} = \bigcup_{e=1}^E \mathbf{f}_{\mathbf{u},ext}^e. \end{aligned} \quad (5.18)$$

Therein, the generalised internal and external nodal force vectors are in equilibrium  $\mathbf{f}_{\mathbf{u},int} = \mathbf{f}_{\mathbf{u},ext}$ . However,  $\mathbf{f}_{\mathbf{u},int}$  is non-linear in the solid extra stress  $\boldsymbol{\sigma}_{Em}^S$  with regard to the solid strain tensor  $\boldsymbol{\varepsilon}_S$ , when plastic deformations occur. This leads to an additional local system of equations  $\mathcal{L}_{\mathbf{i}}^h$  with  $\mathbf{i} := [\mathbf{q}^T, \mathbf{p}^T]^T$  independent equations computed at each integration point  $K$ . All unknown quantities of the global and local system of equations are summarised to the vector  $\mathbf{y} := [\mathbf{u}^T, \mathbf{q}^T, \mathbf{p}^T]^T$ . Proceeding from quasi-static IBVP with the initial condition  $\mathbf{y}(t_0) = \mathbf{y}_0$  and  $t \in [t_0, T]$ , the governing semi-discrete DAE functional  $\mathcal{F} = [\mathcal{G}_{\mathbf{u}}^h, \mathcal{L}_{\mathbf{i}}^h]^T$  in time can be compactly formulated by the following scheme (Ellsiepen [70]):

$$\begin{aligned} \mathcal{F}[t, \mathbf{y}, (\mathbf{y})'_S] &= \begin{bmatrix} \mathcal{G}_{\mathbf{u}}^h(t, \mathbf{u}, (\mathbf{u})'_S; \mathbf{i}) \\ \mathcal{L}_{\mathbf{i}}^h(t, \mathbf{i}, (\mathbf{i})'_S; \mathbf{u}) \end{bmatrix} = \\ &= \begin{bmatrix} \mathbf{M}(\mathbf{u})'_S + \mathbf{k}(\mathbf{u}; \mathbf{i}) - \mathbf{f}_{\mathbf{u},ext} \\ \mathbf{A}(\mathbf{i})'_S - \mathbf{g}(\mathbf{i}; \mathbf{u}) \end{bmatrix} \stackrel{!}{=} \mathbf{0}, \end{aligned} \quad (5.19)$$

where  $\mathbf{M}(\mathbf{u})'_S + \mathbf{k}(\mathbf{u}; \mathbf{z}) := \mathbf{f}_{u,int}$  corresponds to the generalised internal force vector. Therein,  $\mathbf{M}$  is a generalised mass matrix and  $\mathbf{k}$  a generalised stiffness vector. Furthermore, the local system of the plasticity problem is expressed by  $\mathcal{L}_i^h$  including the evolution equations of all integration points of the FE mesh:

$$\mathbf{A}(\mathbf{z})'_S - \mathbf{g}(\mathbf{z}; \mathbf{u}) = \begin{pmatrix} (\boldsymbol{\varepsilon}_{Sp})'_S \\ 0 \\ (\mathbf{p})'_S \end{pmatrix} - \begin{pmatrix} \Lambda \frac{\partial G}{\partial \boldsymbol{\sigma}_{Em}^S} \\ -\Lambda + \frac{1}{\eta} \left\langle \frac{F}{\sigma_0} \right\rangle_r \\ \mathbf{h}(\boldsymbol{\alpha}) \end{pmatrix} = \mathbf{0}. \quad (5.20)$$

However,  $\mathbf{M}$  is a singular mass matrix. This follows from the fact that the momentum balance does not depend on the solid displacement velocity  $(\mathbf{u}_S)'_S$ . On the other hand, the volume balance of the incompressible pore water is independent from the temporal change of water pressure  $p^{WR}$  and, in addition, both pore fluid balances explicitly depend on  $(\mathbf{u}_S)'_S$ . Moreover, the matrix  $\mathbf{A}$  consists of unit matrices resulting from the individual terms in  $\mathbf{z} = [\mathbf{q}^T, \mathbf{p}^T]^T$ . Indeed, the flow rule of the second equation in (5.20) contains no time derivative. Thus,  $\mathbf{A}$  is a singular matrix just as  $\mathbf{M}$ . Due to the properties of both matrices  $\mathbf{M}$  and  $\mathbf{A}$ , the system of *ordinary differential equations* (ODE) (Hairer and Wanner [80]) of the FE problem is transferred to a system of *algebraic differential equations* (DAE). To solve the DAE system, particular strategies are needed, which are discussed in section 5.1.4, cf. Brenan [23] and Ellsiepen [70].

### 5.1.3 Time-domain discretisation

For the numerical treatment of ODE or PDE systems, the temporal-dependent quantities have to be discretised in time using a finite-difference method. It has been shown that, using an implicit time integration method such as the implicit *Euler* scheme, which can be derived from the well-known error controlled *Runge-Kutta* methods (Hairer et al. [79]), gives a stable solution for the DAE system (5.19), cf. Diebels et al. [44] and Ehlers and Ellsiepen [62].

Proceeding from the implicit *Euler* method, the set of unknown values  $\mathbf{y}_n$  at the actual time step  $n$ , where  $n-1$  denotes the old time step at which  $\mathbf{y}_{n-1}$  is known, is approximated by the first-order backward *Euler* method:

$$\mathbf{y}_n = \mathbf{y}_{n-1} + \mathbf{y}'(t_n) \Delta t_n \quad \text{where,} \quad \Delta t_n = t_n - t_{n-1} \quad (5.21)$$

is the time increment. Therein,  $\mathbf{y}_n$  is linearly approximated by neglecting the higher-order terms. Thus, the temporal change  $\mathbf{y}' := (\mathbf{y})'_S$  related to the solid motion is expressed by the increments  $\Delta \mathbf{y}_n$  and  $\Delta t_n$ :

$$\mathbf{y}'(t_n) = \frac{\Delta \mathbf{y}_n}{\Delta t_n} \quad \text{with} \quad \Delta \mathbf{y}_n = \mathbf{y}_n - \mathbf{y}_{n-1}. \quad (5.22)$$

Inserting the time-discrete quantities (5.21) and (5.22) into the DAE functional  $\mathcal{F}$  (5.19), the non-linear DAE system in the incremental representation of the dependencies results in

$$\mathcal{R}_n(\Delta \mathbf{y}_n) := \mathcal{F} \left[ t_n, \mathbf{y}_{n-1} + \Delta \mathbf{y}_n, \frac{1}{\Delta t_n} \Delta \mathbf{y}_n \right] = \mathbf{0}. \quad (5.23)$$

Based on the known values  $\mathbf{y}_{n-1}$  of the previous time step  $n-1$ , the increment  $\Delta \mathbf{y}_n$  is the searched stage solution of  $\mathcal{R}_n$ , which has to be computed iteratively within the current time step  $n$  (Ehlers and Ellsiepen [62]). Expressed in the presentation in global and local systems, the non-linear system  $\mathcal{R}_n$  in (5.23) reads as follows

$$\mathcal{R}_n := \begin{bmatrix} \mathbf{G}(\mathbf{U}_n, \mathcal{I}_n) \\ \mathbf{L}(\mathbf{U}_n, \mathcal{I}_n) \end{bmatrix} = \begin{bmatrix} \mathcal{G}_{\mathbf{u}(n)}^h \left( t_n, \mathbf{u}_{n-1} + \mathbf{U}_n, \frac{1}{\Delta t_n} \mathbf{U}_n, \mathbf{v}_{n-1} + \mathcal{I}_n \right) \\ \mathcal{L}_{\mathbf{v}(n)}^h \left( t_n, \mathbf{v}_{n-1} + \mathcal{I}_n, \frac{1}{\Delta t_n} \mathcal{I}_n, \mathbf{u}_{n-1} + \mathbf{U}_n \right) \end{bmatrix} = \begin{bmatrix} \mathbf{0} \\ \mathbf{0} \end{bmatrix}, \quad (5.24)$$

where  $\mathcal{I}_n := [\Delta \mathbf{q}_n^T, \Delta \mathbf{p}_n^T]^T$  and  $\mathbf{U}_n := \Delta \mathbf{u}_n$  are introduced.

### 5.1.4 Solution of the non-linear system

The non-linear DAE system  $\mathcal{R}_n$  in (5.24) is solved iteratively by the well-known *Newton-Raphson* method with regard to the initial values  $\mathbf{y}(t = t_0) = \mathbf{y}_0$  within the time period  $[t_0, \dots, t_{n-1}, t_n, \dots, T]$ . Concerning this, a linearisation of  $\mathcal{R}_n(\Delta \mathbf{y}_n)$  has to be carried out with respect to  $\mathbf{Y}_n := \Delta \mathbf{y}_n$ . A detailed description of the linearisation procedure of the triphasic model can be found in Blome [10]. Hence, the iterative solution algorithm of the non-linear coupled system of equations in a simple representation reads:

1. to solve  $\mathcal{R}_n^{i+1} = \mathcal{R}_n^i + \frac{d\mathcal{R}_n^i}{d\mathbf{Y}_n^i} \Delta \mathbf{Y}_n^i = \mathbf{0}$
2. update  $\mathbf{Y}_n^{i+1} = \mathbf{Y}_n^i + \Delta \mathbf{Y}_n^i$
3. convergence is not fulfilled :  $\| \mathcal{R}_n^{i+1}(\Delta \mathbf{Y}_n^i) \| > \text{tol} \quad i = i + 1$  back to 1
- convergence is fulfilled :  $\| \mathcal{R}_n^{i+1}(\Delta \mathbf{Y}_n^i) \| < \text{tol}$
4. new time step/update :  $t_n = t_{n-1} + \Delta t_n$  and  $\mathbf{y}_n = \mathbf{y}_{n-1} + \mathbf{Y}_n^{i+1}$ .

Therein,  $\text{tol}$  denotes the maximal tolerance for the computation error of  $\mathcal{R}_n^{i+1}$  and  $i$  is the index of the *Newton* iteration step, whereas the unknown quantities at the current time step  $t_n$  are located at the iteration step  $i + 1$ . The quantity  $\mathbf{J}_n^i = d\mathcal{R}_n^i / d\mathbf{Y}_n^i$  denotes the global tangent or the *Jacobian* matrix and is computed by

$$\mathbf{J}_n^i = \frac{d\mathcal{R}_n^i}{d\mathbf{Y}_n^i} = \left. \frac{\partial \mathcal{F}}{\partial \mathbf{y}} \right|_{\mathbf{z}} + \frac{1}{\Delta t_n} \left. \frac{\partial \mathcal{F}}{\partial \mathbf{y}'} \right|_{\mathbf{z}}, \quad (5.25)$$

where  $\mathbf{z} = [t_n^i, (\mathbf{y}_n^i)^T, (\mathbf{y}_n^{i'})^T]^T$  includes the current set of arguments of  $\mathcal{F}$  in  $\mathcal{R}_n^i$ . Solving the linear system  $\mathcal{R}_n^{i+1}$  with a direct computation of  $\mathbf{J}_n^i$  would lead to an inefficiently

filled structure of the matrix, because of the strong coupling of  $\mathbf{G}$  and  $\mathbf{L}$ . Due to this fact, the efficient sparse structure of the FEM matrix of  $\mathbf{G}_n$  is destroyed. To overcome this problem, the *operator-split method* has been introduced by Miehe [115] and Simo and Taylor [145], which is also known as a two-stage *Newton* solution procedure. Thereby, the global and local system of equations,  $\mathbf{G}$  and  $\mathbf{L}$ , are solved in a decoupled manner in order to benefit from the sparse matrix structure of  $\mathbf{G}$ . Thereby, for each global *Newton* iteration step  $i$  of the solution procedure  $\mathbf{G}_n^{i+1} = \mathbf{0}$ , the local system  $\mathbf{L}_n^{k+1} = \mathbf{0}$  is iteratively solved at the *Gauss* point when plastic yielding occurs, while the primary variables  $\mathbf{u}_n$  are kept constant. The local iteration index is denoted by  $k$ . The time step is accepted if both the local and the global iterations converge. In Table 5.1 and 5.2, the single steps of the solving procedure of  $\mathbf{G}_n$  and  $\mathbf{L}_n$  are illustrated within the frame of an *elastic-predictor* and a *plastic-corrector/return-mapping-step* algorithm (Simo and Hughes [143, 144]). Nevertheless, the dependency of the global balance laws from the local internal variables still has to be considered. This has been taken into account by the consistent linearisation of  $\mathbf{G}_n$  through the elasto-plastic algorithmic procedure better known as the *consistent algorithmic linearisation* introduced by Simo and Taylor [145] (see also in, e.g., Simo and Hughes [144] or Wriggers [180]).

#### *Elastic predictor/plastic corrector algorithm*

Due to the plastic yielding of materials, global and local systems are coupled through the non-linearity of the effective solid stress related to the solid strain,  $\sigma_{Em}^S \sim \varepsilon_S(\mathbf{u}_S, \mathbf{q}, \mathbf{p})$ .

Solution of the non-linear global system $\mathbf{G}_n = \mathbf{0}$ of the FE mesh	
1. Solve $\mathbf{G}_n^{i+1} \stackrel{!}{=} \mathbf{0}$ :	
	$(\mathbf{J}_G)_n^i \Delta \mathbf{U}_n^i = -\mathbf{G}_n^i \quad \text{with} \quad (\mathbf{J}_G)_n^i = \frac{d \mathbf{G}_n^i}{d \mathbf{U}_n^i}, \quad (5.26)$
where $i$ is the global <i>Newton</i> iteration step.	
(a) If $F(\sigma_{Emn}^{S trial}, \mathbf{p}) > 0$ , then solve $\mathbf{L}_n = \mathbf{0}$ as shown in Table 5.2.	
(b) Computation of the consistent material tangent $\mathbb{C}_n^{Si}$ (Eq. (5.37))	
	$\frac{d \Sigma_n^i}{d \varepsilon_{Sn}^i} = \left( \frac{\partial \mathbf{R}_n^{loc i}}{\partial \Sigma_n^i} \right)^{-1} \frac{\partial \mathbf{R}_n^{loc i}}{\partial \varepsilon_{Sn}^i} \rightarrow \mathbb{C}_n^{Si} = \frac{d \sigma_{Emn}^{Si}}{d \varepsilon_{Sn}^i}. \quad (5.27)$
2. Update of the global (primary) variables	
	$\mathbf{U}_n^{i+1} = \mathbf{U}_n^i + \Delta \mathbf{U}_n^i \quad \text{and} \quad i = i + 1 \quad \text{with} \quad i = 1, \dots, i_{max}. \quad (5.28)$
3. Check the global residual related to the user-defined global <i>Newton</i> tolerance	
	$\  \mathbf{U}_n^{i+1} - \mathbf{U}_n^i \  < \mathbf{U}_n^{i+1} \epsilon_{rel}^{tol} + \epsilon_{abs}^{tol} \quad \text{with} \quad i \leq i_{max}. \quad (5.29)$

**Table 5.1:** The global iteration algorithm for the determination of the primary variables  $\mathbf{U}_n$  at the *Gauss* point at time  $t_n$ .



Solution of the local system  $\mathbf{L}_n = \mathbf{0}$  at each single Gauss point

---

For  $F(\boldsymbol{\sigma}_{Emn}^{Strial}, \mathbf{p}) > 0$ , the internal variables  $\boldsymbol{\mathcal{I}}_n = [\Delta \mathbf{q}_n^T, \Delta \mathbf{p}_n^T]^T$  at fixed global (primary) variables  $\mathbf{U}_n$  are determined as follows:

1. Solve  $\mathbf{L}_n^{k+1} \stackrel{!}{=} \mathbf{0}$ :

$$(\mathbf{J}_L)_n^k \Delta \boldsymbol{\mathcal{I}}_n^k = -\mathbf{L}_n^k \quad (5.30)$$

with the Jacobian matrix  $(\mathbf{J}_L)_n^k$ :

$$(\mathbf{J}_L)_n^k = \left. \frac{d\mathbf{L}_n^k}{d\boldsymbol{\mathcal{I}}_n^k} \right|_{\mathbf{U}_n^k = \text{fixed}} = \frac{\partial \mathbf{L}_n^k}{\partial \boldsymbol{\mathcal{I}}_n^k} + \frac{1}{\Delta t_n} \frac{\partial \mathbf{L}_n^k}{\partial (\boldsymbol{\mathcal{I}}_n^k)'}, \quad (5.31)$$

where  $k$  is the local Newton iteration step.

2. Update the internal (history) variables:

$$\boldsymbol{\mathcal{I}}_n^{k+1} = \boldsymbol{\mathcal{I}}_n^k + \Delta \boldsymbol{\mathcal{I}}_n^k \quad \text{and} \quad k = k + 1 \quad \text{with} \quad k = 1, \dots, k_{max}. \quad (5.32)$$

3. Check the local residual related to the user-defined local Newton tolerance:

$$\|\boldsymbol{\mathcal{I}}_n^{k+1} - \boldsymbol{\mathcal{I}}_n^k\| < \boldsymbol{\mathcal{I}}_n^{k+1} \epsilon_{rel}^{tol} + \epsilon_{abs}^{tol} \quad \text{with} \quad k \leq k_{max}. \quad (5.33)$$

4. Check the Kuhn-Tucker conditions in (4.40):

If they are fulfilled, go back to Table 5.1, else reject the time step  $t_n$  and start a new global Newton iteration by bisection of the time step  $\Delta t$ .

**Table 5.2:** The local iteration algorithm to determine the internal variables  $\boldsymbol{\mathcal{I}}_n$  at each single Gauss point within the  $i$ -th global Newton iteration step at time  $t_n$ . For reason of clarity, the index  $i$  is omitted.

The determination of  $\boldsymbol{\sigma}_{Emn}^S$  is carried out in two steps. Firstly, the computation of  $\mathbf{G}_n^{i+1} = \mathbf{0}$  starts with an *elastic predictor step*  $\boldsymbol{\sigma}_{Emn}^{Strial} = \mathbb{C}^{Se}(\boldsymbol{\varepsilon}_{Sn} - \boldsymbol{\varepsilon}_{Spn-1})$ , which is called trial effective solid stress. Afterwards, the yield criterion  $F_n \leq 0$  in (4.35) is evaluated for  $\boldsymbol{\sigma}_{Emn}^{Strial}$ . If the yield criterion is violated,  $F_n > 0$ , the local system of equations  $\mathbf{L}_n^{k+1} = \mathbf{0}$  (Table 5.2) has to be solved numerically applying the Newton method until an effective elastic stress tensor  $\boldsymbol{\sigma}_{Emn}^S = \boldsymbol{\sigma}_{Emn}^{Strial} - \mathbb{C}^{Se} \Delta \boldsymbol{\varepsilon}_{Spn}$  is found by which the yield criterion is fulfilled,  $F_n = 0$ . Concerning this, the internal variables in  $\boldsymbol{\mathcal{I}}_n$  are iteratively determined during the second *plastic corrector step*. Thereby, the elastic trial stress is projected back onto the yield surface through the consistency parameter  $\Lambda_n$ :

$$\underbrace{\boldsymbol{\sigma}_{Emn}^S}_{\text{elastic predictor step}} = \underbrace{\boldsymbol{\sigma}_{Emn}^{Strial} - \mathbb{C}^{Se} \left( \boldsymbol{\varepsilon}_{Spn-1} + \Delta t \Lambda_n \frac{\partial G_n(\boldsymbol{\sigma}_{Emn}^S, \mathbf{p})}{\partial \boldsymbol{\sigma}_{Emn}^S} \right)}_{\text{plastic corrector step}}, \quad (5.34)$$

wherein, the plastic strain rate  $(\boldsymbol{\varepsilon}_{Spn})'_S$  in the increment  $\Delta \boldsymbol{\varepsilon}_{Spn} = \Delta t_n (\boldsymbol{\varepsilon}_{Spn})'_S$  is substituted by the flow rule in (4.43). This procedure is the so-called implicit return map-

ping algorithm. In case of  $F(\boldsymbol{\sigma}_{Emn}^{S_{trial}}, \mathbf{p}) < 0$ , the trial stress is an elastic loading step,  $\boldsymbol{\sigma}_{Emn}^S := \boldsymbol{\sigma}_{Emn}^{S_{trial}}$ , and, thus, the next time increment  $\Delta t_n$  can be applied.

**Remark:** The time step  $t_n$  is accepted if the global and local iteration procedures satisfy the  $L2$ -norm of the increments  $\Delta \mathbf{U}_n$  (or  $\mathbf{G}_n^{i+1}$ ) and  $\Delta \mathbf{I}_n$  (or  $\mathbf{L}_n^{k+1}$ ) of user-defined global and local error tolerances given in absolute and relative values,  $\epsilon_{abs}^{(g/l)tol}$  and  $\epsilon_{rel}^{(g/l)tol}$  within the user-defined maximal *Newton* iteration number  $i_{max}$  (global) and  $k_{max}$  (local), see Table 5.1 and 5.2. In that case, a new time step can be set otherwise the global *Newton* procedure has to be repeated with a bisection of the time step  $\Delta t_n$ .

#### Algorithmic consistent tangent moduli

For the linearisation of  $\mathbf{G}_n$  in Table 5.1, the local dependencies resulting from the plastic behaviour have to be taken into account. Hence, the global *Jacobian* tangent  $\mathbf{J}_G$  yields

$$(\mathbf{J}_G)_n^i = \frac{d\mathbf{G}_n^i}{d\mathbf{U}_n^i} = \frac{\partial \mathbf{G}_n^i}{\partial \mathbf{U}_n^i} + \frac{\partial \mathbf{G}_n^i}{\partial \mathbf{I}_n^i} \frac{d\mathbf{I}_n^i}{d\mathbf{U}_n^i}, \quad (5.35)$$

wherein the first part of the sum denotes the elastic tangent, while the second part is the plastic tangent and is only active if plastic yielding occurs, which depends on the derivative of internal variables with respect to the global ones. Due to the fact that the global and local systems are only coupled by the solid stress  $\boldsymbol{\sigma}_{Emn}^S$  regarding to  $\boldsymbol{\varepsilon}_{Sn}$ , the consistent elasto-plastic material tangent (5.35) can be directly determined from the local problem (Scholz [137])

$$\mathbf{R}_n^{loc}(\boldsymbol{\varepsilon}_{Sn}, \boldsymbol{\Sigma}_n(\boldsymbol{\varepsilon}_{Sn})) = \mathbf{0}, \quad (5.36)$$

which depends on the unknown variables  $\boldsymbol{\Sigma}_n(\boldsymbol{\varepsilon}_{Sn}) := [\boldsymbol{\sigma}_{Emn}^S, \Lambda_n, \mathbf{p}_n^T]^T$ . The equations of  $\mathbf{R}_n^{loc}$  are given in Table 5.3 in a time-discrete formulation. The consistent material tangent results from the derivation of  $\mathbf{R}_n^{loc}$  with respect to the actual strain tensor  $\boldsymbol{\varepsilon}_{Sn}$  applying the chain rule:

$$\frac{d\mathbf{R}_n^{loc}}{d\boldsymbol{\varepsilon}_{Sn}} = \frac{\partial \mathbf{R}_n^{loc}}{\partial \boldsymbol{\varepsilon}_{Sn}} + \frac{\partial \mathbf{R}_n^{loc}}{\partial \boldsymbol{\sigma}_{Emn}^S} \boxed{\frac{d\boldsymbol{\sigma}_{Emn}^S}{d\boldsymbol{\varepsilon}_{Sn}}} + \frac{\partial \mathbf{R}_n^{loc}}{\partial \Lambda_n} \frac{d\Lambda_n}{d\boldsymbol{\varepsilon}_{Sn}} + \frac{\partial \mathbf{R}_n^{loc}}{\partial \mathbf{p}_n} \frac{d\mathbf{p}_n}{d\boldsymbol{\varepsilon}_{Sn}} \stackrel{!}{=} \mathbf{0}. \quad (5.37)$$

Therein, the framed term is the searched consistent material tangent  $\mathbb{C}_n^S = \boldsymbol{\sigma}_{Emn}^S / d\boldsymbol{\varepsilon}_{Sn}$  at the global *Newton* iteration step  $i$ . For  $F_n < 0$ , it corresponds to the fourth order elastic material tensor  $\mathbb{C}_n^S = \mathbb{C}^{Se}$  (4.34).

Elasticity	:	$\mathbf{R}_n^{loc1}$	$= \boldsymbol{\sigma}_{Emn}^S - \mathbb{C}^{Se} \left( \boldsymbol{\varepsilon}_{Sn} - \boldsymbol{\varepsilon}_{Spn-1} - \Delta t \Lambda_n \frac{\partial G_n(\boldsymbol{\sigma}_{Emn}^S, \mathbf{p})}{\partial \boldsymbol{\sigma}_{Emn}^S} \right)$	$= \mathbf{0}$
Visco-plasticity	:	$r_n^{loc2}$	$= \Lambda_n - \frac{1}{\eta} \left\langle \frac{F}{\sigma_0} \right\rangle^r$	$= 0$
Plastic hardening	:	$r_n^{loc2+j}$	$= \frac{p_{jn} - p_{jn-1}}{\Delta t} - p_j^{sat} [C_{p_j}^V (\varepsilon_{vp}^V)'_S + C_{p_j}^D (\varepsilon_{vp}^D)'_S]$	$= 0$

**Table 5.3:** The local system of equations  $\mathbf{R}_n^{loc}$  at the current time iteration step  $n$  and  $i$  denotes the index number  $j = [1 - 4]$  of the hardening parameters  $p_j = \{\beta, \delta, \epsilon, \gamma\}$ .

## 5.2 Parameter identification

For realistic simulations of IBVP, first of all, the physical behaviour of the material used in the investigated IBVP has to be described as well as possible via constitutive equations. By the calibration procedure, the material parameters  $\mathbf{s}$  of the constitutive equations are identified on the basis of experimental data. Therefore, this procedure is also referred to as the indirect problem, while the computation of an IBVP with an already identified parameter set  $\mathbf{s}$  is called the direct problem. From this computation, the stress and the deformation fields of the investigated problem result from the applied boundary conditions. The accuracy of the results depends strongly on the performance of the constitutive equations, i.e., how well they can capture the material behaviour.

The direct problem can be described by the abstract input quantity  $\mathbf{U}$  and the known set of material parameters  $\mathbf{s}$ , while the unknown output quantity  $\Phi$  has to be computed by solving the IBVP. This task of the problem is summarised by the model function  $f$  and can be represented by a compact formulation:

$$\text{Find } \Phi^* \text{ such that } f(\mathbf{s}, \mathbf{U}, \Phi) = 0 \text{ is fulfilled for given } \{\mathbf{s}, \mathbf{U}\}. \quad (5.38)$$

Therein,  $\Phi^*$  denotes the solution of the direct problem for which the model function  $f$  is satisfied. For example, for the simulation of a displacement-controlled triaxial experiment (see Appendix A), the given input quantity  $\mathbf{U}$  is the solid strain  $\epsilon_S$  and the unknown output quantity  $\Phi$  is the solid stress  $\sigma^S$ , whereas the parameter set  $\mathbf{s}$  is known. With regard to the identification process of  $\mathbf{s}$ , the indirect problem has to be solved:

$$\text{Find } \mathbf{s}^* \text{ such that } f(\mathbf{s}, \mathbf{U}, \Phi) = 0 \text{ is fulfilled for given } \{\mathbf{U}, \Phi\}. \quad (5.39)$$

In this case, the quantities  $\mathbf{U}$  and  $\Phi$  are obtained by the experiment. Thus, the parameter set  $\mathbf{s}^*$  has to be found by an inverse computation of the experiment at which the model function  $f$  is satisfied. Regarding to the simulation example of the aforementioned triaxial experiment, the solid strain  $\epsilon_S$  is known as the controlled quantity of  $\mathbf{U}$  as well as the solid stress  $\sigma^S$  as the measured quantity of  $\Phi$ . Generally, a complex material behaviour exhibits a non-linear stress-strain relation. Hence, the material parameters  $\mathbf{s}$  have to be identified in the fashion that the error  $I_n = |\Phi_n(\mathbf{s}) - \tilde{\Phi}_n|$  at each discrete data point  $n$  of  $N$  (number of data points) between output quantities of simulation  $\Phi_n(\mathbf{s})$  and experiment  $\tilde{\Phi}_n$  is minimised as good as possible. To compute the error  $I_n$  at the discrete data point  $n$ , the same input quantity  $U_n$  has to be used for both simulation and experiment, whereas, treating rate-dependent problems, the time variable has to be also taken into account.

However, complex material behaviour represented by non-linear stress-strain relations is described via a variety of material parameters. These parameters cannot be directly determined by an independent set of experiments. Therefore, the indirect problem can only be solved by applying non-linear optimisation methods. This is carried out by an ongoing improvement of the parameter set  $\mathbf{s}_i \rightarrow \mathbf{s}^*$  until the simulation error satisfies a user-defined error tolerance, where  $i$  denotes the iteration steps. Hence, the identification process should be started with well fitted initial values of the material parameters  $\mathbf{s}_0$  in order to reduce the number of iterations until the solution  $\mathbf{s}^*$  is reached.

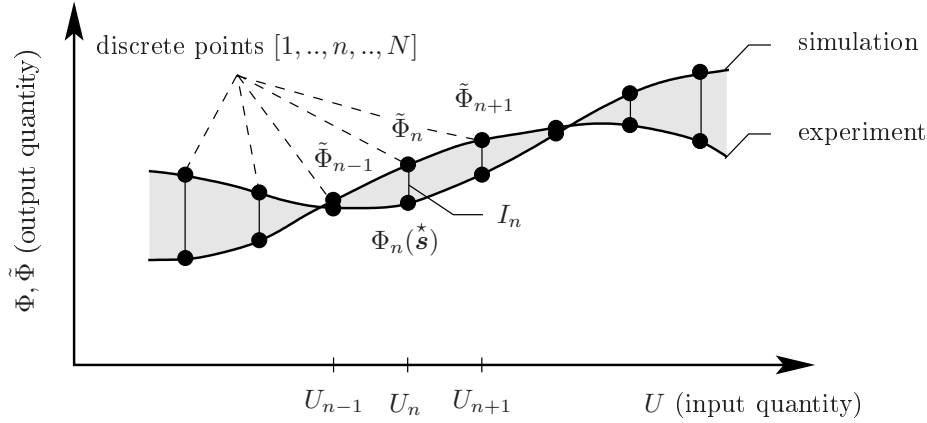


**Figure 5.1:** Comparison of the simulated and experimental data set, where  $I_n$  is the error between the output quantities  $|\Phi_n - \tilde{\Phi}_n|$  determined at each discrete point of  $n$  for given  $U_n$ .

The simplest material law is the 1-dimensional *Hookean* law describing an elastic behaviour. The identification of the constant elastic moduli  $E^S$  is determined directly from the linear part of the stress-strain curve of a 1-d tension test via  $E^S = \Delta\sigma_1/\Delta\varepsilon_1$ . In contrast, due to the high number of parameters of more complex materials, the optimisation problem is over-determined and the parameters cannot be uniquely identified. By this reason, the *Least-Squares Method* is applied, which minimises the object function  $f$  representing the total simulation error. The object function  $f$  is computed by the squared differences between the simulated and the true material behaviour, where the true material behaviour is determined by experiments. In general, for a good approximation of the material behaviour, various experimental data sets with different measured quantities have to be taken into account. Therefore, a multi-criterion object function has to be applied,

$$f(\mathbf{s}) = \frac{1}{2} \sum_{k=1}^K \sum_{n=1}^{N_k} w_n^k \left( \Phi_n^k(\mathbf{s}) - \tilde{\Phi}_n^k \right)^2 \rightarrow \min., \quad (5.40)$$

where  $\quad : \quad w_n^k = \frac{1}{|\Phi_0^k| N_k},$

wherein all computation errors  $I_n$  are summarised. Therein,  $w_n^k$  is a weighting factor, which is used for the normalisation of the output quantities  $\Phi_n^k$  and  $\tilde{\Phi}_n^k$ . If  $w_n^k$  is assumed to be constant for all data points  $N_k$  of the considered experimental data set  $K$ , it can also be rewritten to  $w^k$ . Hence,  $w^k$  is determined by the inverse of the maximally measured value  $|\Phi_0^k|$  of the data set  $K$  as well as the number of data points  $N_k$ . The optimisation parameters  $\mathbf{s}$  of the constitutive equations, which governs the material responds  $\Phi(\mathbf{s})$ , have to be calibrated within a physical range. Therefore, the feasible range of  $\mathbf{s}$  is represented by the equality and inequality constraints and leads to the following constrained non-linear

optimisation problem:

$$\begin{aligned} f(\mathbf{s}) &\rightarrow \min && : \text{ object function ,} \\ h_j(\mathbf{s}) &= 0 && ; \quad j = 1, \dots, N_{eq} : \text{ equality constraints ,} \\ g_i(\mathbf{s}) &\leq 0 && ; \quad i = 1, \dots, N_{iq} : \text{ inequality constraints ,} \end{aligned} \quad (5.41)$$

where  $N_{eq}$  and  $N_{iq}$  denote the number of equality and inequality equations.

### 5.2.1 Gradient-based optimisation procedure

To solve the unconstrained problem in (5.40) by applying gradient-based methods, the value of the object function  $f$  decreases at each iteration step with an improved parameter set  $\mathbf{s}_{i+1}$  with regard to the previous set  $\mathbf{s}_i$

$$f(\mathbf{s}_{i+1}) < f(\mathbf{s}_i). \quad (5.42)$$

The deepest extremal point of  $f$  is found at which the gradient of  $f$  vanishes with respect to the material parameter set  $\mathbf{s}$ ,

$$\frac{df(\mathbf{s})}{d\mathbf{s}} = \sum_{k=1}^K \sum_{n=1}^{N_k} w^k \frac{d\Phi_n^k(\mathbf{s})}{d\mathbf{s}} (\Phi_n^k(\mathbf{s}) - \tilde{\Phi}_n^k) \stackrel{!}{=} \mathbf{0}, \quad (5.43)$$

wherein the components of  $d\Phi_n^k(\mathbf{s})/d\mathbf{s}$  are commonly denoted as the sensitivities of  $\Phi_n^k$ . This point is characterised by the extremal (final) parameter set  $\mathbf{s}^*$ . The non-linear problem in (5.43) is solved by applying the *Newton* method with the iteration procedure

$$\mathbf{s}_{i+1} = \mathbf{s}_i + \alpha \mathbf{n}_i \quad \text{where} \quad \mathbf{n}_i = -\mathbf{H}_i^{-1} \frac{df(\mathbf{s})}{d\mathbf{s}_i} \quad (5.44)$$

is the descent of  $f$  in the direction of the local minimum, and  $\alpha$  is the step-length parameter of the line-search algorithm. The parameter  $\alpha$  has to be chosen in such a way that the best new parameter set  $\mathbf{s}_{i+1}$  is obtained for which  $f$  decreases as steep as possible, e.g., applying the *Armijo-Goldstein* criterion, cf. Dennis and Goldstein [36]. For constrained non-linear problems, care has to be taken that  $\mathbf{s}_{i+1}$  is located within feasible limits. Furthermore,  $\mathbf{H}$  is the *Hessian* matrix of the *Newton* method and represents the second derivative of  $f$ :

$$\mathbf{H} = \mathbf{H}^N = \frac{d^2 f(\mathbf{s})}{d\mathbf{s} d\mathbf{s}^T}. \quad (5.45)$$

Due to  $\mathbf{H}^N$  which is not always positive definite, the direction of the line search is not always oriented to the steepest descent of  $f$  and, beyond that, the computation of the second gradient is very time consuming. Therefore, *Quasi-Newton* methods are commonly applied, because they approximate the *Hessian* matrix  $\mathbf{H} \approx \bar{\mathbf{H}}$  in a linear fashion only using the first gradient of  $f$ . An overview of some popular iteration matrices is given in Table 5.4. However, the BFGS (*Broyden, Fletcher, Goldfarb, Shanno*) method is one

Iteration matrices	
Steepest descent:	$\bar{\mathbf{H}}_i = \mathbf{I}$
Gauss-Newton:	$\bar{\mathbf{H}}_i := \mathbf{H}_i^{GN} = \frac{d^2 f(\mathbf{s})}{d\mathbf{s} d\mathbf{s}^T}$
Levenberg-Marquardt:	$\bar{\mathbf{H}}_i := \mathbf{H}_i^{LM} = \mathbf{H}^{GN} + \mu \mathbf{I}$
BFGS:	$\bar{\mathbf{H}}_i := \mathbf{H}_i^{BFGS}$

**Table 5.4:** Overview of the best-knowing approximation matrices of  $\mathbf{H}_i$ .

of the mostly used and as well efficient methods. The update procedure of the BFGS method is given by

$$\mathbf{H}_{i+1}^{BFGS} = \bar{\mathbf{H}}_{i+1} = \bar{\mathbf{H}}_i + \frac{\mathbf{q}_i \mathbf{q}_i^T}{\mathbf{q}_i^T \mathbf{p}_i} - \frac{\bar{\mathbf{H}}_i \mathbf{p}_i \mathbf{p}_i^T \bar{\mathbf{H}}_i}{\mathbf{p}_i^T \bar{\mathbf{H}}_i \mathbf{p}_i}, \quad (5.46)$$

where  $\mathbf{p}_i = \mathbf{s}_{i+1} - \mathbf{s}_i$  and  $\mathbf{q}_i = \frac{df(\mathbf{s}_{i+1})}{d\mathbf{s}_{i+1}} - \frac{df(\mathbf{s}_i)}{d\mathbf{s}_i}$

are the update vectors of the optimisation parameters and the gradients of the object function  $f$ . However, the  $\mathbf{H}^{BFGS}$  matrix needs an initial value. From the numerical point of view, it is suitable to choose initial values in a such way that the  $\mathbf{H}^{BFGS}$  matrix is symmetric and positive definite. For example, the method of the steepest descent can be applied as the starting matrix  $\mathbf{H}_0^{BFGS} = \mathbf{I}$ . The update of  $\mathbf{H}_{i+1}^{BFGS}$  in (5.46) is carried out after the new parameter set  $\mathbf{s}_{i+1}$  in (5.44) has been solved.

### 5.2.2 Lagrangean dual problem (SQP method)

The constrained non-linear problem (5.41) is commonly solved by a very efficient and popular *Lagrangean* procedure. Thereby, the constrained optimisation problem is transferred into a dual problem by introducing the *Lagrange* multipliers or *dual* variables of the equality and inequality constraints,  $\mu_j$  and  $\lambda_i$ , respectively, cf. [8, 17, 109, 129, 147]. Thus, the *Lagrange* function of the non-linear optimisation problem in (5.41) reads

$$\mathcal{L}(\mathbf{s}, \boldsymbol{\mu}, \boldsymbol{\lambda}) = f(\mathbf{s}) + \sum_{j=1}^{N_{eq}} \mu_j h_j(\mathbf{s}) + \sum_{i=1}^{N_{iq}} \lambda_i g_i(\mathbf{s}) \rightarrow \text{stat.} \quad (5.47)$$

Hereby, the optimisation problem is switched from a minimisation to an extremal problem, which is characterised by a saddle-point or stationary (stat.) problem, respectively. The saddle point defines the optimum solution at which a variation of the primary variable  $\mathbf{s}$  with fixed *dual* variables  $\boldsymbol{\mu}^*$  and  $\boldsymbol{\lambda}^*$  minimises  $f$ , while, vice versa, with fixed  $\mathbf{s}^*$  parameters and a variation of  $\boldsymbol{\mu}$  and  $\boldsymbol{\lambda}$ ,  $f$  is maximised, cf. Mahnken [110]. Nevertheless, the optimum solution  $\mathbf{s}^*$  of the saddle point problem is equivalent to the optimal solution point of the

primary optimisation problem (5.41), cf. Spellucci [147]. For the validity of the solution of (5.47), the optimised parameter set  $\{\mathbf{s}^*, \boldsymbol{\mu}^*, \boldsymbol{\lambda}^*\}$  has to fulfil the *necessary condition* of the so-called *Karush-Kuhn-Tucker* (KKT) condition:

$$\begin{aligned} \frac{d\mathcal{L}}{d\mathbf{s}} &= \frac{df(\mathbf{s}^*)}{d\mathbf{s}} + \sum_{j=1}^{N_{eq}} \mu_j^* \frac{dh_j(\mathbf{s}^*)}{d\mathbf{s}} + \sum_{i=1}^{N_{iq}} \lambda_i^* \frac{dg_i(\mathbf{s}^*)}{d\mathbf{s}} = \mathbf{0}, \\ h_j(\mathbf{s}^*) &= 0, \quad g_i(\mathbf{s}^*) \leq 0, \quad \lambda_i^* \geq 0, \quad \lambda_i^* g_i(\mathbf{s}^*) = 0. \end{aligned} \quad (5.48)$$

Therein, the first equation (5.48)<sub>1</sub> is the *Lagrangean* condition, (5.48)<sub>2,3</sub> are the primal admissibilities, while (5.48)<sub>4</sub> is the dual admissibility, and (5.48)<sub>5</sub> is the complementary condition, cf. Mahnken [110].

Moreover, the *sufficient condition* demands that  $\mathcal{L}$  is convex at the local minimum. Hence, the *Hessian* matrix, which is the second derivative of  $\mathcal{L}$  with respect to  $\mathbf{s}$ , must be positive definite at the solution point

$$\mathbf{v}^T \frac{d^2\mathcal{L}(\mathbf{s}^*, \boldsymbol{\mu}^*, \boldsymbol{\lambda}^*)}{d\mathbf{s} d\mathbf{s}^T} \mathbf{v} > 0, \quad (5.49)$$

where  $\mathbf{v} \neq \mathbf{0}$  is an arbitrary vector of the same dimension as  $\mathbf{s}$ .

### SQP Algorithm

Instead of computing directly the *Lagrangean* problem in (5.48), quadratic subproblems of  $\mathcal{L}$  (5.47) can be solved. These quadratic subproblems resulting from the quadratic approximation of the non-linear *Lagrangean* problem can be computed in a more efficient fashion using the *Sequential-Quadratic-Programming* (SQP) method, cf. Schittkowski [135], Boggs and Tolle [17] and Spellucci [148]. Proceeding from the SQP method, the *Lagrange* function

$$\tilde{\mathcal{L}}(\mathbf{s}, \boldsymbol{\mu}, \boldsymbol{\lambda}) = \tilde{f}(\mathbf{s}) + \boldsymbol{\mu}^T \tilde{\mathbf{h}}(\mathbf{s}) + \boldsymbol{\lambda}^T \tilde{\mathbf{g}}(\mathbf{s}) \rightarrow \text{stat.} \quad (5.50)$$

is defined by quadratic and linear approximations of the object function and the constraint equations, respectively:

$$\begin{aligned} \tilde{f}(\mathbf{s}) &= f(\mathbf{s}) + \frac{df(\mathbf{s})}{d\mathbf{s}} \Delta\mathbf{s} + \frac{1}{2} \Delta\mathbf{s}^T \frac{d^2\mathcal{L}(\boldsymbol{\mu}, \boldsymbol{\lambda}, \mathbf{s})}{d\mathbf{s} d\mathbf{s}^T} \Delta\mathbf{s} \rightarrow \min., \\ \tilde{\mathbf{h}}(\mathbf{s}) &= \mathbf{h}(\mathbf{s}) + \frac{d\mathbf{h}(\mathbf{s})}{d\mathbf{s}} \Delta\mathbf{s} = \mathbf{0}, \\ \tilde{\mathbf{g}}(\mathbf{s}) &= \mathbf{g}(\mathbf{s}) + \frac{d\mathbf{g}(\mathbf{s})}{d\mathbf{s}} \Delta\mathbf{s} \leq \mathbf{0}, \end{aligned} \quad (5.51)$$

where the KKT-conditions of  $\tilde{\mathcal{L}}$  are summarised in  $\mathbf{F}$ :

$$\mathbf{F}(\mathbf{x}) = \frac{d\tilde{\mathcal{L}}}{d\mathbf{x}} = \begin{bmatrix} \frac{d\tilde{f}(\mathbf{s})}{d\mathbf{s}} + \boldsymbol{\mu}^T \frac{d\tilde{\mathbf{h}}(\mathbf{s})}{d\mathbf{s}} + \boldsymbol{\lambda}^T \frac{d\tilde{\mathbf{g}}(\mathbf{s})}{d\mathbf{s}} \\ \tilde{\mathbf{h}}(\mathbf{s}) \\ \tilde{\mathbf{g}}_{\mathbf{W}}(\mathbf{s}) \end{bmatrix} = \begin{bmatrix} \mathbf{0} \\ \mathbf{0} \\ \mathbf{0} \end{bmatrix}. \quad (5.52)$$

Therein,  $\mathbf{x}$  represents the unknown set of the optimisation variables  $\mathbf{x} = [\mathbf{s}^T, \boldsymbol{\mu}^T, \boldsymbol{\lambda}_{\mathcal{W}}^T]^T$ . For an efficient computation of  $\mathbf{F}(\mathbf{x})$ , the *Active Set* strategy is introduced. Thereby, only the inequality constraints with  $\tilde{g}_{i\mathcal{W}} = 0$  are incorporated into the *Active Set* or working set  $\mathcal{W}$ , whereas the computation of the inactive constraints  $\tilde{g}_i < 0$  are redundant, cf. Schnittkowski [135]. Hence, the constraint optimisation problem with inequality conditions is transferred to a non-linear system of equality equations. Accordingly,  $\lambda_{i\mathcal{W}}$  are the *Lagrangean* multipliers of the active set  $\mathcal{W}$ . However, starting the computation with an initial active set  $\mathcal{W}_0$  corresponding to the initial parameter set  $\mathbf{s}_0$ ,  $\mathbf{F}$  in (5.52) can be simply solved in a sequential fashion by the *Newton* method:

$$\begin{aligned} \mathbf{F}(\mathbf{x}_i) + \frac{d\mathbf{F}(\mathbf{x}_n)}{d\mathbf{x}} \Delta\mathbf{x}_n &= \mathbf{0} \\ \text{with } \mathbf{x}_n &= [\Delta\mathbf{s}_n^T, \Delta\boldsymbol{\mu}_n^T, \Delta\boldsymbol{\lambda}_{\mathcal{W}_n}^T]^T \\ &= [(\mathbf{s}_{n+1} - \mathbf{s}_n)^T, (\boldsymbol{\mu}_{n+1} - \boldsymbol{\mu}_n)^T, (\boldsymbol{\lambda}_{\mathcal{W}_{n+1}} - \boldsymbol{\lambda}_{\mathcal{W}_n})^T]^T, \end{aligned} \quad (5.53)$$

where the solution increment  $\Delta\mathbf{s} = \mathbf{n}$  of the quadratic subproblem is the new line-search direction of the improved parameter set  $\mathbf{s}_{n+1} = \mathbf{s}_n + \alpha\Delta\mathbf{s}$ , cf. (5.44). The steplength  $\alpha$  is computed in the fashion that  $\mathbf{s}_{n+1}$  is still located in the feasible set, cf. [8, 109, 129]. The *Newton* iteration in (5.53) is finished if the user-defined error tolerance is satisfied,  $\|\Delta\mathbf{s}_n\| < \text{tol}$ , and the KKT conditions in (5.48) of the *Lagrange* problem or (5.52) of the SQP problem, respectively, are fulfilled. Otherwise, the violated inequality constraint has to be put into the new active set  $\mathcal{W}^{n+1}$ . However, if one or more of *Lagrangean* multipliers  $\lambda_{i\mathcal{W}_n}$  of the actual inequality constraint are negative, the corresponding inequality constraint with the least negative value of  $\lambda_{i\mathcal{W}_n}^{\min} < 0$  has to be removed from the active set  $\mathcal{W}^n$  and the *Newton* iteration step is repeated, cf. [110, 112, 133].

Furthermore, the computation of  $d\mathbf{F}(\mathbf{x})/d\mathbf{x}$  in (5.53),

$$\frac{d\mathbf{F}(\mathbf{x})}{d\mathbf{x}} = \frac{d^2\tilde{\mathcal{L}}}{d\mathbf{x}d\mathbf{x}^T} = \begin{bmatrix} \frac{d^2\tilde{\mathcal{L}}}{d\mathbf{s}d\mathbf{s}^T} & \frac{d\tilde{\mathbf{h}}(\mathbf{s})}{d\mathbf{s}} & \frac{d\tilde{\mathbf{g}}_{\mathcal{W}}(\mathbf{s})}{d\mathbf{s}} \\ \frac{d\tilde{\mathbf{h}}(\mathbf{s})}{d\mathbf{s}} & \mathbf{0} & \mathbf{0} \\ \frac{d\tilde{\mathbf{g}}_{\mathcal{W}}(\mathbf{s})}{d\mathbf{s}} & \mathbf{0} & \mathbf{0} \end{bmatrix}, \quad (5.54)$$

may have difficulties concerning the Hessian matrix  $d^2\tilde{\mathcal{L}}/(d\mathbf{s}d\mathbf{s}^T) \approx \bar{\mathbf{H}}$ , which is not generally positive definite. To overcome this problem, the Hessian matrix is approximated by *Quasi-Newton* methods given in Table 5.4, where the BFGS method is preferred in this thesis. Accordingly, in this case, the solution parameters of the BFGS iteration have the following expressions:  $\mathbf{p}_i = \mathbf{s}_{i+1} - \mathbf{s}_i$  and  $\mathbf{q}_i = d\tilde{\mathcal{L}}(\mathbf{s}_{i+1})/d\mathbf{s} - d\tilde{\mathcal{L}}(\mathbf{s}_i)/d\mathbf{s}$ .

### 5.2.3 Numerical sensitivity analysis

In this thesis, only the mechanical behaviour of sand is calibrated by use of the gradient-based optimisation method. For the computation of the required gradient of the object



function  $df/ds$  (5.43), which maintains the sensitivities of the simulated quantities  $\Phi(\mathbf{s})$  with respect to the material parameters  $\mathbf{s}$ , the *momentum balance* of the overall aggregate has to be taken into consideration. Following the experimental investigation of the mechanical behaviour of dry sand with vacant pore spaces<sup>‡</sup> via drained triaxial tests, the fluid pressure  $p^{FR} = 0$  can be neglected ( $\boldsymbol{\sigma} \approx \boldsymbol{\sigma}_E^S$ ) and the *momentum balance* of the biphasic model is reduced to the expression of a single phase material, Ehlers and Avcı [56]. Proceeding from this, the derivation of  $\mathcal{G}_{MM}$  (5.2) with respect to  $\mathbf{s}$  yields

$$\frac{d\mathcal{G}_{MM}(\mathbf{s}, \boldsymbol{\varepsilon}_S(\mathbf{s}))}{ds_i} = \int_{\Omega} \frac{d\boldsymbol{\sigma}_E^S}{ds_i} \cdot \text{grad } \delta \mathbf{u}_S dv \stackrel{!}{=} 0. \quad (5.55)$$

Therein, the sensitivities of the solid stress  $\boldsymbol{\sigma}_E^S$  to  $\mathbf{s}$  are the quantities, which have to be determined, whereas  $\boldsymbol{\sigma}_E^S$  depends on the constitutive equations governed by the material parameters as well as by the solid strain, which, in turn, depends (implicitly) on the material parameters, too. An implicit derivation of the stress sensitivities reads

$$\frac{d\boldsymbol{\sigma}_E^S}{ds_i} = \frac{\partial \boldsymbol{\sigma}_E^S}{\partial s_i} + \frac{\partial \boldsymbol{\sigma}_E^S}{\partial \boldsymbol{\varepsilon}_S} \frac{d\boldsymbol{\varepsilon}_S}{ds_i}, \quad \text{where} \quad \frac{d\boldsymbol{\varepsilon}_S}{ds_i} = \sum_{j=1}^{N_{\mathbf{u}_S}} \text{grad } \phi_{\mathbf{u}_S}^j \frac{d\mathbf{u}_{Sj}}{ds_i} \quad (5.56)$$

are the sensitivities of the solid strain  $\boldsymbol{\varepsilon}_S$ . Inserting (5.56)<sub>1</sub> into (5.55), a linear system of equation yields

$$\int_{\Omega} \frac{\partial \boldsymbol{\sigma}_E^S}{\partial \boldsymbol{\varepsilon}_S} \frac{d\boldsymbol{\varepsilon}_S}{ds_i} \cdot \text{grad } \delta \mathbf{u}_S dv = - \int_{\Omega} \frac{\partial \boldsymbol{\sigma}_E^S}{\partial s_i} \cdot \text{grad } \delta \mathbf{u}_S dv, \quad (5.57)$$

which can be expressed in a compact form within a time iteration step  $n$ :

$$\mathbf{K}_n \frac{d\mathbf{u}_{Sn}}{ds_i} = -\mathbf{f}_{ni}^s. \quad (5.58)$$

Therein, the term  $\mathbf{K}_n$  is equivalent to the consistent material tangent or the Jacobian matrix, which is already solved for the global system of equation in Table 5.1, while the second term is the solution vector of the unknown sensitivity of the displacement  $d\mathbf{u}_{Sn}/ds_i$  and the right-hand side of (5.58) is the so-called global sensitivity load term  $\mathbf{f}_{ni}^s$ .

The presented sensitivity analysis follows the work by Ehlers and Scholz [67] or Scholz [137]. Based on the *Cosserat*-continuum theory, they have additionally taken the *balance of moment of momentum* into account in order to compute the sensitivities of micropolar parameters (*Cosserat* parameters) controlling the properties of the grain rotations occurring during the localisation of shear bands.

### Computation of $\mathbf{f}_{ni}^s$

The load term  $\mathbf{f}_n^s$  consisting of sensitivities of the solid stress  $\partial \boldsymbol{\sigma}_{En}^S / \partial s_i = d\boldsymbol{\sigma}_E^S / ds_i|_{\mathbf{u}_{Sn}}$  is evaluated at the fixed deformation state ( $\mathbf{u}_{Sn} = \text{const.}$ ) at time step  $n$ . Its computation

---

<sup>‡</sup>For saturated soil (e. g. with air), the triphasic model is reduced to the biphasic model by eliminating the pore water phase  $\varphi^W$ . Thus, the pore-fluid pressure corresponds to the pore-air pressure,  $p^{FR} := p^{AR}$ .

is carried out using the local set of equations  $\mathbf{R}^{loc}$  given in Table 5.3,

$$\mathbf{R}^{loc} = \mathbf{R}^{loc}[\mathbf{s}, \boldsymbol{\sigma}_{En}^S(\mathbf{s}), \mathbf{p}_n(\mathbf{s}), \mathbf{p}_{n-1}(\mathbf{s}), \lambda_n, \boldsymbol{\varepsilon}_{Spn-1}(\mathbf{s})] \equiv \mathbf{0}, \quad (5.59)$$

in consideration of the internal and hardening dependencies,  $\mathbf{q} = [\lambda, \boldsymbol{\varepsilon}_{Sp}]^T$  and  $\mathbf{p} = [\beta, \delta, \epsilon, \gamma]^T$ . By derivation of (5.59) with respect to  $\mathbf{s}$  and to the implicit dependencies, the local system of equations yields

$$\begin{aligned} \left. \frac{d\mathbf{R}_n^{loc}}{d\mathbf{s}} \right|_{\boldsymbol{\varepsilon}_{Sn}} &= \frac{\partial \mathbf{R}_n^{loc}}{\partial \mathbf{s}} + \frac{\partial \mathbf{R}_n^{loc}}{\partial \boldsymbol{\sigma}_{En}^S} \left. \frac{d\boldsymbol{\sigma}_{En}^S}{d\mathbf{s}} \right|_{\boldsymbol{\varepsilon}_{Sn}} + \frac{\partial \mathbf{R}_n^{loc}}{\partial \mathbf{p}_n} \left. \frac{d\mathbf{p}_n}{d\mathbf{s}} \right|_{\boldsymbol{\varepsilon}_{Sn}} + \frac{\partial \mathbf{R}_n^{loc}}{\partial \mathbf{p}_{n-1}} \left. \frac{d\mathbf{p}_{n-1}}{d\mathbf{s}} \right|_{\boldsymbol{\varepsilon}_{Sn}} + \\ &+ \frac{\partial \mathbf{R}_n^{loc}}{\partial \Lambda_n} \left. \frac{d\Lambda_n}{d\mathbf{s}} \right|_{\boldsymbol{\varepsilon}_{Sn}} + \frac{\partial \mathbf{R}_n^{loc}}{\partial \boldsymbol{\varepsilon}_{Spn-1}} \left. \frac{d\boldsymbol{\varepsilon}_{Spn-1}}{d\mathbf{s}} \right|_{\boldsymbol{\varepsilon}_{Sn}} \stackrel{!}{=} \mathbf{0} \end{aligned} \quad (5.60)$$

Introducing the generalised stress vector  $\boldsymbol{\Sigma}_n = [\boldsymbol{\sigma}_{En}^S, \Lambda_n, \mathbf{p}_n^T]^T$ , the linear system of equations (5.60) is solved by

$$\left. \frac{d\boldsymbol{\Sigma}_n}{d\mathbf{s}} \right|_{\boldsymbol{\varepsilon}_{Sn}} = - \left( \frac{\partial \mathbf{R}_n^{loc}}{\partial \boldsymbol{\Sigma}_n} \right)^{-1} \left( \frac{\partial \mathbf{R}_n^{loc}}{\partial \mathbf{s}} + \frac{\partial \mathbf{R}_n^{loc}}{\partial \mathbf{p}_{n-1}} \left. \frac{d\mathbf{p}_{n-1}}{d\mathbf{s}} \right|_{\boldsymbol{\varepsilon}_{Sn}} + \frac{\partial \mathbf{R}_n^{loc}}{\partial \boldsymbol{\varepsilon}_{Spn-1}} \left. \frac{d\boldsymbol{\varepsilon}_{Spn-1}}{d\mathbf{s}} \right|_{\boldsymbol{\varepsilon}_{Sn}} \right) \quad (5.61)$$

at the *Gauss* point. Therein, the generalised right-side vector term is summarised by the already known expressions  $\partial \mathbf{R}_n^{loc} / \partial \mathbf{s}$  and the sensitivities of the internal and the hardening parameters  $\boldsymbol{\varepsilon}_{Spn-1}$  and  $\mathbf{p}_{n-1}$  of the last time step  $n-1$ . The generalised stiffness matrix is  $\partial \mathbf{R}_n^{loc} / \partial \boldsymbol{\Sigma}_n$ , and the unknown solution vector term of the sensitivities is  $d\boldsymbol{\Sigma}_n / d\mathbf{s}$ . Hence, the sensitivity of the load term can be determined by taking  $\partial \boldsymbol{\sigma}_{En}^S / \partial \mathbf{s}$  from the solution vector and inserting in (5.57) or (5.58), respectively.

### Sensitivities of the solid stress, hardening parameters and plastic multiplier

The computation of the sensitivities of  $\boldsymbol{\Sigma}_n = \boldsymbol{\Sigma}_n(\mathbf{s}, \boldsymbol{\varepsilon}_S(\mathbf{s}))$  follows the same procedure as has already been shown in the incorporation of the implicit derivations. Thereby, the total derivative of  $\boldsymbol{\Sigma}_n$  relative to  $\mathbf{s}$  is composed by the partial derivatives,

$$\frac{d\boldsymbol{\Sigma}_n}{d\mathbf{s}} = \frac{\partial \boldsymbol{\Sigma}_n}{\partial \mathbf{s}} + \frac{\partial \boldsymbol{\Sigma}_n}{\partial \boldsymbol{\varepsilon}_{Sn}} \frac{d\boldsymbol{\varepsilon}_{Sn}}{d\mathbf{s}}, \quad (5.62)$$

wherein  $\partial \boldsymbol{\Sigma}_n / \partial \mathbf{s}$  is taken from the solution of (5.61) and  $d\boldsymbol{\varepsilon}_{Sn} / d\mathbf{s}$  is known from (5.56). The derivatives  $\partial \boldsymbol{\Sigma}_n / \partial \boldsymbol{\varepsilon}_{Sn}$  are already determined by solving the system of equations in (5.37).

### Sensitivities of the internal variables

Applying the temporal discretisation of  $(\boldsymbol{\varepsilon}_{Spn})'_S = \Delta \boldsymbol{\varepsilon}_{Spn} / \Delta t_n = (\boldsymbol{\varepsilon}_{Spn} - \boldsymbol{\varepsilon}_{Spn-1}) / \Delta t_n$ , the sensitivities of  $\boldsymbol{\varepsilon}_{Spn}$  are computed by

$$\frac{d\boldsymbol{\varepsilon}_{Spn}}{d\mathbf{s}} = \frac{d\boldsymbol{\varepsilon}_{Spn-1}}{d\mathbf{s}} + \frac{d\Delta \boldsymbol{\varepsilon}_{Spn}}{d\mathbf{s}}, \quad (5.63)$$

where  $d\Delta\boldsymbol{\varepsilon}_{Spn}/d\mathbf{s}$  is the incremental increase of the sensitivities. Due to the time-dependent history, the variables  $\boldsymbol{\varepsilon}_{Spn}$  are governed by the hardening parameters  $\mathbf{p}_n$ ; the dependencies  $\boldsymbol{\varepsilon}_{Spn} = \boldsymbol{\varepsilon}_{Spn}(\mathbf{s}, \mathbf{p}_n(\mathbf{s}))$  have to be taken into account for the computation of the sensitivities of  $\boldsymbol{\varepsilon}_{Spn}$ . Performing the total derivatives to  $\mathbf{s}$  with regard to the implicit dependencies, the sensitivities of  $\Delta\boldsymbol{\varepsilon}_{Spn}$  result in

$$\frac{d\Delta\boldsymbol{\varepsilon}_{Spn}}{d\mathbf{s}} = \frac{\partial\Delta\boldsymbol{\varepsilon}_{Spn}}{\partial\mathbf{s}} + \frac{\partial\boldsymbol{\varepsilon}_{Spn}}{\partial\mathbf{p}_n} \frac{d\mathbf{p}_n}{d\mathbf{s}}. \quad (5.64)$$

Finally, the solutions  $d\boldsymbol{\varepsilon}_{Spn}/d\mathbf{s}$  in (5.63) and  $d\boldsymbol{\Sigma}_n/d\mathbf{s}$  in (5.62) are inserted into the right-hand-side vector of (5.61) as known quantities of the last time step for the computation of the sensitivities of the new time step  $n = n + 1$ . Hence, the searched sensitivities  $\partial\boldsymbol{\sigma}_{En}^S/\partial\mathbf{s}$  can be taken out from the new solution  $d\boldsymbol{\Sigma}_n/d\mathbf{s}$ .



## Chapter 6:

# Calibration of the Partially Saturated Soil Model

In this Chapter, the calibration and validation process of the partially saturated soil model is presented. Based on the *principle of phase separation* (Ehlers [47]), cf. Chapter 4, the elasto-viscoplastic material model of the solid skeleton is fitted to results from dry sand triaxial experiments using the optimisation procedure presented in Section 5.2. The validation of the calibrated model is performed by the computation of small-scale foundation- and slope-failure experiments carried out on dry sand. Based on these experiments, the performance of the new failure concept with a variable failure surface (Section 4.2.2) is compared with the old failure concept with a constant failure surface. On the other hand, the motion of the pore fluids is identified on deformation-free hydraulic conductivity experiments. Then, the coupled processes of soil deformation and the fluid motion of the partially saturated soil model is numerically validated by simulation of technical-scale slope failure experiments by varying the hydraulic as well as the mechanical loading conditions. These slope failure scenarios have been experimentally investigated by Germer and Braun [77]. However, by the reason of strong variations of the experimental results, the reproducibility of the experimental results is not yet ensured and is still an ongoing process of research. Therefore, only numerical investigations of the slope failure scenarios are presented in this contribution.

**Remark:** The presented results in this Chapter elaborated in the framework of this thesis have been already published in the papers Ehlers and Avcı [56] and Ehlers et al. [57].

## 6.1 Mechanical behaviour of dry sand

The elasto-viscoplastic model under consideration is governed by 30 material parameters to be found from experimental data. Apart from the 4 parameters of the elastic part (4.32) of the model, the viscoplastic part contains 26 parameters, where 7 (included in  $\mathbf{S}_H$  and  $\mathbf{S}_D$ ) belong to the basic yield condition  $F(\boldsymbol{\sigma}_E^S, \mathbf{p})$  with 4 of them ( $\mathbf{p} = [\beta, \delta, \epsilon, \gamma]^T$ ) following the hardening/softening law (4.48) yielding 3 further parameters each. In addition, the plastic potential  $G(\boldsymbol{\sigma}_E^S, \mathbf{p})$  requires 2 ( $\psi_1, \psi_2$ ) and the viscoplastic evolution (4.41) 3 ( $\eta, r, \sigma_0$ ) additional parameters, while the new failure concept with variable failure surface (4.49) is based on only 2 ( $\bar{C}_\epsilon^*, \bar{\epsilon}_{lim}^*$ ) additional parameters.

The identification of the involved material parameters is carried out in two basic steps. Firstly, the 4 parameters of the elastic part of the model are determined from loading and unloading loops of both the triaxial compression and hydrostatic experiments. Secondly, the remaining 26 parameters governing the plastic behaviour have to be identified by a rather complex procedure. This procedure starts with a rough identification of the

parameters ‘by guess’ in order to receive a good initial parameter set for the numerical optimisation process. During this process, several types of experiments are considered, such as monotonically loaded compression and hydrostatic tests as well as stress-path-depending ones. Moreover, some of the parameters can be fixed during the numerical optimisation procedure such that the number of the parameters to be determined reduces to only 14. The final set of parameters is then found on the basis of monotonically loaded experiments by applying a numerical optimisation strategy.

### 6.1.1 Calibration of the elasto-viscoplastic model

The triaxial experiments have been carried out with drained conditions and slow loading velocities (quasi-static conditions). Thereby, pore pressure cannot be developed within the specimen,  $p^{FR} \approx 0$ . As a result, the effective mechanical solid stresses correspond to the total mechanical solid stress as well as to the total stress,  $\sigma_{Em}^S \equiv \sigma^S \equiv \sigma$ . In regard of the discussion of the drained triaxial experiments in Chapter 3, no difference between the total and the effective mechanical solid stresses has to be made, e. g.,  $\sigma_1 := \sigma_{E1m}^S$ , cf. Appendix A.

#### Identification of elastic parameters

Cohesionless granular material like dry sand can only carry shear loads via frictional forces between the grains, which therefore have to be under a permanent confining pressure. Furthermore, starting a loading procedure from a fully unloaded state, the material immediately behaves elasto-plastically without a purely elastic domain. Only after preloading, an elastic domain can be recognised.

From loading/unloading loops of triaxial compression tests with a constant confining pressure of  $\sigma_3 = 0.2$  MPa, the shear modulus  $\mu^S$  was directly determined from the diagram (Figure 6.1 (a)). The bulk moduli  $k_0^S$  and  $k_1^S$  were obtained by an estimation of the basis of hydrostatic compression tests with large loading and unloading loops (Figure 6.1 (b)), while the maximal solidity  $n_{max}^S$  was only roughly estimated from hydrostatic stress

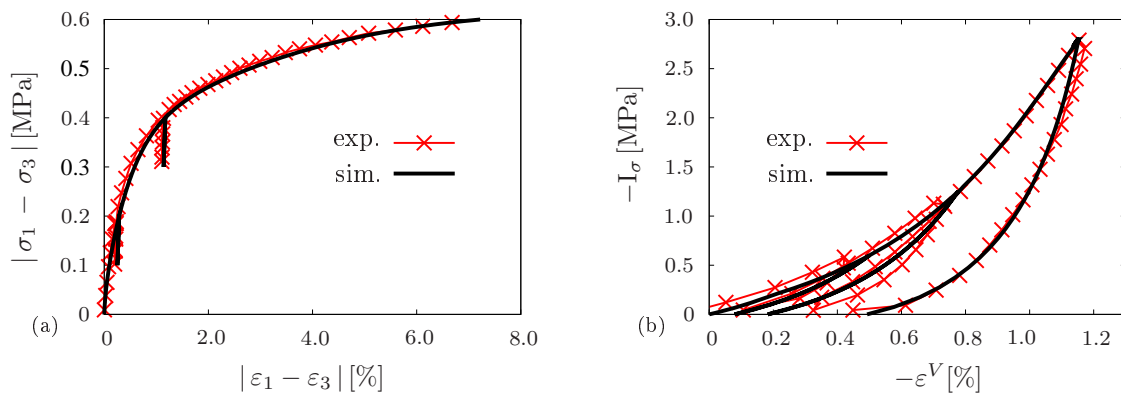


**Figure 6.1:** Unloading/reloading cycles of (a) a triaxial compression test and (b) a hydrostatic test of GEBA sand.

progression, because the compression point cannot be reached by our volume-pressure controller ( $\sigma^H = 0.95$  MPa). The parameter set of the elastic part of the material behaviour are listed in Table C.1 together with the initial solidity  $n_{0S}^S$ .

### Identification of plastic parameters based on monotonic loading tests

During the identification procedure of the 26 parameters governing the plastic or the viscoplastic part of the overall material behaviour, respectively, one has to identify the constant parameters  $\alpha$ ,  $\kappa$  and  $m$  as well as the initial and saturation values  $p_{i0}$  and  $\bar{p}_i$  of the parameters  $\beta$ ,  $\delta$ ,  $\epsilon$ ,  $\gamma$ . Note that all of them are included in the yield condition (4.35). Furthermore, the parameters  $\psi_1$  and  $\psi_2$  of the plastic potential (4.42) have to be found, and the hardening/softening behaviour of the evolution equations (4.48) has to be fixed by the identification of the volumetric and deviatoric evolution constants  $C_{pi}^V$  and  $C_{pi}^D$ . Furthermore,  $\eta$ ,  $r$  and  $\sigma_0$  have to be found governing the evolution (4.48) of the viscoplastic strain, while finally  $\bar{C}_\epsilon$  and  $\bar{\epsilon}_{lim}$  have to be identified to govern the new failure concept.

The overall identification procedure was based on the multi-criterion object function (5.40). Evaluating this for the considered identification problem of plastic parameters, the following object function results

$$\begin{aligned}
 f(\mathbf{s}_{pl}) = & \sum_{t=1}^3 \frac{1}{N_t} \left\{ \frac{1}{\sigma_0^t} \sum_{i=1}^{N_t} (\sigma_{1,\text{sim}}^t - \sigma_{1,\text{exp}}^t)^2 + \frac{1}{\varepsilon_{S0}^{Vt}} \sum_{i=1}^{N_t} (\varepsilon_{S,\text{sim}}^{Vt} - \varepsilon_{S,\text{exp}}^{Vt})^2 \right\} + \\
 & + \frac{1}{N_{\text{hyd}} \varepsilon_{S0}^{V\text{hyd}}} \sum_{i=1}^{N_{\text{hyd}}} (\varepsilon_{S,\text{sim}}^{V\text{hyd}} - \varepsilon_{S,\text{exp}}^{V\text{hyd}})^2 \rightarrow \min
 \end{aligned} \tag{6.1}$$

with  $\sigma_{Em}^S \approx \sigma \rightarrow$  drained condition.

Therein,  $N_t$  and  $N_{\text{hyd}}$  are the numbers of the considered data points of the compression (t) and hydrostatic (hyd) experiments. The reference values  $\sigma_0^t$ ,  $\varepsilon_{S0}^{Vt}$  and  $\varepsilon_{S0}^{V\text{hyd}}$  taken from the experiments, which denote the maximal shear and volume-compression-strain values, are used for the normalisation of the data, and  $\mathbf{s}_{pl}$  is the set of parameters that has to be determined.

In general, cohesionless material like dry sand cannot carry tensile loads. Thus, the parameters  $\alpha$  and  $\kappa$  controlling the range of hydrostatic tension of the yield surface have to vanish. However, for computational convenience and in order to prevent numerical instabilities during simulations, where pure tensile stresses may locally occur during the iteration process,  $\alpha$  and  $\kappa$  are set to small values in order to avoid singularities at the tip of the yield surface. Note that these small values have to be chosen carefully, such that the physical behaviour of the material is basically unaffected. Furthermore, the parameters governing the shape of the yield or failure function in the deviatoric plane ( $m$ ,  $\gamma_0$ ,  $\bar{\gamma}$ ) have been chosen such that the yield envelope can vary between an initial circle ( $m$ ,  $\gamma_0$ ) and a triangle with rounded corners ( $m$ ,  $\bar{\gamma}$ ). Following this, the ratio  $R_c/R_e$  of the compression ( $R_c$ ) over the extension ( $R_e$ ) radius lies between  $R_c/R_e = 1$  and its maximum value. To

guarantee overall convexity of the deviatoric yield curve, cf. [48, 49],  $m$  and  $\gamma$  are restricted to

$$\gamma \leq \max \gamma(m) = \frac{\sqrt{27}}{9m-2}, \quad m \geq 0.54, \quad \text{such that} \quad 0 \leq \gamma \leq 1.786. \quad (6.2)$$

Choosing  $m = 0.54$ , the ratio  $R_c/R_e$  can vary between 1 ( $\gamma = 0$ ) and a maximum value of 1.584 ( $\gamma = 1.786$ ). However, it was found that  $0 \leq \gamma \leq 1.66$  is sufficient to represent all compression/extension radii found during our experiments. This choice also includes the choice of the evolution parameters  $C_\gamma^D$  and  $C_\gamma^V$ , where  $C_\gamma^V$  is assumed to vanish such that the deviatoric yield curve only depends on the deviatoric loading and the yield radius is kept constant during triaxial hydrostatic compression. Furthermore, the failure surface parameters  $C_\epsilon^*$  and  $\epsilon_{lim}^*$  and the viscoplastic parameters  $\eta$ ,  $r$  and  $\sigma_0 = \kappa$  have also been excluded from the optimisation process. As a result,  $\mathbf{s}_{pl}$  finally includes 14 remaining parameters to be determined from (6.1).

During the testing procedure, hydrostatic and conventional triaxial compression tests have been performed, the latter by monotonic shear loading after a constant confining pressure  $\sigma_2 = \sigma_3$  had been applied, cf. Figure 3.5. In particular, five experiments have been considered. These are one hydrostatic compression test (hyd) and four triaxial compression tests ( $t := 1, \dots, 4$ ) with constant confining pressures of  $\sigma_3 = 0.05, 0.1, 0.2$  and  $0.3$  MPa, cf. Figure 6.2. During the compression tests, the axial load was displacement-controlled applied to the specimens with a velocity of  $\dot{u}_1 = 0.5$  mm/s. The solution of the non-linear

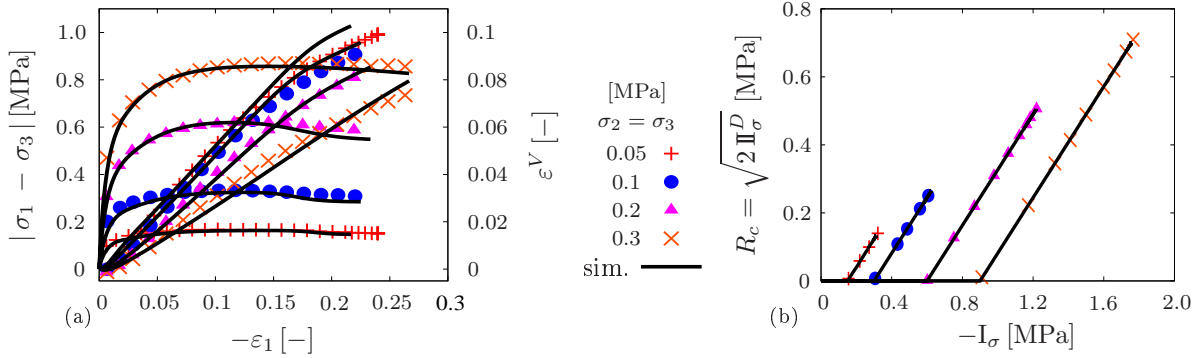


**Figure 6.2:** Triaxial compression tests and numerical simulations: (a) stress and volumetric strain vs. longitudinal strain and (b) stress progression in the hydrostatic plane.

optimisation problem (6.1) is carried out with the gradient-based SQP by use of the BFGS method, cf. Section 5.2.1. The numerical error is computed by the sum of the squared differences between the numerical and experimental values using the *Least-Squares Method*. The major advantage of the gradient-based method are the low computational costs due to a semi-analytical determination of the sensitivities, which are required for the effective solution of the minimisation problem (6.1). During the sensitivity analysis, the main task is the computation of the gradient of the object function  $f(\mathbf{s}_{pl})$  with respect to the material parameters  $\mathbf{s}_{pl}$ , cf. Section 5.2.3.

Starting the identification procedure on the basis of a suitable guess of an initial parameter set, the parameters could be found by (6.1) as is shown in Table C.1. Furthermore, the



four laboratory compression tests and their numerical computation with the parameters of these tables are shown Figure 6.2. It is seen from Figure 6.2 (a) that the optimisation procedure led to a good agreement between the numerical and the experimental results. Figure 6.2 (b) illustrates the increase of the deviatoric stresses in the hydrostatic plane up to failure values. In the standard interpretation of the failure concept, the failure values of the deviatoric stresses of the different compression tests are assumed to be on one fixed failure surface, cf. Figure 6.3 (black line), while the new failure concept presented here implies individual failure surfaces 1–4 for each of the four peak shear stresses. As a matter of fact, the standard failure concept is constrained by a rather large failure surface in order to reproduce all possible peak-shear stresses occurring between the lowest and the highest confining pressure  $\sigma_3$ . The detailed sub-figures of Figure 6.3 exhibit the

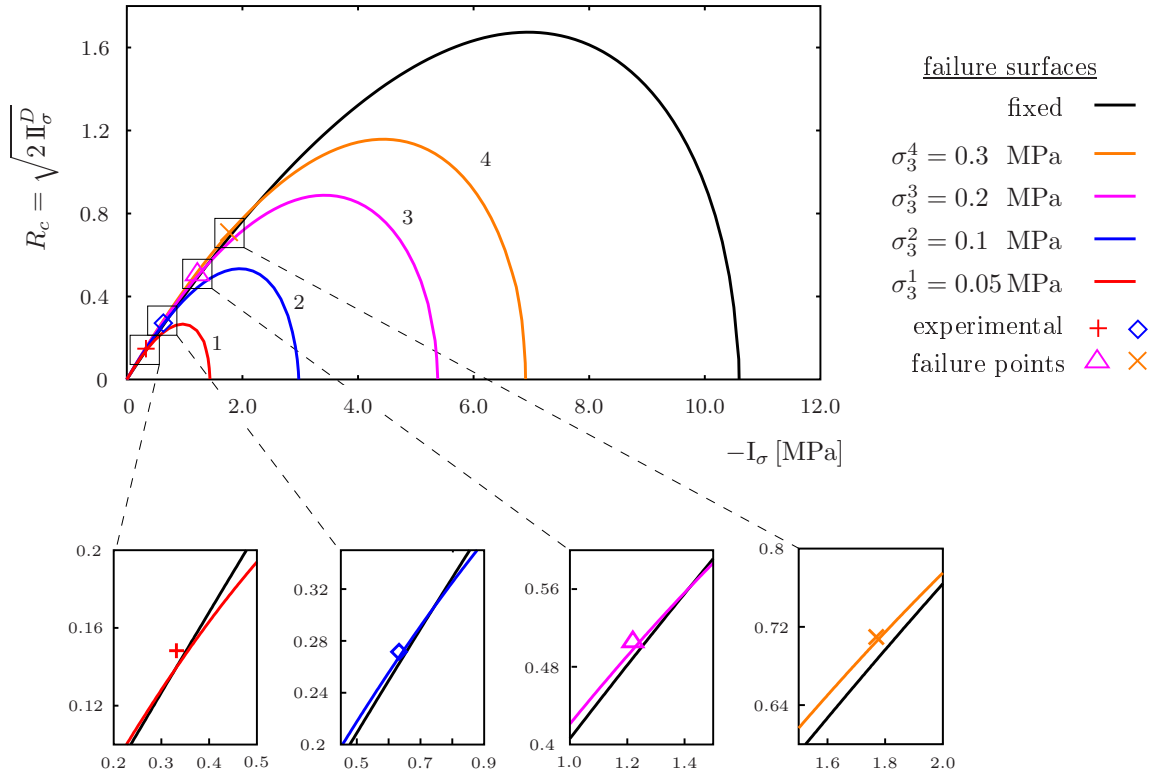


**Figure 6.3:** Fixed failure surface with the old failure concept and stress-dependent failure surfaces of the new failure concept.

experimentally determined failure stresses of the four compression experiments and their numerical counterparts after parameter optimisation. The results of these sub-figures are twofold. On the one hand, it is seen that the experimental results could be matched with only very little deviations. On the other hand, it is furthermore seen that the fixed failure surface does not necessarily encase the failure surfaces 1–4 of the new concept.

To give an example of the complex hardening/softening and failure behaviour of granular material, consider the experimental results and their numerical counterpart of the triaxial compression experiment with a constant confining pressure of  $\sigma_3 = 0.2$  MPa as is shown in Figure 6.4 (a). The evolution of the yield surface is naturally a continuous process, which is numerically realised by growing (hardening) or shrinking (softening) the yield

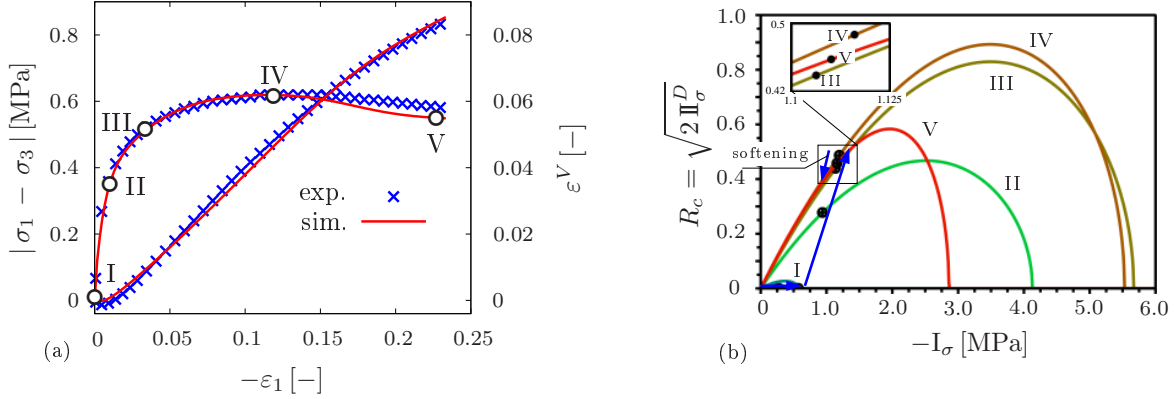


**Figure 6.4:** (a) Triaxial compression test and (b) evolution of the yield surfaces.

envelope at each time step of the computation as long as the piston is driven into the specimen. During the experiment exhibited in Figure 6.4 (a), a continuous displacement-controlled loading process is applied. While the loading passes the stress points I–V, a hardening (I–IV) and a softening behaviour (V) are observed, cf. Figure 6.4 (b). The experiment starts by applying an initial hydrostatic load (stress point I) corresponding to the confining pressure of  $\sigma_3 = 0.2$  MPa. During this hydrostatic loading, only little plastic hardening is generated. As a result, the blue yield surface I in Figure 6.4 (b) is rather small. Thereafter, a shear load is applied by increasing the top load towards stress point II, which generates plastic deformations as the grains start slipping into a denser packing, thus causing a rapid increase of the yield envelope, compare the green curve II in Figure 6.4 (b). Note again that the densification during the shear loading is stronger, when a higher confining pressure is applied. Despite of the increasing dilatation of the sample between stress points II–IV, further shear loading yields a furthermore growing shear envelope up to the peak stress IV with small hydrostatic softening between III and IV. This behaviour is described by equation (4.48), where the deviatoric and volumetric hardening evolves separately. However, despite of the volumetric decrease (loosening) of the yield surface, it is still growing in the deviatoric direction until the final hardening surface IV (failure surface) is reached. This behaviour is due to an increase of frictional forces between the grains generated by increasing frictional stresses as a result of an increasing top load, only limited by the maximal deviatoric stress or the peak stress, respectively. After the peak stress is reached, further loading is only possible with decreasing shear stresses, while the deviatoric hardening is terminated, and the growing volumetric dilatation reduces the frictional forces between the grains, thus leading to stress softening. Therefore, the smooth stress softening between the stress points IV and V is a result of the strong dilatational behaviour and causes a rapid loosening of the intergranular structure. This behaviour is approximated by a volumetric shrinkage of the yield surface (softening) until the final size V is reached in this experiment.

The non-circular (anisotropic) plastic response of the deviatoric yield envelope of sand during shear loading results in an increasing ratio  $R_c/R_e$  from  $R_c/R_e \approx 1$  towards its maximum value. In order to capture this behaviour, six monotonic shear-load experiments (3 triaxial compression experiments and 3 triaxial extension experiments) at con-

stant values of the first stress invariant  $I_\sigma$  have been carried out following the loading path in Figure 3.6, while the results are presented in Figure 6.5. The confining pressures of these experiments have been set to  $\sigma_3 = 0.1$  MPa corresponding to the stress invariants  $I_\sigma^c = I_\sigma^e = -0.3$  MPa, to  $\sigma_3 = 0.2$  MPa ( $I_\sigma^c = I_\sigma^e = -0.6$  MPa) and to  $\sigma_3 = 0.3$  MPa ( $I_\sigma^c = I_\sigma^e = -0.9$  MPa). With increasing values of  $\gamma$  at constant  $m$ , the circular devia-

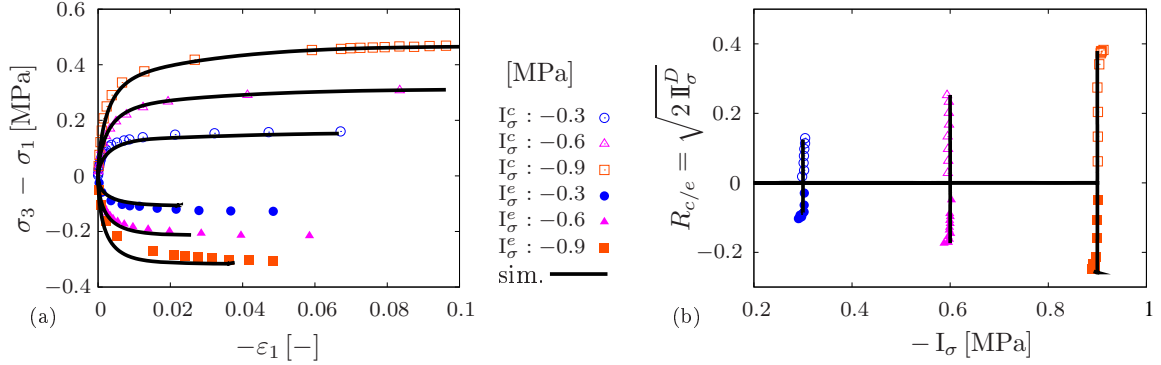


**Figure 6.5:** Triaxial compression/extension tests with constant stress invariants  $I_\sigma^{c/e}$ : (a) shear stresses vs. strain and (b) shear stresses in the hydrostatic plane.

toric envelope evolves towards a triangular shape with rounded corners, cf. Figure 4.1. In Figure 6.5 (b), the stress paths are shown in the hydrostatic plane for each of the three compression and extension experiments, where the respective ratios  $R_c/R_e$  at the limit state are  $(R_c/R_e)^{0.3} / (R_c/R_e)^{0.6} / (R_c/R_e)^{0.9} = 1.25 / 1.38 / 1.51$ . Hence, the higher the state of hydrostatic pressure is, the greater is the increase of the ratio  $R_c/R_e$  or the anisotropic behaviour of sand, respectively.

In case of only monotonic triaxial experiments, the old failure concept with a fixed failure envelope is able to capture the stress-strain behaviour of the compression calibration experiments just as nicely as the new failure concept, cf. Figures 6.1, 6.2 and 6.5, but it will fail to reproduce the failure behaviour of the stress-path experiments taken as a validation of the new model. On the other hand, it will be shown how nicely the new concept can be verified reproducing the experimental evidence of foundation- and slope-failure problems.

## 6.1.2 Loading-path-dependent stress-strain behaviour

### Stress-path test 1

The stress-path test 1 is carried out as a validation experiment according to the schematic diagrams of Figure 3.12 (a), where a conventional monotonic compression test in the hydrostatic stress plane is shown. In the experiment corresponding to these figures, loading and unloading is carried out in various steps. In the first step, a hydrostatic pressure is applied up to a confining pressure of  $\sigma_3^{H2} = 0.3$  MPa at stress point P1. Thereafter, the sample is loaded in the  $\sigma_1$ -direction, thus initiating an increasing shear stress at constant confining pressure until the peak stress is reached at stress point P2. After shear-stress

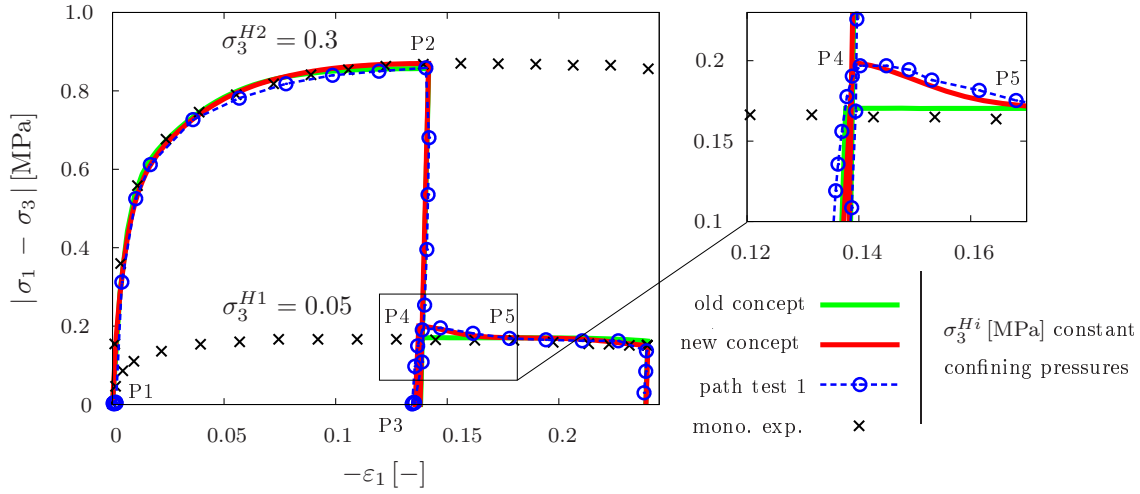


**Figure 6.6:** Experiment and simulation of the stress-path test 1 with growing and fixed failure surfaces.

unloading, the confining pressure is reduced to  $\sigma_3^{H1} = 0.05$  MPa at stress point P3, and then sheared again up to P4 followed by a reduction to P5.

In Figure 6.6, the experimental results of the non-monotonic stress-path test 1 are indicated by circles, while the associated numerical computation is shown by the red solid line. Apart from this, the black crosses exhibit two further conventional monotonic experiments taken at  $\sigma_3^{H1} = 0.05$  MPa and  $\sigma_3^{H2} = 0.3$  MPa. These experiments have been included in the overall parameter determination procedure described before. Here, these experiments are used for a comparison of monotonic and non-monotonic stress paths. Following the red line at  $\sigma_3^{H2} = 0.3$  MPa up to the peak stress corresponds to a shear loading between P1 and P2, also compare Figure 3.11 (a). Thereafter, the shear stress is completely reduced and the confining pressure is changed towards  $\sigma_3^{H1} = 0.05$  MPa (P3). Reloading at  $\sigma_3^{H1} = 0.05$  MPa basically follows the crossed curve of the conventional (monotonic) experiment. However, it is seen from the zoomed region of Figure 6.6 that the shear stress firstly exceeds the peak shear stress that was obtained during the conventional experiment at  $\sigma_3^{H1} = 0.05$  MPa before it reduces to the crossed curve. This behaviour is schematically included in Figure 3.12 (a), where the exceeded value is indicated as P4 belonging to the experiment with the failure envelope reached at P2 with the confining pressure of  $\sigma_3^{H2} = 0.3$  MPa. Since loading beyond P4 is driven displacement-controlled, further shearing disturbs the intergranular structure, the shear stress is unstable at the actual hydrostatic pressure and reduces to P5 belonging to stable values of the monotonic experiment at  $\sigma_3^{H1} = 0.05$  MPa and the green failure surface included in Figure 3.12 (a).

These experimental results confirm the assumption of stress-dependent failure surfaces, cf. Figure 3.12 (a), and furthermore show that granular material always tries to keep the size of the yield surface as small as possible, which obviously corresponds to stable stress states as they are obtained by monotonic loading.

Moreover, when comparing the old failure concept to the new concept presented here, there are no differences in the reproduction of the stress-strain behaviour during the stress paths towards P1 and P2. The strength of the new failure concept only becomes

apparent during the stress paths from P2 towards P3, P4 and P5, where the experimental results cannot be reproduced with the old failure concept with its constant shape.

### Stress-path test 2

The stress path of this validation experiment is basically shown in Figure 3.11 (b) and Figure 3.12 (b), where the loading is governed by the following order:

1. hydrostatic loading up to  $\sigma_3^{H1} = 0.05$  MPa (P1),
2. first shear loading until the peak stress (P2) is reached at constant  $\sigma_3^{H1}$ ,
3. shear unloading followed by an increase of the confining pressure up to  $\sigma_3^{H2} = 0.2$  MPa (P3),
4. second shear loading until the peak stress (P4) is reached at constant  $\sigma_3^{H2}$ ,
5. second shear unloading followed by a reduction of the confining pressure towards  $\sigma_3^{H1} = 0.05$  MPa (P5),
6. third shear loading at constant  $\sigma_3^{H1}$  firstly reaching P6 at the red failure surface of Figure 3.12 (b), while further loading leads to a softening back to P7 equivalent to P2.

In a standard elasto-plastic process with hardening properties, the yield curve is reached again after having passed a loading and an unloading process, when the applied stress again reaches the greatest stress state obtained so far. Reloading up to this point is purely elastic, while further loading is governed by the hardening process. In the stress-strain diagram, cf. Figure 3.11 (b), this is seen from a switch of the loading curve from linear to highly non-linear at the yield point, which is also indicated in Figure 6.7.

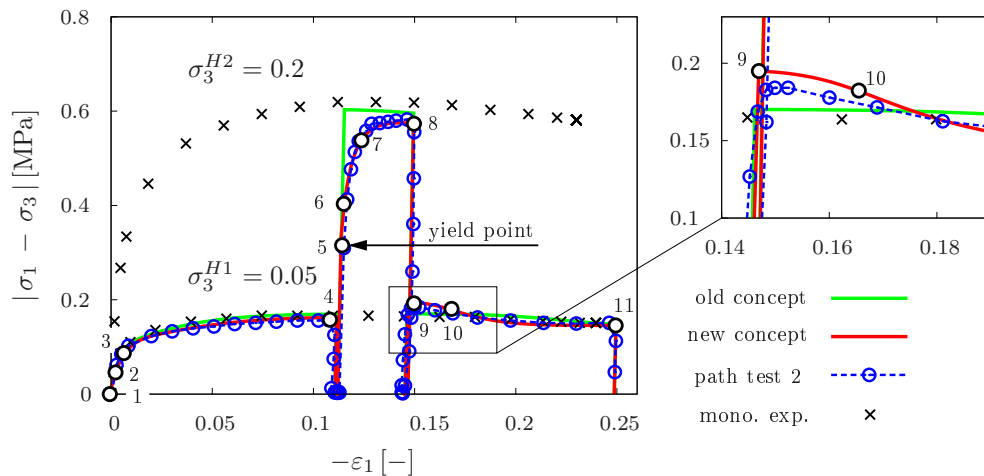
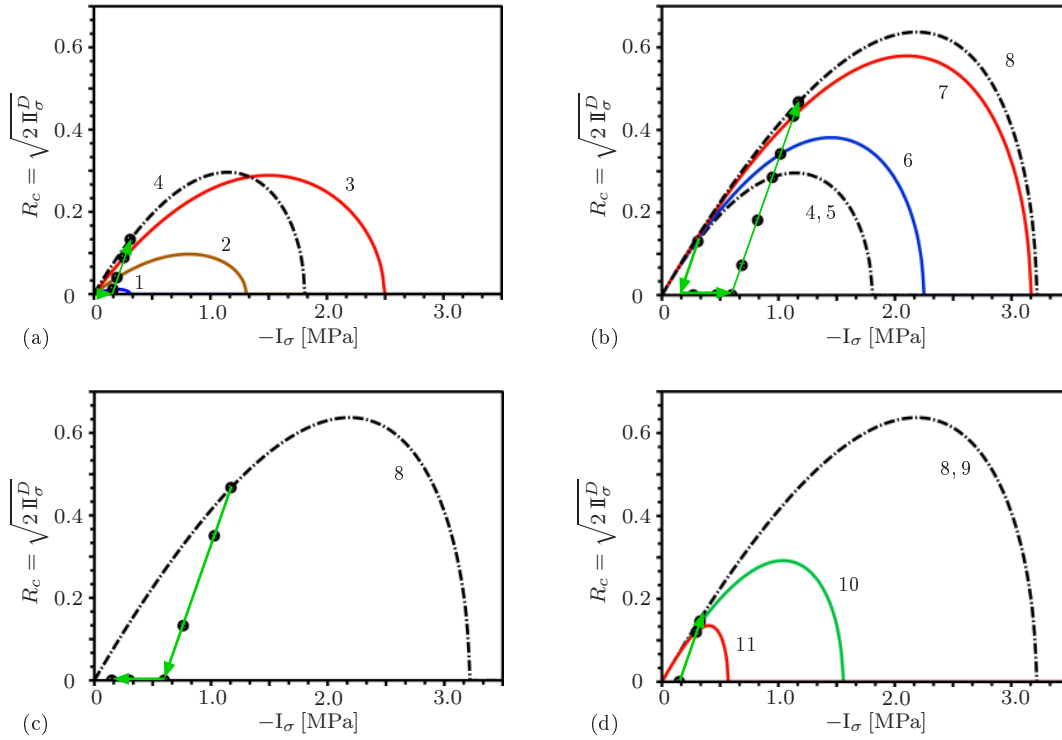


Figure 6.7: Experiment and simulation of the stress-path test 2.

However, in case of granular material, each yield stress belongs to a certain state of the confining pressure. Whenever the confining pressure is changed, the corresponding yield

stress also changes. Following this, the yield-stress values of a stress-path test can only be determined by the change of the stress-strain relation.

Considering the experimental results of the stress-path test 2 exhibited in Figure 6.7, the stress-strain relation during the second shear loading, where the confining pressure has been increased from  $\sigma_3^{H1} = 0.05$  MPa to  $\sigma_3^{H2} = 0.2$  MPa, shows  $|\sigma_1 - \sigma_3|$  ranging between zero shear stress and the peak value at point 8. It is furthermore seen that the stress-strain relation exhibits a linear curve only between zero and point 5. Thereafter, a non-linear behaviour is observed with a steady increase of plastic deformations, which can only be captured using the new failure concept (4.49). In contrast, the old failure concept is only able to model the shear-stress-strain relation during this stress path up to the yield point 5. Thereafter, the old failure concept follows the assumption of only elastic deformations along the straight line until it reaches the failure curve at  $\sigma_3^{H2} = 0.2$  MPa of the monotonic experiment.



**Figure 6.8:** Computational results of evolving yield surfaces during the stress-path test 2: (a) first shear loading at  $\sigma_3^{H1}$ , (b) unloading and second shear loading at  $\sigma_3^{H2}$ , (c) unloading and reduction of  $\sigma_3^{H2}$  to  $\sigma_3^{H1}$ , (d) third shear loading and softening at  $\sigma_3^{H1}$ .

For a better understanding of the yielding behaviour during the loading path of Figure 6.7, the evolution of the yield surface of the new failure concept is presented at selected states of the stress path through the points 1-11 indicated by white circles. Following this, the evolving yield surface shown in Figure 6.8 (a) reaches the failure surface at the peak stress during the first shear loading at point 4 corresponding to the failure surface 4. It should be noted that the yield surface 3 exhibiting the maximal hydrostatic stress must not necessarily be a failure surface. The crucial factor of failure is the size of the failure surface in the deviatoric direction.

Following the second shear loading, cf. Figure 6.8 (b), it should be recognised that the stress points 4 and 5 are on the same yield envelope, where, in case of the second loading, the failure surface 4 of the first loading is stabilised by a higher confining pressure and, therefore, changes its character towards a yield surface. Further loading between stress points 5 and 8 leads to an extension of the yield envelope during plastic hardening governed by (4.49) until the failure surface 8 is reached. Shear unloading and reducing the confining pressure to  $\sigma_3^{H1} = 0.05$  MPa, cf. Figure 6.8 (c), leads to stress point 9 during the third shear loading process, cf. Figure 6.7 (extracted detail). Point 9 firstly belongs to the failure surface 8. However, further compression immediately reduces the size of the yield surface from 9 to 11 during softening again governed by (4.49), cf. Figure 6.8 (d). Note that the applied stress paths are indicated by green arrows in Figure 6.8.

### Stress-path test 3

The influence of a hydrostatic preconsolidation on the shear-stress-strain behaviour is investigated by two further validation experiments following the stress-path test 3, where the corresponding loading path is illustrated in Figure 3.13. Applying a hydrostatic pressure, the specimen reaches the stress point P1 only governed by the maximum value of the volume-pressure controller at  $\sigma_3^H = 0.95$  MPa corresponding to  $I_\sigma = -2.85$  MPa. Thereafter, the confining pressure is reduced to  $\sigma_3^{H1} = 0.05$  MPa or to  $\sigma_3^{H2} = 0.1$  MPa

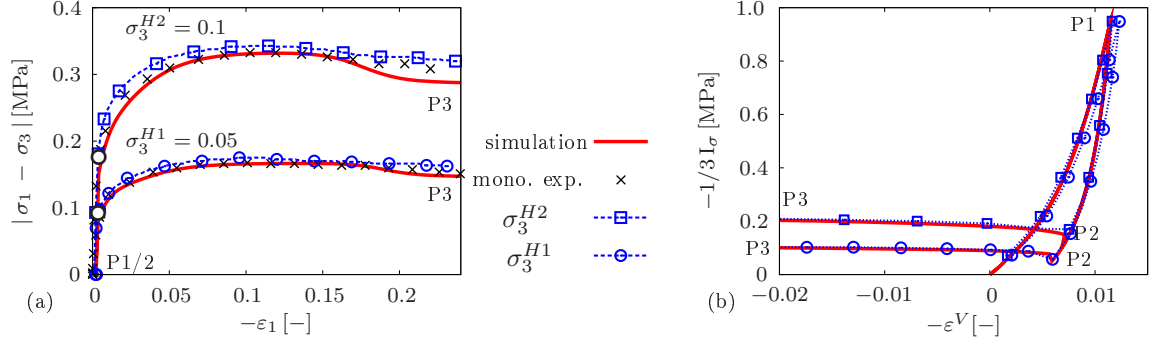


**Figure 6.9:** Preconsolidated triaxial compression tests with confining pressures of  $\sigma_3^{H1} = 0.05$  MPa and  $\sigma_3^{H2} = 0.1$  MPa: (a) shear stress vs. longitudinal strain, (b) hydrostatic stress vs. volumetric strain.

at P2, respectively, and the specimen is sheared towards P3 while keeping the respective confining pressure constant.

The results of these experiments and the corresponding numerical simulations are shown in Figure 6.9, cf. Figure 3.13 (b). Figure 6.9 (b) exhibits the preconsolidation process versus the volumetric strain ranging from zero to approximately 0.014. Thereafter, the hydrostatic unloading is applied and kept constant during shear loading. From Figure 6.9 (a), a linear elastic behaviour of the stress-strain curves is observed until the white circles are reached, whereas the monotonically loaded samples do not show a purely elastic behaviour, compare, for example, Figures 3.9 and 6.4. This is due to the fact that the hydrostatic preconsolidation results in an extension of the yield surface from approximately zero to a certain extent, while the conventional compression tests without preconsolidation

exhibit elasto-plastic deformations and plastic hardening up to the failure load during the whole shear-loading process. However, comparing the peak-stress values of the preconsolidated sample with the monotonically loaded reference compression tests with the same confining pressures of  $\sigma_3^{H1} = 0.05$  MPa and  $\sigma_3^{H2} = 0.1$  MPa, cf. Figure 6.2, it is found that the failure behaviour is only marginally influenced by preconsolidation, cf. Figure 3.13 (b). This effect can also be explained by the development of the yield surface during the preconsolidation process, where the main increase of the yield envelope is obtained in hydrostatic direction, while there is only a very small increase in the deviatoric direction. As a result, the deviatoric yield curve approximately remains a circle with  $R_c/R_e \approx 1$ .

Figure 6.10 (a) exhibits the development of the yield surface during preconsolidation with the final black dashed-dotted line, while Figures 6.10 (b) and (c) show the different hardening-softening curves at  $\sigma_3^{H1}$  (b) and  $\sigma_3^{H2}$  (c). It is also seen from these figures that shear loading following the hydrostatic preconsolidation firstly extends the yield surface

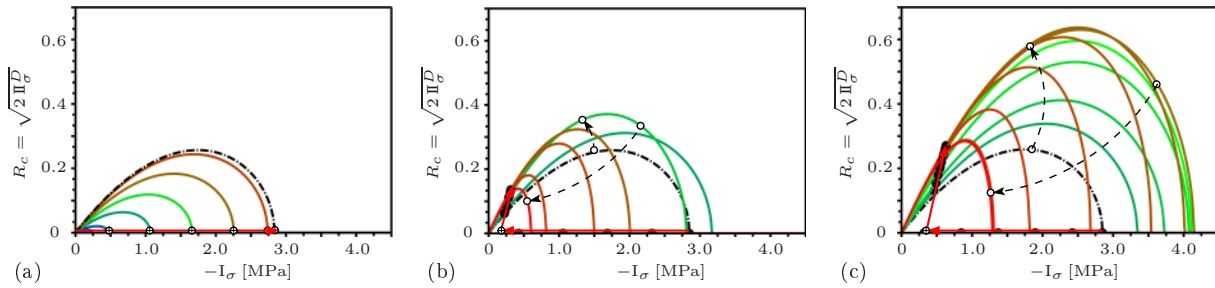


**Figure 6.10:** Evolution of the yield surface: (a) preconsolidation phase up to  $I_\sigma^{H2} = -2.85$  MPa, (b) shearing phase at constant  $\sigma_3^{H1} = 0.05$  MPa and (c) at constant  $\sigma_3^{H2} = 0.1$  MPa.

in the direction of deviatoric compression up to the failure surface at the peak stress and shrinks thereafter due to softening, while the hydrostatic extension also shrinks, cf. the dashed lines with direction arrows included in Figures 6.10 (b) and (c).

Finally, it is concluded from the experiments on granular material that the plastic yielding during pure hydrostatic loading is limited by the stiff grains, which are rigid and uncrushable under moderate pressures usually found in geotechnical applications. Thus, hydrostatic loading under such a moderate pressure is not restricted by the failure limit. This can be concluded from the knowledge that an increase of the hydrostatic pressure finally does not cause the grains to slide into a denser packing. As a consequence, the hydrostatic evolution of the yield surface is terminated, and the volumetric elastic stress-strain curve tends towards a vertical tangent, cf. Figure 6.9 (b).

### 6.1.3 Numerical model validation via simulation of sand box experiments

The large number of material parameters results in a difficult and not always unique parameter identification process based on the experimental evidence. As a result, it is basically possible that there is more than only one parameter set sufficient to match homogeneous triaxial experiments. This possibility led to a further restriction of the physical range of parameters by not only considering monotonically loaded experiments



but also stress-path-depending ones. To check whether or not one can rely on the physical model and the included material parameters when field problems have to be evaluated, it is useful to control the whole model by the numerical simulation of non-homogeneous validation experiments. Obviously, the validation experiments must proceed from the same initial solid density like that of the triaxial experiments used during the overall parameter identification procedure.

The validity and application of the used model was proven through the computation of foundation- and slope-failure problems initiated by local shear-failure events. However, other failure problems can be also picked out from the range of possible validation experiments. In particular within the framework of this thesis, an experimental sand box has been constructed to carry out 3-d foundation- and slope-failure tests, approximately restricted by plane-strain conditions resulting from rigid sand-box walls.

### Sand box

The experimental sand box is 50 cm long, 30 cm wide, and 27 cm high. Its mainly consists of steel, except of the front and back sides, which are made of glass such that the development of shear bands can be observed, cf. Figure 6.11. For a better visibility of the shear bands, stripes of black-coloured sand have been inserted in vertical columns at the

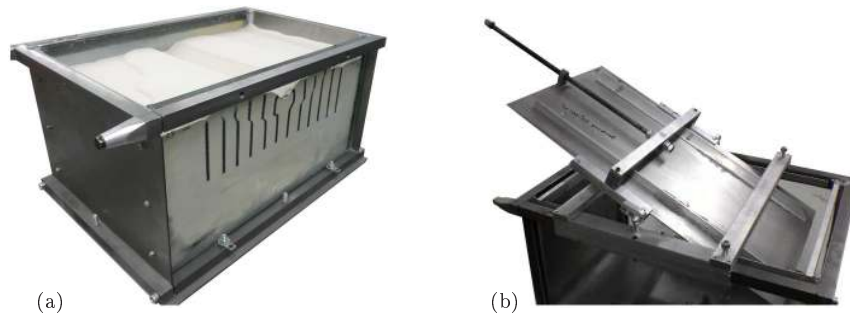


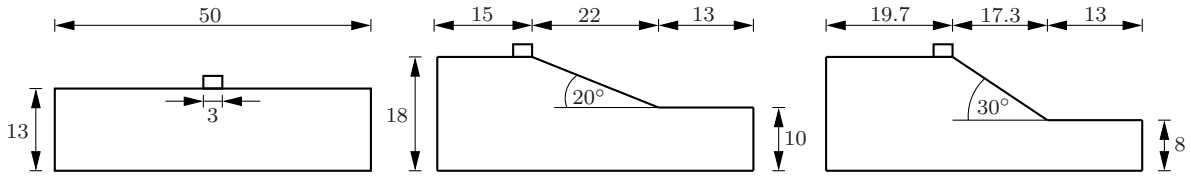
**Figure 6.11:** (a) *Experimental box* and (b) *mechanical device for adjusting the slope angle*.

glassy side walls of the box. The frictional forces between the sand and the glass were eliminated by applying lubricated transparent latex sleeves with a thickness of 0.35 mm on the inside of the glass walls. When the box is filled, the GEBA sand is compacted on a vibration table until the same initial solid density of  $\rho_{0S}^S = 1.55 \text{ g/cm}^3$  (dense sand) is reached, which was also used for the triaxial experiments.

In order to prepare the setup for the slope-failure experiments, a slope was created by pushing a thin steel plate into the sand with an angle of either  $20^\circ$  or  $30^\circ$ , while the remaining sand above the plate was removed. In order to avoid any boundary effects on the foundation-failure experiment, one has to consider that the horizontal projection of the expected shear band yields approximately 13 times of the load plate width, which was experimentally and numerically determined by use of load plate widths of 3 and 5 cm. Finally, a load-plate width of 3 cm was chosen in order to avoid any disturbing effects on the shear-band evolution obtained from the left and right walls of the box. Furthermore, the slope- and foundation-failure experiments have been performed displacement-controlled at a velocity of 1 mm/min under 2-d plane-strain conditions.

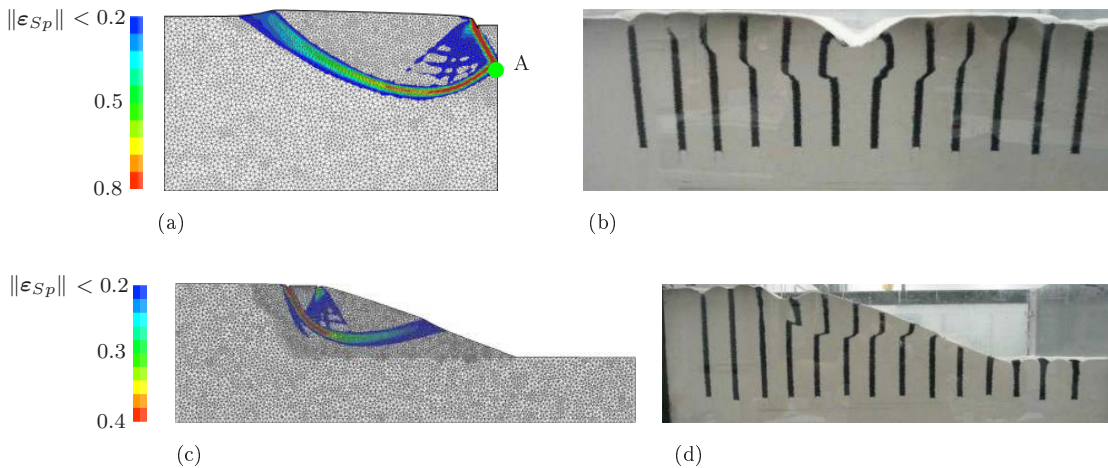
## 2-d failure experiments and numerical simulation

Figure 6.12 shows the geometry and the dimensions of the foundation- and slope-failure experiments used for the validation of the proposed model and the included parameter set. For the numerical simulation of the failure experiments by use of the finite element method, the spatial domain is separated in two discretisation areas, where the area with the expected shear band is discretised with a finer triangular mesh than the remainder of the computation domain. This will lead to a finer and more realistic resolution of the shear band and will simultaneously help to reduce the computation time.



**Figure 6.12:** Geometry and dimensions of the experimental box tests [cm].

The shear bands of the foundation- and the slope-failure experiments are illustrated in Figure 6.13 (b) and (d) together with the corresponding numerical simulations depicted in Figure 6.13 (a) and (c). The evolving shear bands are detected by the norm  $\|\epsilon_{Sp}\|$  of the accumulated plastic strains, where small negligible values below 0.06 have been deleted for clarity reason. Note that the foundation-failure experiment was computed by assuming axial symmetry in order to reduce the computation time. A visual investigation of the computed shear bands reveals an almost identical shape in comparison with the experimentally obtained shear bands of Figure 6.13 (b) and (d).



**Figure 6.13:** Failure sand-box experiments and numerical simulations of shear bands illustrated by  $\|\epsilon_{Sp}\|$ : (a) and (b) foundation-failure problem, (c) and (d) slope-failure problem with a slope angle of  $20^\circ$ .

The corresponding stress-displacement curves of the load plate are shown in the diagrams of Figure 6.14. Therein, Figure 6.14 (a) presents the numerical results obtained with the new failure concept by application of equation (4.49), while Figure 6.14 (b) shows the results of the simulations using the old failure concept with a fixed failure surface.

In general, the proposed new failure surface performs very well, as it is able to almost exactly match the measured results of all three experiments. In this regard, even the softening behaviour is nicely reproduced. Considering the numerical results of the old failure concept, cf. Figure 6.14 (b), neither the peak stress nor the softening is reasonably captured. The reason for this poor performance of the old concept is found in the hydrostatic stress levels during the failure experiments, which may strongly differ from the hydrostatic stress levels during the calibration experiments for which the fixed failure surface was exactly adapted.

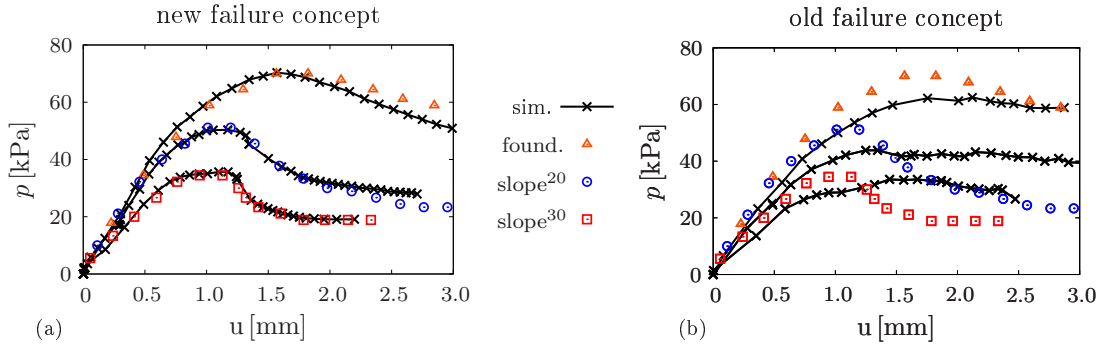


**Figure 6.14:** Stress-displacement curves for the foundation-failure experiment (found.) and both slope-failure experiments with slope angles of  $20^\circ$  (slope<sup>20</sup>) and  $30^\circ$  (slope<sup>30</sup>) computed by (a) the new failure concept and (b) the old failure concept.

It is concluded from these results representing non-homogeneous deformations of granular material that a fixed failure surface, although it can reproduce specific calibration experiments, completely fails in case of general applications with different hydrostatic stress levels. In contrast, the new failure concept allows to compute suitable failure surfaces for every shear-stress level at any corresponding hydrostatic stress, which leads to a better approximation of the failure behaviour of an arbitrary initial-boundary-value problem. Moreover, Figure 6.15 shows the evolution of the yield surface in point A of Figure 6.13 (a) at the initial state (initial y-s), at the failure state (f-s), and at the end of the softening (y-s after softening) during the foundation-failure simulations. The results obtained with the new failure concept are shown in Figure 6.15 (a), while the results based on the old

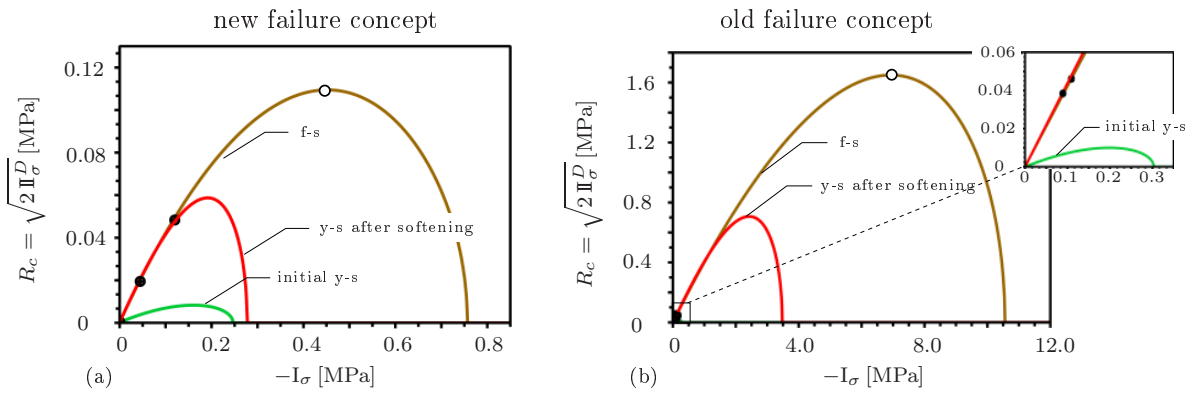


**Figure 6.15:** Evolution of the yield surface in point A during the foundation-failure simulation at different calculation times using (a) the new failure concept and (b) the old failure concept.

failure concept are depicted in Figure 6.15 (b), in both cases with the initial yield surface in green. The stress states reached initially (approx. at the origin of the coordinate system), at failure and after softening is indicated by black points on the yield surfaces. However, the failure and softening values of the old failure concept can only be seen in the extracted detail of Figure 6.15 (b) because of the enormous size of the yield surface at the failure state. A comparison of the black stress points at failure with the circles at the theoretically highest deviatoric stress reveals that the yield surface of the old failure concept predicts a more than 10 times larger failure surface in comparison to the new failure concept. Thus, the old failure concept yields large plastic deformations when increasing the yield surface until the failure surface is reached at peak loading. Furthermore, it also needs high plastic deformations to shrink the large yield surface towards softening behaviour. Hence, the peak stresses of all three simulations obtained with the old failure concept are reached at larger deformations compared with the experiments. Finally, there is almost no prediction of a stress decrease after having passed the peak stress, cf. Figure 6.14 (b).

## 6.2 Model calibration of the mobile pore fluids

The hydraulic properties of the GEBA sand are determined on the basis of the experimental data provided by VEGAS\* using the *van Genuchten* capillary-pressure-saturation relation given in (4.59) and (4.58). The adapted hydraulic parameters are listed in Table C.2. In Figure 6.16 (left), the experimental results and the fitted curve of the capillary pressure-saturation relation are shown. For the relative permeability relations of the fluids in (4.59), no experimental data were available. Therefore, the dependency of the fluid permeabilities on the saturation of the GEBA sand is chosen equivalently to that of a typical uniform fine sand, see Figure 6.16 (right).

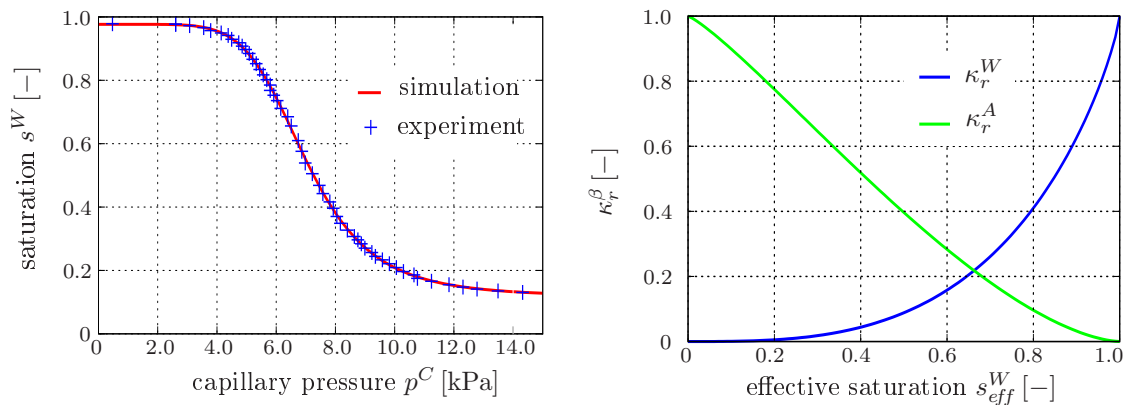


**Figure 6.16:** (left) Capillary pressure-saturation-relation and (right) relative permeability functions.

---

\*VEGAS (Versuchseinrichtung zur Grundwasser- und Altlastensanierung) - Research Facility for Sub-surface Remediation of the University of Stuttgart

## 6.3 Numerical study of slope instabilities under different hydraulic and mechanical loading scenarios

In this subsection, the influence of capillary and flow effects on the deformation and stability behaviour of slopes is investigated. To this end, using the previously described and calibrated triphasic TPM model, numerical simulations of a technical-scale sand slope under different loading and hydraulic conditions are carried out and compared.

### 6.3.1 The slope conditions

A sketch of the slope is depicted in Figure 6.17 (left). The boundary conditions of the slope problem are adapted in such a way that they mimic the supposed mechanisms which might trigger real hillslope instabilities. In particular, the following boundary conditions have been implemented: a uniformly distributed mechanical load (force controlled) excited by a rigid but movable loading platen on top of the slope to determine the maximum failure load  $q_{max}$  as an indicator of the slope stability. Moreover, hydraulic conditions are prescribed by independently increasing or decreasing the water head on the left ( $h_{wl}$ )

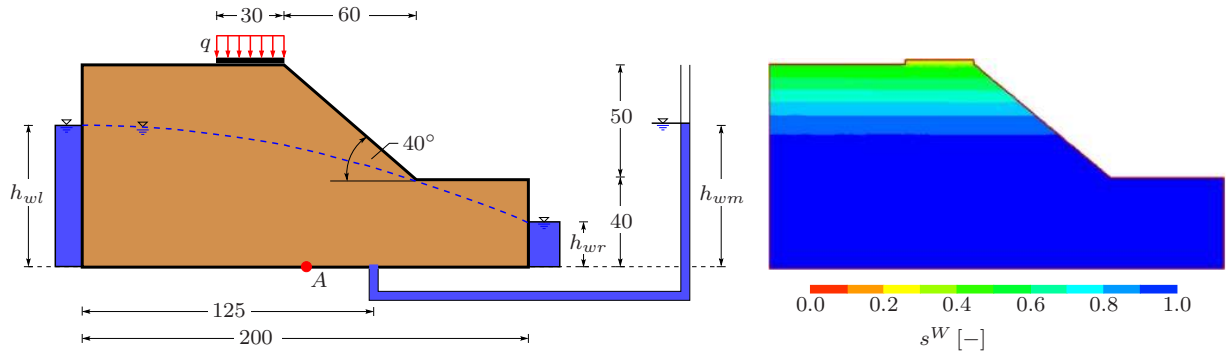


**Figure 6.17:** (left) Geometry and dimension of the slope in centimetres and (right) computed water saturation for a water table on the left side of the slope ( $h_{wl}$ ) = the water head on the right side of the slope ( $h_{wr}$ ) = 10 cm;  $q$  is the mechanical load and  $s^W$  is the water saturation.

and the right ( $h_{wr}$ ) boundary of the slope or by increasing the pore-water pressure at the bottom under the slope intersection ( $h_{wm}$ ). Please note that the considered GEBA sand is very fine and exhibits a distinct partial saturated zone of about 100 cm. Accordingly, proceeding from a constant water head of  $h_{wl} = h_{wr} = 10$  cm as the initial condition for the unsaturated slope simulations, the domain is more than 80 % saturated with water up to a height of about 58 cm, cf. Figure 6.17 (right).

The computations were carried out by using the same discretisation of the domain for all slope cases, cf. Figure 6.18. The part of the slope where the expected shear band develops is much finer discretised in order to be closer to the right solution. The complete number of the triangle finite elements amounts to 11 347. Based on the quadratic ansatz functions for the displacement  $\mathbf{u}_S$  and the linear interpolation approach of the fluid pressures  $p^{WR}$  and  $p^{AR}$ , the fine discretisation of the slope leads to a high number of degrees of freedom

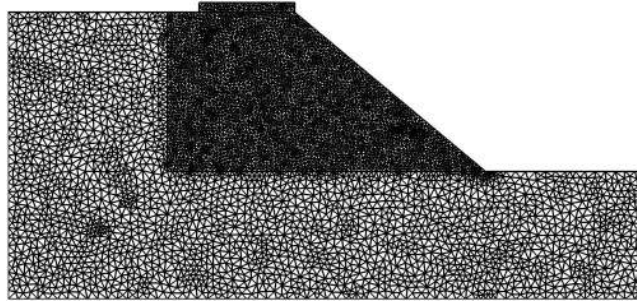


**Figure 6.18:** FE mesh with 11 347 triangle elements.

(dof) of 147 511 and, therewith, to a high computation time. But the good resolution of shear bands confirms the choice of the fine mesh.

### 6.3.2 Numerical results and discussion

In Table 6.1, all computed failure scenarios are listed, where for all cases the load is applied linearly increasing with time,  $q(t) = 10t$  kPa/min. In addition to the partially saturated conditions, the dry case without considering the water phase using a reduced

parameter	case Dry	case A	case B	case C	case D
$h_{wl}$ [cm]	–	10	65	10	10 (initial)
$\dot{h}_{wl}$ [cm/s]	–	10	11/600	–	11; 11/600
$h_{wr}$ [cm]	–	10	10	10	10
$\dot{h}_{wm}$ [cm/s]	–	–	–	11; 11/600	–
$t_{hyd}$ [s]	–	–	–	30.8; 264	20.7; 647
$q_{max}$ [kPa]	$\approx 138$	$\approx 230$	$\approx 153$	$\approx 220$	$\approx 220$

**Table 6.1:** Boundary values and loading data of the investigated slope scenarios.

biphasic model was numerically investigated. The slope in the dry case and the cases A and B is loaded until failure, but in A and B only after reaching a stationary water table controlled by  $h_{wl}$  and  $h_{wr}$ . In contrast, the cases C and D are first loaded by  $q$  to a maximum of 220 kPa, which is below the failure load of case A, and afterwards subjected to changes in the hydraulic conditions. In particular, in case C, the water head below the slope intersection is increased with two velocities of  $\dot{h}_{wm} = 11$  cm/s (the fast case) and  $(11/600)$  cm/s (the slow case) starting from the initial water table of 10 cm, while the water head at the left and right side of the slope is kept constant at  $h_{wl} = h_{wr} = 10$  cm. In case D, the water level on the left side is increased in the same way as case C with the water head velocity  $\dot{h}_{wl} = 11$  cm/s and  $(11/600)$  cm/s.

It becomes directly apparent from the failure loads in Table 6.1 that there is a significant influence of the water saturation. Comparing the dry case with case A, there is an increase of the maximum load prior to failure of about 92 kPa (66,7 %) which can only be explained by the stabilising capillary pressure effects in the partially saturated zone. Even in case B, where the pore-water flow driven by the hydraulic gradient destabilises the slope, the computed peak load is still 15 kPa (10,9 %) above the one of the dry case.

In Figure 6.19 (left), the water table at failure for case A is visualised, which shows a slight drawdown under the slope. This can be explained by the fact that a dilatant shear band develops sucking pore water from the surrounding into the localisation zone, which is confirmed by the streamline pathways depicted in Figure 6.19 (right). In Figure 6.20, the water table, the streamlines and shear bands of case B are given. Also in this case, the

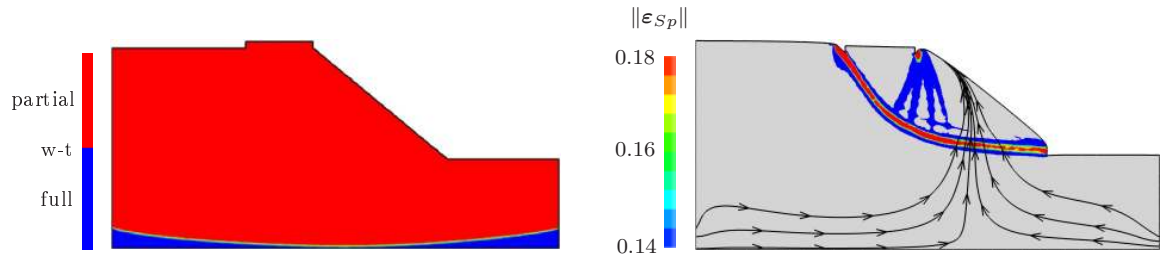


**Figure 6.19:** Case A at time 1389s: (left) water table (w-t) at slope failure and (right) streamlines of water seepage flow and shear band.

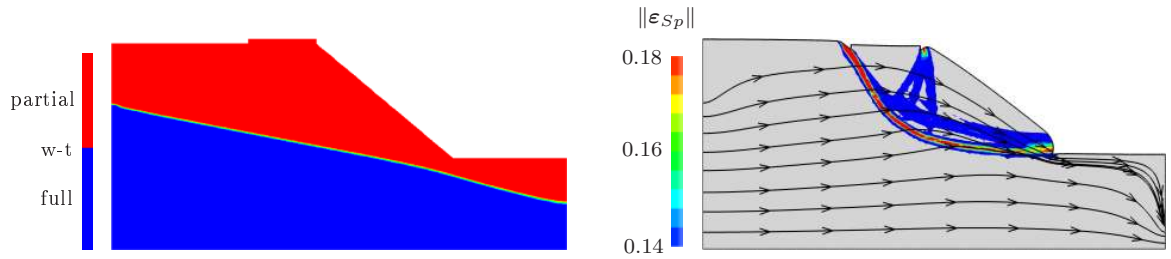


**Figure 6.20:** Case B at time 1290s: (left) water table (w-t) at slope failure and (right) streamlines of water seepage flow and shear band.

accumulation of dilatant plastic strains yields a destabilising shear band which develops faster than in case A because of buoyancy and flow effects induced by the increased water head at the left boundary. Please note that the maximum value of  $h_{wl}$  is chosen such that the water table does not exceed the slope intersection to avoid the erosive leak of water at the slope side. From the streamlines of the water seepage flow (Figure 6.20, right), it is clearly seen that the pore water flows from the left to the right side through the slope without passing the slope intersection. Moreover, it is observed that the streamlines at the left side of the slope move upwards because of the capillary effects and of the evolving dilatant shear band. The suction of water into the dilatant shear zone is not that much pronounced as in case A as this effect is superposed by the pore-water flow driven by the potential difference.

In case C, after applying the top load of 220 kPa, an increase of the pore-water pressure under the slope intersection triggers the destabilisation of the slope. The pressure source is located 125 cm away from the left boundary of the slope as depicted in Figure 6.17 (left) and has a width of 5 cm. In case D, the water head  $h_{wl}$  at the left boundary of the

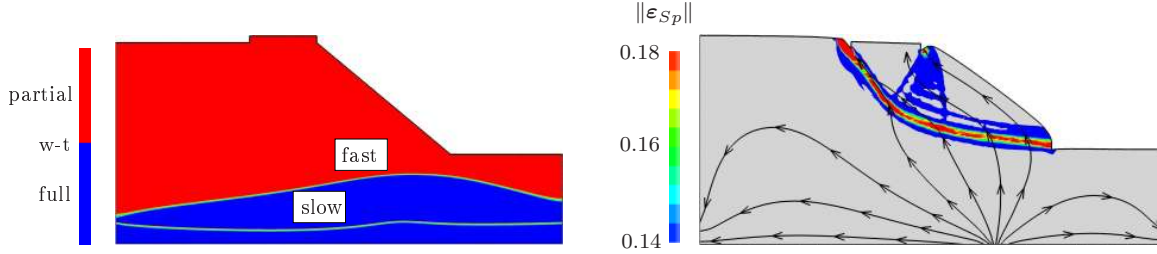


**Figure 6.21:** Case C: (left) water table (w-t) at failure (higher dividing line:  $\dot{h}_{wm} = 11 \text{ cm/s}$ ; lower line:  $\dot{h}_{wm} = (11/600) \text{ cm/s}$ ) and (right) streamlines of water seepage flow and shear band at 30.8 s after increase of the load (the fast case).

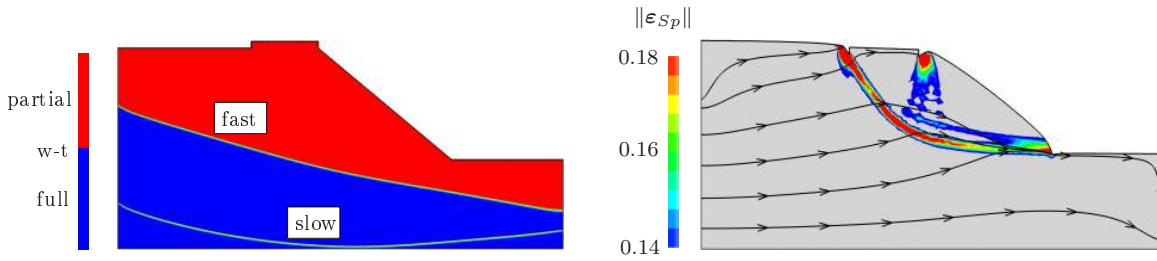


**Figure 6.22:** Case D: (left) water table (w-t) at failure (higher dividing line:  $\dot{h}_{wm} = 11 \text{ cm/s}$ ; lower line:  $\dot{h}_{wm} = (11/600) \text{ cm/s}$ ) and (right) streamlines of water seepage flow and shear band at 20.7 s after increase of the load (the fast case).

the slope is increased. For both cases, the maximum achievable height of the water head is 65 cm, which is applied within different time intervals in order to find out if a fast increase of the pore-water pressure or the water head, respectively, has any influence on the stability habits of the slope. It is observed that the slope failure triggered by a slow increase ( $11/600 \text{ cm/s}$ ) of  $\dot{h}_{wm}$  and  $\dot{h}_{wl}$  in cases C and D, respectively, occurs at a lower water table than for a fast increase ( $11 \text{ cm/s}$ ) as depicted in Figures 6.21 (left) and 6.22 (left). Apparently, the slope instability is not only dependent on the absolute height of the water table but also on the increase rate of the pore pressure or the water head, respectively. Transferring this finding to real hillslopes may explain why landslides also happen during or after long-lasting but moderate rainfall events associated with a slow but continuous increase of the water table.

To illustrate the shear band development, the accumulated plastic strains at different time states for case C are shown in Figure 6.23. As can be seen, the shear band originates from the load platen and from the intersection of the slope, which finally join together building a smooth slip line, whereby the shear band proceeding from the slope intersection mainly evolves. After the mechanical load is applied, only marginal plastic deformations occur at the load platen, which do not affect the overall stability of the slope before the



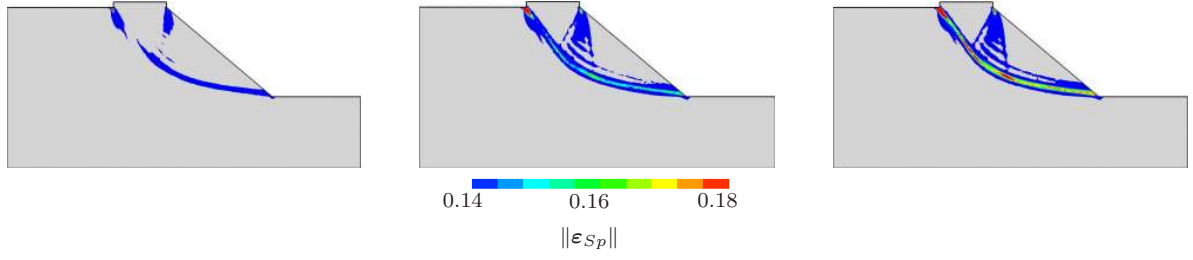


**Figure 6.23:** The accumulated plastic strains  $\|\epsilon_{sp}\|$  of Case C (the 5-s case): (left) the intermediate state at 20.7s and (middle) 27.3s after applying the load, and (right) the state at failure at 29.4s.

hydraulic loading is initiated. Figure 6.23 (left) depicts the beginning of the shear-band development after the first 20.7s of the hydraulic loading process, which in the course of the continuously increased water pressure develops very fast within the next 7-9s until failure (Figure 6.23, right). In these stress-controlled simulations, the failure point has been defined as the state, where a sudden displacement increase of the load platen is observed. In fact, test case C was born from the idea that some natural slopes may get unstable due to an inherent confined water system that directly responds to rainfall events with a sudden pressure increase under the slope intersection.

In Figure 6.24, the load-settlement curves of the load platen are plotted for all cases of Table 6.1. Clearly, the curves underline the aforementioned considerable positive influence of the capillary effects on the slope stability. Regarding the time-settlement  $u-t$  and time-

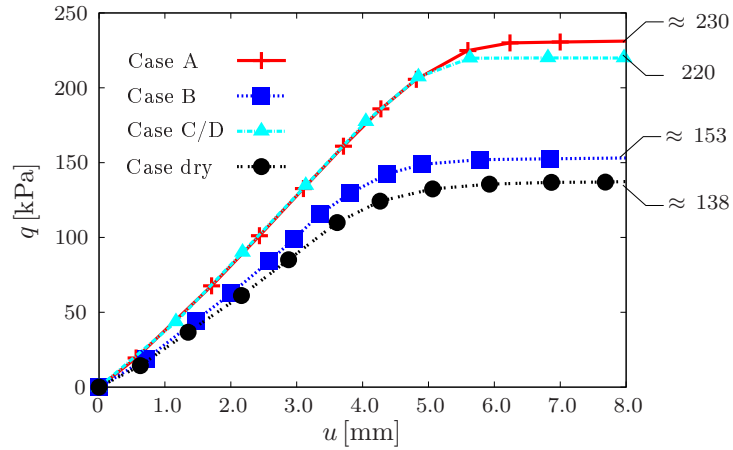


**Figure 6.24:** Load-displacement curves of the load platen;  $q$  is the mechanical load and  $u$  is the vertical displacement.

water-pressure  $p^{WR}-t$  curve in point A (see Figure 6.17) of the load platen of cases C and D plotted in Figure 6.25, it is observed that the failure behaviour is rather dependent on the increase rate of  $\dot{h}_{wm}$  or  $\dot{h}_{wl}$ , respectively, than on the type of the hydraulic boundary condition. Therein, lines with triangles are the fast cases and that ones with squares are the slow cases of hydraulic loading. It is clearly recognisable that the slope failure is induced with a fast increase of the water head at a higher water table. Moreover, in

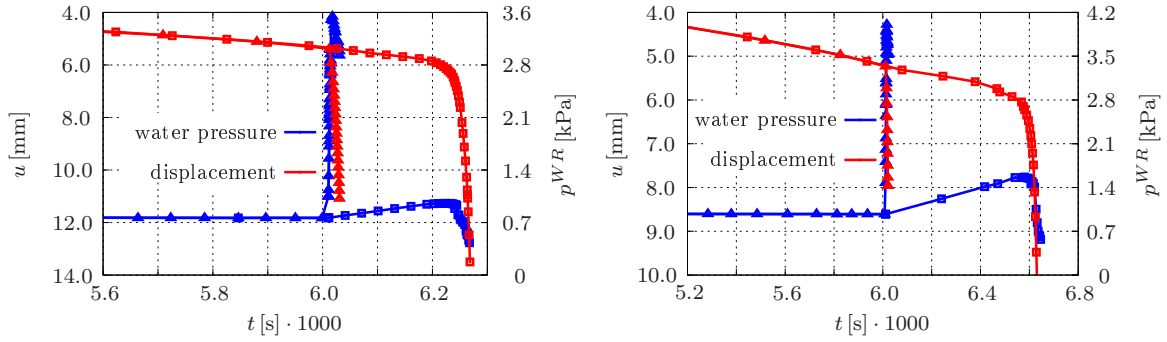


**Figure 6.25:** Displacement and water pressure in point A (see Figure 6.17) versus time proceeding of (left) cases C and (right) case D.

case C, the failure of the fast one occurs in 30.8 s, while, in case D, it occurs in 20.7 s. However, for the slower case C, the failure happens (264 s) much earlier than in case D (647 s). The reason therefore could be that in case D, the fast increase of the water table weakens almost the whole slope due to the high water table, while the influence in case C is constrained to the local surrounding at the water injection point near the slope intersection. In contrast, the slow case C fails clearly rather (264 s) and at lower pore water pressure  $p^{WR} \approx 1$  kPa in point A (Figure 6.24) as the corresponding case D (647 s) and ( $p^{WR} \approx 1.55$  kPa). The reason for this is that the slope intersection reacts more sensitive to the loading of case C than of case D. Therefore, the slope fails earlier and at a lower pore-water pressure.

Furthermore, the water pressure drops rapidly with an evolving dilatant shear band. The pressure drop in the vicinity of the shear band may be a signal for the development of a slope failure due to a continuous increase of plastic deformations. This phenomenon may be used as a failure indicator for potentially dangerous natural slopes (Ehlers et al. [57] and Germer and Braun [77]). The coherences between a pore-water pressure drop and the slope movement can be detected in the field of natural slopes and has to be found out by detailed field investigations via long-term monitoring systems.

Although our numerical results are physically sound and clearly reveal the considerable influence of capillary and flow processes on slope instabilities, there is still the need of experimental evidence to verify our findings on a quantitative basis. Therefore, our research partners from VEGAS constructed a technical-scale sand slope experimental setup for testing the presented cases (see Germer and Braun [76, 77]).

# Chapter 7:

## Numerical Investigation of a Slow-Moving Landslide

In this chapter, a numerical investigation of a natural hillslope is presented. The slope under study is the ‘Heumös’ hillslope, which is continuously moving with a low motion rate. It is of utmost interest to know, under which boundary and loading conditions a sudden landslide may happen. Therefore, to investigate the characteristics of this slope motion, a DFG founded Research Unit\* was founded in 2006. Regarding the complexity of the coupled flow and deformation processes and geological structure of the Heumeos hillslope demands an interdisciplinary research team consisting of specialists in their individual research field of hydrology, geologic, geophysics and computational geomechanics.

The chapter begins with a brief introduction of the general characteristics of the hillslope, where detailed geological information on the Heumös slope can be found in the work of Lindenmaier [107] and Wienhöfer et al. [178]. The idealisation process of the slope for a numerical treatment is still a great challenge due to the high complexity of the hydraulic processes, the slope geometry and its strongly heterogeneous material distribution. For that reason, numerical investigations of the Heumös hillslope have been firstly restricted to 2-d model approaches along a significant cross section. This cross section has been profoundly investigated and structured by Rumpf et al. [131], while Ehlers et al. [57] have numerically examined a simplified cross section of the slope based on Lindenmaier [107]. Due to missing of some important substructural and geometrical information, the deformation process of the Heumös slope could not be correctly reproduced on the basis of this cross section.

### 7.1 Characteristics of the hillslope

The Heumös slope near the village Ebnet shown in Figure 7.1 is located in the Vorarlberg Alps in Austria close to the city Dornbirn. The slope has a length of about 2 km, a width of 500 m and spans a height difference of 400 m. The hillslope body is very heterogeneous with the slope material consolidated in the Rhine Glacier period for more than thousand years, where the slope was covered with an ice layer thickness up to 1000 m. In Figure 7.2, the motion rates of the slope are marked with red ellipses. Therein, the slope is categorised in three parts depending on the motions rates (Depenthal and Schmitt [37]). The northern part of the slope is moving downhill to the east with a measured cumulative surface displacement of about 10 cm per year, whereas the lower part is more active with

---

\*The Research Unit 581 with the title ‘Coupling of flow and deformation processes for modelling the movement of natural slopes’ has been founded to investigate the slow-motion process of the Heumös hillslope. This project was supported by the Deutsche Forschungsgemeinschaft (DFG). Detailed informations concerning the project can be found at <http://www.grosshang.de>.



**Figure 7.1:** The Heumös slope in Ebnet, Vorarlberg (Austria): (left) the view from north to south and (right) from east to west.

a slope motion rate over 10 cm per year, while the middle part is almost fixed. However, there is no distinct indication that large precipitation depths better correlate with the slope movement than moderate but long-lasting rainfall events. Nano-seismic monitoring rather reveals an almost continuous ‘creep flow’ of the hillslope but with varying velocities (Figure 7.2), which, however, cannot be associated with the observed hydrological signals (Walter et al. [169]). Based on the long-term measurements and observations over the past 15 years, it is supposed that the movement is mainly triggered by a confined aquifer system under the slope, which is fed by a fast infiltration region at the southern hillside (Wienhöfer et al. [178]). The precipitation on the slope surface could mostly not infiltrate into deeper regions of the slope body, because of the low permeability of its superficial soil stratum. Therefore, most of the surface water flows off into the creeks. The increase of the water table in the confined aquifer observed by piezometric head measurements results from subsurface flow of water infiltrating from the macro pores and fissures in the forest soil at the immobile steep arboreous southern slope. The complex hydrological

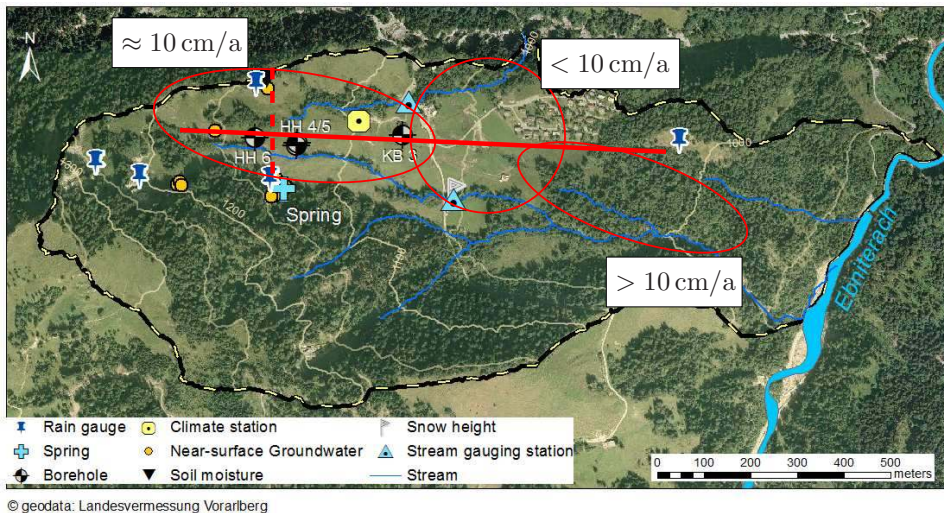


**Figure 7.2:** Topview of the Heumös slope: annual average mass movement of the slope measured at the slope surface (Depenthal and Schmitt [37]); the red line from west to east represents the investigated cross-section and the dotted red line illustrated the north-south cross-section (Ehlers et al. [57]); HH4, HH5 and HH6 are boreholes.

situations, which are believed to govern the motion behaviour of the Heumös slope, are described and discussed in more detail in the works by Lindenmaier [107] and Wienhöfer et al. [178].

However, by observing the slope surface, several shear bands can be detected. Hence, it can be concluded that the hillslope is not consisting of a monolithic slip body. Instead, it behaves as a slope body which is segmented into several small sliding bodies. Certainly, this statement has to be still experimentally verified.

## 7.2 Idealisation of the hillslope to a 2-d cross section

In Figure 7.2, a sketch of the slope in topview is shown. The red line represents the cross section through the slope, which intersects close to the point of the boreholes HH4 and HH5. The structural information of the slope cross section depicted in Figure 7.3 have been determined by Rumpf et al. [131] applying refraction seismic methods. Thereby, the identified topography of the slope bedrock shows very hilly progression compared to the assumption of Lindenmaier [107]. Moreover, Rumpf et al. [131] structured the slope in three stratum, where the differentiation of the stratum has been based on the p-wave (primary wave) velocity differences. However, p-waves only give qualitative statements of the density variation of the slope material, i. e., the boundary stratum is not unconditionally the boundary of a specific material type. Nevertheless, for the simulation, only the upper two strata are considered, while the bedrock is assumed to be rigid and is modelled as a fixed kinematic boundary condition of the middle stratum.

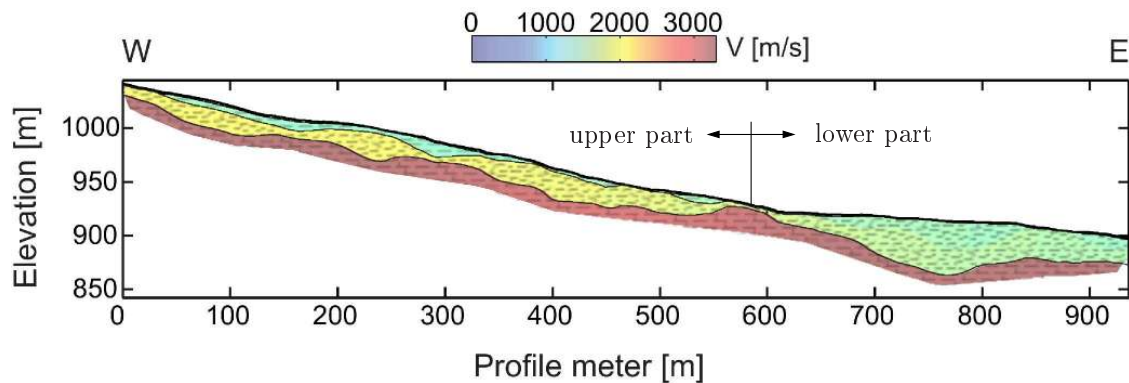


**Figure 7.3:** The substructure of the investigated cross-section is subdivided into three strata determined by refraction seismic (Rumpf et al. [131]).

Furthermore, at the point about 580 m of the slope (see Figure 7.3), the bedrock increases very closely to the slope surface and impedes further mass movement of the upper slope part. Comparing this statement with the detected surface movements at the middle red ellipse in Figure 7.2, there have also been detected very low deformation rates (Rumpf et al. [131]). As a consequence, the upper and lower movement of the slope can be analysed in a decoupled fashion with regard to the fixed barrier. In this contribution, the upper part of the Heumös slope illustrated in Figure 7.3 is numerically studied concerning a 2-d model approach of the slope.

The slope material composition can be roughly summarised into two different material types of clayey silt and sand, which are assumed to be homogeneously distributed over the corresponding stratum, respectively. Comparing both stratum, the top stratum (clayey silt) is more impermeable and has more cohesion, but owns a lower material strength because of the smaller friction angle than the middle stratum (sand). However, due to the lack of detailed material data, for the first qualitative simulations, the GEBA-sand material-parameter sets given in Tables C.1 and C.2 are applied for both stratum, whereas, for the top stratum, only the following material parameters are changed concerning to the mentioned general physical differences between both stratum, where the original GEBA-sand parameters are noted in the brackets:  $K_{0S}^S = 5 \cdot 10^{-14}$  ( $2 \cdot 10^{-10}$ )  $\text{m}^2$ ,  $\kappa = 0.015$  (0.004) MPa and  $\beta^* = 0.16$  (0.266). Following this, the cross sections are spatially discretised by triangular finite elements, where an adaptive meshing strategy with respect to the error indicator of the water saturation  $s^W$  and the accumulated plastic deformations  $\|\epsilon_{Sp}\|$  is used during the simulations in order to accurately resolve the water table and the shear bands.

In the last several years, the heaviest precipitation event was in the year 2006 with 248 mm precipitation in 38 h (Wienhöfer et al. [178]). Based on this value and a deduction of the surface runoff and the evapotranspiration, Ehlers et al. [57] have taken an effective pore-water pressure related to an infiltration rate of 80 mm/wk prescribed over distinct regions along the northern and southern hillside of the north-south cross section (red dotted line in Figure 7.2) representing the fast infiltration areas, whereas along this cross section no deformation have been observed under the applied loading conditions. The infiltrated subsurface water is dammed in the middle of the slope section and flows downhill along the west-east cross section (red line in Figure 7.2) and increases the water table. The impound water under the west-east extent of the slope is modelled by a high pore-water-pressure increase associated with an infiltration rate per week (wk) of accumulated  $\dot{h}_{pw} =$

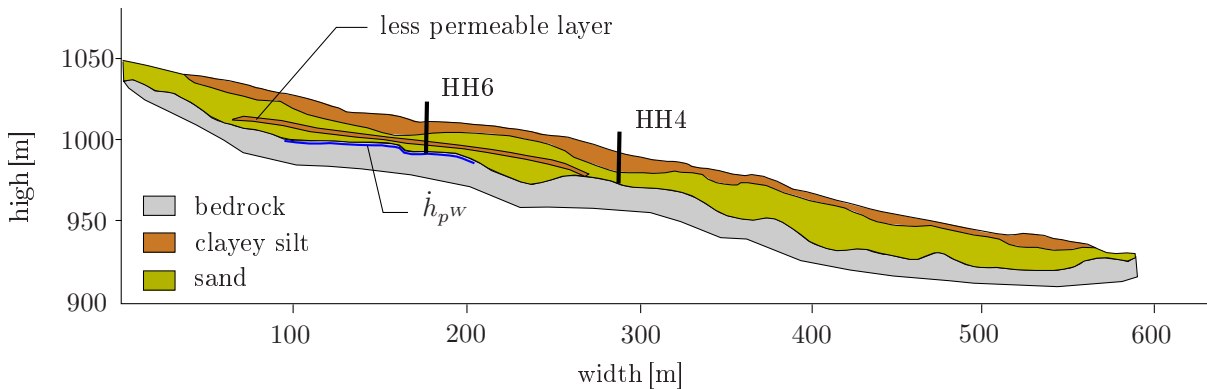


**Figure 7.4:** Representative cross-section through the Heumös slope from west to east;  $\dot{h}_{pw}$  is the pore water infiltration rate per week.

3500 mm/wk in the upper part of the west-east cross section along the extent of the southern hillside. The hydraulic boundary conditions for the numerical treatment are chosen in the way as illustrated in Figure 7.4 to mimic the described situation at the Heumös slope. Furthermore, the impermeable or less permeable layer is integrated into the middle stratum in order to model a confined aquifer situation presumed by Wienhöfer

et al. [178]. However, such an impermeable layer could not be detected by Rumpf et al. [131]. Nevertheless, the Heumös slope has been numerically studied without and with the less permeable layer for which the same material as of the top stratum was adopted.

## 7.3 Numerical results and discussion

### Computations without an impermeable layer

For a numerical study of the flow and deformation processes of the Heumös slope, the current ground water table and the current state of slope deformations induced, for instance, by the gravitation force have to be approximated. The computation starts with an unstressed soil material, where the ground water table and the gravitation force are continuously increased until their correct values are reached. During these load steps, plastic deformations are developed due to the dead load of the slope and buoyancy forces. The simulated current (initial) state ( $t = t_0$ ) of the Heumös slope presented in Figure 7.6 (top) shows irreversible plastic deformations, while the corresponding initial saturation  $s^W$  is illustrated in Figure 7.5 (top).

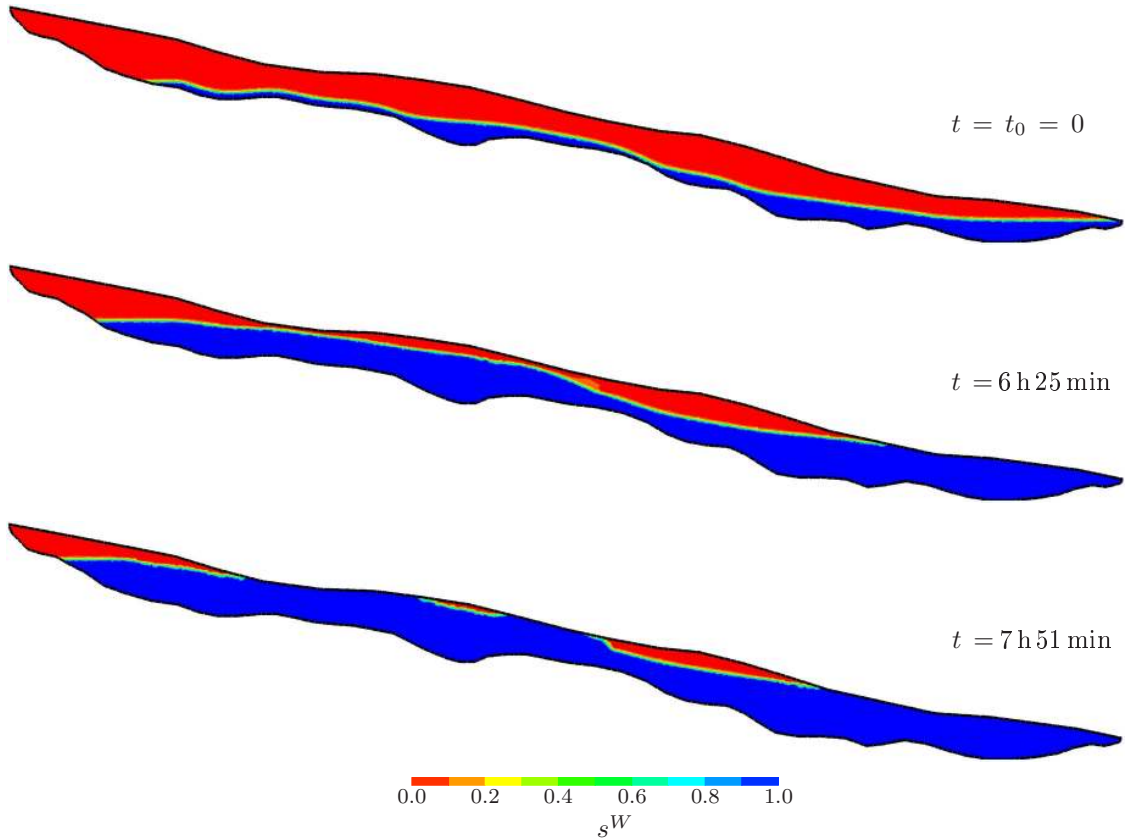


**Figure 7.5:** Evolution of the water saturation  $s^W$ .

The localisation of shear bands under a dead load is mainly concentrated at the step part of the bedrock substructure. With increase of the water head  $h_{pw}$ , only little increase of plastic deformations can be observed, although the water table is close to the surface,



cf. Figure 7.5 (middle) and 7.6 (middle) at time 6 h and 25 min counting from the initial state. Further rise of the water head leads to increasing plastic deformations of the already existing shear bands. Additionally, several new shear bands are developing, cf. Figure 7.5 (bottom) and 7.6 (bottom). In particular, the initiation of the new shear bands is concentrated in the aforementioned steep part of the bedrock as well as at the border of the clayey silt and sand stratum. The rigidity difference between both stratum induces deformations resulting from kinematic constraints. Thus, these two factors mainly represent the weakened zones of the Heumös slope.

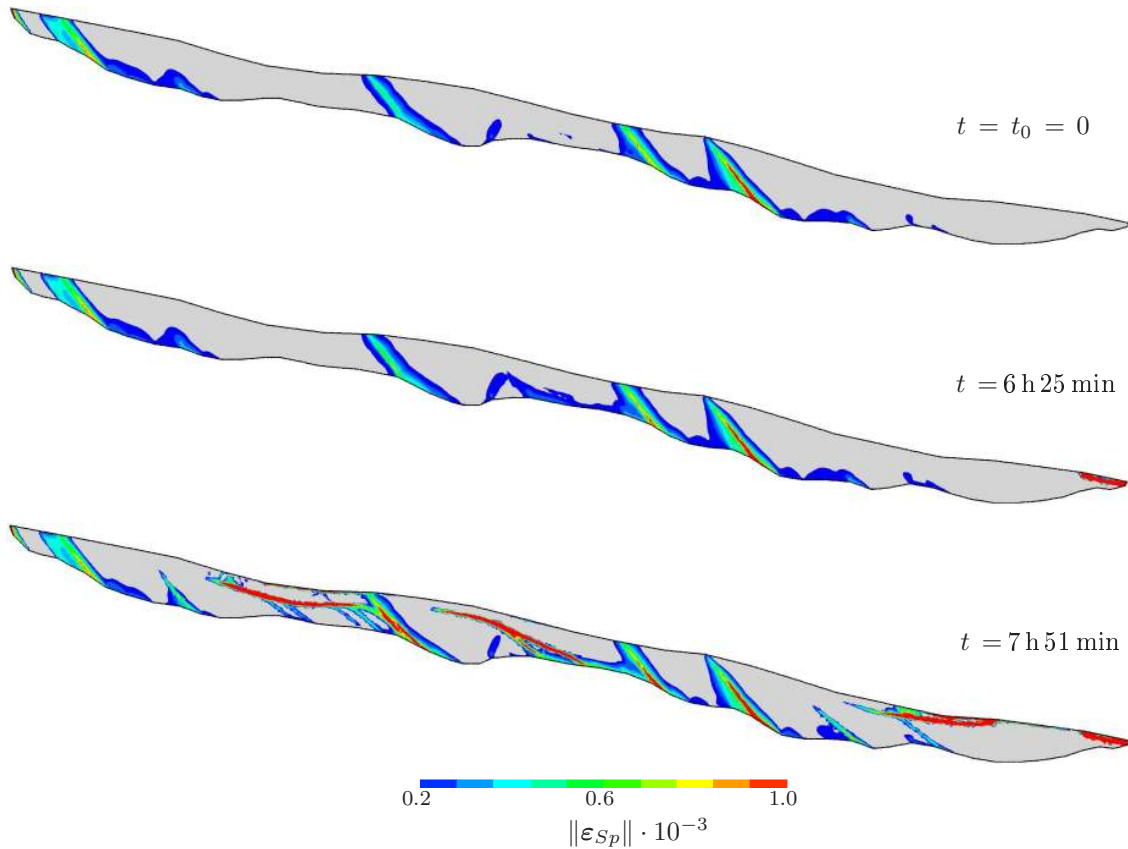


**Figure 7.6:** Evolution of shear bands determined by the accumulated plastic strains  $\|\varepsilon_{Sp}\|$ .

**Remark:** Due to the flat slope inclination with an average of  $19^\circ$ , the slope motion is mainly triggered by increasing the saturation degree, because of the growing dead load. Consequently, this leads to a further increase of plastic deformations. Indeed, the deformation rates are very small in comparison to slopes with steep inclination, which, consequently, prone to fail abruptly. The simulation results of the Heumös slope mimic a creeping slope motion, which is segmented into several independent parts with varying motion rates. The resulting shear-band structure of the slope shows that a monolithic slope body does not exist. It can be carefully asserted that it is not necessary to expect a sudden failure of the Heumös slope.

### Computations with impermeable layer

Figure 7.7 shows the simulation results with integration of a less permeable stratum within



the middle stratum in order to analyse a confined pressure situation of the Heumös slope. By comparison of the developed shear-band structures in Figure 7.7 (top) with those in Figure 7.6 (bottom), only few differences can be observed in the region of the additional stratum, but almost the same water-saturation distribution exists after 8 h and 35 min, cf. Figure 7.7 (bottom).

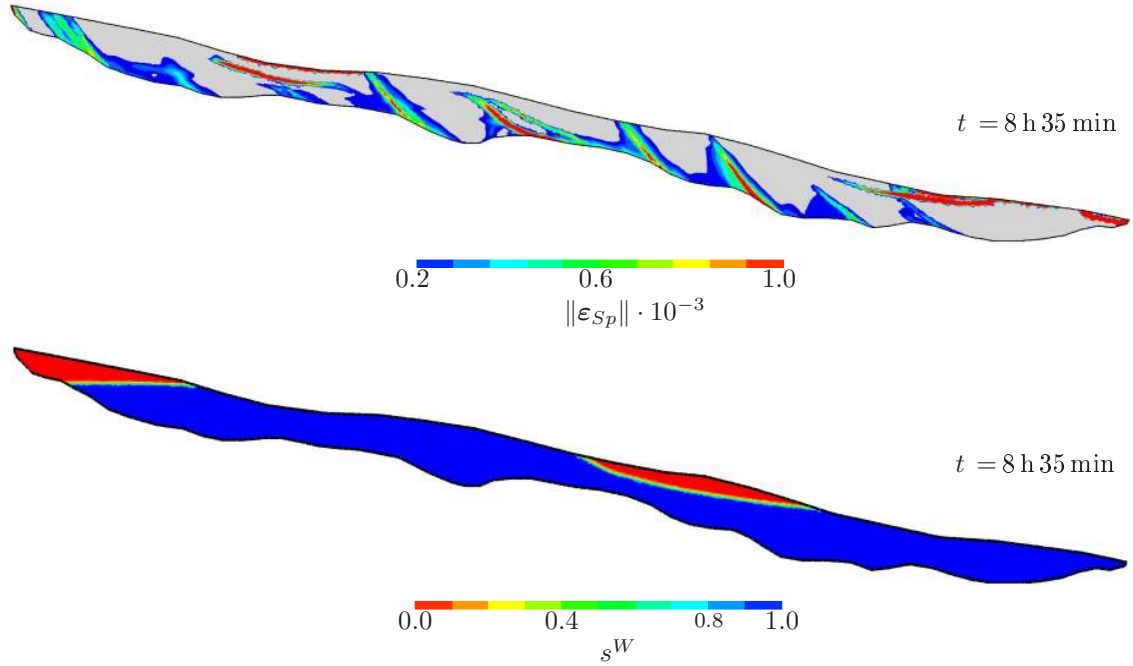


**Figure 7.7:** (top) Developed shear bands and (bottom) the corresponding water saturation.

**Remark:** For the case that slope deformations are triggered by a highly confined aquifer, some conditions have to be fulfilled by the slope, which may not exist at the Heumös slope. This means that the pore-water-saturated stratum of the subsurface has to be entirely sealed by a water-impermeable stratum in order to dam the influx of pore water resulting from, e. g., a heavy rainfall event, at the saturated stratum. Considering the case that the water-saturated stratum is only sealed in the upper direction by an impermeable stratum, the pore-water pressure must increase rapidly, otherwise, the water-saturated stratum acts as an aquifer. Thus, the pore-water pressure continuously increases until a pressure situation is reached by which the pore spaces of the saturated soil stratum are enlarged. Accordingly, this soil-expansion process leads to slope deformations. However, due to the high dead load of the slope, a very high pore-water pressure within the saturated soil stratum is needed in order to trigger these soil deformations. In regard to the Heumös slope, such a high confined pressure situation as described could not be observed.



## Chapter 8:

# Modelling Internal Soil Erosion

In this chapter, an internal soil erosion model for partially saturated soil is presented. Proceeding from the triphasic soil model discussed in Chapter 4, an erosion phase is introduced. It represents the grains, which are detached from the grain matrix by the streaming pore water. These grains can be considered as fluidised grains transported by the pore water. The modelling approach for the soil erosion is based on the work of Steeb and Diebels [151]. They have introduced a triphasic internal-erosion soil model for saturated soils derived in a thermodynamic consistent manner within the framework of the TPM. Therefore, the internal erosion model presented in this chapter is only restricted to the subjects of the idealisation of the erodible soil, governing balances and constitutive equations. Applying this model, several numerical problems of soil piping, cold (sand) production for quarrying oil-sand mixture by loading of a high fluid pressure and two embankment failure scenarios are investigated. By the reason of the complexity of the internal erosion process, several simplifications of the erosion model have been made in order to compute, in particular, the embankment problems without undertaking major modification of the partially saturated soil model. Concerning this, the main simplification is, for example, that the transport of the detached grains from the soil matrix is not further considered. Hence, the focus here is not lying in the complete and preferably accurate description of the erosion process with regard to the movement and the deposition of grains as well as the clogging of pores, but rather in the development of soil porosity. Due to the growing porosity, the mechanical and hydraulic soil behaviour are affected and, as a consequence, the probability of embankment or dam failure increases.

### 8.1 Restrictions of the erosion-soil model

The amount of the eroded grains, which are locally detached through the streaming pore water (seepage velocity), can total up to several percent of the solid volume, but they are distributed relatively fast in the streaming pore water. Therefore, the density of the pore fluid is assumed to correspond approximately to the pore-water density and, furthermore, the motion of the pore fluid behaves like the streaming pore water with occupying the same flow velocity. Proceeding from this, the fluidised grains and the pore fluid can be treated together as one pore fluid. In this context, the clogging of pores and the deposition of the fluidised grains are not considered. Moreover, these and further assumptions and restrictions made for the erosion model read:

- The susceptibility of the soil to the internal erosion can be determined on the basis of the soil-grain size distribution curve (GDS). The GDS temporally changes during the internal erosion process and, therewith, the susceptibility to internal erosion, too. This is not currently integrated within the applied continuum-mechanical soil

model, cf. [134].

- The pore water and the fluidised grains are considered as a suspension and summarised to the pore-liquid phase.
- The velocity of the suspension is assumed to be equal to the pore-water velocity.
- An increase of suspension viscosity through the eroded particles is not included.
- Fluid velocities are only restricted to linear *Darcy*-flow conditions.
- The grain-weight-dependent velocity of free moving grains within the pore liquid is not considered  $\rightarrow$  segregation of grains, cf. [167].
- Clogging of pore channels and deposition of detached grains are not considered.
- The transport of the fluidised grains is disregarded.

However, having in mind that, for a long-term analysis of constructions with repeatedly changing loading conditions, the transport of fluidised grains has to be taken into consideration, but also many other physical aspects. As mentioned in the introduction of this chapter, the presented erosion-soil model is preferably kept simple in order to get a better comprehension of the physical interacting processes of soil deformation, fluid flow and growing porosity induced by internal erosion within embankments.

## 8.2 Partially saturated soil-erosion model

Taking into account the detachment of grains from the solid structure, the soil model is extended by the erosion constituent  $\alpha = E$  representing the fluidised grains. The detached grains are distributed within the pore water and are generally perpetually in motion as long as the pore-fluid velocity is able to transport them through the pore channel network of the soil. The free moving grains behave as a liquid or a disperse phase within the water phase like a suspension. Following this, the erosion phase  $\varphi^E$  and the water phase  $\varphi^W$  can be summed up to a liquid phase  $\varphi^L$ , where  $\varphi^E$  and  $\varphi^W$  are the liquid components, respectively. Therewith, the overall aggregate consists of  $\varphi = \varphi^S \cup \varphi^A \cup \varphi^L$ , which corresponds to the description of the well-known triphasic model presented in Section 4.1. Proceeding from this, the local composition of the volume fractions yields

$$\sum_{\alpha=1}^k n^{\alpha} = n^S + n^A + n^L = n^S + n^A + n^W + n^E = 1. \quad (8.1)$$

Therein, the volume fraction  $n^L$  of the liquid suspension phase is composed of  $n^W$  and  $n^E$ , while the soil porosity is computed by

$$n^F = \sum_{\beta=1}^l n^{\beta} = 1 - n^S = n^A + n^L, \quad (8.2)$$

where  $\beta$  represents the fluid components  $\beta = \{A, L\}$ . Due to the fact that the model of the internal erosion is only restricted to model the porosity development, the same model approach of the partially saturated soil in (4.1) with the constituents  $\alpha = \{S, A, W\}$  is analogously applied for the erosion-soil model with  $\alpha = \{S, A, L\}$  by replacing  $\varphi^W$  with  $\varphi^L$ . Moreover, the diffusion velocities of the liquid components  $\mathbf{d}_{WL}$  and  $\mathbf{d}_{EL}$  are introduced, wherein the component velocities are referred to the liquid velocity  $\dot{\mathbf{x}}_L$ , cf. (2.14)<sub>2</sub>.

### Balance of mass

By integrating analytically the local mass balance in (2.42)<sub>1</sub> using the helpful hint\*, the density of the constituent  $\varphi^\alpha$  yields (cf. Ehlers et al. [65])

$$\rho^\alpha = \rho_{0\alpha}^\alpha \exp \left( \int_{t_0}^t \frac{\hat{\rho}^\alpha}{\rho^\alpha} dt \right) (\det \mathbf{F}_\alpha)^{-1}, \quad (8.3)$$

where  $\rho_{0\alpha}^\alpha$  is the initial density in the reference configuration. Depending on the condition of the mass production  $\hat{\rho}^\alpha > 0$  or  $\hat{\rho}^\alpha < 0$ , the density  $\rho^\alpha$  grows or degenerates, respectively. A more general expression of (8.3) is derived by a multiplicative split into a deformation-governing process and a mass-production process:

$$\rho^\alpha = \rho_{t\alpha}^\alpha (\det \mathbf{F}_\alpha)^{-1} \quad \text{with} \quad \rho_{t\alpha}^\alpha = \rho_{0\alpha}^\alpha \exp \left( \int_{t_0}^t \frac{\hat{\rho}^\alpha}{\rho^\alpha} dt \right). \quad (8.4)$$

Therein,  $\rho_{t\alpha}^\alpha$  can be interpreted as the density of a constituent at time  $t$  in the fictive reference configuration or the intermediate configuration. This deformation-free part enables to keep the geometrical compatibility analogical to the finite elasto-plasticity (Haupt [84] and Ehlers [48]). Thus, the total deformation gradient  $\mathbf{F}_{\alpha,tot} = \mathbf{F}_\alpha \mathbf{F}_{\alpha,gr}$  is multiplicatively separated into a deformation-free gradient  $\mathbf{F}_{\alpha,gr}$  describing the mass production process and a deformation-dependent part  $\mathbf{F}_\alpha$ . Proceeding from a geometrically linear approach for the deformation gradient  $\ln(\det \mathbf{F}_S) \approx \operatorname{div} \mathbf{u}_S + 1 = (1 - \varepsilon_S^V)^{-1}$  and taking the incompressibility of the solid phase ( $\rho^{SR} = \text{const.}$ ) into account, the volume solid fraction  $n^S$  follows from (8.4) to

$$n^S = n_{tS}^S (1 - \varepsilon_S^V) \quad \text{with} \quad n_{tS}^S = n_{0S}^S \exp \left( \int_{t_0}^t \frac{\hat{n}^S}{n^S} dt \right), \quad (8.5)$$

where  $n_{tS}^S$  is the solidity at the intermediate state, while its change is induced by the volume solid production  $\hat{n}^S$ , and  $\varepsilon_S^V$  is the volumetric solid strain.

---

\*Using the expression  $\operatorname{div} \dot{\mathbf{x}}_\alpha = \frac{(\det \mathbf{F}_\alpha)'_\alpha}{\det \mathbf{F}_\alpha}$  and applying the separation of variables on the mass

balance (2.42)<sub>1</sub>, the following integration parts result:  $\int_{\rho_{0\alpha}^\alpha}^{\rho^\alpha} \frac{d\rho^\alpha}{\rho^\alpha} + \int_{\det \mathbf{F}_{0\alpha}}^{\det \mathbf{F}_\alpha} \frac{d(\det \mathbf{F}_\alpha)}{\det \mathbf{F}_\alpha} = \int_{t_0}^t \frac{\hat{\rho}^\alpha}{\rho^\alpha} dt$ .

Evaluating the sum of the mass production (2.41)<sub>1</sub> with assuming the same effective density  $\rho^{SR} = \rho^{ER} = \text{const.}$  for all grains, it follows that the volume productions of the solid and eroded phases are equal:

$$\sum_{\alpha=1}^k \hat{n}^{\alpha} = \hat{n}^S + \hat{n}^E = 0 \rightarrow \hat{n}^E = -\hat{n}^S, \quad (8.6)$$

whereas, the pore-water and pore-air phases are not involved in the mass exchange of the erosion process,  $\hat{n}^W = \hat{n}^A = 0$ .

The temporal change of the erosion phase resulting from the volume production  $\hat{n}^E$  and the grain transport is determined by the volume balance of  $\varphi^E$ ,

$$-\hat{n}^S = (n^E)'_S + n^E \operatorname{div}(\mathbf{u}_S)'_S + \operatorname{div}(n^E \mathbf{w}_E), \quad (8.7)$$

where  $\hat{n}^E$  is substituted by  $\hat{n}^S$  (8.6)<sub>1</sub>, or, additionally, related to the liquid motion using  $\mathbf{w}_E = \mathbf{w}_L + \mathbf{d}_{EL}$ :

$$-\hat{n}^S = (n^E)'_S + n^E \operatorname{div}(\mathbf{u}_S)'_S + \operatorname{div}(n^E \mathbf{w}_L) + \operatorname{div}(n^E \mathbf{d}_{EL}). \quad (8.8)$$

Both formulations are given with respect to the solid motion. Furthermore, for describing the suspension behaviour, the mass balances of  $\varphi^W$  and  $\varphi^E$  have to be summed up:

$$-\hat{n}^S \rho^{SR} = (\rho^{LR})'_S n^L + \rho^{LR} (n^L)'_S + \rho^{LR} n^L \operatorname{div}(\mathbf{u}_S)'_S + \operatorname{div}(\rho^{LR} n^L \mathbf{w}_L), \quad (8.9)$$

where the effective density  $\rho^{LR}$  is no more constant. It is varying with a change of  $n^E$ .

As mentioned, when only the modelling of the porosity development of the soil is the point of interest and not the transport process of fluidised grains itself, some principle assumptions can be made in order to simplify the governing equations, cf. Section 8.1. For example, following the fact that the fluidised grains are immediately dispersed within the water phase after detaching from the solid phase, it can be supposed that  $\rho^{LR} \approx \rho^{WR}$  is constant. As a result, the material time derivative of  $\rho^{LR}$  in (8.9) is dropped out of the equation. Hence, the mass balance of the liquid suspension (8.9) is reduced to the volume balance of a materially incompressible liquid phase:

$$-\frac{\rho^{SR}}{\rho^{LR}} \hat{n}^S = (n^L)'_S + n^L \operatorname{div}(\mathbf{u}_S)'_S + \operatorname{div}(n^L \mathbf{w}_L). \quad (8.10)$$

The motion of the fluidised grains within the pore-water phase with regard to grain separation by weights has been investigated by Vardoulakis [167]. However, by the reason that the erosion (suffusion) process is a slowly proceeding process, it is assumed in the first approximation to take the velocity of the pore water for the fluidised grains and to neglect the diffusion velocity  $\mathbf{d}_{EL}$ . This leads to  $\mathbf{w}_L := \mathbf{w}_W = \mathbf{w}_E$ .

Based on the assumption that the transport of fluidised grains is not considered in the following description of internal erosion using the volume balance (8.10), the volume fraction  $n^E$  is no more an independent quantity and is computed by  $n^E = n_{0S}^S - n_{tS}^S$ , while  $n_{tS}^S$  is determined by (8.5) governed by  $\hat{n}^S$  for which a constitutive assumption has to be formulated. Concerning the materially compressible air phase  $\varphi^A$ , the mass balance in (4.6)<sub>2</sub> is applied without any modifications.

### Balance of momentum

Following quasi-static problems ( $\ddot{\mathbf{x}}_\alpha \equiv \mathbf{0}$ ), the local momentum balance (2.42)<sub>2</sub> of the constituent  $\varphi^\alpha$  using the formulation with the direct production term  $\hat{\mathbf{p}}^\alpha$  (2.40)<sub>1</sub> leads to the following form:

$$\mathbf{0} = \operatorname{div} \mathbf{T}^\alpha + \rho^\alpha \mathbf{b}^\alpha + \hat{\mathbf{p}}^\alpha \quad \text{with} \quad \hat{\mathbf{p}}^\alpha = \hat{\mathbf{s}}^\alpha - \hat{\rho}^\alpha \dot{\mathbf{x}}_\alpha. \quad (8.11)$$

By the sum of all individual momentum balances given by (8.11)<sub>1</sub> and involving (2.41)<sub>2</sub>, the overall momentum balance of the erodible partially saturated soil yields

$$\mathbf{0} = \operatorname{div} (\mathbf{T}^S + \mathbf{T}^L + \mathbf{T}^A) + \rho \mathbf{b} + \rho^{SR} \hat{n}^S (\mathbf{w}_L + \mathbf{d}_{EL}). \quad (8.12)$$

Based on the applied restrictions of the internal erosion process,  $\mathbf{d}_{EL}$  is assumed to be zero. However, the momentum production term triggered by  $\hat{n}^S$  compared with the total stress  $\sum_{\alpha=1}^k \operatorname{div} \mathbf{T}^\alpha$  is several orders smaller. According to that it could be neglected as well.

**Remark:** Considering the overall aggregate  $\varphi$ , the sum of (8.11) reads

$$\sum_{\alpha=1}^k \rho^\alpha \ddot{\mathbf{x}}_\alpha = \sum_{\alpha=1}^k (\operatorname{div} \mathbf{T}^\alpha + \rho^\alpha \mathbf{b}^\alpha + \hat{\mathbf{p}}^\alpha), \quad \text{where} \quad \sum_{\alpha=1}^k \hat{\mathbf{s}}^\alpha = \sum_{\alpha=1}^k (\hat{\mathbf{p}}^\alpha + \hat{\rho}^\alpha \dot{\mathbf{x}}_\alpha) = \mathbf{0} \quad (8.13)$$

is the constraint for the total momentum production, cf. (2.41)<sub>2</sub>. Inserting the definition of barycentric motions, cf. (2.46),

$$\ddot{\mathbf{x}} = \frac{1}{\rho} \sum_{\alpha=1}^k [\rho^\alpha \ddot{\mathbf{x}}_\alpha - \operatorname{div} (\rho^\alpha \mathbf{d}_\alpha \otimes \mathbf{d}_\alpha) + \hat{\rho}^\alpha \dot{\mathbf{x}}_\alpha], \quad (8.14)$$

in (8.13), the momentum balance of the overall aggregate  $\varphi$  results

$$\rho \ddot{\mathbf{x}} = \operatorname{div} \mathbf{T} + \rho \mathbf{b} \quad \text{with} \quad \mathbf{T} = \sum_{\alpha=1}^k (\mathbf{T}^\alpha - \rho^\alpha \mathbf{d}_\alpha \otimes \mathbf{d}_\alpha). \quad (8.15)$$

Note that regarding the overall aggregate  $\varphi$ , the diffusion velocities are cancelling each other ( $\sum_{\alpha=1}^k \rho^\alpha \mathbf{d}_\alpha = \mathbf{0}$ ). For quasi-static problems with little change of the velocities in time, the accelerations of the individual constituents can be neglected,  $\ddot{\mathbf{x}}_\alpha \equiv \mathbf{0}$  in (8.14), but the acceleration terms of diffusion velocities and mass productions remain and, therewith, the barycentric acceleration  $\ddot{\mathbf{x}}$  is not zero. However, proceeding from a slowly internal erosion (suffusion) process, the diffusion process proceeds without any noticeable accelerations and, thus, the  $\operatorname{div} (\rho^\alpha \mathbf{d}_\alpha \otimes \mathbf{d}_\alpha)$  terms is very small. This also pertains to the amount of the mass production rate  $\hat{\rho}^\alpha$ , which is very slow, too.

### 8.3 Saturated soil erosion model

To account the local composition of the mixture continuum of the erodible saturated soil, the saturation condition of the volume fractions is composed by

$$\sum_{\alpha=1}^k n^{\alpha} = n^S + n^F = n^S + n^E + n^W = 1, \quad (8.16)$$

where the fluid components are  $\beta = \{E, W\}$ . The volume fraction of the fluid phase is composed to  $n^F = n^E + n^W$ . Proceeding from the simple approach of internal erosion (8.1), the set of governing equations consists of the volume balance (8.5) of the solid phase, the volume balances of the overall aggregate formulated with respect to solid motion:

$$0 = \operatorname{div}(\mathbf{u}_S)'_S + \operatorname{div}(n^F \mathbf{w}_F), \quad (8.17)$$

and the momentum balance of the overall aggregate

$$\mathbf{0} = \operatorname{div}(\mathbf{T}^S + \mathbf{T}^F) + \rho \mathbf{b} + \rho^{SR} \hat{n}^S \mathbf{w}_F \quad \text{with} \quad \mathbf{d}_{EF} = \mathbf{0}. \quad (8.18)$$

### 8.4 Constitutive settings

A thermodynamically consistent evaluation of the entropy inequality is omitted here. A detailed elaboration can be found in the work by Diebels and Steeb [151] and Steeb et al. [153]. According to this, the internal erosion or the mass production has to be proportional to the square of the seepage velocity. This was also announced, e.g., by Vardoulakis [167], Wan and Wang [172] or Wan and Fell [170] resulting from experimental observations. However, for the constitutive approach of  $\hat{n}^S$ , the amount of the seepage velocity is commonly used. In this contribution, a slightly modified approach for  $\hat{n}^S$  compared to Steeb et al. [152] is applied. Furthermore, the constitutive equations of the solid phase are also influenced by the increasing porosity. In particular, these are the degradation of the elastic stiffness and the plastic strength, cf. [124, 153], whereas the hydraulic equations remain unchanged. This is why the variation of the solidity is already considered with the deformation-dependent intrinsic permeability coefficient  $K^S$  governed by the volume fraction  $n^S$ , cf. (4.54) or (4.55).

#### Elastic law

The decrease of the solid fraction triggered by the internal erosion process can be analogously described as a damage-like behaviour for brittle materials by introducing the damage variable  $d$  (Kachanov [91]). Proceeding from the isotropic damage behaviour, the damage variable  $d = A/A_0$  describes the homogeneously distributed loss of material area related to the ratio of the undamaged initial area  $A_0$  and the damaged area  $A$ , where  $d$  is still positive,  $^\dagger d \geq 0$ . The ratio of the remaining material area  $1 - d = (A_0 - A)/A_0$

---

<sup>†</sup>During the deposition of grains occurring in areas of low seepage velocity, the grains can be accumulated at locations, where up to the present time no erosion has taken place. This would lead to an increase of the initial solidity, i. e., the damage variable would be negative  $d < 0$ .



corresponds to the expression formulated by the ratio of the solid volume fractions at the stress free intermediate state  $n_{tS}^S$  to the initial state  $n_{0S}^S$  and reads  $1 - d = n_{tS}^S/n_{0S}^S$ . On the basis of the damage factor  $D = n_{tS}^S/n_{0S}^S$ , the mechanical properties are reduced as the free *Helmholtz* energy  $\Psi^{Sd} = D \Psi^{Se}$  given in (4.28). Proceeding from the derivative of  $\Psi^{Sd}$  with respect to  $\varepsilon_{Se}$ , the elastic effective solid stress  $\sigma_{Em}^S$  is reduced by degrading the elastic material parameters by the damage factor  $D$ , viz.

$$\sigma_{Em}^S = 2 \mu_E^S \varepsilon_{Se}^D + \left[ k_{0E}^S + k_{1E}^S \left( \frac{\varepsilon_{Se}^{V \text{crit}}}{\varepsilon_{Se}^{V \text{crit}} - \varepsilon_{Se}^V} - 1 \right) \right] \varepsilon_{Se}^V \mathbf{I} \quad (8.19)$$

where:  $\mu_E^S = D^{n_e} \mu^S$ ,  $k_{0E}^S = D^{n_e} k_0^S$ ,  $k_{1E}^S = D^{n_e} k_1^S$ ,  $D = \frac{n_{tS}^S}{n_{0S}^S}$ ,

are the reduced elastic parameters, whereby the exponent  $n_e$  describes a non-linear degradation process of the solid stiffness.

### Plastic law

The strength of granular materials depends on different factors. For example, the general yielding and failure behaviour of granular materials is typically characterised by its initial density (loose or dense sand). In addition, the stress level at which the shear stress is applied is decisive for the mobilisation of the friction strength of granular materials, because the higher the confining pressure (compaction) the higher the failure stress, cf. Section 4.2.2. According to this, the increase of the porosity has a negative impact on the failure behaviour. During the internal erosion process, the structural cohesion between the grains is continuously lost and the real failure state of the material (without erosion) is no more reachable. This structural change of the failure behaviour has been taken into account by reducing two plastic parameters by the damage factor  $D^{n_p}$ :

$$\beta_E^* = D^{n_p} \beta^* \quad \text{and} \quad \kappa_E = D^{n_p} \kappa. \quad (8.20)$$

Therein,  $\beta^*$  represents the inclination of the failure surface, while  $\kappa$  depicts the cohesion of the soil, while the exponent  $n_p$  describes a non-linear degradation of the yield strength. Note that the inclination of the evolving yield surface is affected by the erosion just after the failure surface is reached. This happens much earlier due to a decrease of the failure surface triggered by increasing porosity. Numerical studies of plastic material parameters have shown that using only the parameters  $\beta^*$  and  $\kappa$  is sufficient to describe the influence of internal erosion on the yielding behaviour.

### Simplified plastic hardening model

Moreover, to scale down the complexity of the presented sophisticated yielding model given in section 4.2.2, the hardening effect can be restricted by reducing the number of the evolving plastic hardening parameters with minor changes of the real soil behaviour. Additionally, the computation time of the IBVP is strongly reduced.

Proceeding from an unloaded soil, the plastic yielding begins immediately with the first loading. This leads to the complex elasto-viscoplasticity model presented in section 4.2. In some cases, it is appropriate to simplify the model complexity. For example, some triaxial experimental data are lacking and the identification of all required parameters is no more possible on the basis of the available experimental data set, which, of course, would be necessary to give a precise description of the complex soil behaviour. Moreover, a reduction of the model would be also appropriate, if only the general physical processes of a complex IBVP are numerically investigated. However, the decisive factor here is, how the material model can be reduced in order to be still close to the real soil behaviour.

The non-linear stress-strain behaviour governed mainly by the plastic hardening proceeds until the limit shear-stress, which is described by the corresponding failure surface. The size of the failure surface is variable and is defined by the confining pressure or the hydrostatic stress level (4.49). In order to avoid the complex hardening procedure, the initial yield surface can be set to the smallest size of the failure surface, which corresponds to a very low confining pressure level. This is realised by setting the initial hardening parameter values  $p_{0i} = \bar{p}_i^*$  to the same value of the limit parameters  $\bar{p}_i^*$  excluding of  $\epsilon$ , which is set to  $\epsilon_0 = \bar{\epsilon}_0^*$ . Thus,  $\epsilon$  can be still evaluated until the limit value of  $\epsilon \rightarrow \bar{\epsilon}^*$  bounded by  $\bar{\epsilon}_{lim}^*$ . This implies that the material was shear-preloaded until the peak shear stress at a very low stress level so that the initial hardening behaviour is eliminated, i. e., the material firstly behaves linear elastically until the enlarged initial yield surface is reached. If the shear stress exceeds the yield surface, only then, the hardening process starts.

To illustrate this approach, the simulation results of the triaxial compression test with a constant confining pressure of  $\sigma_2 = \sigma_3 = 0.2 \text{ MPa}$  using the simplified and complete hardening approach are presented in Figure 8.1. Therein, the initial linear elastic behaviour of the simplified model (red line, sim-simpl) is well recognisable compared to the non-linear procedure of the general complex hardening model (green line, sim-gen), whereas the volume strain  $\epsilon^V$  is only slightly affected. Moreover, for a good modelling of plastic shear

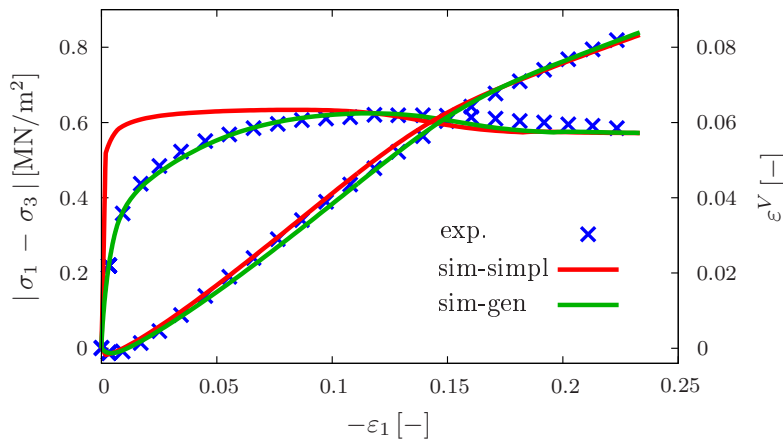


**Figure 8.1:** Triaxial compression test with a confining pressure of  $\sigma_2 = \sigma_3 = 0.2 \text{ MPa} = \text{const.}$  and the corresponding simulation applying the general (sim-gen) and the simplified hardening model (sim-simpl).

zones, one has to consider the softening effect of the material. Therefore, the parameter  $\delta$  mainly governing the softening behaviour has to be taken into account in the hardening process.

Hence, the presented procedure gives users the opportunity to simplify the complex plasticity model corresponding to the hardening behaviour under consideration of the real strength of the soil. For the reason that the evolution of the hardening parameters  $\beta$  and  $\gamma$  is not taken into account and the evolving of  $\epsilon$  and  $\delta$  starts just after exceeding the enlarged elastic part, the computation costs are also reduced intensively. Nevertheless, if it is necessary, the model complexity can be simply increased.

### Erosion law

Steeb et al. [152] have proposed an approach for the solid volume production  $\hat{n}^S$ . Therein, the amount of erodible grains is limited by a constant saturation  $n_{lim}^E$ , but, generally it depends on the strength of the seepage velocity of the pore liquid (suspension)  $\mathbf{w}_L$  or pore fluid  $\mathbf{w}_F$  for the saturated soil, respectively. That means the higher  $\mathbf{w}_L$ , the more grains can be detached from the solid skeleton. In order to take this into account, the initial limit of erodible grains  $n_{0lim}^E$  is increased by  $|\mathbf{w}_L|$ , which is expressed by the variable  $n_{lim}^E$ . However,  $n_{lim}^E$  is restricted by the maximal limit  $n_{max}^E$ , because the considered internal erosion process is actually constrained by the fine grain content (internal suffusion). Under consideration of these aspects, the solid volume production yields

$$\hat{n}^S = -n^E \left[ \exp \left( 1 - \frac{n^E}{n_{lim}^E} \right) - 1 \right] \zeta |\mathbf{w}_L| \quad (8.21)$$

$$\text{with } \begin{cases} \hat{n}^S < 0, & \text{if } |\mathbf{w}_L| > |\mathbf{w}_L^*|, \\ \hat{n}^S = 0, & \text{if } |\mathbf{w}_L| \leq |\mathbf{w}_L^*|, \\ n_{lim}^E = n_{0lim}^E (1 + \omega |\mathbf{w}_L|) & \text{with } n_{lim}^E \leq n_{max}^E. \end{cases}$$

Therein,  $\omega$  controls the growth of  $n_{lim}^E$  and  $\zeta \geq 0$  governs the process velocity. However, the erosion process is only activated, when the soil specific limit value  $|\mathbf{w}_L^*|$  is exceeded. However, for the first computation of  $\hat{n}^S$ , a very small initial value of  $n^E$  is necessary, otherwise,  $\hat{n}^S$  is always zero.

## 8.5 Numerical Examples

In this section, several numerical examples of erosion-soil problems are presented. At the beginning, two water-saturated soil piping problems are shown. In this context, there is no total loss of grains at local points during the erosion process of the treated piping problem, such as occurs at a real tube-flow problem. Thus, for the pipe, only a decrease of the solidity is assumed. Further examples to internal erosion problems are the numerical investigation of embankments, where the embankment is constructed without and with a high impermeable internal core. For the embankment problems, the presented partially saturated soil model is applied.

### 8.5.1 1-d piping of a fully saturated column

Figure 8.2 illustrates a popular example of saturated soil piping for testing erosion models, cf. [152, 168, 172]. For the numerical treatment of this problem, the water-saturated column is homogeneously fixed at the left side and at the bottom, where also the pore-fluid pressure  $\bar{p}^{FR} = \dot{p}t = -0.1t$  [KPa/s] is applied. Furthermore, from the top, the column is loaded displacement-controlled by  $\bar{u}_S = \dot{u}t = 0.5t$  [mm/s]. The left and right boundaries have no-flow conditions, while the right side admits free flow.

For this example, it is assumed that the erosion process starts immediately after applying  $\bar{p}^{FR}$  by setting  $|\dot{\mathbf{w}}_F| = 0$ . The variability of the maximal limit of erodible grains is not considered,  $n_{lim}^E \equiv n_{0lim}^E = 0.1$  ( $\omega = 0$ ). For a better analysis of the coupled erosion-mechanical yielding behaviour, the yield criterion in (4.35) has been reduced to the *von Mises* ideal plasticity model without taking any hardening behaviour into account. The material parameters, which come into consideration, are given in Table 8.1, while the remaining plastic parameters are set to zero. The elastic behaviour is modelled by the general *Hookean* elasticity law by setting the bulk modulus  $k_1^S$  in (8.19) to zero.

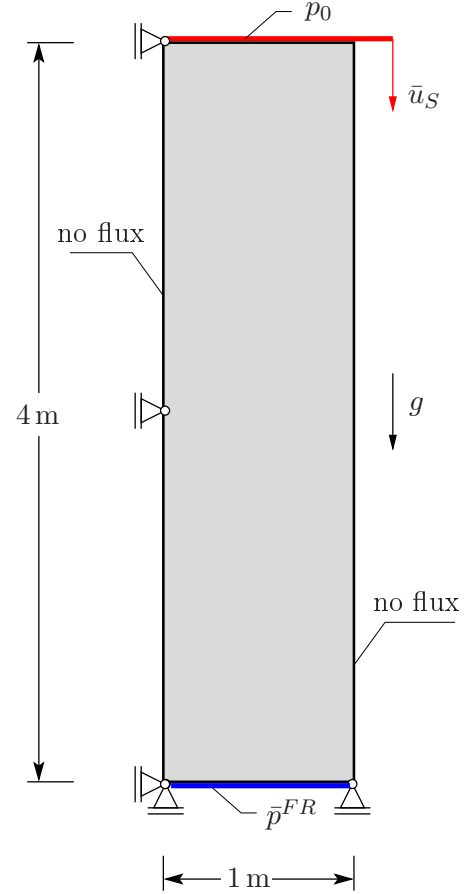


**Figure 8.2:** Sketch of the 1-d column piping problem.

The piping problem in Figure 8.2 has been computed by the *Darcy* permeability parameter of *Ehlers-Eipper* (EE) (4.54) and the formulation *Kozeny-Carman* (KC) given in (4.55) in order to investigate their influences on the erosion progression. The results are illustrated in Figure 8.3. Figure 8.3 (a) shows the development of the solidity  $n^S$ , while (b) presents the solid degeneration rate  $\hat{n}^S$ . Due to the lack of experimental data, an arbitrary value for the erosion parameter  $\zeta = 800$  s/m is chosen. This parameter is denoted for the KC-law with  $\zeta^{KC}$  and for the EE-law with  $\zeta^{EE}$ . The exponent of the EE-law is taken to  $\pi = 1$ . Due to the fact that the solid deformation is generally several order smaller than the soil degeneration, the change of  $n^S$  induced by the soil deformation is hardly observable in Figure 8.3 (a), but rather the soil degeneration. Comparing the results, the EE-law behaves more sensitive to high values of  $\zeta^{EE}$  compared to the KC-law. Accordingly, the progress of  $n^S$  and  $\hat{n}^S$  slows down with lower values of  $\zeta^{EE}$ . The EE-law agrees well with the KC-law by fitting  $\zeta^{EE}$  to 0.6 s/m and  $\pi$  to 3.6. However, Steeb et al. [152] have numerically investigated the behaving of the EE-law by variation of the exponent  $\pi$ . They compared the results with those of the KC-law by applying the same parameter  $\zeta$  for both laws. Therefore, the results were not corresponding.

Parameters of the elastic behaviour and of the initial state					
$\mu^S$	=	200	MPa	$n_{max}^S$	= 1.0 [-]
$k_0^S$	=	333	MPa	$n_{0S}^S$	= 0.75 [-]
$\rho^{SR}$	=	2.65	g/cm <sup>3</sup>	$K_{0S}^S$	= $1 \cdot 10^{-11}$ m <sup>2</sup>
$\rho^{WR}$	=	1.0	g/cm <sup>3</sup>	$\mu^{WR}$	= $1 \cdot 10^{-3}$ Pa · s
Parameters of the plastic and erosion behaviour					
$\kappa$	=	0.7	1/MPa	$\psi_1 = \psi_2$	= 1.0 m/s
$n_e = n_p$	=	1.0	[-]	$n_{0lim}^E$	= 0.1 [-]

**Table 8.1:** Material parameters of the Hookean law, the Mises plasticity law without hardening and the erosion law.

Figures 8.4 (a) and (b) illustrate the reduction of the shear modulus  $\mu^S$  and the stress-displacement curves, respectively, computed with  $\zeta^{EE} = 800$  and 0.6 s/m. For high values of  $\zeta^{EE}$ , the shear modulus  $\mu^S$  decreases very fast until 130 MPa compared to the lower

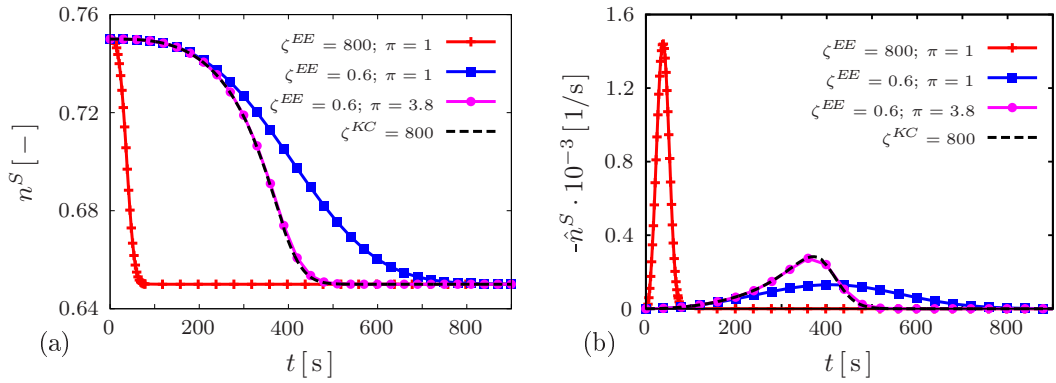


**Figure 8.3:** 1-d piping simulation results: (a) solid fraction  $n^S$ ; (b) solid production  $\hat{n}^S$ .

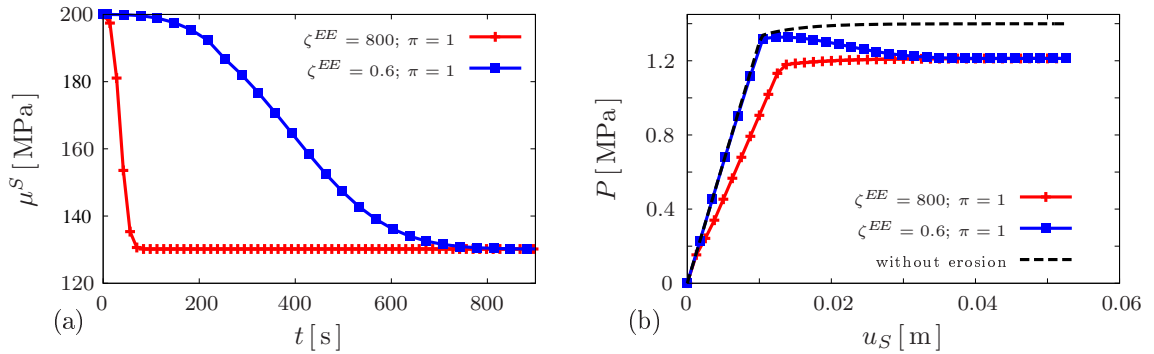


**Figure 8.4:** 1-d piping simulation results: (a) shear modulus  $\mu^S$ ; (b) loading-displacement curves related to the loading boundary.

$\zeta^{EE}$  and the stress progression is more flat than in the case without erosion (black-dashed line). The stress of the black dashed line converges to the limit of  $P \approx 1.3$  MPa, whereas the fast erosion process ( $\zeta^{EE} = 800$  s/m) reaches  $P \approx 1.2$  MPa, while the slow case ( $\zeta^{EE} = 0.6$  s/m) softens to the same low stress limit immediately after the high stress limit has been reached like a top-down approach. Hence, it could be shown that the stiffness and the strength are noticeably reduced compared with the case without erosion.

### 8.5.2 Cold production in oil saturated sand

Similar processes like soil erosion in embankments occur during the sand production by quarrying a petroleum-sand mixture from the several hundred meter deep located substratum. Thereby, a high gas pressure is applied through a borehole in order to press the viscous oil-sand mixture into a compound of boreholes and then it is sucked up to the surface (Tremblay et al. [158]). This procedure is also called *cold production*. During the sand removal process, several networks of wormholes are formed. As a consequence, the porosity of the soil increases leading to instability problems with a sudden sinking of the ground. Regarding the safety aspects, it is important to know, how wormholes propagate. For this propose, the sand production process has been experimentally investigated by many researches, e. g., cf. Tronvoll and Fjaer [159], Tremblay et al. [158], Tremblay and Oldakowski [156] and Papamichos et al. [123]. Besides experimental research, numerical treatment of such a challenging task of the petroleum industry is getting more and more important, in particular, for the simulation of sand production, cf. [124, 152, 172]. It is expected that the efficiency of quarrying oil can be improved by use of computer simulations. This may also contribute to a safe oil production.

The wormhole-propagation experiment of Tremblay et al. [158] is sketched in Figure 8.5. For the test, an oil-saturated compacted sample was used, which had on its right side

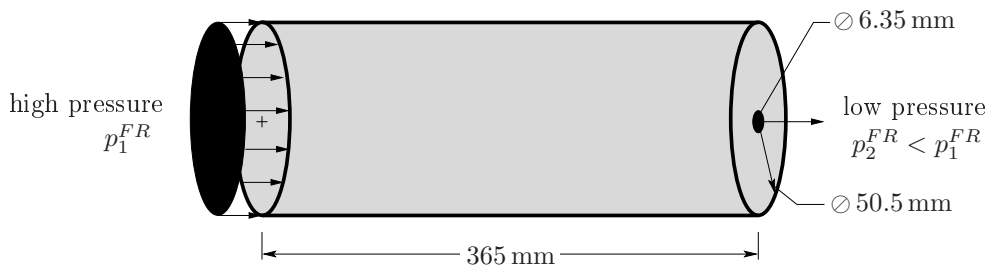


**Figure 8.5:** Sand sample with the hydraulic loading condition.

an outlet orifice with a diameter of  $\varnothing 6.35$  mm, where the sand production is initiated. In order to press the heavy oil with a viscosity of  $21.5 \text{ Pa} \cdot \text{s}$  through the sample, a high fluid pressure of  $1.2 \text{ MPa}$  was applied at the left side of the sample. The sample is fixed by a cylindrical steel box, which obstruct any deformations. To visualise the porosity development, Tremblay et al. [158] have recorded the porosity distribution of the sample by CT (computed tomography) scans along the longitudinal section of the sample, which is illustrated in Figure 8.6. Looking closer to the initial solid density distribution shown in Figure 8.6 (a), it seems that some areas have a slightly lower solidity. This area of

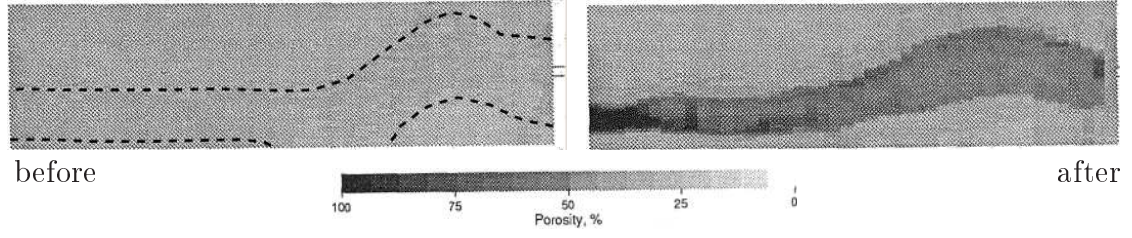


**Figure 8.6:** Porosity propagation along the axis of the wormhole: (a) at the initial state; (b) after developing (Tremblay et al. [158]).

lower solidity is bordered by dashed lines in Figure 8.6 (a). Despite the specimen was previously compacted with very high pressure, an ideally homogeneous distribution of the material through the whole sample could not be reached. Moreover, the wormhole interestingly proceeds in those parts of the specimen with low porosity, cf. Figure 8.6 (b) at the final state, even the inhomogeneity of the solidity is very smooth. Moreover, another specimen with a different smooth solid fluctuation has been tested by Tremblay et al. [157]. Analogically to the presented one, the wormhole has been propagated to the areas with the lower solidity.

Due to the fact that the wormhole is eccentrically propagating regarding to the longitudinal axis, only 3-d computation of the problem can actually mimic the real development of the wormhole. However, Wan and Wang [171] used a rotationally symmetric approach for the geometry, which may be not appropriated, because it reproduces only axial symmetrically distributed results in respect to the longitudinal axis. Nevertheless, for the first approach, the experiment was only qualitatively simulated along the longitudinal cross section as a 2-d plain-strain problem.

The experiment was computed with two different initial solidity distributions. The first one starts from a homogeneous distribution with  $n_{0s}^S = 0.635$ , while the second one has a smooth fluctuation of the porosity at the initial state, which is shown in Figure 8.8 (a). Further material parameters are given in Table 8.2. At the beginning, the wormhole

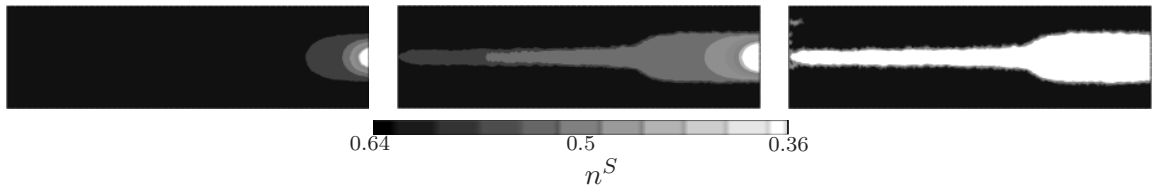


**Figure 8.7:** Degradation of  $n^S$  starting with a homogeneous solidity distribution.

develops fast into the longitudinal direction and also spreads into the width at the outlet, cf. Figure 8.7. The diameter of the wormhole shrinks gradually in direction to the inlet as a result of the fluid pressure gradient. Comparing with the second case in Figure 8.8, the wormhole develops into the part of a minor lower density. Thus, the propagation of wormholes is greatly affected by the fluctuation of the solidity even the fluctuation is low.

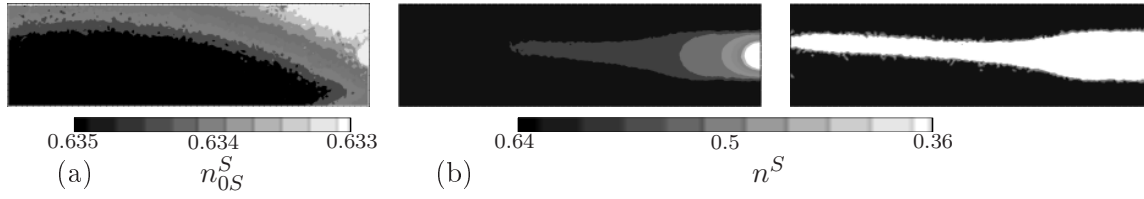


**Figure 8.8:** (a) Initial solidity  $n_{0S}^S$  (inhomogeneous distribution), (b) degeneration of  $n^S$ .

Parameters of the elastic behaviour and of the initial state					
$\mu^S$	=	1 000	MPa	$n_{max}^S$	= 1.0 [-]
$k_0^S$	=	1 666	MPa	$n_{0S}^S$	= 0.635 [-]
$\rho^{SR}$	=	2.65	g/cm <sup>3</sup>	$k_{0W}^W$	= $9.918 \cdot 10^{-5}$ m/s
$\rho^{WR}$	=	0.985	g/cm <sup>3</sup>	$\mu^{WR}$	= 21.5 Pa · s
Parameters of the erosion behaviour					
$n_{0lim}^E$	=	0.28	[-]	$\zeta$	= $1.79 \cdot 10^{-2}$ s/m
$ \mathbf{w}_F^* $	=	0.45	m/s	$n_e$	= 0 [-]
$\omega$	=	0		$\pi$	= 1.0 [-]

**Table 8.2:** Material parameters of the Hookean law and the erosion law.

### 8.5.3 Numerical investigation of embankment problems

Numerical investigation of embankment failure problems have been carried out by many researches, e. g., Ehlers et al. [64], Chai and Carter [27] and Oka et al. [122], and is still a challenge and ongoing subject of research. These simulations were performed without considering the soil erosion problem. The objective of the presented computations of embankments is that the destabilisation of the construction is mainly triggered by the internal erosion process (increase of soil porosity). Using the triphasic soil model with the extension to the internal erosion presented in Chapter 8.2, two embankment problems have been investigated. Their boundary conditions have been chosen in such a way that without the occurrence of an internal erosion, a stable behaviour would be predicted for the embankments.

Proceeding from the simplified plasticity model described in Section 8.4, the evolution of the yield surface concerning to the parameters  $\gamma$  and  $\beta$  is deactivated by setting these parameters to the values of the failure surface,  $\gamma_0 \equiv \gamma^*$  and  $\beta_0 \equiv \beta^*$ , while  $\epsilon$  is set to  $\epsilon_0 \equiv \epsilon_0^*$ . This corresponds to the failure state defined by the unloaded virgin sand. For both embankment simulations, the elasto-viscoplastic and hydraulic parameters of the GEBA sand given in Tables C.1 and C.2 have been applied. However, a minor cohesion



of  $\kappa = 0.013$  MPa is applied to prevent numerical instabilities as a result of small tension stresses during the computation. To regularise the ill-posed plasticity problem, a marginal viscosity of  $\eta = 200$  s and an overstress of  $\sigma_0 = 0.013$  MPa are used. These numerical aids are chosen in such a way that their influences on the mechanical behaviour are negligibly small. Furthermore, the parameters of the erosion properties are chosen for each problem differently. These are given within the corresponding subsections.

### Soil embankment

Embankments are permanently loaded by the dammed water, which is continuously varying. The level of the dammed water is determinative for the strength of the seepage velocity within the embankment. Thus, in dependence of the dammed water table (w-t), the erosion process is accelerated or stopped. From an engineering point of view, it can be very helpful to know how the dammed water affects the progression of the internal erosion and, accordingly, the failure of the embankment. Concerning this, the embankment sketched in Figure 8.9 is numerically investigated with varying the w-t at the left slope of the embankment. In order to avoid a premature weakness or even failure of the

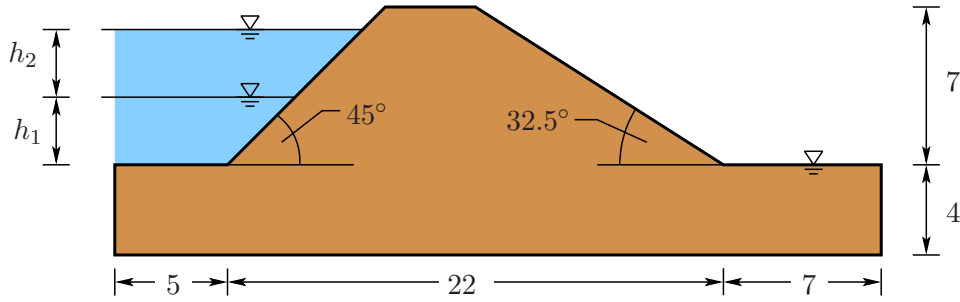
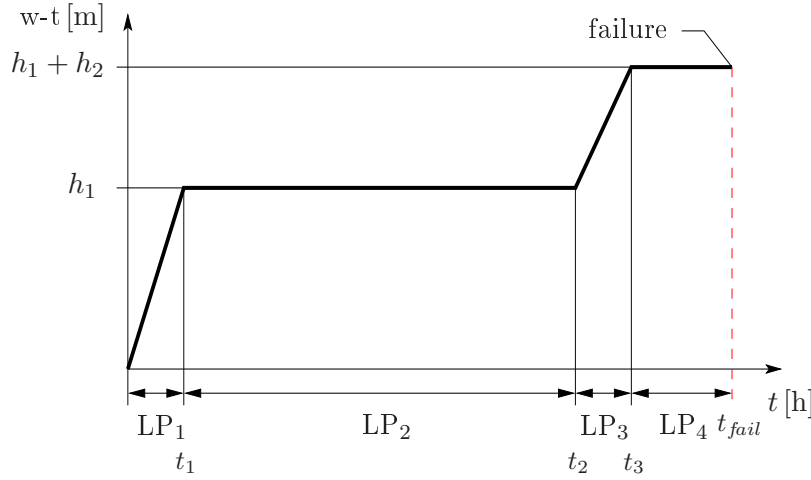


Figure 8.9: Geometry and dimensions of the embankment in [m].

slope through the buoyancy force induced by increasing the w-t, the inclination of the right slope is chosen quite flat. In contrast, the left slope could be chosen much steeper, because the weight of the dammed water stabilises the slope.

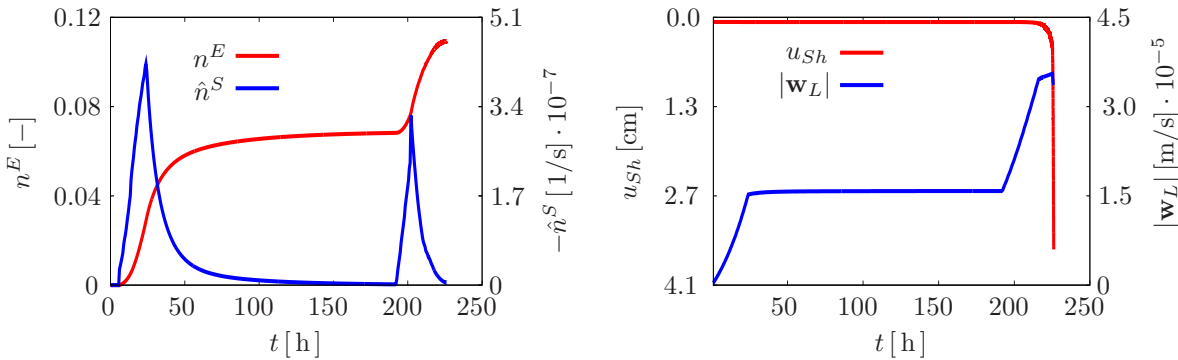
The embankment is loaded in four load steps. The load progression is sketched in Figure 8.10. The initial stage of the w-t is located on both sides of the embankment at the level of the slope toes. In the first load path  $LP_1$ , the w-t is slowly increased on the left side to the height of  $h_1 = 3$  m within the time  $t_1 = 24$  h and, thereafter, in  $LP_2$ , it is kept constant for a duration of  $t_2 - t_1 = 168$  h. In  $LP_3$ , the w-t is increased further by the height of  $h_2 = 2$  m in  $t_2 - t_3 = 24$  h. Finally, the failure of the slope will occur in  $LP_4$  at  $t_{fail}$ , where the w-t is kept constant. The erosion process just starts after the seepage velocity exceeds the value  $|\mathbf{w}_L| = 7.6 \cdot 10^{-6}$  m/s, which already happens in  $LP_1$ . Further erosion parameters are  $n_{0lim}^E = 0.05$ ,  $\omega = 10^4$  s/m and  $\zeta^{EE} = 100$  s/m.

The amount  $n^E$  and the rate  $\hat{n}^S$  of eroded grains of the right slope toe are illustrated in Figure 8.11 (left). Therein, close to the end of  $LP_2$ ,  $n^E$  approaches the limit of  $\approx 0.07$  controlled by  $\omega$  and  $|\mathbf{w}_L|$ , cf. equation (8.21). Thereby,  $\hat{n}^S$  decreases to zero after the peak value at  $LP_1$  has been reached. In Figure 8.11 (right), the proceeding of  $|\mathbf{w}_L|$  is shown.



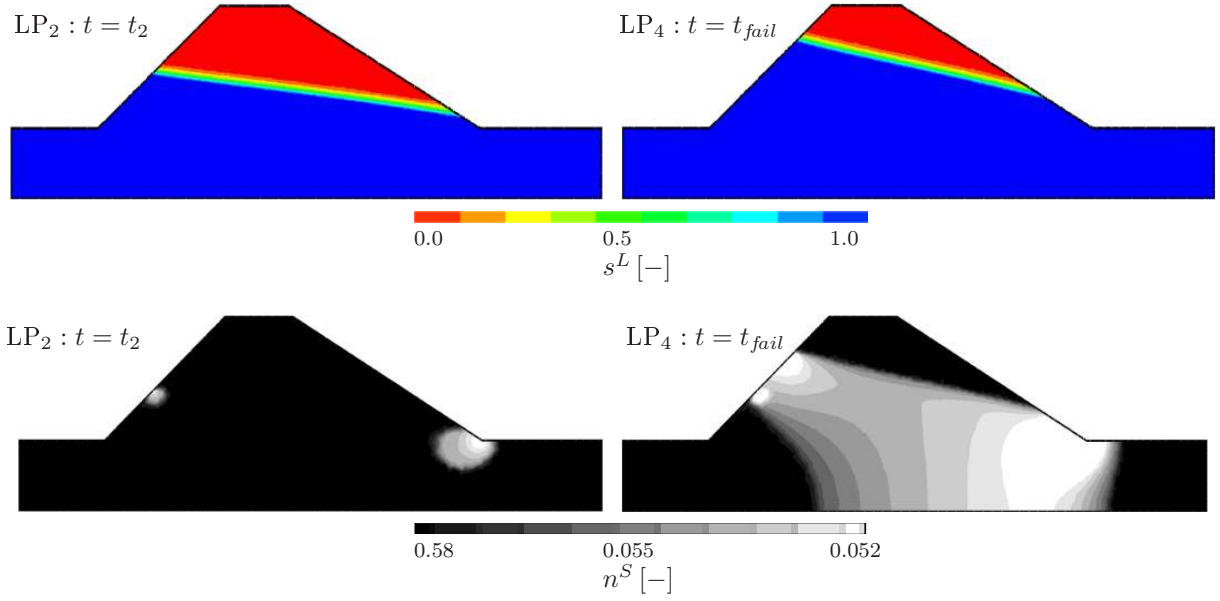
**Figure 8.10:** Loading phases  $LP_i$  corresponding to the time ( $t$ ) and the  $w$ - $t$  ( $h$ ) with respect to the slope toe:  $t_1 = 24$  h,  $t_2 = 192$  h,  $t_3 = 216$  h and  $t_{fail} \approx 226.5$  h;  $h_1 = 3$  m and  $h_2 = 2$  m.

It increases each time with rising of the  $w$ - $t$ . During  $LP_4$  where the  $w$ - $t$  is constant,  $|\mathbf{w}_L|$  still increases due to growing soil porosity until  $n^E$  has been reached the new limit value of  $\approx 0.1$ . Moreover, the failure occurs at time  $t_{fail} \approx 226.5$  h characterised by a strong increase of the horizontal displacement  $u_{Sh}$  at the right slope toe, cf. Figure 8.11 (right). Immediately before the failure occurs,  $|\mathbf{w}_L|$  drops slightly. This is a consequence of the development of a dilatant shear band, cf. Figure 8.13 (right). Thereby, the pore water is sucked up into the shear band and, therewith, the liquid pressure  $p^{LR}$  as well as  $|\mathbf{w}_L|$  is dropped. Similar physical processes could also be observed by simulations of the slope failure problems in Section 6.3.



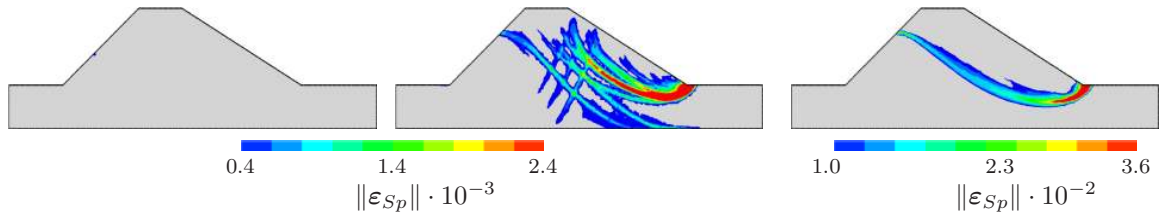
**Figure 8.11:** Progression of  $n^E$  and  $\hat{n}^S$  (left) and  $u_h$  and  $\mathbf{w}_L$  over time  $t$  of the right slope toe.

Moreover, in Figure 8.12 (top), the distribution of  $s^L$  is illustrated. Figure 8.12 (top-left) shows the state of  $s^L$  at the end of  $LP_2$ , whereas the Figure (top-right) the state at failure. The corresponding distributions of  $n^S$  are depicted in Figure 8.12 (bottom). During the first two loading paths, the eroded part is primarily concentrated at the right slope toe (Figure 8.12 (bottom-left)), whereby not any shear band is initiated, yet, cf. Figure 8.13 (left). With the rise of the  $w$ - $t$ ,  $u_{Sh}$  starts to grow particularly at the end of the load path. During  $LP_4$ , the eroded area is more and more extending and the overall



**Figure 8.12:** Simulation results at the end of  $LP_2$  and at the failure state in  $LP_4$ : (top) liquid saturation  $s^L$ ; (bottom) solidity  $n^S$ .

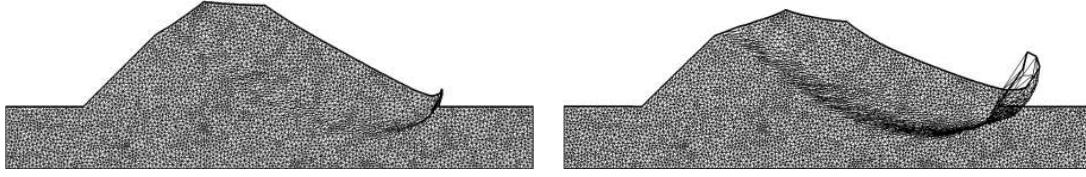
structure is continuously weakened by evolving of several shear bands, cf. Figure 8.13, and  $u_{Sh}$  of the slope toe increases faster. In Figure 8.13, low values (below 0.007) of the accumulated plastic strain  $\|\epsilon_{Sp}\|$  are not visualised for clarity reason. By gradually weakening the internal structure of the embankment, several shear bands are developed, which are mainly triggered by the dead load. However, one dominant shear band seems to enforce. It is proceeding from the right slope toe to the top. But it gets more and more deflected by the other shear bands at the middle part of the embankment to the water side, cf. Figure 8.13 (right).



**Figure 8.13:** Evolution of shear bands: (left) at the end of  $LP_2$ ; (middle) intermediate state in  $LP_4$  at  $t = 225$  s; (right) at failure state in  $LP_4$  at time  $t_{fail}$ .

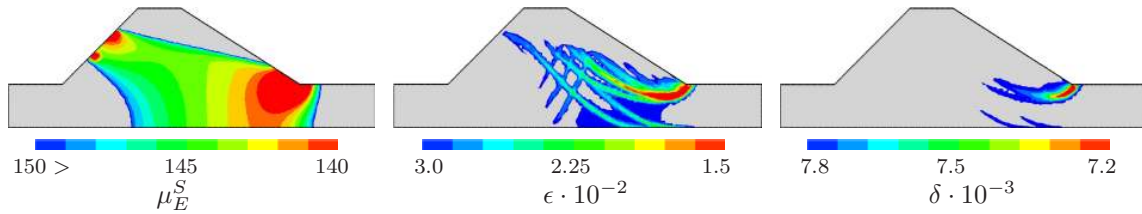
The complete embankment deformation induced by the shear bands is illustrated in Figure 8.14 by the deformed FE mesh at the final state discretised with 8 614 triangle elements. In Figure 8.14 (left), the deformation of the FE mesh is shown with a 10-times magnification. Despite of this, hardly any mesh deformations within the internal area are observed, because of the very high deformation values at the surrounding area of the slope toe, which suppress low deformed elements in the internal area of the embankment. However, using a magnification of 100-times, the deformation behaviour of the embankment is more clear, cf. Figure 8.14 (right).

Moreover, in Figure 8.15 (left), the reduction of the elastic stiffness  $\mu_E^S$  is illustrated at an



**Figure 8.14:** Deformed mesh at the final state (left) 10-times and (right) 100-times magnification of the deformations.

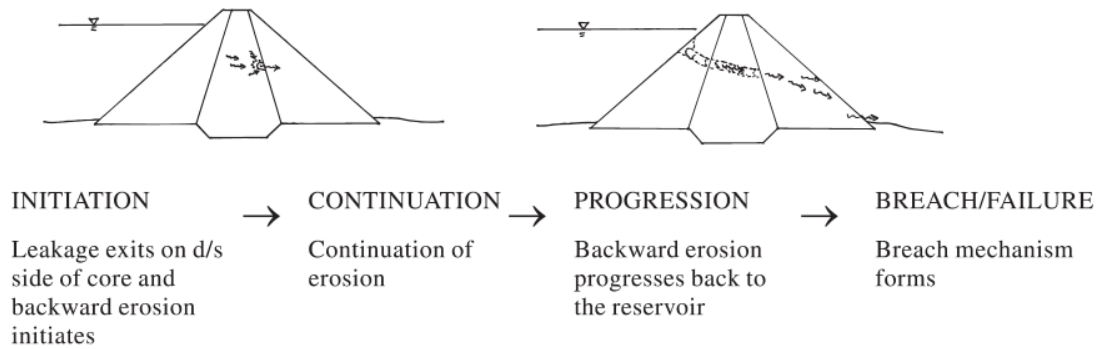
arbitrarily chosen intermediate state ( $t = 225$  s). As might be expected, the distribution  $\mu_E^S$  over the embankment is identical to the degradation of  $n^S$ , cf. Figure 8.12. At the same intermediate state, the evolution of the plastic material parameters  $\epsilon$  and  $\delta$  is presented in Figure 8.15 (middle) and (right). Therein, it can be recognised that the progression of  $\epsilon$  corresponds very close to the shear band progressions, cf. Figure 8.13 (middle). Thereby,  $\delta$  mainly performs the softening behaviour of the soil and is only activated at high stresses compared to  $\epsilon$ . Thus,  $\delta$  is more concentrated at the dominant shear band.



**Figure 8.15:** Evolving of the material parameters (left)  $\mu^S$ , (middle)  $\epsilon$  and (right)  $\delta$ .

### Soil embankment with a less permeable central core

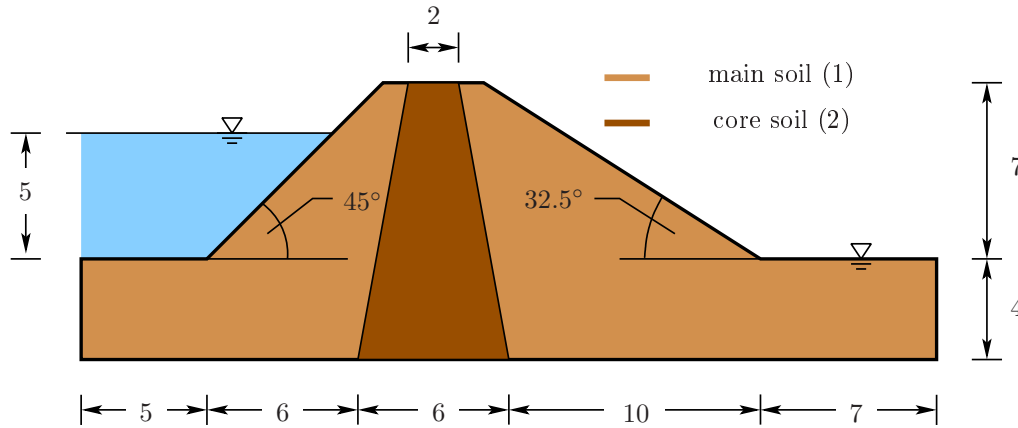
Such embankments with internal core are built mainly by a loose raised soil and an almost impermeable internal core compared to the surrounding soil material. The task of the internal core is to protect the infiltration process of the dammed water through the embankment. By the pressure difference between the dammed water and the air side, a



**Figure 8.16:** Initiation of embankment failure caused by backward erosion: illustrating the development of a pipe within the core through backward erosion triggered by hydraulic gradient (Figure is abstracted from Foster et al. [71]).

high hydraulic gradient within the core is induced. Thus, a high seepage force develops within the core. Due to this fact, an erosion process can be triggered starting from the interface at the low-water side of the core and gradually proceeds through the core. In addition, the seepage velocity is continuously strengthened by increasing porosity. As a consequence, the backward erosion process is initiated, which finally generates a pipe through the core and proceeds until the reservoir. By growing porosity within the core and under the condition that the water level of the reservoir is still constant during the erosion process, the water table in the core and at the air side of the embankment will increase. This could lead to a collapse of the construction induced by buoyancy. Figure 8.16, which is adopted from Fell et al. [71], schematically illustrates the already described process of initiation and progression of internal erosion through an embankment. However, there are many other failure mechanism of embankments, which depend on the geometry, material properties and loading conditions, etc. The goal of the following embankment simulation is to recapture of the illustrated physical procedure and to investigate the initiation of the embankment failure.

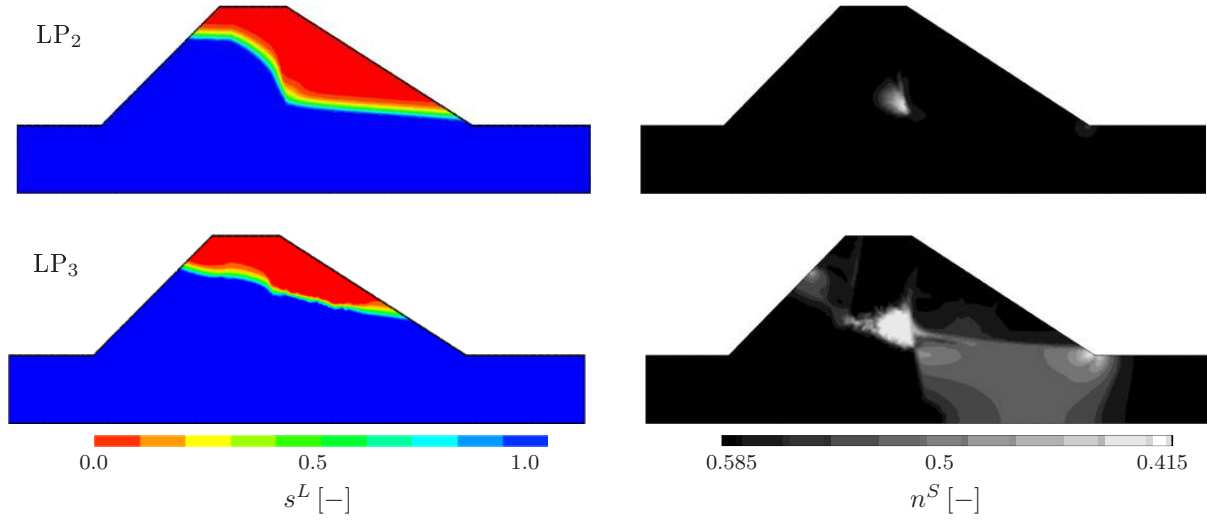
In order to study numerically the failure process of embankments with internal core, the IBVP shown in Figure 8.17 has been generated. The dimensions are the same as of the soil embankment presented before. The embedded internal core amounts a 20



**Figure 8.17:** Geometry and dimensions of the embankment with central core in [m].

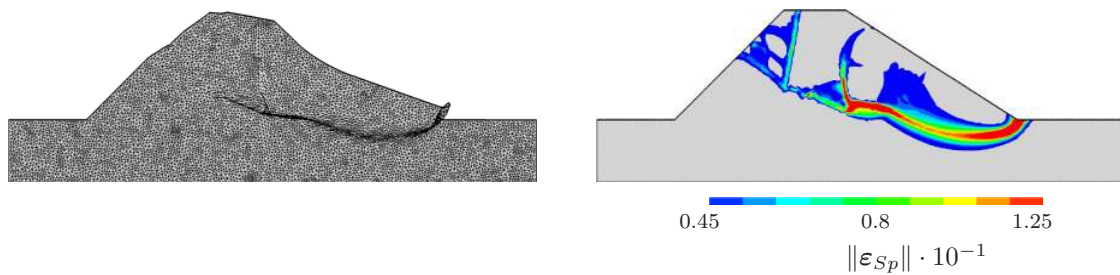
times less permeability than the surrounding soil. To simplify the interpretation of the numerical results, the same material parameters have been used for the whole embankment except of the cohesion  $\kappa^{(1)/(2)} = 0.013/0.35$  MPa, the intrinsic permeability  $K_{0S}^{S(1)/S(2)} = 2 \cdot 10^{-12}/10^{-13}$  m<sup>2</sup> and the erosion velocity  $\zeta^{EE(1)/EE(2)} = 150/1500$  s/m. Note that the erosion velocity parameter  $\zeta^{EE(2)}$  of the internal core is chosen 10 times larger than of the embankment soil  $\zeta^{EE(1)}$  in order to enforce the erosion process within the core. Regarding the loading paths of this problem, they have been kept simple. Thereby, the water table is firstly increased at the left side of the embankment in 24 h to 5 m and, afterwards, it is kept constant.

Figure 8.18 shows the development of  $s^L$  and  $n^S$  of the embankment immediately after increasing the water table to 5 m and at the state of failure. The degradation of  $n^S$  is



**Figure 8.18:** (top) Simulation results after the second loading phase and (bottom) during the third loading phase (failure state): (left) liquid saturation  $s^L$  and (right) solidity  $n^S$ .

initiated by the hydraulic gradient within the core. Due to increasing porosity,  $\mathbf{w}_L$  is enforced, where gradually a porous pipe through the core is created and proceeds in direction to the reservoir. As a consequence, the water table gradually starts to increase at the water-protected side of the embankment, cf. Figure 8.18 (bottom-left). Thereby, the right slope gets under buoyancy and, in the end, the embankment fails. The deformation state at failure is shown in Figure 8.19 (left) by the deformed FE mesh with 10-times magnification of the deformations. Therein, it can be recognised that the complete embankment is in motion along the main shear band, cf. Figure 8.19 (right).



**Figure 8.19:** (left) Deformed FE mesh at the final state with 10-times magnification and (right) the evolved shear band.

Despite of the restrictions of the internal erosion process mentioned in Section 8.1, significant physical processes of embankment problems could be well recaptured by the presented partially saturated soil erosion model.

# Chapter 9:

## Conclusion

### 9.1 Summary

The main focus of the presented thesis lies on realistic simulations of IBVP in the field of geomechanics using a partially saturated soil. To reach this goal, the partially saturated soil has been intensively analysed based on the topics of the experimental investigation, the constitutive modelling, the parameter identification and model validation. An overview to these topics was given in the introduction.

Due to the coupled deformation and flow process of partially saturated soils, accurate experimental investigations of their mechanical and hydraulic behaviour are very sophisticated. Based on the principle of phase separation, the mechanical properties of the GEBA sand were experimentally investigated at dry conditions via triaxial experiments, while the hydraulic behaviour was determined with deformation-free experiments. On the basis of these experiments, constitutive approaches for the triphasic model have been derived thermodynamically consistent in the framework of the Theory of Porous Media (TPM). Concerning this, the fundamentals of the well-documented TPM concept was briefly presented.

The most important point in the matter of material modelling is the experimental investigation, because false measurements or faulty experimental equipments produce faulty data sets. Based on faulty results, wrong conclusions and assumptions of the material behaviour would be drawn and, thus, would lead to incorrect constitutive modelling approaches. Before carrying out the triaxial experiments, the test setup was optimised concerning some error sources. In particular, the main error was involved in the triaxial cell. Hence, a new stiff triaxial cell was constructed. Including the triaxial cell and other error sources, the measuring error of the complete triaxial device system could be reduced to a reasonably low value.

The yield as well as the failure behaviour of dense sand was investigated by use of drained monotonic and non-monotonic triaxial experiments. Especially, it could be shown through triaxial stress-path-depending compression tests that the standard approach to limit the hardening of the yield surface by a fixed failure surface is not correct. The evolution of the yield surface has been limited by a hydrostatic stress-dependent failure surface. The good agreement with all experiments shows that the presented approach is promising for realistic simulations of quasi-static IBVP of cohesionless-frictional materials. Furthermore, the triphasic soil model for describing the partially saturated soil was numerically validated by simulations of different slope failure scenarios at the technical scale. The results showed that the presented TPM model is well suited to mimic the physical behaviour of multiphase materials such as partially saturated sand and also reliably predicted shear failure triggered by the hydraulic conditions.

For a numerical analysis of IBVP, the governing balance equations of the triphasic model have been transferred into weak formulations and discretised in space and time. Because of the elasto-plastic behaviour of the solid matrix, the resulting DAE system of global and local equations was iteratively solved in the sense of a two-stage *Newton* procedure. To consider the dependencies of the global tangent of the governing equations from the local history variables, the algorithmically consistent material tangent was implemented. Furthermore, for the identification of the material parameters, the FE tool was coupled with the gradient-based non-linear SQP optimisation method. To solve the *Hessian* matrix of the extremal of the constraint optimisation problem, the BFGS method was applied. Hereto, the required sensitivities of the fitted quantities with respect to the optimised material parameters were computed semi-analytically.

Moreover, the capability of the TPM model was tested by simulations of the Heumös hillslope. Although the Heumös hillslope is flat, it is still creeping at several parts with different velocities. Therewith, it could be concluded that several slope bodies are existing. For the numerical analysis, the hillslope was described by a long representative cross-section proceeding from a simplified material composition of the slope body. The cross-section is divided into three stratum, while the lowest one is the bedrock with a very hilly topology. Based on a hydraulic loading condition representing a large precipitation depth, the FEM simulations revealed several shear bands between the stratum interfaces as well as at deep parts of the bedrock. Thus, the numerically detected shear bands separate the Heumös slope in several slip bodies, which may explain the observed motion situation of the Heumös slope concerning the assumption of several slope bodies.

The triphasic model was further extended to model internal soil erosion problems. Concerning this, an erosion phase has been introduced, which represents the fluidised grains. However, the very complex erosion process was strongly subjected to restrictions, because the objective of the numerical investigation of erosion problems was focused on the analyses of embankment destabilisations induced by losing solidity. The increase of the soil porosity degrades the material stiffness and strength, which leads to the weakening of the soil construction. These changes of the material behaviour have been taken into account by reducing the elastic (reducing the stiffness) and plastic (shrinking the failure surface) material parameters in dependence of the porosity development as in damage procedures.

## 9.2 Outlook

The presented new concept of a stress-dependent failure surface can be further improved by determining the complete shape of an individual failure surface for a chosen confining pressure state. Repeating this for different confining pressures, the evolution of the failure surface can be approximated. Based on these results, the model concept of yielding and failure evolution can be further optimised. Furthermore, the evolution of the yield surface is only restricted to the isotropic hardening. This has to be extended to kinematic hardening in order to consider large stress reversal from compression to extension range and vice versa.

The reliability of the computations of natural slopes depends mainly on the quality of



the model input data, which has to be obtained from field measurements. This is one of the challenges faced by hydrologists and geophysicists because the valuable simulation of real-scale problems requires 3-d information about the subsurface structure and the mechanical and hydraulic properties. The application of computer simulations to elucidate the complex hydraulic pressure and flow systems that might trigger hillslope movements poses also challenges to the numerical algorithms. In fact, the numerical treatment of strongly coupled, inelastic solid-fluid IBVP on real-scale 3-d domains requires high computing power exploiting parallel and distributed solution strategies which are far from being standard.

The complexity of the presented internal soil erosion model has to be increased, for example, concerning the transport of the grains, in order to treat more sophisticated IBVP. Furthermore, non-linear fluid motion laws have to be implemented in order to simulate the areas correctly, where very high and low porosity areas are connected. This is generally the case between the main soil and the erosion pipe. Moreover, 3-d simulations of embankment failure triggered by internal erosion are an important and challenging goal for future work.



# Appendix A:

## Elementary Triaxial tests

### A.1 Deformation behaviour

Triaxial experiments have been carried out with lubricated latex membranes on the endplates of the cylindrical specimen in order to minimise the friction force between the endplate and the specimen. Therewith, an almost homogeneous deformation behaviour is ensured. In Figure A.1, the undeformed (left) and the deformed (right) specimen are illustrated, wherein the edges of the deformed specimen are almost plane like the initial state, cf. Müllerschön [118]. However, a specimen with non-lubricated endplates would lead to bulging of the specimen because the volume deformations are impeded at the boundaries of the specimen. However, this leads to an inhomogeneous deformation development within the specimen and to the evolution of shear bands.

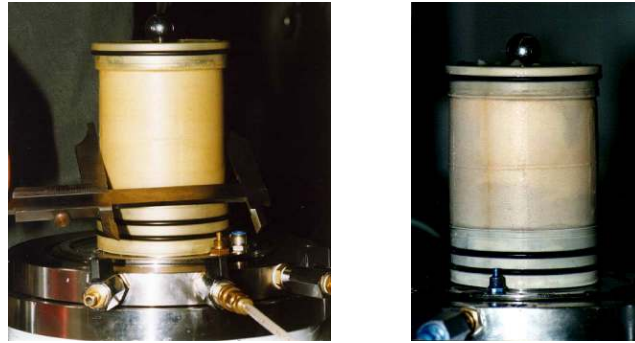


**Figure A.1:** (left) Undeformed (initial) state and (right) homogeneous deformed state of a cylindrical sand specimen.

### A.2 Boundary conditions

Due to homogeneous deformations of the specimen, the radial and tangential stresses  $\sigma_r$  and  $\sigma_\varphi$  expressed by the cylindrical coordinates  $r$  (radius) and  $\varphi$  (polar angle) are equal  $\sigma_r = \sigma_\varphi$ , because, within the specimen, no stress gradients are developing. Hence, the stresses expressed in Cartesian coordinates are also equal,  $\sigma_2 = \sigma_3$ , where the stress tensor  $\boldsymbol{\sigma}$  can be reduced to the principle stress vector, cf. Müllerschön [118]:

$$\boldsymbol{\sigma} = \begin{pmatrix} \sigma_1 & 0 & 0 \\ 0 & \sigma_3 & 0 \\ 0 & 0 & \sigma_3 \end{pmatrix} \mathbf{e}_i \otimes \mathbf{e}_j \hat{=} \begin{pmatrix} \sigma_1 \\ \sigma_3 \\ \sigma_3 \end{pmatrix} \mathbf{e}_i. \quad (\text{A.1})$$

Using the rotational and axial symmetric conditions of the cylindrical specimen, the computation model can be reduced to a 2-d plane strain problem, cf. Figure A.2.

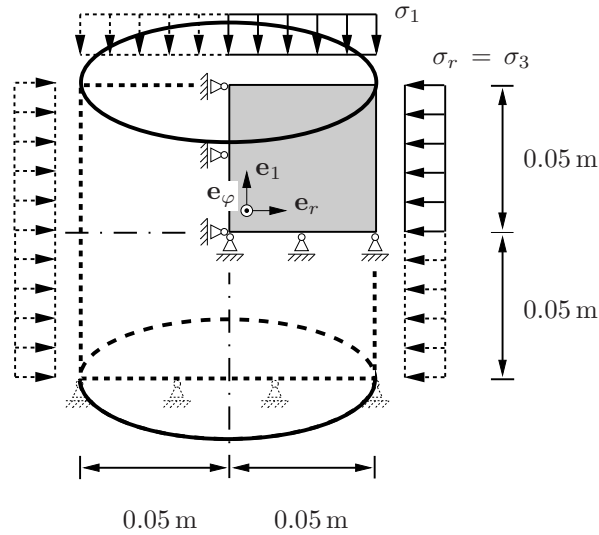


**Figure A.2:** Idealisation of the cylindrical specimen for numerical computations.

## Appendix B: Important Relations

### B.1 Derivations of the total and effective quantities

$$\begin{aligned}
\boldsymbol{\sigma}^S &= -n^S p^{AR} \mathbf{I} + p^C s^W n^S \mathbf{I} + \boldsymbol{\sigma}_{Em}^S \\
&= -n^S p^{AR} \mathbf{I} + (p^{AR} - p^{WR}) s^W n^S \mathbf{I} + \boldsymbol{\sigma}_{Em}^S \\
&= -n^S p^{AR} \mathbf{I} + p^{AR} (1 - s^A) n^S \mathbf{I} - p^{WR} s^W n^S \mathbf{I} + \boldsymbol{\sigma}_{Em}^S \\
&= -n^S (s^A p^{AR} + s^W p^{WR}) \mathbf{I} + \boldsymbol{\sigma}_{Em}^S \\
&= -n^S p^{FR} \mathbf{I} + \boldsymbol{\sigma}_{Em}^S, \\
\mathbf{T}^A &= -n^A p^{AR} \mathbf{I} + \mathbf{T}_E^A \approx -p^A \mathbf{I}, \\
\mathbf{T}^W &= -n^W (p^{AR} - p^C) \mathbf{I} + \mathbf{T}_{Em}^W = -n^W p^{WR} \mathbf{I} + \mathbf{T}_{Em}^W \approx -p^W \mathbf{I}, \\
\hat{\mathbf{p}}^A &= p^{AR} \text{grad } n^A + \hat{\mathbf{p}}_E^A \\
\hat{\mathbf{p}}^W &= p^{AR} \text{grad } n^W + p^C s^W \text{grad } n^S + \hat{\mathbf{p}}_{Em}^W \\
&= p^{AR} \text{grad } n^W - (p^{AR} - p^{WR}) \text{grad } n^W + p^C n^F \text{grad } s^W + \hat{\mathbf{p}}_{Em}^W \\
&= p^{WR} \text{grad } n^W + p^C (s^A \text{grad } n^W - s^W \text{grad } n^A) + \hat{\mathbf{p}}_{Em}^W.
\end{aligned} \tag{B.1}$$

$$\begin{aligned}
\text{With: } p^C n^F \text{grad } s^W &= p^C [(n^W + n^A) \text{grad } s^W] \\
&= p^C [\text{grad } (s^W n^A) - s^W \text{grad } n^A + \text{grad } (s^W n^W) - s^W \text{grad } n^W] \\
&= p^C [\text{grad } n^W - s^W \text{grad } n^W - s^W \text{grad } n^W] \\
&= p^C [(1 - s^W) \text{grad } n^W - s^W \text{grad } n^A] \\
&= p^C [s^A \text{grad } n^W - s^W \text{grad } n^A] .
\end{aligned}$$



# Appendix C:

## Identified Triphasic Model of the GEBA Sand

### C.1 Parameters of the solid skeleton

Parameters of the elastic behaviour and of the initial state:					
$\mu^S$	=	150	MPa	$n_{max}^S$	= 0.5935 [-]
$k_0^S$	=	25	MPa	$n_{0S}^S$	= 0.585 [-]
$k_1^S$	=	50	MPa	$K_{0S}^S$	= $2 \cdot 10^{-10}$ m <sup>2</sup>
$\rho^{SR}$	=	2.65	g/cm <sup>3</sup>		
Parameters of the plastic behaviour:					
initial yield surface (hardening parameters)					
$\delta_0$	=	$7.8 \cdot 10^{-3}$	1/MPa	$\beta_0$	= 0.095 [-]
$\epsilon_0$	=	0.1	1/MPa	$\gamma_0$	= 0.0 [-]
limit values of the hardening parameters representing the failure surface					
$\delta^*$	=	$7.3 \cdot 10^{-3}$	1/MPa	$\beta^*$	= 0.267 [-]
$\epsilon_0^*$	=	0.046	1/MPa	$\gamma^*$	= 1.66 [-]
parameters controlling the evolution of the failure surface					
$C_\epsilon^*$	=	0.293	1/MPa	$\epsilon_{lim}^*$	= 0.01 1/MPa
parameters controlling the evolution of the yield surface					
$C_\delta^V$	=	120	[-]	$C_\delta^D$	= 22 [-]
$C_\epsilon^V$	=	690	[-]	$C_\epsilon^D$	= 280 [-]
$C_\beta^V$	=	280	[-]	$C_\beta^D$	= 280 [-]
$C_\gamma^V$	=	0.0	[-]	$C_\gamma^D$	= 30 [-]
Additional yield surface, plastic potential and viscoplastic parameters					
$\kappa$	=	$1 \cdot 10^{-4}$	1/MPa	$\alpha$	= 0.01 [-]
$m$	=	0.54	[-]	$\eta$	= 100 s
$\psi_1$	=	1.1	[-]	$r$	= 1.5 [-]
$\psi_2$	=	0.64	[-]	$\sigma_0$	= $1 \cdot 10^{-4}$ 1/MPa

**Table C.1:** *Elasto-viscoplastic material parameters, cf. Ehlers and Avci [56].*

## C.2 Parameters of the partially saturated zone

Hydraulic parameters of partially saturated soil					
$s_{res}^W$	=	0.118	[-]	$s_{res}^A$	= 0.0233 [-]
$\alpha_{gen}$	=	1.421	1/kPa	$j_{gen}$	= 6.251 [-]
$h_{gen}$	=	1.0	[-]	$\epsilon_{gen}$	= 1.5 [-]
$\gamma_{gen}$	=	0.001	[-]	$\pi$	= 1.0 [-]

**Table C.2:** Van Genuchten material parameters of the GEBA sand.



# Bibliography

- [1] Alonso, E. E.; Gens, A. & Josa, A.: A constitutive model for partially saturated soils. *Géotechnique* **40** (1990), 405–430.
- [2] Alva-Hurtado, J. & Selig, E.: Survey of laboratory devices for measuring soil volume change. *Geotechnical Testing Journal* **4** (1981), 11–18.
- [3] Ammann, M.: *Parallel finite element simulations of localization phenomena in porous media*. Dissertation, Report No. II-11 of the Institute of Applied Mechanics (CE), University of Stuttgart 2005.
- [4] Bäck, T. & Schwefel, H.-P.: An Overview of Evolutionary Algorithms for Parameter Optimization. *Evolutionary Computation* **1** (1993), 1–23.
- [5] Bathe, K.-J.: *Finite-Elemente-Methoden*. Springer-Verlag, Berlin 1990.
- [6] Bendahmane, F.; Marot, D. & Alexis, A.: Experimental parametric study of suffusion and backward erosion. *Journal of Geotechnical and Geoenvironmental Engineering* **134** (2008), 57–67.
- [7] Benz, T.: *Small-strain stiffness of soils and its numerical consequences*. Dissertation, Report No. 55 of the Institute for Geotechnical Engineering, University of Stuttgart 2007.
- [8] Bertsekas, D. P.: *Nonlinear programming*. Athena Scientific, Belmont, Mass. 1995.
- [9] Bishop, A. W.: The effective stress principle. *Teknisk Ukeblad* **39** (1959), 859–863.
- [10] Blome, P.: *Ein Mehrphasen-Stoffmodell für Böden mit Übergang auf Interface-Gesetze*. Dissertation, Bericht Nr. II-10 aus dem Institut für Mechanik (Bauwesen), Universität Stuttgart 2003.
- [11] de Boer, R.: *Vektor- und Tensorrechnung für Ingenieure*. Springer-Verlag, Berlin 1982.
- [12] de Boer, R.: On plastic deformations of soils. *International Journal of Plasticity* **4** (1988), 371–391.
- [13] de Boer, R.: Highlights in the historical development of porous media theory: toward a consistent macroscopic theory. *Applied Mechanics Review* **49** (1996), 201–262.
- [14] de Boer, R.: *Theory of Porous Media*. Springer-Verlag, Berlin 2000.
- [15] de Boer, R. & Ehlers, W.: *Theorie der Mehrkomponentenkontinua mit Anwendung auf bodenmechanische Probleme*. Forschungsberichte aus dem Fachbereich Bauwesen, Heft 40, Universität-GH-Essen 1986.

- [16] de Boer, R. & Ehlers, W.: The development of the concept of effective stresses. *Acta Mechanica* **83** (1990), 77–92.
- [17] Boggs, P. T. & Tolle, J. W.: Sequential quadratic programming. *Acta Numerica* **4** (1995), 1–51.
- [18] Bolzon, G.; Schrefler, B. A. & Zienkiewicz, O. C.: Elastoplastic soil constitutive laws generalized to partially saturated states. *Géotechnique* **46** (1996), 279–289.
- [19] Bowen, R. M.: Theory of mixtures. In Eringen, A. C. (Ed.): *Continuum Physics*. Vol. III, Academic Press, New York 1976, pp. 1–127.
- [20] Bowen, R. M.: Incompressible porous media models by use of the theory of mixtures. *International Journal of Engineering Sciences* **18** (1980), 1129–1148.
- [21] Bowen, R. M.: Compressible porous media models by use of the theory of mixtures. *International Journal of Engineering Sciences* **20** (1982), 697–735.
- [22] Braess, D.: *Finite Elemente*. Springer-Verlag, Berlin 1997.
- [23] Brenan, K. E.; Campbell, S. L. & Petzold, L. R.: *Numerical Solution of Initial-Value Problems in Differential-Algebraic Equations*. North-Holland, New York 1989.
- [24] Brezzi, F. & Fortin, M.: *Mixed and Hybrid Finite Element Methods*. Springer-Verlag, New York 1991.
- [25] Brooks, R. N. & Corey, A. T.: Properties of porous media affecting fluid flow. *ASCE: Journal of the Irrigation and Draining Division* **92** (1966), 61–68.
- [26] Castro, G.: On the behavior of soils during earthquakes - liquefaction. In Cakmak, A. S. (Ed.): *Soil Dynamics and Liquefaction*. Elsevier Science Pub., Amsterdam 1987, pp. 169–204.
- [27] Chai, J. & Carter, J. P.: Simulation of the progressive failure of an embankment on soft soil. *Computers and Geotechnics* **36** (2009), 1024 – 1038.
- [28] Chen, Z.; Steeb, H. & Diebels, S.: A EVI-space-time Galerkin method for dynamics at finite deformation in porous media. *Computational Mechanics* **43** (2009), 585–601.
- [29] Ciarlet, P. G.: *Mathematical elasticity, Vol. 1*. North-Holland, Amsterdam 1988.
- [30] Coleman, B. D. & Noll, W.: The thermodynamics of elastic materials with heat conduction and viscosity. *Archive for Rational Mechanics and Analysis* **13** (1963), 167–178.
- [31] Cosserat, E. & Cosserat, F.: *Théorie des corps déformables*. A. Hermann et fils, Paris 1909, (Theory of Deformable Bodies, NASA TT F-11 561, 1968).
- [32] Dafalias, Y. F. & Herrmann, L. R.: Bounding surface plasticity. II: Application to isotropic cohesive soils. *Journal of Engineering Mechanics* **112** (1986), 1263–1291.

- [33] Dafalias, Y. F. & Popov, E. P.: A model of nonlinearly hardening materials for complex loading. *Acta Mechanica* **21** (1975), 173–192.
- [34] Darcy, H.: *Les Fontaines Publiques de la Ville de Dijon*. Dalmont, Paris 1856.
- [35] Darve, F. & Laouafa, F.: Instabilities in granular materials and application to landslides. *Mechanics of Cohesive-frictional Materials* **5** (2000), 627–652.
- [36] Dennis, J. R. & Schnable, R. B.: *Numerical Methods for Unconstrained Optimization and Nonlinear Equations*. Siam, Philadelphia 1996.
- [37] Depenthal, C. & Schmitt, G.: Monitoring of a landslide in Vorarlberg/Austria. In S. Stiros, S. & Pytharouli, S. (Eds.): *Proceedings 11th of the International FIG Symposium on Deformation Measurements, Santorini (Thera) Island, Greece*. Geodesy and Geodetic Applications Laboratory, Department of Civil Engineering 2003, pp. 289–295.
- [38] Desai, C. S.: A general basis for yield, failure and potential functions in plasticity. *International Journal for Numerical and Analytical Methods in Geomechanics* **4** (1980), 361–375.
- [39] Desai, C. S.: A hierarchical approach constitutive modelling of geological materials. *International Journal for Numerical and Analytical Methods in Geomechanics* **10** (1986), 225–257.
- [40] Desai, C. S.: *Mechanics of Materials and Interfaces: The Disturbed State Concept*. CRC Press LLC, Boca Raton, Florida 2001.
- [41] Desrues, J.; Chambon, R.; Mokni, M. & Mazerolle, F.: Void ratio evolution inside shear bands in triaxial sand specimens studied by computed tomography. *Géotechnique* **46** (1996), 529–546.
- [42] Diebels, S.: *Mikropolare Zweiphasenmodelle: Formulierung auf der Basis der Theorie Poröser Medien*. Habilitation, Bericht Nr. II-4 aus dem Institut für Mechanik (Bauwesen), Universität Stuttgart 2000.
- [43] Diebels, S. & Ehlers, W.: On fundamental concepts of multiphase micropolar materials. *Technische Mechanik* **16** (1996), 77–88.
- [44] Diebels, S.; Ellsiepen, P. & Ehlers, W.: Error-controlled *Runge-Kutta* time integration of a viscoplastic hybrid two-phase model. *Technische Mechanik* **19** (1999), 19–27.
- [45] Drucker, D. C. & Prager, W.: Soil mechanics and plastic analysis of limit design. *Quart. Appl. Math.* **10** (1952), 157–165.
- [46] Ehlers, W.: On thermodynamics of elasto-plastic porous media. *Archive of Mechanics* **41** (1989), 73–93.

- [47] Ehlers, W.: *Poröse Medien – ein kontinuumsmechanisches Modell auf der Basis der Mischungstheorie*. Habilitation, Forschungsberichte aus dem Fachbereich Bauwesen, Heft 47, Universität-GH-Essen 1989.
- [48] Ehlers, W.: Constitutive equations for granular materials in geomechanical context. In Hutter, K. (Ed.): *Continuum Mechanics in Environmental Sciences and Geophysics*. CISM Courses and Lectures No. 337, Springer-Verlag, Wien 1993, pp. 313–402.
- [49] Ehlers, W.: A single-surface yield function for geomaterials. *Archive of Applied Mechanics* **65** (1995), 246–259.
- [50] Ehlers, W.: Grundlegende Konzepte in der Theorie Poröser Medien. *Technische Mechanik* **16** (1996), 63–76.
- [51] Ehlers, W.: Continuum and numerical simulation of porous materials in science and technology. In und V. N. Ghionna, G. C. & Giovine, P. (Eds.): *Modeling and Mechanics of Granular and Porous Materials*. Birkhäuser, Boston 2002, pp. 244–292.
- [52] Ehlers, W.: Foundations of multiphasic and porous materials. In Ehlers, W. & Bluhm, J. (Eds.): *Porous Media: Theory, Experiments and Numerical Applications*. Springer-Verlag, Berlin 2002, pp. 3–86.
- [53] Ehlers, W.: Challenges of porous media models in geo- and biomechanical engineering including electro-chemically active polymers and gels. *International Journal of Advances in Engineering Sciences and Applied Mathematics* **1** (2009), 1–24.
- [54] Ehlers, W.: *Poröse Medien – ein kontinuumsmechanisches Modell auf der Basis der Mischungstheorie*. Habilitation, Bericht Nr. II-22 aus dem Institut für Mechanik (Bauwesen), Universität Stuttgart 2012.
- [55] Ehlers, W.: *Vector and tensor calculus: An introduction*. Lecture notes, Institute of Applied Mechanics (CE), University of Stuttgart 2012, <http://www.mechbau.uni-stuttgart.de/ls2/Downloads/vectortensor.pdf>.
- [56] Ehlers, W. & Avci, O.: Stress-dependent hardening and failure surfaces of dry sand. *International Journal for Numerical and Analytical Methods in Geomechanics* **37** (2013), 787–809.
- [57] Ehlers, W.; Avci, O. & Markert, B.: Computation of Slope Movements Initiated by Rain-Induced Shear Bands in Small-Scale Tests and In Situ. *Vadose Zone Journal* **10** (2011), 512–525.
- [58] Ehlers, W. & Blome, P.: A triphasic model for unsaturated soils based on the Theory of Porous Media. *Mathematical and Computer Modelling* **37** (2003), 507–513.
- [59] Ehlers, W. & Bluhm, J. (Eds.): *Porous Media: Theory, Experiments and Numerical Applications*. Springer-Verlag, Berlin 2002.

- [60] Ehlers, W. & Eipper, G.: Finite elastic deformations in liquid-saturated and empty porous solids. *Transport in Porous Media* **34** (1999), 179–191.
- [61] Ehlers, W. & Ellsiepen, P.: On the adaptive computation of shear bands in frictional geomaterials. In Sändig, A. M.; Schiehlen, W. & Wendland, W. L. (Eds.): *Multifield Problems – State of the Art*. Springer-Verlag, Berlin 2000, pp. 135–142.
- [62] Ehlers, W. & Ellsiepen, P.: Theoretical and numerical methods in environmental continuum mechanics based on the Theory of Porous Media. In Schrefler, B. A. (Ed.): *Environmental Geomechanics*. CISM Courses and Lectures No. 417, Springer-Verlag, Wien 2001, pp. 1–81.
- [63] Ehlers, W.; Ellsiepen, P.; Blome, P.; Mahnkopf, D. & Markert, B.: *Theoretische und numerische Studien zur Lösung von Rand- und Anfangswertproblemen in der Theorie Poröser Medien*. Abschlußbericht zum DFG-Forschungsvorhaben Eh 107/6-2, Bericht aus dem Institut für Mechanik (Bauwesen), Nr. 99-II-1, Universität Stuttgart 1999.
- [64] Ehlers, W.; Graf, T. & Ammann, M.: Deformation and localization analysis in partially saturated soil. *Computer Methods in Applied Mechanics and Engineering* **193** (2004), 2885–2910.
- [65] Ehlers, W.; Krause, R. & Markert, B.: Modelling and remodelling of biological tissue in the framework of continuum biomechanics. *PAMM* **11** (2011), 35–38.
- [66] Ehlers, W. & Müllerschön, H.: Parameter identification of a macroscopic granular soil model applied to dense Berlin sand. *Granular Matter* **2** (2000), 105–112.
- [67] Ehlers, W. & Scholz, B.: An inverse algorithm for the identification and the sensitivity analysis of the parameters governing micropolar elasto-plastic granular material. *Archive of Applied Mechanics* **77** (2007), 911–931.
- [68] Ehlers, W. & Volk, W.: On shear band localization phenomena of liquid-saturated granular elasto-plastic porous solid materials accounting for fluid viscosity and micropolar solid rotations. *Mechanics of Cohesive-frictional Materials* **2** (1997), 301–320.
- [69] Ehlers, W. & Volk, W.: On theoretical and numerical methods in the theory of porous media based on polar and non-polar elasto-plastic solid materials. *International Journal of Solids and Structures* **35** (1998), 4597–4617.
- [70] Ellsiepen, P.: *Zeit- und ortsadaptive Verfahren angewandt auf Mehrphasenprobleme poröser Medien*. Dissertation, Bericht Nr. II-3 aus dem Institut für Mechanik (Bauwesen), Universität Stuttgart 1999.
- [71] Fell, R.; Wan, C.; Cyganiewicz, J. & Foster, M.: Time for development of internal erosion and piping in embankment dams. *Journal of Geotechnical and Environmental Engineering* **129** (2003), 307–314.

- [72] Ferrari, A.; Laloui, L. & Bonnard, C.: Hydro-mechanical modelling of a natural slope affected by a multiple slip surface failure mechanism. *CMES - Computer Modeling in Engineering & Sciences* **52** (2009), 217–235.
- [73] Fredlund, D. G. & Rahardjo, H.: *Soil Mechanics for Unsaturated Soils*. Wiley, New York 1993.
- [74] Geiser, F.; Laloui, L. & Vulliet, L.: On the volume measurement in unsaturated triaxial test. *Proceedings of the Asia Conference on Unsaturated Soil, UNSAT-ASIA* (2000), 669–675.
- [75] van Genuchten, M. T.: A closed-form equation for predicting the hydraulic conductivity of unsaturated soils. *Soil Science Society of America Journal* **44** (1980), 892–898.
- [76] Germer, K. & Braun, J.: Slope failure process in a laboratory flume. In Malet, J.-P.; Remaitre, A. & Boggard, T. A. (Eds.): *Landslide Processes - From geomorphological mapping to dynamic modeling*. Strasbourg: Centre Européen sur les Risques Géomorphologiques (CERG) editors 2009, pp. 115–118.
- [77] Germer, K. & Braun, J.: Effects of Saturation on Slope Stability: Laboratory Experiments Utilizing External Load. *Vadose Zone Journal* **10** (2011), 477–486.
- [78] Graf, T.: *Multiphasic Flow Processes in Deformable Porous Media under Consideration of Fluid Phase Transitions*. Dissertation, Report No. II-17 of the Institute of Applied Mechanics (CE), University of Stuttgart 2008.
- [79] Hairer, E.; Lubich, C. & Roche, M.: *The Numerical Solution of Differential-Algebraic Equations by Runge-Kutta Methods*. Springer-Verlag 1989.
- [80] Hairer, E. & Wanner, G.: *Solving Ordinary Differential Equations, Vol. 2: Stiff and Differential-Algebraic Problems*. Springer-Verlag, Berlin 1991.
- [81] Hartmann, S.; Lühns, G. & Haupt, P.: An efficient stress algorithm with applications in viscoplasticity and plasticity. *International Journal for Numerical Methods in Engineering* **40** (1997), 991–1013.
- [82] Hassanizadeh, S. M. & Gray, W. G.: General conservation equations for multi-phase systems: 1. Averaging procedure. *Advances in Water Resources* **2** (1979), 131–144.
- [83] Haupt, P.: On the concept of an intermediate configuration and its application to a representation of viscoelastic-plastic material behavior. *International Journal of Plasticity* **1** (1985), 303 – 316.
- [84] Haupt, P.: Foundation of continuum mechanics. In Hutter, K. (Ed.): *Continuum Mechanics in Environmental Sciences and Geophysics*. CISM Courses and Lectures No. 337, Springer-Verlag, Wien 1993, pp. 1–77.
- [85] Haupt, P.: *Continuum Mechanics and Theory of Materials*. Springer-Verlag, Berlin 2000.

- [86] Heider, Y.: *Saturated Porous Media Dynamics with Application to Earthquake Engineering*. Dissertation, Report No. II-25 of the Institute of Applied Mechanics (CE), University of Stuttgart 2012.
- [87] Heinz, J. & Spellucci, P.: A succesful implementation of the Pantoja-Mayne SQP-Method. *Optimization Methods and Software* **4** (1994), 1–28.
- [88] Hill, R.: *The Mathematical Theory of Plasticity*. Oxford Classic Texts in the Physical Sciences, Clarendon Press 1998.
- [89] Hughes, T. J. R.: *The Finite Element Method*. Prentice-Hall, London 1987.
- [90] Indraratna, B.; Nguyen, V. T. & Rujikiatkamjorn, C.: Assessing the potential of internal erosion and suffusion of granular soils. *Journal of Geotechnical and Geoenvironmental Engineering* **137** (2011), 550–554.
- [91] Kachanov, L. M.: *Introduction to Continuum Damage Mechanics*. Kluwer Academic Publishers, Dordrecht 1986.
- [92] Kim, M. K. & Lade, P. V.: Single hardening constitutive model for frictional materials, I. Plastic potential function. *Computers and Geotechnics* **5** (1988), 307–324.
- [93] Kleiber, M.: Kinematics of deformation processes in materials subjected to finite elastic-plastic strains. *International Journal of Engineering Science* **13** (1975), 513–525.
- [94] Klubertanz, G.; Laloui, L. & Vulliet, L.: Identification of mechanisms for landslide type initiation of debris flows. *Engineering Geology* **109** (2009), 114–123.
- [95] Ko, H.-Y. & Scott, R. F.: A new soil testing apparatus. *Géotechnique* **17** (1967), 40–57.
- [96] Krenk, S.: Characteristic state plasticity for granular materials part I: Basic theory. *International Journal of Solids and Structures* **37** (2000), 6343–6360.
- [97] Lade, P. V.: Experimental observations of stability, instability, and shear planes in granular materials. *Archive of Applied Mechanics* **59** (1989), 114–123.
- [98] Lade, P. V.: Instability, shear banding, and failure in granular materials. *International Journal of Solids and Structures* **39** (2002), 3337–3357.
- [99] Lade, P. V. & Duncan, J. M.: Cubical triaxial tests on cohesionless soil. *ASCE: Journal of Soil Mechanics and Foundations Division* **99** (1973), 793–812.
- [100] Lade, P. V. & Kim, M. K.: Single hardening constitutive model for frictional material, II. Yield criterion and plastic work contours. *Computers and Geotechnics* **6** (1988), 13–29.
- [101] Lade, P. V. & Prabucki, M.-J.: Softening and preshearing effects in sand. *Soils and Foundations* **35** (1995), 93–104.

- [102] Laloui, L. & Nuth, M.: An introduction to the constitutive modelling of unsaturated soils. *Revue Européenne de Génie Civil* **9** (2005), 651–669.
- [103] Lee, E. H.: Elastic-plastic deformation at finite strains. *Journal of Applied Mechanics* **36** (1969), 1–6.
- [104] Lemaitre, J. & Chaboche, J.-L.: *Mechanics of solid materials*. Cambridge University Press, Cambridge 1990.
- [105] Leong, E. C.; Agus, S. S. & Rahardjo, H.: Volume change measurement of soil specimen in triaxial test. *Geotechnical Testing Journal* **27** (2004), 1–9.
- [106] Lewis, R. W. & Schrefler, B. A.: *The Finite Element Method in the Static and Dynamic Deformation and Consolidation of Porous Media*, 2nd Edition. Wiley, Chichester 1998.
- [107] Lindenmaier, F.: *Hydrology of a large unstable hillslope at Ebnit, Vorarlberg: identifying dominating processes and structures*. Dissertation, RVK 65345, Institut für Geoökologie, Universität Potsdam 2008.
- [108] Lubliner, J.: *Plasticity theory*. Macmillan, New York 1990.
- [109] Luenberger, D. & Ye, Y.: *Linear and nonlinear programming*, 3rd Edition. Springer, New York 2008.
- [110] Mahnken, R.: *Duale Methoden für nichtlineare Optimierungsprobleme in der Strukturmechanik*. Dissertation, Forschungs- und Seminarberichte aus dem Bereich der Mechanik der Universität Hannover, Bericht-Nr. F 92/3, Universität Hannover 1992.
- [111] Mahnken, R.: *Theoretische und numerische Aspekte zur Parameteridentifikation und Modellierung bei metallischen Werkstoffen*. Habilitation, Forschungs- und Seminarberichte aus dem Bereich der Mechanik der Universität Hannover, Bericht-Nr. F. 98/2, Universität Hannover 1998.
- [112] Mahnken, R. & Stein, E.: The identification of parameters for visco-plastic models via finite-element methods and gradient methods. *Modelling and Simulation in Materials Science and Engineering* **2** (1994), 597–616.
- [113] Mahnkopf, D.: *Lokalisierung fluidgesättigter poröser Festkörper bei finiten elasto-plastischen Deformationen*. Dissertation, Bericht Nr. II-5 aus dem Institut für Mechanik (Bauwesen), Universität Stuttgart 2000.
- [114] Markert, B.: *Porous Media Viscoelasticity with Application to Polymeric Foams*. Dissertation, Report No. II-12 of the Institute of Applied Mechanics (CE), University of Stuttgart 2005.
- [115] Miehe, C.: *Kanonische Modelle multiplikativer Elasto-Plastizität. Thermodynamische Formulierung und numerische Implementierung*. Dissertation, Forschungs- und Seminarberichte aus dem Bereich der Mechanik der Universität Hannover, Bericht-Nr. F 93/1, Universität Hannover 1993.



- [116] von Mises, R.: Mechanik von plastischen Formänderung von Kristallen. *ZAMM* **8** (1928), 161–165.
- [117] Mualem, Y.: A new model for predicting the hydraulic conductivity of unsaturated porous media. *Water Resources Research* **12** (1976), 513–522.
- [118] Müllerschön, H.: *Spannungs-Verzerrungsverhalten granularer Materialien am Beispiel von Berliner Sand*. Dissertation, Bericht Nr. II-6 aus dem Institut für Mechanik (Bauwesen), Universität Stuttgart 2000.
- [119] Nelder, J. A. & Mead, R.: A Simplex Method for Function Minimization. *Computer Journal* **7** (1965), 308–313.
- [120] Noll, W.: A mathematical theory of the mechanical behavior of continuous media. *Archive for Rational Mechanics and Analysis* **2** (1958), 197–226.
- [121] Nova, R. & Wood, D. M.: A constitutive model for sand in triaxial compression. *International Journal for Numerical and Analytical Methods in Geomechanics* **3** (1979), 255–278.
- [122] Oka, F.; Kimoto, S.; Takada, N.; Gotoh, H. & Higo, Y.: A seepage-deformation coupled analysis of an unsaturated river embankment using a multiphase elasto-viscoplastic theory. *Soils and foundations* **50** (2010), 483–494.
- [123] Papamichos, E.; Tronvoll, J.; Skjaerstein, A. & Unander, T. E.: Hole stability of Red Wildmoor sandstone under anisotropic stresses and sand production criterion. *Journal of Petroleum Science and Engineering* **72** (2010), 78–92.
- [124] Papamichos, E. & Vardoulakis, I.: Sand erosion with a porosity diffusion law. *Computers and Geotechnics* **32** (2005), 47–58.
- [125] Pearce, J. A.: *The Behaviour of Soft Clay in a New True Triaxial Apparatus*. Ph. D. thesis, University of Cambridge 1971.
- [126] Perzyna, P.: Fundamental problems in viscoplasticity. *Advances in Applied Mechanics* **9** (1966), 243–377.
- [127] Poorooshasb, H. B.; Holubec, I. & Sherbourne, A. N.: Yielding and flow of sand in triaxial compression: Part I. *Canadian Geotechnical Journal* **3** (1966), 179–190.
- [128] Poorooshasb, H. B.; Holubec, I. & Sherbourne, A. N.: Yielding and flow of sand in triaxial compression: Parts II and III. *Canadian Geotechnical Journal* **4** (1967), 376–397.
- [129] Rao, S. S.: *Engineering optimization: theory and practice*. Wiley, New York 2009.
- [130] Rempfer, H.-U.: *Damage in Multi-Phasic Materials Computed with the Extended Finite-Element Method*. Dissertation, Report No. II-23 of the Institute of Applied Mechanics (CE), University of Stuttgart 2012.

- [131] Rumpf, M.; Böniger, U. & Tronicke, J.: Refraction seismics to investigate a creeping hillslope in the Austrian alps. *Engineering Geology* **151** (2012), 37–46.
- [132] Schanz, M. & Struckmeier, V.: Wave propagation in a simplified modelled poro-elastic continuum: Fundamental solutions and a time domain boundary element formulation. *International Journal for Numerical Methods in Engineering* **64** (2005), 1816–1839.
- [133] Scheday, G.: *Theorie und Numerik der Parameteridentifikation von Materialmodellen der finiten Elastizität und Inelastizität auf der Grundlage optischer Feldmeßmethoden*. Dissertation, Bericht Nr. I-10 aus dem Institut für Mechanik (Bauwesen), Universität Stuttgart 2003.
- [134] Scheuermann, A.; Steeb, H. & Kiefer, J.: Theory and numerics of erosion processes in fluid-saturated porous media. In Papanastasiou, P.; Papamichosa, E.; Zervos, A. & Stavropoulou, M. (Eds.): *9th International Congress of the Hellenic Society of Theoretical and Applied Mechanics (HSTAM)*. The Hellenic Society for Theoretical and Applied Mechanics 2010, pp. 275–282.
- [135] Schittkowski, K.: Solving nonlinear least squares problems by a general purpose SQP-method. *Trends in Mathematical Optimization* **84** (1988), 295–309.
- [136] Schittkowski, K.: *Optimization in Industrial Engineering: SQP-Methods and Applications*. Technical Report, Radioss User Meeting, Mecalog, Nice, June 2005.
- [137] Scholz, B.: *Application of a Microplar Model to the Localization Phenomena in Granular Materials*. Dissertation, Report No. II-15 of the Institute of Applied Mechanics (CE), University of Stuttgart 2007.
- [138] Schrefler, B. A.: Computer modelling in environmental geomechanics. *Computers and Structures* **79** (2001), 2209–2223.
- [139] Schrefler, B. A.; Sanavia, L. & Majorana, C.: A multiphase media model for localization and post-localization simulation in geomaterials. *Mechanics of Cohesive-frictional Materials* **1** (1996), 95–114.
- [140] Schrefler, B. A. & Scotta, R.: A fully coupled model for two-pase flow in deformable porous media. *Computer Methods in Applied Mechanics and Engineering* **190** (2001), 3223–3246.
- [141] Schwarz, H. R.: *Methode der finiten Elemente*. Teubner, Stuttgart 1991.
- [142] Schwefel, H.-P.: *Evolution and optimum seeking*. Wiley, New York 1995.
- [143] Simo, J. C. & Hughes, T. J. R.: General return mapping algorithms for rate independent plasticity. In Desai, C. S. (Ed.): *Constitutive Laws for Engineering Materials: Theory and Applications*. Elsevier Science Publishing, New York 1987, pp. 221–231.
- [144] Simo, J. C. & Hughes, T. J. R.: *Computational inelasticity*. Springer, New York 2000.

- [145] Simo, J. C. & Taylor, R. L.: Consistent tangent operators for rate-independent elastoplasticity. *Computer Methods in Applied Mechanics and Engineering* **48** (1985), 101–118.
- [146] Skempton, A. W.: Significance of Terzaghi's concept of effective stress (Terzaghi's discovery of effective stress). In Bjerrum, L.; Casagrande, A.; Peck, R. B. & Skempton, A. W. (Eds.): *From Theory to Practice in Soil Mechanics*. Wiley, New York 1960, pp. 42–53.
- [147] Spellucci, P.: *Numerische Verfahren der nichtlinearen Optimierung*. Birkhäuser, Basel 1993.
- [148] Spellucci, P.: A new technique for inconsistent QP problems in the SQP-Method. *Mathematical Methods of Operations Research* **47** (1998), 335–400.
- [149] Spellucci, P.: A SQP method for general linear programs using only equality constrained subproblems. *Mathematical Programming* **82** (1998), 413–448.
- [150] Steeb, H.: Internal erosion in gas-flow weak conditions. *American Institute of Physics* **1227** (2010), 115–134.
- [151] Steeb, H. & Diebels, S.: A thermodynamic-consistent model describing growth and remodeling phenomena. *Computational Materials Science* **28** (2003), 597–607.
- [152] Steeb, H.; Diebels, S. & Vardoulakis, I.: Theory and numerics of erosion processes in fluid-saturated porous media. In Vermeer, P. A.; Ehlers, W.; Herrmann, H. J.; & Ramm, E. (Eds.): *Modelling of Cohesive-Frictional Materials*. Taylor and Francis, London 2004, pp. 307–319.
- [153] Steeb, H.; Diebels, S. & Vardoulakis, I.: Modeling internal erosion in porous media. In Siegel, T. C.; Luna, R.; Hueckel, T. & Laloui, L. (Eds.): *Computer Applications In Geotechnical Engineering*. American Society of Civil Engineers 2007, pp. 1–10.
- [154] Sterpi, D.: Effects of the Erosion and Transport of Fine Particles due to Seepage Flow. *International Journal of Geomechanics* **3** (2003), 1532–364.
- [155] Tatsuoka, F. & Ishihara, K.: Yielding of sand in triaxial compression. *Soils and Foundations* **14** (1974), 63–76.
- [156] Tremblay, B. & Oldakowski, K.: Wormhole growth and interaction in a large sand pack. *Journal of Petroleum Science and Engineering* **34** (2002), 13–32.
- [157] Tremblay, B.; Sedgwick, G. & Forshner, K.: Imaging of sand production in a horizontal sand pack by X-ray computed tomography. *SPE Reservoir Engineering Formation Evaluation* **11** (1996), 94–98.
- [158] Tremblay, B.; Sedgwick, G. & Forshner, K.: Simulation of cold production in heavy-oil reservoirs: wormhole dynamics. *SPE Reservoir Engineering* **12** (1997), 110–117.

- [159] Tronvoll, J. & Fjaer, E.: Experimental study of sand production from perforation cavities. *International Journal of Rock Mechanics and Mining Sciences & Geomechanics Abstracts* **31** (1994), 393–410.
- [160] Truesdell, C.: *Rational Thermodynamics*, 2nd Edition. Springer-Verlag, New York 1984.
- [161] Truesdell, C.: Thermodynamics of diffusion. In Truesdell, C. (Ed.): *Rational Thermodynamics*. 2nd Edition, Springer-Verlag, New-York 1984, pp. 219–236.
- [162] Truesdell, C. & Noll, W.: *The Nonlinear Field Theories of Mechanics*. Band III/3., Springer-Verlag, Berlin 1965.
- [163] Truesdell, C. & Toupin, R. A.: The classical field theories. In Flügge, S. (Ed.): *Handbuch der Physik*. Vol. III/1, Springer-Verlag, Berlin 1960, pp. 226–902.
- [164] Tsaparas, I.; Rahardjo, H.; Toll, D. G. & Leong, E. C.: Controlling parameters for rainfall-induced landslides. *Computers and Geotechnics* **29** (2002), 1–27.
- [165] Vallejo, L. E.: Interpretation of the limits in shear strength in binary granular mixtures. *Canadian Geotechnical Journal* **38** (2001), 1097–1104.
- [166] Vallejo, L. E. & Mawby, R.: Porosity influence on the shear strength of granular material-clay mixtures. *Engineering Geology* **58** (2000), 125–136.
- [167] Vardoulakis, I.: Fluidisation in artesian flow conditions: Hydromechanically unstable granular media. *Géotechnique* **54** (2004), 165–177.
- [168] Vardoulakis, I.; Stavropoulou, M. & Papanastasiou, P.: Hydro-mechanical aspects of the sand production problem. *Transport in Porous Media* **22** (1996), 225–244.
- [169] Walter, M.; Walser, M. & Joswig, M.: Mapping Rainfall-Triggered Slidequakes and Seismic Landslide-Volume Estimation at Heumoes Slope. *Vadose Zone Journal* **10** (2011), 487–495.
- [170] Wan, C. F. & Fell, R.: Assessing the potential of internal instability and suffusion in embankment dams and their foundations. *Journal of Geotechnical and Geoenvironmental Engineering* **134** (2008), 401–407.
- [171] Wan, R. & Wang, J.: Modelling of sand production and wormhole propagation in an oil saturated sand pack using stabilized finite element methods. *Journal of Canadian Petroleum Technology* **43** (2004), 45–52.
- [172] Wan, R. G. & Wang, J.: Modelling of sand production and erosion growth under combined axial and radial flows. *Journal of Canadian Petroleum Technology* **43** (2004), 33–38.
- [173] Wang, J. & Wan, R.: Computation of sand fluidization phenomena using stabilized finite elements. *Finite Elements in Analysis and Design* **40** (2004), 1681–1699.

- [174] Wang, Q. & Lade, P.: Shear banding in true triaxial tests and its effect on failure in sand. *Journal of Engineering Mechanics* **127** (2001), 754–761.
- [175] Wieners, C.: Taylor-Hood elements in 3D. In Wendland, W. L. & Efendiev, M. (Eds.): *Analysis and Simulation of Multifield Problems*. Springer-Verlag, Berlin 2003, pp. 189–196.
- [176] Wieners, C.; Ammann, M.; Diebels, S. & Ehlers, W.: Parallel 3-d simulations for porous media models in soil mechanics. *Computational Mechanics* **29** (2002), 73–87.
- [177] Wieners, C.; Ammann, M. & Ehlers, W.: Distributed point objects: a new concept for parallel finite elements applied to a geomechanical problem. *Future Generation Computer Systems* **22** (2006), 532–545.
- [178] Wienhöfer, J.; Lindenmaier, F. & Zehe, E.: Challenges in Understanding the Hydrologic Controls on the Mobility of Slow-Moving Landslides. *Vadose Zone Journal* **10** (2011), 496–511.
- [179] Wood, D. M.; Maeda, K. & Nukudani, E.: Modelling mechanical consequences of erosion. *Géotechnique* **60** (2010), 447–457.
- [180] Wriggers, P.: *Nonlinear Finite Element Methods*. Springer Berlin Heidelberg 2008.
- [181] Yamada, Y. & Ishihara, K.: Anisotropic deformation characteristic of sand under three dimensional stress conditions. *Soils and Foundation* **19** (1979), 79–94.
- [182] Yamamuro, Y. & Lade, P. V.: Drained sand behaviour in axisymmetric tests at high pressures. *Journal of Geotechnical Engineering* **122** (1996), 109–119.
- [183] Ziems, J.: *Beitrag zur Kontakterosion nichtbindiger Böden in porösen Medien*. Dissertation, Universität Dresden 1969.
- [184] Zienkiewicz, O. C. & Taylor, R. L.: *The Finite Element Method: The Basis*, 5 Edition, Vol. 1. Butterworth-Heinemann, London 2000.
- [185] Zienkiewicz, O. C. & Taylor, R. L.: *The Finite Element Method: Solid Mechanics*, 5 Edition, Vol. 2. Butterworth-Heinemann, London 2000.



# Curriculum Vitae

## Personal Data:

Name:	Okan Avci
Address:	Reuchlinstraße 2 70 178 Stuttgart
Date and place of birth:	March 25, 1977 in Waldshut-Tiengen, Germany
Nationality:	German
Marital status:	unmarried

## Education:

09/1982 – 07/1986	elementary school “Grundschule”: Schalksburgschule Albstadt
09/1986 – 07/1992	secondary school “Hauptschule”: Schalksburgschule Albstadt
09/1992 – 07/1993	secondary school “Werkrealschule”: Hohenbergschule Albstadt
09/1993 – 06/1996	secondary “Wirtschaftsgymnasium”: Kaufmännische Schule Albstadt
06/1996	degree: “Allgemeine Hochschulreife” (high school diploma)
10/1996 – 10/2004	studies in civil engineering at the University of Stuttgart major subject: “Konstruktives Bauingenieurwesen”
10/2004	degree: “Diplom-Ingenieur (Dipl.-Ing.) Bauingenieurwesen”

## Professional Occupation:

01/2005 – 12/2011	Teaching Assistant and Research Associate at the Institute of Applied Mechanics (Civil Engineering) at the University of Stuttgart
04/2013 – 08/2013	Computational Engineer at the LASSO Ingenieurgesellschaft mbH



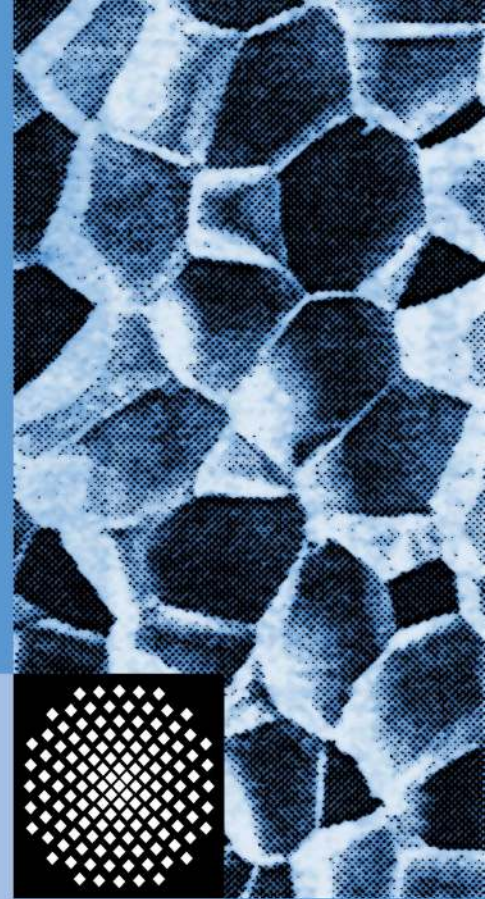


## Released Report Series

- II-1 Gernot Eipper: *Theorie und Numerik finiter elastischer Deformationen in fluid-gesättigten porösen Festkörpern*, 1998.
- II-2 Wolfram Volk: *Untersuchung des Lokalisierungsverhaltens mikropolarer poröser Medien mit Hilfe der Cosserat-Theorie*, 1999.
- II-3 Peter Ellsiepen: *Zeit- und ortsadaptive Verfahren angewandt auf Mehrphasenprobleme poröser Medien*, 1999.
- II-4 Stefan Diebels: *Mikropolare Zweiphasenmodelle: Formulierung auf der Basis der Theorie Poröser Medien*, 2000.
- II-5 Dirk Mahnkopf: *Lokalisierung fluidgesättigter poröser Festkörper bei finiten elasto-plastischen Deformationen*, 2000.
- II-6 Heiner Müllerschön: *Spannungs-Verformungsverhalten granularer Materialien am Beispiel von Berliner Sand*, 2000.
- II-7 Stefan Diebels (Ed.): *Zur Beschreibung komplexen Materialverhaltens: Beiträge anlässlich des 50. Geburtstages von Herrn Prof. Dr.-Ing. Wolfgang Ehlers*, 2001.
- II-8 Jack Widjajakusuma: *Quantitative Prediction of Effective Material Parameters of Heterogeneous Materials*, 2002.
- II-9 Alexander Droste: *Beschreibung und Anwendung eines elastisch-plastischen Materialmodells mit Schädigung für hochporöse Metallschäume*, 2002.
- II-10 Peter Blome: *Ein Mehrphasen-Stoffmodell für Böden mit Übergang auf Interface-Gesetze*, 2003.
- II-11 Martin Ammann: *Parallel Finite Element Simulations of Localization Phenomena in Porous Media*, 2005.
- II-12 Bernd Markert: *Porous Media Viscoelasticity with Application to Polymeric Foams*, 2005.
- II-13 Saeed Reza Ghadiani: *A Multiphasic Continuum Mechanical Model for Design Investigations of an Effusion-Cooled Rocket Thrust Chamber*, 2005.
- II-14 Wolfgang Ehlers & Bernd Markert (Eds.): *Proceedings of the 1st GAMM Seminar on Continuum Biomechanics*, 2005.
- II-15 Bernd Scholz: *Application of a Micropolar Model to the Localization Phenomena in Granular Materials: General Model, Sensitivity Analysis and Parameter Optimization*, 2007.

- II-16 Wolfgang Ehlers & Nils Karajan (Eds.): *Proceedings of the 2nd GAMM Seminar on Continuum Biomechanics*, 2007.
- II-17 Tobias Graf: *Multiphasic Flow Processes in Deformable Porous Media under Consideration of Fluid Phase Transitions*, 2008.
- II-18 Ayhan Acartürk: *Simulation of Charged Hydrated Porous Materials*, 2009.
- II-19 Nils Karajan: *An Extended Biphasic Description of the Inhomogeneous and Anisotropic Intervertebral Disc*, 2009.
- II-20 Bernd Markert: *Weak or Strong – On Coupled Problems In Continuum Mechanics*, 2010.
- II-21 Wolfgang Ehlers & Bernd Markert: *Continuum Biomechanics*, 2012.
- II-22 Wolfgang Ehlers: *Poröse Medien - ein kontinuumsmechanisches Modell auf Basis der Mischungstheorie*, 2012. Nachdruck der Habilitationsschrift aus dem Jahre 1989 (Forschungsbericht aus dem Fachbereich Bauwesen der Universität-GH-Essen, **47**, Essen 1989).
- II-23 Hans-Uwe Rempler: *Damage in Multi-Phasic Materials Computed with the Extended finite-Element Method*, 2012.
- II-24 Irina Komarova: *Carbon-Dioxide Storage in the Subsurface: A Fully Coupled Analysis of Transport Phenomena and Solid Deformation*, 2012.
- II-25 Yousef Heider: *Saturated Porous Media Dynamics with Application to Earthquake Engineering*, 2012.
- II-26 Okan Avci: *Coupled Deformation and Flow Processes of Partially Saturated Soil: Experiments, Model Validation and Numerical Investigations*, 2013.





ISBN 3-937399-26-7  
(D 93 – Dissertation, Universität Stuttgart)